UNIVERSITY OF THE
WITWATERSRAND,
JOHANNESBURG

Synthesis of photocatalysts/heterojunctions for abatement of a specific pollutant in aqueous media

Ashiegbu Darlington C.

1580874

Supervisors:

Prof J.H. Potgieter

Dr. A. Kuvarega

A thesis submitted to the Faculty of Engineering and the Built Environment, University of the Witwatersrand, Johannesburg, in fulfilment of the requirements for the degree of Doctor of Science in Engineering.

Johannesburg, 2022

Declaration

I declare that this thesis is my unaided work. It is being submitted for the degree of Doctor of Philosophy in Engineering to the University of the Witwatersrand, Johannesburg. It has not been submitted before for any degree or examination to any other University, and all sources I have used or quoted have been indicated and acknowledged by means of complete references.

D.C.A

Darlington .C. Ashiegbu

30th day of May 2022

Dedication

To my late Father Lemmy Ashiegbu, you saw ahead. Keep resting Dad.

To my loving and supporting fiancée, Ntsako Mkhabela

To my kids, Chimamanda Ashiegbu and Somtochukwu Ashiegbu

To my loving and sweet mother, Bernadette Ashiegbu

To my only sibling, Chinelo Lilian Ashiegbu

Acknowledgement

My warmest gratitude goes to Prof J.H. Potgieter who doubles as my supervisor for his continued support throughout my PhD study. For his inspiration, endurance, willingness to help and tremendous knowledge. Prof, your encouragement supported me all through my research. Your support all through my studies kept me going. Sir, you are a great counsellor and tutor, may God bless you and your family abundantly. My sincere gratitude to Dr Alex Kuvarega, my co-supervisor. Thank you Sir for your ideas, inputs and help in directing the study focus.

To my family, friends, colleagues and fellow students, thank you all for your support and assistance.

Many thanks to Mr Phali Caleb Motlasi, Petra Dinham, Hopewell Gumede, Dr Michael Bodunrin, Shola Akingbami, Dr Thomas Aniokete, Ugochukwu Ikegwu and Stanley Okamgba. Thank you guys for assisting and guiding me through my experiments.

My special thanks to Prof Nosipho Moloto of Wits School of Chemistry, Dr Rudolph Erasmus and all the staff at Wits MMU.

I would also like to thank all staff members at the School of Chemical and Metallurgical Engineering for their support.

Finally, I would like to thank NRF-TWAS African Renaissance PhD Fellowship Programme [Grant number: 99776]

List of Publications

Ashiegbu, D.C., Potgieter, H. Facile synthesis of photocatalysts for photocatalytic abatement of 2-chlorobiphenyl. SACEC 2021. ISBN 978-1-991213-99-0.

Ashiegbu, D.C., Potgieter, H. Photodestruction of 2-chlorobiphenyl with a series of photocatalysts and heterostructures utilizing simulated solar radiation. Acta Chimica Slovenica. 2022. (**Under review**).

Gordon, A., Leaper, M.C., Potgieter, H., **Ashiegbu, D.C**, Sibanda, V. Treatment of dark humic water using Photocatalytic Advanced Oxidation (PAO) processes under visible and UV light. Water and Environment Journal. 2022. (**Under review**).

Ashiegbu, D.C., Nosipho, M., Potgieter, H. Superior performance of a ZnO-10%BiOI photocatalyst in the destruction of 2-Chlorobiphenyl. Chemical Engineering Communications. 2022. (**Under review**).

Potgieter, H and **Ashiegbu, D.C**. Effect of some process parameters by a heterojunction assisted photodestruction of 2CBP. (**Currently being developed**)

Table of Contents

Table of Figures

List of Tables

Acronyms

2CBP	2-chlorobiphenyl
AOPs	Advanced oxidation process
BET	Brunauer, Emmett and Teller specific surface area
BG	Band gap
BiOI	Bismuth oxyiodide
BJH	Barrett-Joyner-Halenda Pore Size and Volume Analysis
CB	Conduction band
DI	Deionized water
e^-	Electron
EDS	Energy dispersive x-ray spectroscopy
EtOH	Ethanol
Ev	Electron volts
FE-SEM	Field emission scanning electron microscope
FWHM	Full width at half maximum
h^+	Holes
KI	Potassium iodide
MB	Methylene blue
MO	Methylene orange
NPs	Nanoparticles
O2-	Superoxide anion
OH	Hydroxyl radical
POPs	Persistent organic pollutants
PZC	Point of zero charge
RhB	Rhodamine blue
RPM	Revolutions per minute
SSA	Specific surface area
UV	Ultra violet
UV-Vis	Ultraviolet visible
VB	Valence band
VOCs	Volatile organic compounds
WO_3	Tungsten oxide
XRD	X-ray diffraction
ZAD	Zinc acetate dihydrate

Abstract

The current organic pollutant abatement practices are mostly unsustainable, inefficient, ineffective and in some instances inadequate. In some cases, these applications have been known to convert contaminants from one phase to another, causing extra costs in order to eliminate secondary pollutants. Photocatalysis is capable of in-situ production of OH, and O_2^- in addition to the production of electrons and holes for the remediation of organic pollutants into less harmful products. Metal oxide semiconductor photocatalysts like ZnO and WO_3 are of importance in wastewater remediation under solar irradiation (UV/visible) due to their unique features including non-toxicity, easy synthesis, suitable band edge positions and photogeneration of active oxygen species in aqueous media. BiOI, which is a ternary metal oxide semiconductor, has also received excellent reviews in this regard, owing to its visible light absorption property and stability. Unfortunately, these photocatalysts are plagued by the same problem of quick charge carrier recombination. This work reports the semiconductor assisted photodegradation of 2-chlorobiphenyl which is a chemically and biologically stable pollutant in addition to its persistence in aqueous media. Previous studies of 2CBP only utilized TiO_2 for the degradation of 2CBP in very low concentration. This thesis consists of **five main parts**. The **first part** is concerned with the synthesis of ZnO, WO_3, BiOI and heterostructures of ZnO-WO_3 and ZnO-BiOI with different weight loadings of WO_3 and BiOI respectively. Direct, facile and fast synthesis techniques were used in the synthesis of all the semiconductor photocatalysts in this work. The **second part** deals with the characterization of all the as synthesized photocatalysts. Various characterization techniques such as surface morphology (SEM), elemental analysis (EDS), specific surface area measurements (BET), crystallinity (XRD) and optical studies (UV-vis spectrophotometer) were employed. The mean crystallite sizes were established from the diffraction peaks using the Debye-Scherrer relation, while the optical BG were estimated using Tauc plots from the UV-vis absorption spectra. Observations from the SEM images showed diverse morphologies for all the as prepared photocatalysts. EDS results revealed only the presence of the reference elements with good stoichiometric values, thus depicting purity of the samples and excellent synthesis. The XRD patterns showed crystalline patterns with no impurity peaks. The XRD data also showed that the introduction of WO_3 and BiOI into the ZnO lattice were successful. Slight red shifts in the absorbance of ZnO as WO_3 and BiOI were incorporated into ZnO were observed. The absorption tails of the heterostructures were well inside the visible light region. All the calculated band gaps decreased/narrowed with increased content of WO_3 and BiOI into ZnO (5, 10 20 %), with the exception of ZnO-WO_3 10 %. The calculated band gaps were **3.24, 2.0, 1.23, 3.08, 3.0, 2.20, 2.56, 3.16, 2.17 eV** representing the band gap values for **ZnO, WO_3, BiOI, ZnO-BiOI 5 %, ZnO-BiOI 10 %, ZnO-BiOI 20 %, ZnO-WO_3 5 %, ZnO-WO_3 10 % and ZnO-WO_3 20 %** respectively. Nitrogen adsorption-desorption isotherms indicated that nearly all the composites were of the Type IV isotherm. Increments in the surface area measurements were observed in the heterostructures when compared with the bare and undoped composites. The **third part** of this thesis focused on the application of the as synthesized photocatalysts in the photocatalytic degradation of 2-chlorobiphenyl (2CBP). BiOI (49 %) was observed to exhibit the best photocatalytic activity when compared with ZnO and WO_3 for the bare and undoped catalysts, while ZnO-BiOI 10 % (57 %) showed the best photo-activity for all the catalysts in the degradation of 2CBP. ZnO-WO_3 10 % (53 %) also showed significant activity in this regard. The **fourth part** of the thesis deals with reaction kinetics of the pollutant destruction by the various photocatalysts The kinetics of the photocatalytic reactions were fitted to a pseudo-first order kinetics model. The ZnO-BiOI 10 % composite exhibited the highest rate constant of **0.0054 min^{-1}**. Observations from the kinetic modelling also show that ZnO-WO_3 10 % exhibited significant photocatalytic activity when compared to ZnO-WO_3 20 % and ZnO-WO_3 5 % (**0.0049, 0.0016, 0.0019 min^{-1},** respectively). BiOI showed the highest photocatalytic

performance among the undoped photocatalysts, with a calculated rate constant of 0.0029 min^{-1}, which was over 2 fold higher than its bare counterparts (ZnO – 0.0012; WO_3-0.0010 min^{-1}). The R-square values obtained affirm that the photocatalytic degradation experiments all follow a pseudo-first order kinetic model. The **fifth part** of this study focused on the influence of different process parameters and conditions on the photodegradation of 2CBP, when using the most efficient catalyst (ZnO-BiOI 10 %.) Photodegradation of 2CBP decreased under very acidic conditions (pH 2: 20 %) and decreased more significantly in alkaline media (pH 11.3: 5 %), The most efficient activity was observed at the natural pH of the 2CBP solution (pH 7.2: 57 %). When the concentration of 2CBP was varied at 20, 35 and 50 ppm, photodegradation efficiency reduced. At lower concentrations of 5 and 10 ppm, there was an observed improvement in the photocatalytic activity. When the initial catalyst dose was doubled to 70 mg, the photocatalytic efficiency improved to 71 %. At much higher catalyst doses of 85 (68 %), 100 (30 %) and 150 (4 %) mg, the photocatalytic activity reduced. Thus, the optimum efficiency in this work was observed at 35 mg catalyst weight, 10 ppm pollutant concentration at a pH of 7.2. A proposed photodegradation mechanism of ZnO-BiOI 10 % was put forward for the degradation of 2CBP.

1. INTRODUCTION

1.1 Background

The meteoric growth of the human population worldwide, coupled with accelerated industrial growth and energy demands, the emission of toxic pollutants and industrial wastes into the air, water, and land, has led to the contamination of our environment, climate change, and an increase in diseases. Nearly four hundred million tons of volatile organic compounds (VOCs), persistent organic pollutants (POPs), heavy metals, toxic sludge, solvents etc. are dumped by industries into water bodies globally, which cause adverse environmental problems (Xiao *et al*., 2015). Industrial effluent discharge is an ever-present issue challenging access to potable water globally. Humans and indeed all life forms all over the world are severely affected as a result of the consumption of impure water and the presence of organic, inorganic, and microbial contaminants in water (Bora & Mewada, 2017). Consequently, remediation/clean-up of organic pollutants have become increasingly necessary. However, the process is expensive, costing nations and corporations a lot of money. In order to achieve pollutant and carbon free water, it has become imperative to develop and implement artificial methods for water and waste water treatment for the survival of the human race (Colmenares *et al*., 2015).

The current practises in organic pollutant remediation (ozonation, reverse osmosis, filtration, adsorption, biological treatment, coagulation, incineration) have been reported to be inefficient and inadequate (García-Montaño *et al*., 2008). Incineration can result in the emission of toxic volatile gases, while physical methods (adsorption, filtration, reverse osmosis, coagulation) have been reported to be expensive and may not totally eliminate organic pollutants, but may transform them to harmful intermediates (Vinita *et al*., 2010; Zelmanov & Semiat, 2008). A long treatment time is required in biological treatment processes, coupled with the presence of toxic and recalcitrant pollutants immune to the aforementioned, which may also cause unpleasant odours. Ozonation, although effective in some cases, has been reported to be unstable and also affected by temperature, pH and salts (García-Montaño *et al.,* 2008). For example, liquid effluents can be adsorbed onto a solid adsorbent which treats the liquid, but the pollutant is transferred onto the adsorbent which becomes the new pollutant. This means that the process merely converted the contaminant from liquid to solid phase, thus leading to extra costs and treatments to eliminate the secondary pollutants (Ong *et al*., 2018; Bora & Mewada, 2017).

In light of these issues, a pressing demand exists for the advancement and implementation of novel advanced treatment technologies for organic pollutant abatement in water and wastewater resources (Pirhashemi *et al*., 2018). Advanced Oxidation Processes (AOPs) have received a lot of attention (research) in the last two decades and are now being used in organic pollutant abatement because they are inexpensive, efficient, and environmentally friendly. Advanced oxidation processes (shown in Figure 1.1) are capable of in-situ production of hydroxyl radicals (OH), superoxide anion (O_2^-), and electron/hole (e^-/h^+) pairs for remediation of organic pollutants into CO_2, H_2O and less harmful products (Swaminathan *et al*., 2014; Colmenares *et al*., 2015; Pirhashemi *et al*., 2018). Amongst the various AOPs (Fenton Processes, UV/H_2O_2, $O_3/H_2O_2/UV$, O_3/UV, photocatalysis etc) as shown in Figure 1.1, photocatalysis has been reported as the most novel, promising and “green” alternative. The various advanced oxidation processes are shown in Figure 1.1.

A variety of semiconductor photocatalysts (TiO_2, ZnO, Fe_2O_3, CdS, GaP and ZnS etc) have been deployed for the purpose of photo-oxidation of pollutants, with TiO_2 remaining the most studied and utilized material to date (Štrbac *et al*., 2018; Kusumam *et al*., 2016). This is because of its high oxidative power, economy, photostability, non-toxicity, chemical stability and quick electron transfer to molecular oxygen under UV light (Linsebigler *et al*., 1995; Dindar & Içli, 2001; Draper & Fox, 1990; Okte *et al*., 2001; Štrbac *et al*., 2018; Vu *et al*., 2013; Adhikari *et al*., 2015). Despite all listed positives, TiO_2 has been reported to suffer from major drawbacks, such as difficulty in recovering and utilization of fine titania powders (which has prevented its large scale utilization in photocatalytic processes), higher cost (compared with ZnO), high charge carrier recombination, and low absorption rate over the UV spectrum, amongst others (Pelizzetti & Minero, 1994; Dindar & Içli, 2001; Vu *et al.*, 2013; Mauro *et al.*, 2017; Ahmad *et al.*, 2016; Štrbac *et al.*, 2018; Scuderi *et al.*, 2014).

Due to their near identical bandgap, availability, similar degradation mechanism, large free-exciton binding energy (which ensures prolonged exciton emission even above room temperature), and lower cost, ZnO has been identified as a promising candidate capable of competing with TiO_2 because of the exhibition of better absorption efficiency over a larger percentage of the solar spectrum (Colmenares *et al.*, 2015; Ong *et al.*, 2018; Sakthivel *et al.*, 2003; Daneshvar *et al.*, 2004; Štrbac *et al.*, 2018; Adhikari *et al.*, 2015; Chiu *et al.*, 2010; Mauro *et al.*, 2017). In addition, several researchers suggested a higher efficiency of ZnO over TiO_2 in the generation of photoactive species, easy fabrication via crystal growth anchored on a variety of supports using low temperature, higher electron mobility (about two folds higher than TiO_2) and a higher quantum efficiency (in numerous studies) (Sakthivel *et al.*, 2003; Kusumam *et al.*, 2016; Vu *et al.*, 2013; Mauro *et al.*, 2017; Štrbac *et al.*, 2018; Law *et al.*, 2005; Chiu *et al.*, 2010; Samadi *et al.*,2015; Tian *et al.*, 2012; Daneshvar *et al.*, 2004; Anta *et al.*, 2012; Kansal *et al.*, 2008). Regrettably, ZnO also suffers from similar drawbacks as TiO_2 due to their wide bandgap, absorption only in the UV spectrum, high carrier recombination, vulnerability to dissolution at acidic pH, low quantum efficiency and photo-corrosion over prolonged illumination (in aqueous solutions).

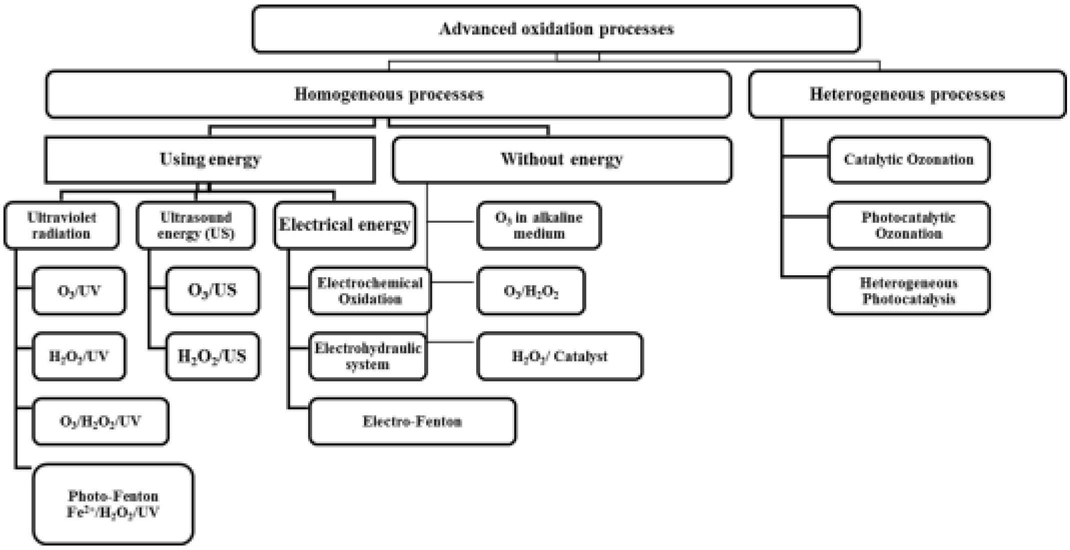

Figure 1. 1. AOT processes for waste water treatment (Tijani et al., 2014).

1.2. Problem Statement

These days, researchers are increasingly focused on overcoming the challenges and increasing the photocatalytic efficiency of ZnO photocatalysts. Several studies have suggested the narrowing of the wide bandgap through incorporation of metal or non-metal dopants, integration with other semiconductors with smaller bandgaps, construction of heterojunctions between two or more semiconductors, hydrogenation (annealing in hydrogen environment), anchoring on carbon nanostructures, etc. (Kumar & Rao, 2017; Kumar & Rao, 2015; Thejaswini *et al.*, 2017; Štengl *et al.*, 2015; Liu *et al.*, 2012; Ibhadon & Fitzpatrick, 2013; Yan *et al.*, 2013). These protocols have been reported to reduce the interfacial charge recombination as a result of Schottky barrier formation, increased surface oxygen vacancies, bandgap narrowing, improved structural stability and charge carrier separation kinetics. It also causes an improvement in light absorption efficiency above the UV range due to localized surface plasmon resonance (SPR) of the incorporated metal particles (when metal doping is utilized) (Wu *et al.*, 2012; Zheng *et al.*, 2013; Schneider *et al.*, 2014; Pirhashemi *et al.*, 2018; Jiang *et al.*, 2017; Wang *et al.*, 2017; Liu *et al.*, 2012).

Schneider *et al.* (2014) reported that metal incorporation of semiconductors causes the formation of small "oxide islands", that extend the lifetime of photogenerated e^-/h^+ pairs, and in turn intensifies the transfer process rate leading to increased photocatalytic activity. In addition, transition metal doping of semiconductors has been suggested to introduce electron capture sites, which could alter the crystallinity of the semiconductor and lead to reduced e^-/h^+ recombination centres. A variety of methodologies have been utilized for doping, such as: metal-ion implantation, chemical vapour deposition, sol-gel, wet impregnation and hydrothermal.

In this present study, the development of a cheap, fast and direct method to degrade 2-chlorobiphenyl (2CBP) in water through the development of photocatalysts configuration/design containing a combination of ZnO, and WO_3 or BiOI is proposed. This study has attempted to limit the recombination weaknesses associated with ZnO to increase its efficiency by etching with two low band gap semiconductors. The semiconductors BiOI and WO_3 were used due to their low band gap (~1.7 eV, ~2.7 eV respectively) which ensures the exploitation of a larger percentage of the solar spectrum. In addition, the positions of their conduction and valence bands are different from ZnO, which is important for a more effective separation of photoinduced e^-/h^+ and photodegradation (the band gaps of various semiconductors are shown in Figures 1.2 and 1.3). The as synthesized heterostructures are compared with the bare/undoped counterparts in order to ascertain the most efficient catalyst, with respect to the study.

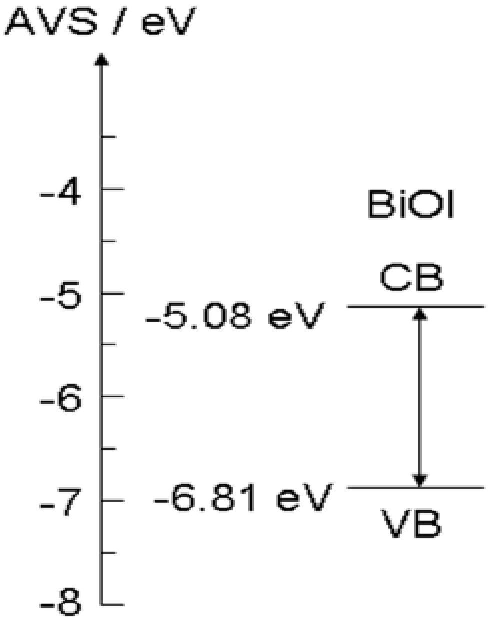

Figure 1. 2. Bang gap structure of BiOI showing the positions of VB and CB (Cheng et al., 2010)

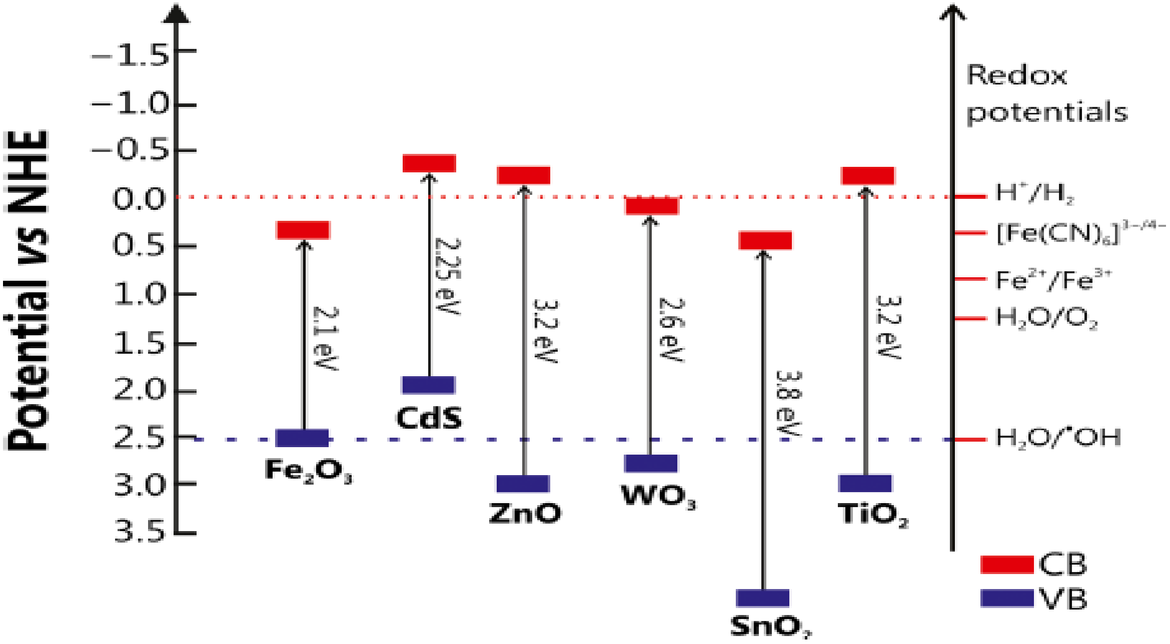

Figure 1. 3. Bandgap structures of WO_3 and ZnO showing their VB and CB positions (Bessegato et al., 2015).

1.3. Aim and Research Objectives

This study is aimed at the facile synthesis of photocatalysts in addition to developing metal oxide heterostructures and ternary oxide semiconductor heterostructures capable of degrading 2-chlorobiphenyl. The study also evaluates and compares the performance of the as synthesized photocatalysts to ascertain the most efficient one. Objectives of this research include (but are not limited to):

- To synthesize ZnO
- To synthesize WO_3
- To synthesize BiOI
- To construct ZnO-WO_3 heterostructures
- To fabricate ZnO-BiOI heterostructures
- To characterize the as synthesized ZnO, WO_3 and BiOI composites
- To characterize all as synthesized heterostructures
- To utilize ZnO, WO_3 and BiOI in the photodegradation of 2-chlorobiphenyl
- To investigate the use of various as prepared heterostructures in the photodegradation of 2-chlorobiphenyl
- To model the reaction kinetics of the photodegradation study
- To investigate the effect of pH on the photocatalytic degradation of 2CBP by application of the best performing photocatalyst and modelling the reaction kinetics

- To investigate the effect of initial pollutant concentration on the photocatalytic degradation of 2CBP by application of the best performing photocatalyst and modelling the reaction kinetics

- To investigate the effect of initial photocatalyst dose on the photocatalytic degradation of 2CBP by application of the best performing photocatalyst and modelling the reaction kinetics.

1.4. Research questions

Considering the aforementioned background, problem statement and aim of this study, this research was intended to provide answers to the following questions:

- Will the performance of ZnO improve with the etching of a metal oxide heterojunction?
- Will the performance of ZnO improve with the etching of a ternary oxide semiconductor?
- Will an increased surface area lead to a better photocatalytic activity?
- What is the optimum weight loading of BiOI/WO_3 on ZnO for the best photocatalytic activity?
- What will be the reaction kinetics of the photodegradation experiments?
- What effects do initial pollutant concentration, catalyst dose and pH have on the photocatalytic process and reaction kinetics?

1.5 Hypothesis

This research will attempt to show that 2-chlorobiphenyl can be degraded by the fabricated heterojunctions of ZnO-BiOI and ZnO-WO_3. Etching WO_3 and BiOI with ZnO will improve the photocatalytic activity of ZnO.

1.6. Research Scope

This study proposes to synthesize ZnO nanoparticles and subsequently modify it by the incorporation of WO_3 and BiOI. After the modification, the development of two composite heterojunctions with increased surface area, suppressed recombination and inhibited photocorrosion, efficient and effective charge electron-hole pairs separation, more active sites, narrowed band gap and ultimately utilize the clean and inexhaustible solar energy with some of the catalysts absorbing in the visible light region is proposed. The as synthesised photocatalysts will be used for the photocatalytic degradation of 2-chlorobiphenyl which is the model pollutant in this study. The research will investigate and model the reaction kinetics and the photodegradation mechanism. In addition, the catalyst with the best photocatalytic performance in the degradation of 2CBP will be identified.

From investigations, various studies have already been conducted and are still being conducted on the modification of ZnO for improved and efficient photodegradation activity. To the best of our knowledge, there are no studies in the area of synthesis and fabrication of ZnO-BiOI, and ZnO-WO_3 heterojunctions via a simple hydrothermal process at very low temperature for the photocatalytic destruction of 2-chlorobiphenyl. No studies using BiOI, ZnO-WO_3 and ZnO-BiOI for the photocatalytic destruction of 2-chlorobiphenyl have been identified. A comparison of the performance of all synthesized photocatalysts and heterojunctions will also be made.

1.7. Thesis lay-out

This thesis will be divided into 7 chapters, namely:

a) *Chapter 1 (Introduction)*: This chapter presents the project's background, problem statement, aim and objectives, research questions, hypothesis, scope of study, thesis outline and contribution to knowledge.

b) *Chapter 2 (Literature Review)*: In this chapter, available literature is reviewed. The literature review discusses structure and properties of ZnO, as well as previous studies on synthesis and photocatalysis of ZnO. Also discussed are the factors which affect the photocatalytic performance of ZnO, and strategies adopted towards modifying ZnO for enhanced photocatalytic activity. In addition, the dopants utilized in our study (WO_3 and BiOI) are reviewed with respect to knowledge gaps associated with the study. This chapter culminates with the discussion of our model pollutant and the gaps associated with its study.

c) *Chapter 3 (Materials and Methods)*: In this chapter, all materials, methods, and instruments used during this study are presented. In addition, the synthesis of the nanocomposites, the light source, the reagents, starting materials, pollutant, and the developed GC-MS procedure are discussed.

d) *Chapter 4 (Synthesis and characterization of ZnO, WO_3, BiOI, ZnO-BiOI, ZnO-WO_3 nanoparticles)*: This chapter presents the synthesis of ZnO, ZnO-BiOI and ZnO-WO_3 nanoparticles. It also discusses the various characterization techniques for the as synthesized nanoparticles and discussion of the findings from the various characterization measurements.

e) Chapter 5 (Photocatalytic degradation of 2-chlorobiphenyl using ZnO, BiOI, WO_3, ZnO-BiOI, ZnO-WO_3): This chapter discusses the photocatalytic study on the degradation of 2-chlorobiphenyl using our fabricated photocatalysts. The various weight loadings of BiOI and WO_3 and their effects on the photocatalytic efficiency are also highlighted. This chapter also identifies the best performing photocatalyst and subsequently discusses the photocatalytic degradation mechanism.

f) Chapter 6 (Experimental variables such as; effect of pH, effect of catalyst dose, effect of pollutant concentration): This chapter follows from our previous chapter where all the as synthesized catalysts have been applied for the abatement of 2-chlorobiphenyl. The photocatalyst with the observed best photocatalytic efficiency will be tested for experimental variables such pH, catalyst dose, and pollutant concentration. The reaction kinetics of the photocatalytic process are also modelled in this chapter

g) *Chapter 7 (Conclusions and recommendations)*

1.8. Contribution to knowledge

The following research contributions were made from this study:

- A 10 % ZnO-BiOI was identified as the optimum loading on ZnO to form a heterostructure for the best photocatalytic activity.
- As loading of WO_3/BiOI on ZnO increased, increase in surface area did not follow any particular trend.
- The smallest bandgap did not necessarily exhibit the best photocatalytic activity in this research.
- A GC-MS procedure was developed for the quick identification and monitoring of 2CBP for the photocatalytic process. This procedure takes into consideration and addresses the quick fragmentation of the 2CBP.
- Kinetic models of pseudo-first order was developed for the all the photocatalytic degradation experiments in this research, including for effects of initial pollutant concentration, catalyst dose and pH.

In conclusion, a promising photocatalyst was developed which can be applied in water treatment to cause the destruction of common and recalcitrant organic pollutants in a safe and effective manner. This new knowledge in the field can find wide potential application in industry.

2. LITERATURE REVIEW

2.1. PROPERTIES AND STRUCTURE OF ZnO

For several years, ZnO (polycrystalline) had been used in a variety of applications, such as paint pigmentation, sunscreen, facial powders, piezoelectric transducers, transparent conduction electrodes, etc. (Lettieri *et al.*, 2009). Over the past two decades, ZnO (which is a II-IV semiconductor) has attracted a lot of research interest as a result of the advancement of new synthesis methods for fabricating high quality one dimensional crystals for use in electronic and optoelectronic devices and also its interesting properties such as a direct and wide bandgap (3.2eV - 3.37eV), absorption in the near UV range, transparent conductivity, piezoelectricity, large excitation binding energy (60meV) (which could guarantee efficiency in excitonic emission at room temperature), its amphoteric nature, and deep violet/borderline ultraviolet absorption at room temperature. In addition, ZnO has an effective electron mass (M*) of 0.24-0.30m_e, effective hole mass (m_h*) of 0.45- 0.60m_e, and electron hole mobility of 200 $cm^2 V^{-1} s^{-1}$. These properties make ZnO tolerant to large electric fields, operations requiring high-power and elevated temperature (Choi *et al.*, 2012; Jagadish & Pearton, 2006; Behera, 2008; Taylor *et al.*, 2012; Wang *et al.*, 2004; Rao & Kumar, 2012; Lee *et al.*, 2016; Yang, 2010; Johar *et al.*, 2015).

At ambient pressure and temperature, the ZnO structure is usually present as the hexagonal wurtzite phase, which consists of alternating planes placed on vertexes of a tetrahedron with lattice parameters $a=0.3296$ *nm and* $c=0.5206$ *nm*. The piezoelectricity and pyroelectric properties of ZnO is suggested to be as a result of its tetrahedron configuration, which makes it suitable for use as a sensor, energy generation, acoustic wave resonators and acoustic-optic modulators, converter and photocatalysis (Naveed Ul Haq et al., 2017; Lettieri *et al.*, 2009; Peirò, 1999; Coleman & Jagadish, 2006; Wang, 2008) . In addition, Coleman & Jagadish

(2006) stated that the polarity of ZnO is responsible for its spontaneous polarization, growth, etching and defect generation.

ZnO is one of a few compounds which has been synthesized in a variety of different structures as shown in Figure 2.1. As evinced in Figure 2.2, ZnO can occur as 1-dimensional structures (nanorods, nanoneedles, nanotubes, nanowires etc), 2-dimensional structures (nanospheres, nanoplates, nanopellets etc) and 3-dimensional (nanoflowers, dandelions, coniferous urchin-like etc) (Banerjee *et al*., 2003; Hahn, 2011; Frade *et al*., 2012; Wahab *et al*., 2007; Wu *et al.*, 2002; Chen *et al.*, 2007; Liu *et al*., 2005; Nikoobakht *et al*., 2013; Chiu *et al*., 2010; José-Yacamán *et al*., 2005; Polshettiwar *et al.*, 2009; Xie *et al*., 2005; Bitenc & Crnjak Orel, 2009; Liu *et al*., 2006).

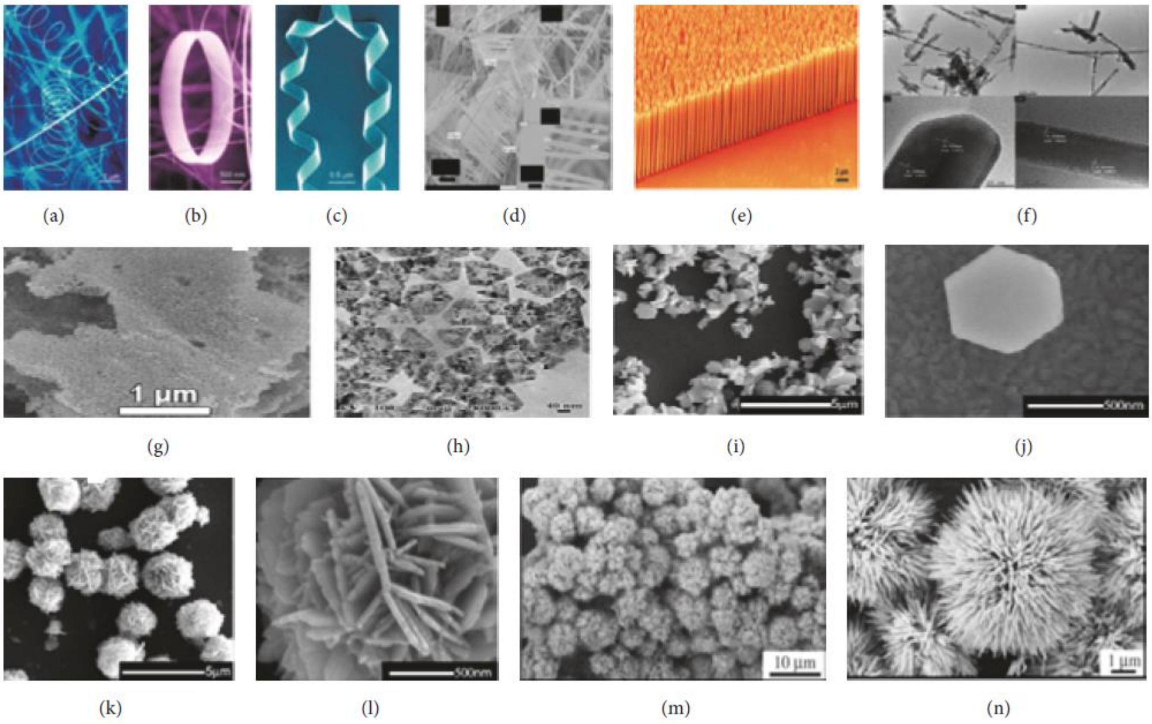

Figure 2. 1. Structures of ZnO; 1-dimensional: (a) nanosprings, (b) nanorings, (c) nanohelix, (d) nanocombs, (e) nanowires (f) nanorods. 2-dimensional; (g) nanosheets, (h) nanopellets, (i) nanoplates. 3-dimensional; (k) nanoflower, (l) nanoflower, (m) nanomesosphere, (n) nanourchins(Wang, 2008; Lu et al., 2011; Liu et al., 2016; Xie et al., 2005; Raveendran et al., 2003; Naveed Ul Haq et al., 2017).

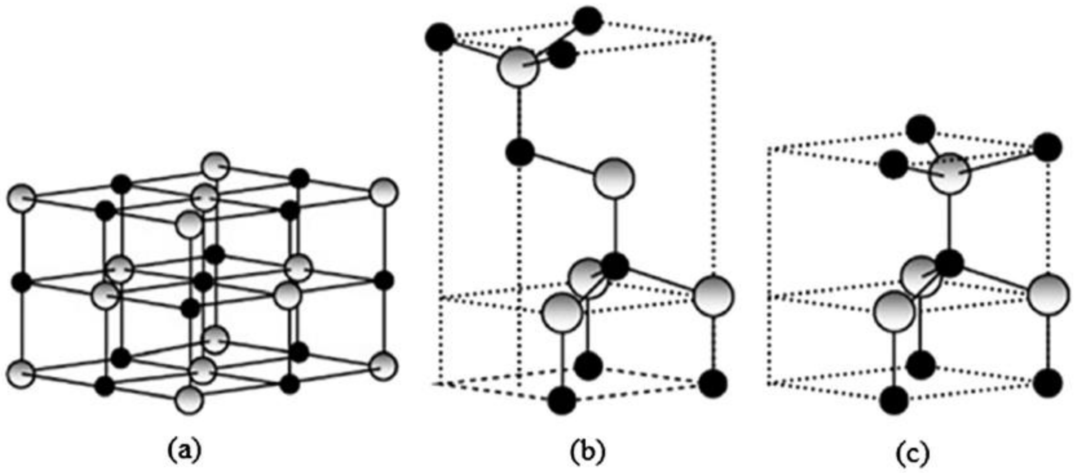

Figure 2. 2. The different structural models of ZnO (a) rocksalt, (b) cubic ZnO blende (c) hexagonal wurtzite phase(Lee et al., 2016). Coloured black and grey spheres designate Zn and O atoms, respectively.

2.2. Synthesis of ZnO

Zinc oxide nanostructures have been synthesised via a lot of approaches and methods. Semiconductor bandgap energy and charge carrier separation are very dependent on crystal phase, crystallinity and size. Li & Li (2006) reported the relationship between bandgap energy and the size of semiconductor compounds as being inversely proportional. This confirms the direct relationship between good preparation methods/conditions and photocatalytic efficiency. Several synthetic approaches are used for ZnO synthesis. These methods are classified as chemical, biological and physical methods with the chemical approaches further subdivided into liquid (solution) and gas (vapour) phase synthesis (Naveed Ul Haq *et al*., 2017; Ong *et al*., 2018). For this study, the focus will be on the sol-gel method for ZnO synthesis.

A solution based method, which is regarded as the easiest approach and consumes less energy, allows for easy control of morphology through the manipulation of parameters such as conditions of reaction, starting materials and solvents (Banerjee *et al*., 2012; Ong *et al*., 2018). Wet chemical methods, solvothermal, electrochemical deposition, sol-gel, precipitation, electrospinning, hydrothermal, microemulsion and microwave methods are all grouped under solution based approaches with the sol-gel process widely considered among researchers as the most appealing due to its homogeneity, excellent stability, economical cost of production, and easy repeatability, thus allowing for easy control of morphology of the nanoparticles and the guarantee of highly pure and uniform structured ZnO (Fang *et al*., 2013; Chandrasekaran *et al*., 2012; Wan *et al*., 2012; Yue *et al*.,, 2009; Ushio & Sumiyoshi, 1993; Wang *et al*., 2013; Lim *et al*., 2011; Naveed Ul Haq *et al.*, 2017**;** Jiao *et al*., 2013**;** Ong *et al*., 2018; Kolodziejczak-Radzimska & Jesionowski, 2014).

The sol-gel process, which is illustrated in Figure 2.3, involves utilizing a molecular starting material in a homogeneous solution which undergoes several transformations such as (i) hydrolysis (ii) polymerization (iii) condensation as a result of dehydration (iv) nucleation and (v) growth (Hu *et al*., 2000; Pierre, 1998; Znaidi, 2010). Znaidi (2010) describes the processes involved in the sol-gel process as (a) solution preparation (b) coating and (c) heat treatment. The solution preparation involves the concentration and nature of the precursor, solvent and additive and the solution aging time; the coating method involves the thickness and substrate for the coating system; and finally heat treatment involves pre-heat and post-heat treatment. There are basically two sol-gel routes being used by researchers currently: metal salts in aqueous solutions or metal alkoxides in organic solvents. Several researchers have utilized the sol-gel approach in ZnO synthesis. For example, the sol-gel route was utilized by Benhebal *et al*., (2013) in the synthesis of ZnO powder by using ZAD ($Zn(CH_3COO)_2•2H_2O$), oxalic acid and ethanol (solvent). The synthesized ZnO powder conformed to the hexagonal wurtzite phase of pure ZnO, with high purity and good crystallinity.

A sol-gel approach was utilized in ZnO nanostructure synthesis by Hasnidawani *et al*. (2016). Zinc acetate dihydrate (ZAD), NaOH and ethanol were used as materials. ZAD and NaOH were dissolved in 15 ml and 10 ml of distilled water respectively, and solutions stirred vigorously for about 5 minutes. After stirring, NaOH was intoduced into the solution containing

ZAD, and magnetically stirred for another 5minutes. A 100ml volume of ethanol was titrated into this mixed solution dropwise, and a white precipitate was observed. The formed precipitate was characterised using XRD, SEM and EDX. SEM images showed a rod-like morphology, the EDX result showed Zinc content of - 55.38 % and Oxygen content of - 44.62 %, thus confirming that the ZnO power has excellent purity, while the XRD result showed sharp and intense peaks indicating crystallinity and single phase as indexed on JCPDS card no 36-1451. The most intense peak was recorded at an angle of 33.8616 in the 101 plane.

Mahdavi & Ashraf Talesh (2017) also utilized the sol-gel method to synthesize ZnO nanoparticles. ZAD was added into a solution of methanol to prepare the ZnO sol. After stirring for 45 minutes, a transparent solution was obtained. To adjust the pH to 9, NaOH was introduced dropwise, and the milky white suspension was vigorously stirred for 10 minutes at room temperature. The sol was subsequently stirred for 60 minutes and centrifuged. The obtained sediment was dried for 120 minutes at 100^oC and a white powder was retrieved. Subsequent XRD and TEM characterization confirmed the crystallinity and purity of the samples, and the sample was confirmed to be well within the nanoscale.

Other studies have also utilized the sol-gel approach in the synthesis of ZnO nanoparticles and the results obtained during characterization are all in agreement. All samples conformed to the characteristic hexagonal wurtzite phase of ZnO, thus confirming that the sol-gel method yields composites on the nanoscale with high crystallinity and purity (Ciciliati *et al*., 2015; Ali *et al*., 2014; Mahdavi & Ashraf Talesh, 2017).

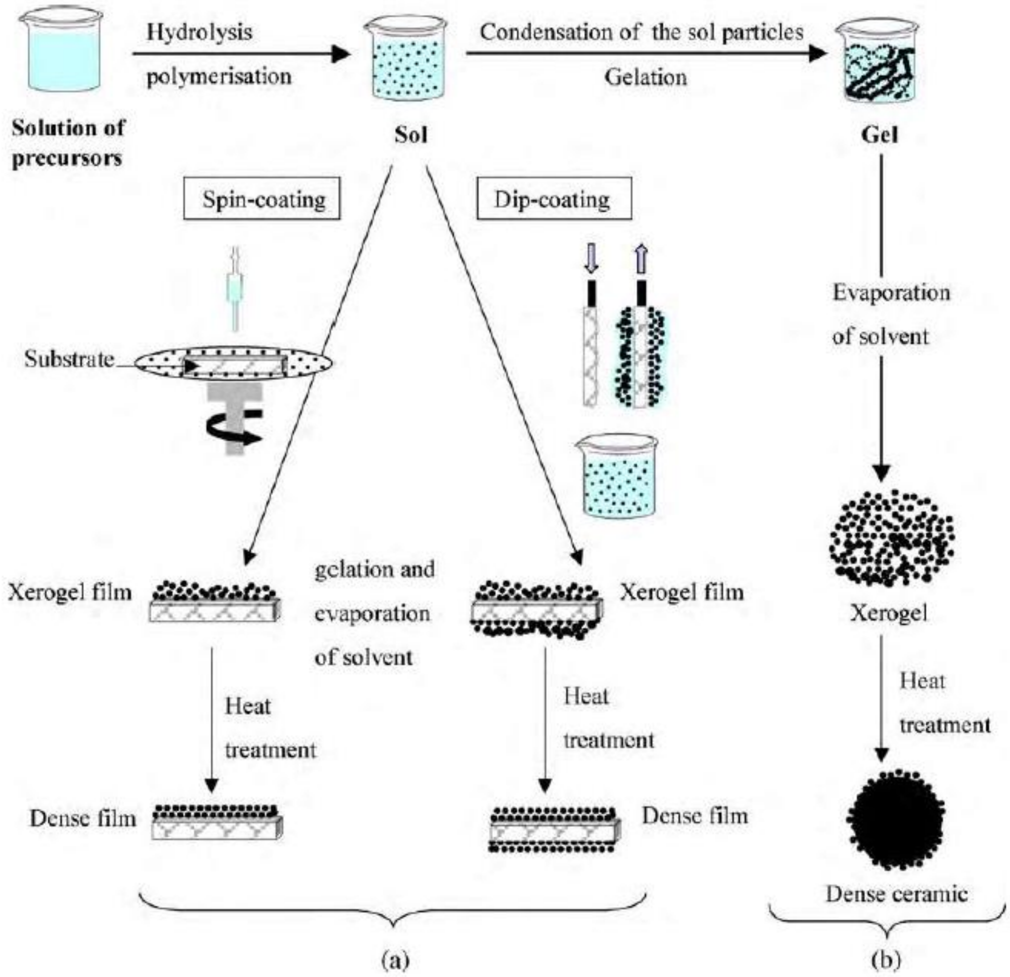

Figure 2. 3. Two different synthesis methods using the sol-gel route (a) colloidal sol transformed to films; (b) colloidal sol transformation from gel to powder (Znaidi, 2010).

2.3. Photocatalytic activity of ZnO

Some studies confirm that ZnO exhibits greater photocatalytic performance and efficiency than TiO_2 due to its higher electron mobility (200-300 $cm^2\ V^{-1}\ s^{-1}$) when compared to that of TiO_2 (0.1-4.0 $cm^2\ V^{-1}\ s^{-1}$), which speeds up electron transfer for better quantum efficiency (Kumar & Rao, 2015b; Akyol, *et al.*, 2004; Lizama, *et al.*, 2002; Mijin *et al.*, 2009; Colón *et al.*, 2008). Electron mobility is very important in photocatalysis, particularly when the photocatalyst acts as an electron acceptor. This means that excited organic molecules will transfer electrons into the photocatalysts CB, leading to conversion of the organic pollutant to its cationic radical. The electrons, which moved into the conduction band, adsorbed O_2 on the photocatalysts's surface to form a series of very active species O^{2-}, H_2O_2, $OH^{\cdot}$ (Li *et al.*, 2010; Kumar & Rao, 2015). Furthermore, the oxidation potential of the hydroxyl radicals generated by ZnO (3.06V) has been reported to be higher than those generated by TiO_2 (2.7V), because of the positions of the VB (valence band) of both ZnO (slightly lower position) and TiO_2 (Chandiran *et al.*, 2014; Anta *et al.*, 2012; Kumar & Rao, 2015).

Zinc oxide has been described as a promising, capable and suitable substitute (to TiO_2) compared to other photocatalysts such as CdS, ZnS, and SnO_2 (Kansal *et al.*, 2008) and has been reported to show better photocatalytic activity than other metal oxide photocatalysts like WO_3, V_2O_5, MoO_2, In_2O_3 and CeO_2 (Chan *et al.*, 2011). There have been several research studies conducted to compare the photodegradation efficiencies of different photocatalysts. Some researchers reported higher efficiency of ZnO compared to other photocatalysts. For example, the study by Dindar & Içli (2001) compared the photodegradation activities of TiO_2, ZnO and Fe_2O_3 in the photodegradation of phenol under direct and focused sunlight irradiation. The experimental conditions were such that the phenol solutions were freshly prepared for each experiment and stored in the dark until the photoreaction. The absorption and fluorescence emission spectra of phenol were measured prior to and after irradiation. A sodium lamp was used to simulate sunlight under laboratory conditions (because of its semblance with the solar radiation spectrum) and concentrated sunlight was achieved with the aid of Fix Focus FF 3.5-HTC GmbH equipment. Photo-reactivity of ZnO was observed to be as high as that of TiO_2 under focused sunlight. This was attributed to its absorption characteristics within the 300-400nm region, although TiO_2 reactivity was higher under normal sunlight. This work highlighted the promising nature of ZnO as a photocatalyst capable of substituting for expensive TiO_2 in water purification under sunlight (Dindar & Içli, 2001).

In another study highlighting the decolourization efficiency of ZnO, Gouvêa and colleagues (2000) compared ZnO and TiO_2 decolourization efficiencies for the reactive dyes Remazol brilliant blue R, Remazol black B, Reactive Blue 221 and Reactive Blue 222. At a reaction time of 120 minutes, ZnO mineralized the dyes at up to 80 %, thus exhibiting better photocatalytic capability than TiO_2. It was deduced that higher efficiency of ZnO can be attributed to its adsorption capacity, which accounts for 10 % decolourization ratio in dyes against 4 % for TiO_2 (Gouvêa *et al*., 2000). This study showed ZnO as a suitable substitute to TiO_2 in assisted photodegradation of organic dyes.

In 2002, Lizama led researchers to perform a study by utilizing and comparing model catalyst P-25 and nanosized ZnO in the photodegradation of RB-19 under optimized conditions. After photoexcitation experiments, the aliquots were filtered and analysed using a UV-Vis spectrophotometer. A calibration curve was used to determine the dye concentration, TOC was determined with a TOC analyser, acute toxicity was analysed using a Microtox 500 toxicity analyser (measured as EC_{50}) and *vibrio fischeri* bacteria was utilized as an indicator for toxicity. Experimental results showed a higher discolouration rate with ZnO when compared with TiO_2 within nearly 15 minutes when 0.8 gL^{-1} of ZnO was used at a pH of 11 against 40 minutes for TiO_2 with 0.5 gL^{-1} at a pH of 11. Total decolouration was observed at 25 minutes and 50 minutes for ZnO and TiO_2, respectively. Other researchers observed similar activity for both catalysts in the photodegradation of reactive dye Orange 16 (Poulios & Aetopoulou, 2017). This behaviour of the ZnO catalyst exhibiting a higher photo-activity was credited to higher production of H_2O_2 on the surface of the catalyst when compared with TiO_2 during photoexcitation (Kormann *et al*., 1988).

Akyol and co-workers in 2004 investigated and compared the photocatalytic activities of ZnO, TiO_2, SnO and SnO_2 powder suspensions in the photo-decolourization of Remazol Red (RR), an azo dye. This study was carried out with the aid of a quartz batch reactor and a UV-C light source. A volume of 300 mL dye solution was prepared with deionized water and agitated in the dark (to equilibrate adsorption-desorption) after the addition of catalyst. At intervals, 5mL aliquots were taken out and centrifuged (3500 rpm) for 10 minutes. Photocatalytic decolourization was investigated by characteristic absorbance of RR at λ_{max} = 525 nm using a spectrophotometer (UV-vis). After a reaction time of 45 minutes, ZnO exhibited superior photocatalytic activity as RR was completely decolourized. No other catalyst completely decolourized RR. SnO exhibited the lowest photocatalytic performance. Other studies by researchers also substantiated the results obtained from this study (Daneshvar *et al*., 2004; Sakthivel *et al*., 2003). The superior activity of ZnO was linked to its higher quantum efficiency, the charge carrier densities of the other catalysts, their crystal structure, and crystallinities. The PZC of ZnO was observed to be 9, which is also corroborated by several other studies (Kanel & Al-Abed, 2011; Huang *et al*., 1993; Shafaei *et al*., 2010).

There have been huge strides made in the synthesis, characterization, and utilization of ZnO nanoparticles in the photodestruction of numerous organic pollutants. Regrettably, researchers are still challenged by a wide range of limitations with regards to the development and application of ZnO photocatalyst as a major material in the abatement of wastewater and polluted water with regards to their complete mineralization.

2.4. Factors affecting the photocatalytic performance of ZnO

According to Gupta *et al*. (2015), some of the positives of ZnO photocatalyst include: mineralization of organic pollutants, easy to manipulate, applicability to both liquid and gaseous phases of pollutants, ability to degrade a variety of organic pollutants, readily available and cheap etc. However, several factors often limit the efficiency of the photocatalyst. Some of these factors include: morphology, temperature, pH, recombination, initial pollutant concentration, light intensity, catalyst loading, crystallinity, surface area, etc (Tolosa *et al*., 2011).

2.4.1. Morphology

Photocatalytic properties/activity can be hugely affected by size and shape. This is why control of morphology is very necessary in the synthesis of photocatalytic nanoparticles *(*Mclaren *et al*., 2009; Mehrjouei *et al*., 2015). The electronic and photocatalytic properties of ZnO depend on surface morphology, size, crystal structure, aspect ratio, crystal density and crystallographic orientation (Wang, 2004; Garcia & Semancik, 2007).

Precursor concentration, nature and additives concentration, and aging conditions are important factors that affect ZnO morphology. The quality of ZnO nanoparticles for photocatalysis is very significant as it affects the efficiency of the photocatalyst. For example, Mclaren and co-workers in 2009 performed a study to ascertain effect of morphology on photoactivity. The study was such that the group synthesized ZnO nanoparticles with rod-like and spherical morphologies via a simple solution method. Oleic acid was confirmed to influence morphology of nanoparticles and is known to prevent agglomeration in nanoparticles, as well as inhibiting growth of nanoparticles. XRD patterns of both samples were confirmed to be of the standard bulk wurtzite structure and corresponded to P63mc, as indexed in the JCPDF No. 36-1451. The as-synthesized nanoparticles were utilized in the photodecolourization of methylene blue (MB). The particles shaped in the form of a rod exhibited lower photodecolourization efficiency of MB when compared with the spherical ZnO, as the spherical ZnO was observed to exhibit 5-fold greater efficiency. A probable explanation for this could be attributed to exposure of a larger proportion of polar faces, which led to a higher photocatalytic activity.

The Kumaresan group (2017) effectively tuned the morphology of ZnO nanoparticles in their study by increasing the pH (NH_4OH) of the precursor solution ($ZnCl_2$), which changed the morphology from spindle like nanorods to a structure bearing the semblance of a flower. The precursor solutions with varying pH’s of 7, 9, 11 and 13 were used in the preparation of ZnO nanoparticles via a hydrothermal route. The nanoparticles prepared with a precursor solution of pH 9 had the morphology of a spheroidal and hexagonal disk and showed an increased photo-activity in the degradation of RhB dye (94 % efficiency). The nanoparticles with morphologies of spindle like nanorods (pH 7), porous nanorods (pH 11) and nanoflowers (pH 13) structures exhibited degradation efficiencies of 67 %, 48 % and 73 % respectively.

A similar finding was observed in the study by Li *et al*., (2008) who synthesized various ZnO nanoparticles (rods, disks, rings and screw caps) via a simple hydrothermal route. As shown in Figure 2.4, these ZnO nanoparticles with varying morphologies were utilized as catalysts for N-formylation of aniline. Results obtained also depicted a morphology dependent photocatalytic activity. Samples which had greater fraction of polar planes contained more O_2 vacancies and exhibited higher photocatalytic activities. The as-synthesized ZnO nanoparticles (NPs) with the shape of a screw cap had greater amounts of oxygen vacancies and thus, exhibited the highest photocatalytic activity. This is further evidence that morphology is an important factor in designing highly effective and efficient photocatalysts. Suffice to say that enhanced photocatalytic activity mostly depends on surface area and morphology, due to the exposed surface area for photoexcitation and adsorption. Particle morphology substantially affects photocatalytic activity (Li & Haneda, 2003). ZnO indeed exhibits significant activity with further shrinkage in particle size (Sirelkhatim *et al*., 2015).

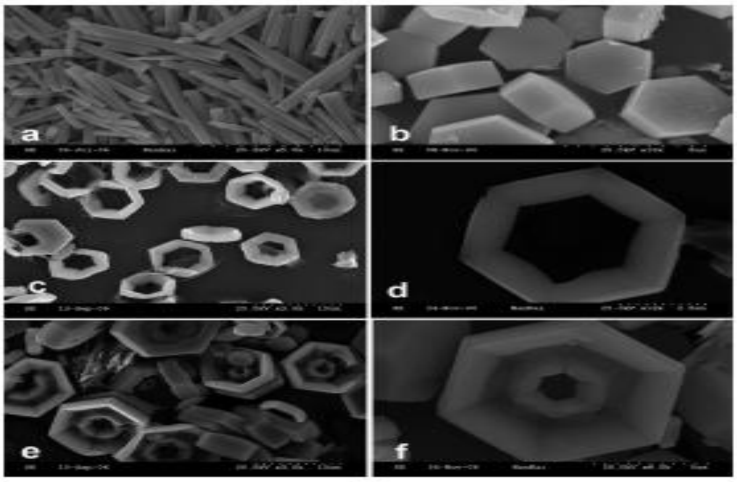

Figure 2. 4. SEM images of as prepared ZnO NPs with varying morphologies(a) disks (b) rings (c, d showing a large magnification of a ring), and screw caps (e, f showing a large magnification of a screw cap) (Li et al., 2008)

2.4.2. Recombination

During photoexcitation, efficient charge separation is sustained by electron mobility properties of ZnO. Researchers have attributed the high electron mobility of ZnO to its filled d^{10} electron configuration, which leads to a high donor concentration of about 4×10^{16} cm^{-3} (Look, 2001; Jayah *et al*., 2015; Inoue, 2009). Unfortunately, several studies show a very high rate of recombination (compared to TiO_2) despite the high electron mobility (higher than TiO_2), leading to a very low photoconversion efficiency (Chandiran *et al*., 2014; Xiong, 2007).

The process by which electrons and holes obliterate each other i.e. electrons occupying the empty space corresponding to the hole leading to the disappearance of both carriers is known as recombination. Recombination can also be explained as the process whereby an electron which had been photoexcited from the VB to the CB falls back into the empty VB, which means that recombination is the inverse process of electron-hole pair generation. Bora & Mewada (2017) explained that immediately after photoexcitation, if the electrons and holes are not scavenged immediately, they combine very quickly to neutralise each other. This phenomenon may occur in the form of surface recombination (surface of the photocatalyst) or volume recombination (bulk of the photocatalyst).

According to Schneider *et al*. (2014), photocatalytic efficiency can be evaluated by measuring photonic efficiency. Photonic efficiency is the rate at which reaction products are formed, divided by the incident photon flow and in most cases, it has been found to be small. This is due to the quick recombination of nearly all the photogenerated e^-/h^+ immediately after photoexcitation. The rate of recombination is proportional to the concentration of both e^-/h^+ i.e. as electron and hole concentrations increases, recombination rate compensates for it. Holes and electrons can recombine and be obliterated, leading to release of energy in the form of light (or heat in the case of non-radiative recombination). Recombination limits the photocatalytic activities of ZnO because energy is dissipated, leading to quantum efficiency reduction. Electron-hole pair recombination must be retarded to allow for an efficient charge transfer process to occur at the surface of the photocatalyst. A lower photocatalytic activity than expected is usually linked to recombination, while a higher activity is attributed to suppressed recombination (Ohtani, 2013). Wen *et al*. (2015) determined that recombination takes place within femtoseconds to microseconds, thereby inhibiting photocatalytic activity.

To improve the photocatalytic activities of photocatalysts and inhibit recombination, there needs to be an enhancement of the charge transport to the surface sites of the photocatalyst, which in turn boosts the charge carrier dynamics of the photocatalyst. This can be achieved by utilizing strategies that include: improving the surface area, reduction in the size of the nanoparticles, decreasing the defect sites both in the bulk and surface, coupling with nanocarbon materials, metal ion doping, transition metal doping, non-metal doping, heterojunctions construction etc. Metals like Ag, Au, Sn, Pd, Pt can be etched into ZnO to create a Schottky barrier at the photocatalyst's surface in order to control recombination (Armelao *et al*., 2007). They have also been known to act as charge sinks for photoexcited $\mathbf{e^-}$

in the CB, thereby retarding recombination. Heterogeneous coupling is another method used to inhibit recombination, as it can direct generated e^-/h^+ to different surfaces of photocatalysts. When hetero-structured photocatalysts with different band gaps are coupled, photoexcited (**e^-**) from the CB of the photocatalyst with the greater potential will be transferred to the CB of the other coupled semiconductor with a smaller potential, and likewise the electrons. This causes the movement of e^-/h^+ to the surface of a different photocatalyst leading to recombination inhibition and increased photoefficiency (Raji *et al*., 2018).

Enhanced light irradiation intensity has been linked to recombination inhibition. This is due to higher electron-hole generation under enhanced irradiation which inhibits recombination (Mondal & Sharma, 2016). At poor light irradiation, electron-hole pair separation will compete with recombination, thus reducing the formation of free radicals, and leads to poor photocatalytic activity (Alhakimi *et al*., 2003; Hagfeldt & Grätzel, 1995; Choi *et al*., 1994). Modification of photocatalysts for improved light absorption capacity in the visible light range will lead to improved photocatalytic activity and inhibit recombination.

2.4.3. Surface area

A high number of atoms present on the surface of a photocatalyst will improve its adsorption properties for better photocatalytic activity. Nano-structured materials have nano-sized diameters, which makes charge separation much easier because of the transfer of photogenerated e^-/h^+ pairs from the bulk to the surface. A large specific surface area will typically comprise more active sites for adsorption of contaminants, photon absorption, and for hydroxyl radicals' formation, which leads to more photocatalytic reaction centres.

Moafi *et al*. (2013) demonstrated the importance of surface area in improved photocatalytic performance by synthesizing different W-doped ZnO nanocomposites with varying W loadings, and subsequent application in the photodecolourization of methylene blue under irradiation (UV range). Their efficiencies were compared with undoped ZnO and P25 nanoparticles. The nanoparticles comprised undoped ZnO, ZnO-W (0.5 %), ZnO-W (1 %), ZnO-W (2 %), ZnO-W (4 %), ZnO-W (6 %), and ZnO-W (8 %) with BET surface area measurements of 32.0 m^2g^{-1}, 49.2 m^2g^{-1}, 77.5 m^2g^{-1}, 86.8 m^2g^{-1}, 112.6 m^2g^{-1}, 104.3 m^2g^{-1}, and 93.7 m^2g^{-1} respectively. After an hour of irradiation, W-doped ZnO (4 % wt) composite with the largest surface area was identified to have exhibited the best photocatalytic activity with an efficiency of 87 %. The degradation efficiencies of the photocatalysts were in the order: 4mol% > 6 mol% > 8 mol% > 2 mol% > 1 mol % > 0.5 mol% > P25 > ZnO. The particle sizes of the ZnO-W (X) nanoparticles were smaller when compared with those of the undoped ZnO because of W-O-Zn formed on the surface of the doped samples. This prevented the growth of the nanocrystal grains and enhanced the specific surface area. The results obtained from this study demonstrated that W doped into ZnO at an optimum load of 4 %wt enhanced the specific surface area of the photocatalyst and created additional active sites for pollutant adsorption, increased photon absorption and thus, improvement in the photocatalytic activity.

The importance of specific surface area (SSA) for enhanced photocatalytic activity was also established in a study by (Flores *et al.*, 2014). Flores and colleagues synthesized ZnO with different morphologies via ultrasound-assisted hydrolysis of ZAD. The BET SSA of the as-prepared ZnO nanostructures were 6.43, 3.83, 18.88, and 9.31 m^2g^{-1}, and were utilized in the photocatalytic degradation of MB. After 4 hours of irradiation, the nanostructure with the largest specific surface area (18.88 m^2g^{-1}) exhibited the most significant activity in the photodecolourization of methylene blue. The superior performance of the nanostructure with a surface area measurement of (18.88 m^2g^{-1}) was attributed to the presence of more active sites, and a larger contact area with the MB. This caused more MB molecules to be adsorbed on the surface of the photocatalyst. Other studies have also observed a higher photocatalytic activity of photocatalysts with larger BET specific surface area (Mekasuwandumrong *et al*., 2010; Wang *et al*., 2007; Ameen, 2012).

2.4.4. Temperature

Photocatalytic efficiency during degradation of organic compounds increases with increased temperature. As temperature is increased, free radicals are generated because of the formation of bubbles in the solution. Recombination is inhibited at increased temperature and oxidation rate of organic pollutants is enhanced. Zyoud *et al*. (2015) observed an increase in MO (methyl orange) degradation at temperatures ranging from 20-40^{o}C reaching up to 85 % efficiency after 60 minutes of irradiation. At a temperature in the region of 10^{o}C, only 65 % degradation efficiency was observed after 60 minutes of irradiation.

Karimi *et al*. (2014) ascertained the influence of temperature in the photodestruction of direct green and reactive orange dyes with nano-strontium titanate as the photocatalyst. An electromagnetic heater was utilized to vary the temperature in the ranges of 30^{o}C to 50^{o}C. An increase in degradation efficiency was observed as temperature increased. This is caused by the formation of free radicals due to increased temperature, which caused bubbles in the solution to rise. Furthermore, the increased temperature could have caused a surge in the oxidation rate of the dye at the interface, and inhibited recombination. In the study by Behnajady *et al*. (2006), a similar trend was observed. The increased degradation efficiency as a result of increased temperature was caused by the inhibition of recombination, which led to an increased photocatalytic activity. Activation energy increases with increasing operating temperature.

Hussein & Abass (2010) observed the influence of temperature on the photocatalytic treatment of textile industrial wastewater by utilizing ZnO NPs. A mass of 350 mg ZnO was utilized in the study, while temperature was varied from 17-46^{o}C. Textile industrial wastewater was decolourized with time as temperature was increased. The results indicated a notable increase in photocatalytic activity of ZnO NPs as temperature increased. After 50 minutes of irradiation (mercury lamp), 350 mg of ZnO completely decolourized the textile industrial wastewater at 46^{o}C. A decolourization efficiency of 52.3 % was observed at a reduced temperature of 17^{o}C. A similar result was also obtained when the photocatalyst was changed from ZnO to TiO_2. Suffice to say that temperature is an important parameter for efficient photocatalytic activity.

2.4.5. pH values

According to Rajamanickam & Shanthi (2016), solution pH is an important parameter which influences photodegradation, because photocatalytic efficiency is affected by the solution. Similarly, Tolosa *et al*. (2011) explained that controlling the pH of a solution is imperative as it affects the photocatalytic efficiency of photocatalysts. Hydroxyl radicals' generation depends very much on the pH of the solution. Adsorption of pollutants happens at the surface of a photocatalyst and this is why pH is a key parameter in organic pollutants and dyes abatement (Zielińska *et al*., 2003; Kashif & Ouyang, 2009).

Depending on the type and concentration of an organic compound, pH effects will vary from acidic to alkaline solutions. In the study by Rajamanickam & Shanthi (2016), the pH of a 4-nitrophenol solution was adjusted from 1-5, and there was a sharp improvement in photocatalytic activity of the ZnO (0.1–4 µm) nanoparticles under solar light. Photodegradation efficiency improved from 54.9 % to 79.9 % after 60 minutes of irradiation. When the pH was adjusted to 11, photodegradation increased to 98.3 %. A similar finding was made in the research by Salem *et al*. (2015), who studied the photodegradation of Acid Green 25 (AG 25) using ZnO under natural sunlight. The lowest activity was observed at pH 7, while the highest degradation efficiency was observed at pH 9 after 30 minutes of irradiation. A probable explanation of this is the tendency of ZnO to agglomerate at low pH, which leads to the reduction of pollutant adsorption and photon absorption, while in alkaline range, there is increased formation of OH radicals (Sharma *et al*., 1995). Furthermore, ZnO is known to dissolve in strong acids, which makes photocatalytic activity investigation of ZnO in acidic media quite challenging.

The pzc for TiO_2 and ZnO are 6.25 and 8.9, respectively (Kanel & Al-Abed, 2011; Huang *et al*., 1993), although Shafaei *et al*. (2010) offer a slightly different opinion (6.25 and 9.3, respectively). Under alkaline conditions, a photocatalysts' surface exhibits a negative charge and exhibits a positive charge in acidic conditions. This means that adsorption and dissociation properties of organic molecules at the surface of a photocatalyst, and oxidation potential of the valence band, are significantly affected by the pH value, which also affects the rate of pollutant degradation (He *et al*., 2010; Li *et al*., 2008). Rajabi *et al*., (2013) explained that destruction rate of organic pollutants can be reduced at higher pH (pH > 12), due to competition between hydroxyl ions and organic molecules on the catalyst’s surface. At lower pH, cationic organic molecules’ adsorption on the photocatalyst surface is reduced, due to the positive charge of the surface of the photocatalyst, which leads to a decline in cationic organic molecules adsorption. Thus, it is important to ascertain the optimum pH for different organic solutions (Gnanaprakasam *et al*., 2015).

2.4.6. Photocorrosion

Photocorrosion and photo-instability are part of the limitations associated with utilizing ZnO in aqueous solution as photocatalyst for wastewater treatment. Reaction between holes and surface O_2 cause dissolution of ZnO and the vacant sites on the ZnO surface cause photocorrosion. Photocorrosion occurs because of the partial dissolution of Zn and failure of the ZnO structure caused by intense irradiation. In addition, studies have shown that photodecomposition of ZnO follows two pathways. Two holes are trapped on the surface, leading to the quick formation of an O_2 molecule and fast removal of ZnO from the surface. During photoexcitation, there is usually a characteristic charge separation. There is usually a reaction between holes and a surface O_2 atom occasioned by the transfer of h^+ to the solid-solution interface, leading to the escape of O_2 (Rudd & Breslin, 2000). This will cause photocorrosion as photoinduced holes will be consumed, leading to weak photocatalytic activity and ultimately collapse of the ZnO crystal structure. Photocorrosion is shown by Equations 2.1 and 2.2:

$$ZnO + 2\,h^+ + nH_2O \rightarrow Zn(OH)n^{(2-n)}+ + 1/2O_2 + nH^+ \qquad 2.1$$

$$ZnO + 2\,h^+ \rightarrow Zn^{2+} + 1/2O_2 \qquad 2.2$$

During photocorrosion, the elemental metal is the final product in the presence of air (Kisch, 2013). It is expected that ZnO will exhibit excellent photocatalytic activity if photocorrosion can be inhibited (Li *et al*., 2010). Researchers have proposed and investigated several methods to beat photocorrosion. Sapkal and group in 2012 constructed a heterojunction comprising ZnO-TiO_2 in an attempt to suppress photocorrosion via a spray pyrolysis technique. Their investigation showed a significant reduction in photo-activity of pure ZnO (36.9 %) in the photodegradation of MB. However, when TiO_2 was incorporated into the ZnO lattice, the efficiency was observed to be as high as 99.4 %. The poor activity of pure ZnO was attributed to photocorrosion. The photostability of the ZnO was evaluated by atomic absorption spectra, which was utilized to detect Zn in the final MB solution. Approximately 24 % ZnO was observed to have been dissolved in the photocatalytic process. No Zn was detected when TiO_2 was incorporated. The incorporation of TiO_2 onto ZnO surface inhibited photocorrosion, leading to the enhancement of ZnO photostability.

The research by Xu and colleagues in 2008 highlighted the effects of photocorrosion. The study was conducted to observe effect of photocorrosion on the photoactivity of pure ZnO in the degradation of methylene blue. The first three cycles showed encouraging photocatalytic activity as MB was degraded up to 85 % for the first cycle. After 50 hours of irradiation, no photocatalytic activity of ZnO was observed, as only 12 % MB was degraded after 80 minutes of irradiation. In order to inhibit photocorrosion, Yu and group (2015) fabricated a composite comprising a ZnO-ZnS shell structure synthesized via a microwave assisted hydrothermal method. The structure of the ZnO-ZnS heterojunction was made up of a built-in electric field, which facilitates charge carrier transitions. Since the ZnS CB has more negative potential than ZnO and the VB of ZnO is more positively charged than ZnS, photoexcited $\mathbf{e}^-$ will deviate from the photogenerated $\mathbf{h}^+$ in the VB of the ZnO core and the ZnS shell to the CB. The efficient movement of $\mathbf{h}^+$ from the ZnO core to the ZnS shell was found to effectively prevent them from attacking the surface O_2, which led to the suppression of photocorrosion. The ZnS shell protected the surface O_2 from exposure to the solution as well as localized them. The photo-activity of the heterojunction was found to be much greater than pure ZnS and ZnO as MB was completely degraded up to 93.7 % in 60 minutes when compared to 59.2 % and 20.0 % of ZnS and ZnO, respectively. After 3 cycles, ZnO-ZnS composite was still able to degrade MB at 90 % in 60 minutes as against 13.5 % for pure ZnO. This highlights the huge significance of photocorrosion which inhibits the full potential of ZnO.

2.4.7. Catalyst Loading

Generally, degradation rate of organic pollutants will increase with an increase in photocatalyst concentration. This is attributed to increased hydroxyl radicals generation because of the presence of more active sites at higher doses. As catalyst load increases, there is a tendency for it to agglomerate due to particle-particle interaction, culminating in a reduced surface area for light absorption, and decreased photocatalytic activity (Ahmed *et al.*, 2011). As catalyst load increases, active sites will increase. However, at a certain point, light penetration will decrease significantly due to excess particle concentration (Adesina, 2004). According to Ahmed *et al.* (2011), excess catalyst loading will lead to an increase in turbidity, light scattering, and a lower photocatalytic activity.

Kashif & Ouyang (2009) studied the influence of catalyst loading on the photodestruction of phenol by utilizing different concentrations of TiO_2 (50-500 mg/L). Results indicated an increase in degradation rate up to 200mg/L when TiO_2 concentration was increased. However, as TiO_2 concentration increased beyond 200mg/L, a decline in degradation rate was observed. A probable explanation for this is, increased number of TiO_2 particles caused an increase in photon absorption, leading to the adsorption of more phenol molecules. However, as TiO_2 concentration was further increased, it led to a reduction in photodegradation of phenol because of agglomeration of free TiO_2 particles, which led to a decline in the number of active sites present. Excess TiO_2 caused excess opacity, and a screening effect, which acted as a shield hindering light penetration. This means that surface area available for light harvesting was reduced, leading to poor photocatalytic activity (Kashif & Ouyang, 2009; Chen *et al*., 2007; Lea & Adesina, 1998).

Behnajady *et al*. (2006) investigated the photodegradation of C.I. Acid Yellow 23 (AY 23) by ZnO photocatalyst. It was discerned that as catalyst concentration was increased from 150 to 750 mg/L, degradation efficiency improved from 49.1 to 93 % after 60 minutes of irradiation. Further loading of ZnO photocatalyst up to 900 mg/L led to decreased degradation efficiency (82 %). This was attributed to increased turbidity of the suspension, and a reduction in light penetration, due to an increase in scattering effect. It was concluded that 750 mg/L of ZnO photocatalyst is the optimum catalyst load able to significantly degrade 40 mg/L of AY 23. This result is illustrated in Figure 2.5.

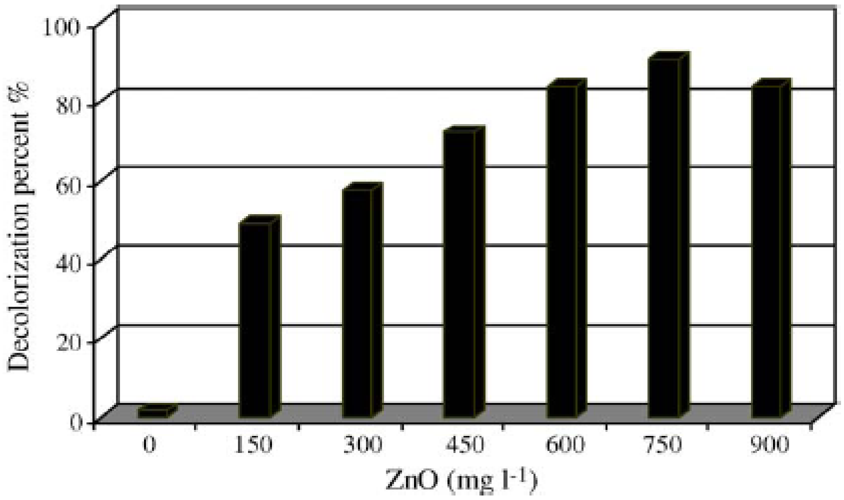

Figure 2. 5. Influence of ZnO concentration (loading) on photodegradation of AY 23 (40 mg/L) (Behnajady et al., 2006).

Zyoud *et al*. (2015) investigated the photo-mineralization of MO by ZnO**.** Different amounts of ZnO photocatalyst (0.05, 0.10, 0.20 or 0.30 g) were utilized in 100mL 10 ppm MO solution. Similar behaviour corroborating the study by various researchers (Behnajady *et al*., 2006; Kashif & Ouyang, 2009; Mai *et al*., 2008) were observed as catalyst concentration was increased. Efficiency of the photocatalyst decreased as catalyst loading increased. This was attributed to increased light blocking as catalyst loading increased. Short wave tail photons are blocked from entering the reaction mixture, and ZnO nanoparticles in the reaction mixture are unable to receive photons as catalyst concentration is increased. Smaller particles of ZnO agglomerated into larger particles leading to a reduction in active sites. It was concluded that using smaller amounts of ZnO nanoparticles increased the efficiency without lowering the average reaction rate**.**

2.4.8. Initial pollutant concentration

Degradation efficiency decreases with increased pollutant concentration. This is because increased pollutant concentration will cause an increase in the amount of pollutant adsorbed onto the photocatalyst's surface, leading to a reduction in the active sites, and formation of hydroxyl radicals.

Pardeshi & Patil (2009) investigated the photodegradation of resorcinol at varying initial concentrations (50-350 ppm), by utilizing ZnO photocatalyst under sunlight irradiation. At 100 ppm, resorcinol solutions were completely mineralized when 250 mg/100 ml of ZnO was utilized. However, at concentrations exceeding 100 ppm of resorcinol, degradation efficiency was much lower. A probable explanation for this is that, more molecules of resorcinol are adsorbed on the surface of the photocatalyst as initial concentration of resorcinol is increased. Hydroxyl radicals and superoxide anions formed on the surface of the photocatalyst at constant irradiation are overwhelmed by the increasing resorcinol molecules, leading to decreased photocatalytic activity. In addition, photons are obstructed before they reach the surface of the photocatalyst as concentration of resorcinol increases. This leads to reduced photon absorption and decreased photocatalytic efficiency. This means that 100 ppm of initial pollutant concentration was determined as the optimum concentration of resorcinol which can be degraded by 250 mg of ZnO.

A similar observation was made in the photodegradation of aqueous methylene orange by ZnO NPs under simulated sunlight in the study by Zyoud *et al*. (2015). Methylene orange concentration ranging from (10, 20, 30 and 40 ppm) attained degradation efficiencies of 100 %, 70 %, 66 % and 45 %, respectively after 60min of irradiation with 0.1g of ZnO nanoparticles. This corroborates the study by Pardeshi & Patil (2009). Several studies investigating initial concentration of pollutants and its effect on photocatalytic activity have been investigated by various researchers (Shafaei *et al*., 2010; Kashif & Ouyang, 2009; Pouretedal *et al*., 2009; Sobana & Swaminathan, 2007; Mai *et al*., 2008) with each observing the same behavioural trend.

2.4.9. Light intensity

UV/Visible/Sunlight generates photons needed to induce charge separation and transfer. As more radiation become incident on the photocatalyst, the production of $OH^{\cdot}$ increases, causing increased degradation rate and diminishing recombination. This means that light intensity is a determining factor in photocatalytic activity. A low irradiated light intensity leads to a competition between the separated electron-hole pair and recombination, which causes a reduction in the formation of free radicals and decreased photocatalytic activity.

Herrmann in (2005) explained the relationship between light intensity and the photodegradation rate of organic pollutants with Equation 2.3:

$$Q_{\text{overall}} = \frac{rate\ of\ reaction}{rate\ of\ absorption\ of\ radiation} \qquad 2.3$$

where Q_{overall} is the quantum yield of light absorbed by any photocatalyst. Light intensity (Φ) is dependent on the photon energy flux, which is the energy of photons per second per unit area incident on the suspension. The quantum yield $\Phi(\lambda)$ is the ratio of number of molecules undergoing a chemical transformation to number of photons absorbed at that particular period.

The effect of light intensity on kinetics of photocatalytic reaction has been classified into three categories (Vinu & Madras, 2011; Zangeneh et al., 2015):

- When light intensity is low (0– 20 mW/cm^2), reaction rate tends to increase linearly as light intensity increases (first order). This is due to retardation of electron-hole recombination because generation of electron-hole is more predominant.
- At intermediate light intensity (~25 mW/cm^2), the rate of reaction is dependent on the square root of light intensity (half order). This is because of the competition between recombination and separation of the generated electron-hole pair, which causes a diminished effect on the rate of reaction.

- When light intensity is high, reaction rate becomes independent of light intensity due to the saturation of surface of the photocatalyst, which causes a limitation in mass transfer.

The impact of incident light intensity on the decolouration of MO was evaluated by Zyoud *et al.* (2015). Two 100mL solutions of MO with varying concentrations (10 and 20 ppm) and 0.10g of ZnO powder were utilized under varying light intensities (1.90, 5.12, 8.78 and 19.0 mW/cm^2). After an irradiation time of 30 minutes, MO with concentration of 10ppm attained 100 % degradation at the higher light intensities (5.12, 8.78 and 19.0 mW/cm^2), while the lower intensity light (1.9 mW/cm2) had an efficiency of 50 %. Similarly, after an irradiation time of 30 minutes, results obtained for the MO with concentration of 20 ppm showed 70 % degradation under the higher intensity light and only 30 % for the less intense light.

Numerous studies with regards to metal oxide photodegradation of organic contaminants have been undertaken in the region of UV-light (<400nm), which corresponds to E_{bg} of TiO_2 and ZnO. UV-light, which is ~5 % of the solar spectrum, confines photocatalytic investigations, evolution, and photocatalytic activities/capabilities of TiO_2 and ZnO. Modification of photocatalysts for visible light absorption (nearly 47 % of the solar spectrum) is the future of photocatalysis.

2.5. Modification of ZnO

Current studies have shown ZnO as a suitable photocatalyst capable of oxidizing organic pollutants in water because of its availability, low toxicity and simple synthesis processes. However, problems still abound in the utilization of ZnO as an efficient photocatalyst as it requires modifications to overcome its limitations. Some of the inherent limitations of ZnO include wide band gap, low quantum because of the quick recombination of the photogenerated **e^-/h^+**, photocorrosion, and poor photo-activity under visible light occasioned by the wide **BG**

(Qi *et al*., 2017; Kandavelu *et al*., 2004; Li & Haneda, 2003). Photocorrosion is the disintegration of ZnO structure and near/partial dissolution of Zn caused by induced self-oxidation of the compound (Vu *et al*., 2013; Neppolian *et al*., 2002).

To synthesize ZnO with effective and efficient photocatalytic activity, there has to be a consideration of the charge separation and recombination lifetime of the charge carriers, solar spectrum response range (ability to absorb visible light), and the quantum yield of the photocatalyst (Gouma & Lee, 2012). Furthermore, increased photocatalytic efficiency can be achieved by isolating one of the charge carriers, recombination inhibition through the fabrication of heterojunctions and doping (Kayaci *et al*., 2014). Researchers have proposed that introduction of these defects will form intermediate bands within the **BG** and allow the harvest of visible light, especially for wide gap photocatalysts (Hoffmann *et al*., 1995; Kayaci *et al*., 2014b; Vempati *et al*., 2012).

Various studies have advocated several methods and processes to boost the photocatalytic activity of ZnO. Some of these methods include metal and non-metal doping, as well as construction of heterojunctions.

2.5.1. Metal Doping

Studies have confirmed metal dopants like Ag, Mn, Cu, Co, Fe, Ce, Eu, and Al will cause a red-shift in the optical absorption edge of ZnO to the lower energies and increase the photo-activity in the longer wavelengths (visible light region) (Samadi *et al*., 2015). When metal cations interact with the CB or VB of ZnO, band gap narrowing occurs, induced by intra-band gap levels formation. This new state is capable of absorbing light beyond the UV wavelengths. Factors such as electronegativity, ionic radius and concentration are important to consider because the metal dopants occupy substitutional or interstitial sites within the ZnO lattice.

2.5.1.1. Transition Metal Doping

Studies have shown that transition metals doped in the ZnO lattice causes a tuning of the band gap, making ZnO a visible light catalyst. Transition metal ions replace Zn^{2+} with tetrahedral O coordination in the ZnO lattice, leading to the BG narrowing due to sp-d exchange interactions between the CB electrons and ***d*** electrons of the transition metals (Rehman *et al*., 2009; Wu *et al*., 2011). In addition, transition metal incorporation will inhibit crystal growth and cause morphology modification as well as modification of the ZnO crystallite sizes, and also introduce many crystal defects such as O_2 vacancies, which act as electron traps for effective separation of electrons and holes (Samadi *et al*., 2015; Thennarasu & Sivasamy, 2013). The mechanism of transition metal doped ZnO can be summed up as follows: (i) electrons are excited from ZnO VB to CB; (ii) inducement of d-d internal transitions by the dopant; and (iii) charge transfer between ZnO CB and the dopant d-state and also between ZnO VB and the dopant d-state. This means that the photogenerated holes will remain in the VB of ZnO and then transfer to the surface to form active OH radicals, while the excited electrons will be trapped in the transition metal sites and react with absorbed O_2 to produce O_2^- (Yang *et al*., 2013; Chakma & Moholkar, 2015).

A study was conducted by Wang *et al*. (2004) to investigate the characteristics and photo-activities of Ag doped ZnO nanocrystals. The Ag ions etched in ZnO nanocrystalline particles were synthesized by spraying an aqueous solution of Ag ions coordinated with NH_3 into $Zn(NO_3)_2$ aqueous solution under intense stirring. NaOH was utilized as pH adjuster. The solution was magnetically stirred for 30 minutes and subsequently heated to 60°C. NH_4HCO_3 was poured into the solution to form Ag doped $Zn_5(CO_3)_2(OH)_6$ precipitate. This precipitate was washed with deionized water and filtered with a vacuum pump. After dehydration at 100°C for 24 hours, the obtained powder was subjected to hybrid induction and laser heating (HILH) at 1100°C. Results obtained from characterization showed that the Ag doped ZnO had the characteristic wurtzite structure with uniform sizes and morphology. It was also observed that increased Ag loading on the ZnO lattice further decreased the particle sizes. XRD characterization revealed that increased Ag loading caused narrowing and low diffraction spectrum, which was also observed by Hosseini *et al*. (2015). This phenomenon can be explained by the ionic radii differences between Ag^+ (0.126 nm) ions and Zn^{2+} (0.074 nm) ions. UV-Vis analysis showed that the Ag loading caused the ZnO to absorb in the visible light range. The as synthesized nanoparticles were utilized in the photodegradation of MB and phenol. Ag (2 %wt) doped ZnO nanocrystalline particles completely degraded 100 % MB in 60 minutes, while it took 150 minutes to completely degrade phenol. When phenols undergo oxidation, they form quinones/quinonoid type species that are yellow in colour and have high extinction coefficients in the visible region, this accounts for observed yellow colour during the reaction. This was attributed to possible oxidation of hydroxylated products and further oxidation to CO_2 and other transient species. This phenomenon was also observed in a different study (Chun *et al*., 2000). This study clearly showed that transition metal modified ZnO nanoparticles show a vastly improved photocatalytic activity.

Hosseini *et al*. (2015) experienced similar findings in the photodegradation of methyl violet (MV) while utilizing 2 % wt Ag incorporated into the ZnO lattice. The study also showed improvement of ZnO photo-activity because of the incorporation of Ag, which created oxygen vacancy defects and increased the surface area. The reaction between CB electrons and O_2 in the solution created reactive oxygen species, which was responsible for the decolourization (Amornpitoksuk *et al*., 2012). The conduction band energy level of ZnO is higher than the Fermi level of Ag-ZnO, and this will cause electrons to flow from ZnO nanoparticles to Ag nanoparticles (Kuriakose *et al*., 2014a). Oxygen vacancy defects and Ag NPs on ZnO surface will trap electrons and prevent recombination. Molecules of MV will be photoexcited to transfer electrons to the ZnO CB to produce O_2^- and VB holes will react with OH^- to produce hydroxyl radicals $^{\bullet}OH$, leading to decolourization. This is illustrated in Figure 2.6. In addition, the energy barrier of the Ag semiconductor junction will enhance charge separation and inhibit recombination as proposed in Figure 2.6 (Zhang *et al*., 2014).

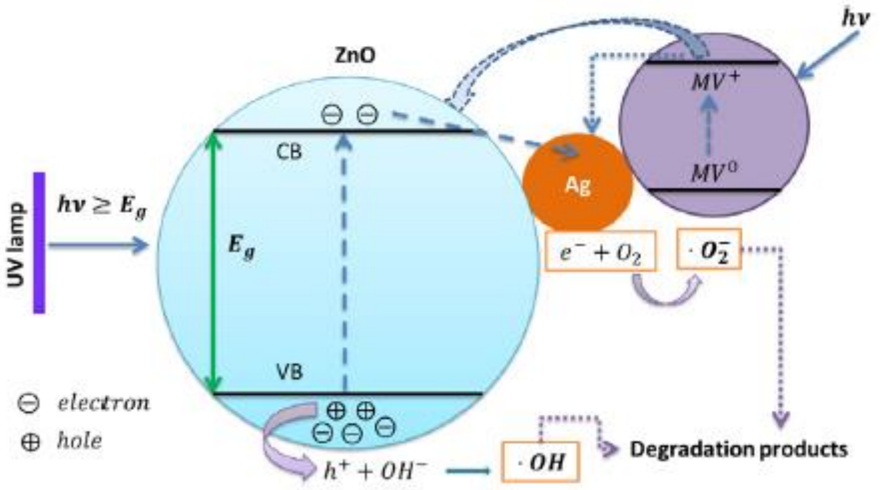

Figure 2. 6. Proposed photocatalysis mechanism of Ag-ZnO NPs under irradiation(Hosseini et al., 2015).

Kuriakose and Mohapatra (2014) increased the photocatalytic performance of ZnO by doping it with Cobalt. The Co-ZnO composite was synthesized via a facile wet chemical process which used $ZnCl_2$ and hexamethylenetetramine (HMTA). XRD results showed that the synthesized Co-ZnO NPs were in the hexagonal wurtzite phase of crystalline ZnO as indexed on JCPDS no. 36-1451, as no additional peaks related to impurities or cobalt oxide were detected. UV-Vis analysis showed broad absorption peaks in the visible region (400 nm and 520 nm), which was due to the incorporation of the Cobalt. SEM analysis revealed that the as synthesized nanoparticles were nanorods and nanodisks. The optimum loading of Co was determined to be 5 % wt. Co-ZnO was utilized in the decolourization of MB under sunlight irradiation. MB was completely degraded within 8 minutes of irradiation. The photocatalytic efficiency of Co-ZnO remain unchanged even after 3 runs. Incorporation of Co within the ZnO lattice caused higher crystallinity, increased active sites, large surface area and promoted charge separation efficiency. Suffice to say that optimum doping of ZnO with Co improves photocatalytic efficiency. Other studies observed similar trends and enhanced photocatalytic activity when Co was incorporated into ZnO (Vahtrus *et al*., 2016; Yuhas et al., 2006; Lu *et al*., 2011).

2.5.1.2. Rare-earth Metal Doping

Another aspect being traversed by researchers to enhance the photoactivity of ZnO, is by incorporating rare-earth (RE) metals into ZnO lattice. Studies have shown that RE metals introduce changes in the BG energy of ZnO. These changes have been attributed to the formation of a localized impurity level band, possible fluctuations caused by the ionized impurities, charge transfer between ZnO VB or CB and 4f/5d states of RE metals, and RE ability to trap electrons and inhibit recombination (Iqbal *et al*., 2009). Despite the advances made in the doping of ZnO with RE metals, there are still concerns with respect to low saturation concentration of RE ions in the ZnO lattice because of the differences in ionic size/radii and inappropriate positions of the energy levels of the RE ions relative to ZnO CB and VB (Khatamian *et al*., 2012).

Recent studies have highlighted the doping of ZnO with RE metals such as Cerium, Europium, Lanthanum, Dysprosium, etc. Cerium (Ce) has been successfully doped in ZnO for improved photocatalytic performance by researchers (Kannadasan *et al*., 2014; Rezaei, 2013; Faisal *et al*., 2013; Ahmad *et al*., 2015). It has been established that Ce increases the photo-activity and stability of ZnO, although Ce^{4+} and Ce^{3+} are larger than the Zn^{2+} ion (Samadi *et al*., 2015). Cerium introduces small impurity states below the conduction band of ZnO, thereby creating new electronic transition states induced from VB of ZnO to numerous new energy levels, and shifts its absorption edge to visible light (Anandan & Miyauchi, 2011).

In a recent study by Ahmad and colleagues (2015), they successfully enhanced the photocatalytic performance of ZnO nanopowders by grafting it with Ce via a combustion method (Ahmad *et al*., 2015). XRD diffractograms of the ZnO and Ce-ZnO revealed the hexagonal wurtzite phase. However, additional peaks of Ce-ZnO sample at 28.5° and 33.1° showed the possible presence of Ce in the ZnO as indexed in JCPDS No. 81-0792, although the peaks were deteriorated due to the presence of Ce. This was also observed in other studies with peaks at 28.6° and 28.7°, respectively when they incorporated beyond 0.1M Ce in the ZnO lattice (Kannadasan *et al*., 2014; Faisal *et al*., 2013). Diffuse reflectance spectroscopy (DRS) of ZnO showed the absorption at 387 nm (UV range), while the Ce doped samples absorbed at longer wavelengths. This was attributed to the incorporation of Ce visible light absorption.

The photoactivities of ZnO and Ce-ZnO were studied in the destruction of Rhodamine blue (RhB) under UV and visible light irradiation. Optimum loading of 3 % wt Ce doped into ZnO showed the highest activity under both UV light and visible irradiation as RhB was completely degraded in 2 hours. The Ce loading increased the movement of photogenerated electrons to the outer systems. During the photocatalytic process, loading of Ce accelerated transfer of electrons to dissolved oxygen, and this caused a reduction of O_2 by the transfer of trapped electrons from Ce to O_2. This led to efficient inhibition of recombination, which caused increased photocatalytic efficiency. However, further loading of Ce above 3 % wt decreased the photocatalytic activity as a result of excessive loading, which caused the Ce to serve as recombination centers. The optimum loading of Ce was utilized for 5 cycles, and there was no observed decrease in efficiency. Rezaei and collegues (2013) observed similar efficiency in their study when they utilized Ce-ZnO, synthesized by a refluxing approach, in the photodegradation of MB. Then efficiency of Ce-ZnO in this study also corresponded to the studies by Kannadasan and colleagues and Faisal group (Kannadasan *et al*., 2014; Faisal *et al*., 2013).

In the study by Khatamian *et al*. (2012), who grafted La into the ZnO lattice, it was observed that La also shifted the absorption edge towards the visible light region. The optimum loading of La^{3+} was observed to be 4 mol%. The remarkable photocatalytic activity of La^{3+} incorporated into ZnO in the photodegradation of 4-nitrophenol (4-NP) could be attributed to its ability to act as an electron scavenger under irradiation, which makes it react with the O_2^- species and suppress recombination of the photogenerated electron-hole pairs. In addition, etching La^{3+} into ZnO causes strong absorption of OH^- ions on ZnO surface due to a large number of O_2 vacancies, which serve as surface-bound traps for the photogenerated holes. However, increased loading of La^{3+} causes the penetration depth of light into ZnO to exceed the space charge layer. This makes it easy for the photogenerated electron-hole pairs to recombine, leading to a lower photocatalytic performance. Thus, an optimum concentration of La^{3+} ions is mandatory to match the thickness of charge layer and light penetration depth to effectively separate the photogenerated electron-hole pairs.

2.5.2. Non-metal Doping

Non-metal doping of ZnO has been widely applied to stall recombination of the photogenerated electron-hole pairs. Doping ZnO with non-metal dopants raises the upper edge of the VB, leading to band gap narrowing. Khaki *et al*. (2017) attributes this to the electronic states of the non-metals, positioned above the VB edge of the semiconductor. This will enable the non-metal doped ZnO to utilize the light energy efficiently for enhanced separation of the photogenerated electrons and holes (Pirhashemi *et al*., 2018).

Carbon doping has attracted a lot of attention and led to numerous studies among researchers due to its ability to make ZnO absorb in visible light, and its efficiency in promoting and channeling the photogenerated electron-hole pairs to nanosized carbons on the photocatalyst's surface (Kumar & Rao, 2015a). Bechambi and coworkers (2015) describe carbon as a very good dopant because of its chemical stability, strong mechanical strength and excellent electronic properties.

Bechambi research group conducted a study to understand the photodegradation of bisphenol by incorporating carbon into ZnO. C-ZnO was synthesized by a hydrothermal approach and characterized with XRD and UV-Vis spectroscopy. X-ray diffraction results showed sharp and intense peaks of hexagonal wurtzite ZnO, without any other impurity peaks. This confirmed the high crystallinity of the composite. However, peak positions showed a slight movement towards the lower angles, which means that oxygen atom was substituted in the ZnO matrix, and carbon inhibited the growth of ZnO. UV-Vis analysis revealed a slight shift towards longer wavelengths for the C-doped ZnO. This could also be as a result of the formation of shallow energy levels inside the band gap. In the photocatalytic study, 4 % wt C was observed to be the optimum loading of C into ZnO as bisphenol was completely degraded after 24 hours of irradiation. Incorporating carbon into ZnO suppressed recombination by creating an ability to act as electron trap to maintain the charge separation of the electrons-hole pairs. Loading beyond this resulted in lower photocatalytic activity. Stability of 4 % wt C-ZnO was confirmed as the sample crystal structure remained unchanged even after the catalyst was used for 4 cycles. Other studies corresponded with this finding in the degradation of p-nitrophenol, RhB and phenol (Wang *et al*., 2014; Kochuveedu *et al*., 2013). Samadi and co-researchers (2013) evaluated the influence of oxygen vacancies and interstitial carbon by incorporating carbon into the ZnO lattice via an electrospinning technique. Photodegradation of MB by C-ZnO was observed to be very high under visible light irradiation. They attributed this to the synergistic effect between an O_2 vacancy and interstitial carbon within the ZnO lattice, which in turn inhibited recombination.

2.5.3. Construction of heterojunctions

It is imperative to spatially segregate e^-/h^+ into different compartments to effectively counter recombination and isolate the redox sites on the catalyst's surface. Heterojunctions are currently being synthesized, studied and are gaining increasing attention from researchers because of their ability to inhibit recombination and isolate redox sites on the surface of the catalyst. Assembling nanomaterials (electronically) with different crystal structures and band positions results in total utilization of incident photons, leading to efficient charge separation by the electric field at the interface. Radiative lifetime is increased by heteroepitaxial growth of one semiconductor over another, which will cause epitaxial bonding interfaces, and highlighting excited separated charge carriers, which in turn reduces overlapping of electron-hole wave functions (Kumar & Rao, 2017; Wang *et al*., 2014; Li *et al*., 2015).

Semiconductors when coupled together exhibit much better performance when compared with their undoped counterparts. This is because the composite will take advantage of the coupled semiconductor and its functionalities that originates from the interfacial structure that it would originally not attain in its single phase. For example, ZnO, TiO_2 and WO_3 can be coupled among themselves to form ZnO-TiO_2, TiO_2-WO_3 and ZnO-WO_3 composites, which will exhibit better photocatalytic activity and performance compared to their single phases. ZnO has been known to suffer from photocorrosion, but when coupled with TiO_2 for instance, the over-layer prevents the photocorrosion of ZnO and improves light absorption properties of the coupled heterojunction, because ZnO has a higher absorption efficiency than TiO_2. In addition, there is a transfer of electrons from ZnO to TiO_2. (Li *et al*., 2010; Giannakopoulou *et al.*, 2014).

The research by Sathishkumar *et al*., (2011) gives more insight into heterojunctions. Their study focused on the engineering of a CuO-ZnO heterojunction for the visible light assisted photodegradation of Acid Red 88 (AR88) in aqueous solution. The composite was prepared by calcining ZnO at 400°C for 5 hours, and subsequent mixture with $CuSO_4{\cdot}5H_2O$ (0.2454 g, 8 mol%). This was followed by stirring for 48hours to allow for proper penetration of Cu ions into the ZnO crystal matrix. Through heating at 100°C for 24 hours, the supernatant water is evaporated, and the resultant product finally calcined at 550°C for 5 hours. XRD results showed diffraction peaks at 32.8 (110), 52.3 (020) and 58.5 (202) which indicated that the Cu in the

ZnO is mainly of the CuO phase (JCPDS card no. 89-5896). Furthermore, a deviation from the corresponding lattice parameters of standard ZnO was observed with values of [JCPDS card no. 36-1451] a= 0.326 nm, and c = 0.522 nm. A probable explanation is that both metal oxides combined via intra-grain coupling as opposed to inter-granular coupling. Also, broadening of peaks was linked to grain refinement due to the incorporation. By analyzing the absorption coefficient using the Tauc approach, the band gap was extrapolated, with a value of 2.9 eV which suggests that the band gap narrowed from 3.2 eV.

Photocatalytic activity of different loadings of the CuO-ZnO (0.2–1.8 g/L) heterojunction were observed by the decomposition of AR88 under visible light irradiation. This was studied by monitoring the decrease in absorption spectra of AR88 (λ_{max} =506 nm) using a UV-Vis for 60 minutes. The optimum loading of CuO-ZnO with the best photo-activity was observed to be 1.4g/l ($1.43\times10^{-3\ s-1}$), which was much higher (approximately 2 times) than the rate observed for pure ZnO (0.63×10^{-3} s^{-1}). The observed high photo-activity of CuO-ZnO was ascribed to the higher number of photons the heterojunction absorbed at that concentration. In addition, visible light illumination caused electron transfer from the cathodic band of one semiconductor (CuO) to the anodic band of the other, while hole transfer occurred from the anodic VB of ZnO to the VB of CuO, thus inhibiting recombination. This is illustrated in Equation 2.4. The CuO coupled with ZnO enhances the transfer of electrons in the CB of ZnO to outer oxygen, which dissolves in water and degrades AR88. Also, the heterojunction caused an increased number of active sites for the interaction of AR88 and CuO-ZnO, which in turn increased the photodegradation process.

$$\mathrm{CuO}\ (e^- + h^+) + \mathrm{ZnO}\ (e^- + h^+) \rightarrow \mathrm{CuO}\ (h^+ + h^+) + \mathrm{ZnO}\ (e^- + e^-) \qquad 2.4$$

2.6. Rationale for fabricating a WO_3 - ZnO Heterojunction

The use of WO_3 is a very interesting and promising photocatalyst, because it has mostly been overlooked over the years and it is regarded as one of the comparatively less studied photocatalysts. From extensive literature surveys, only a handful of review studies have been carried out with reference to WO_3. In addition, the distribution of published research work on WO_3 photocatalysis between 2006-2015 is less than 350 research papers (as reported by Web of Science using WO_3 and photocatalysis as key words), thus, showing the rising trend and potential for more studies on WO_3. This also leaves a lot of room to explore and learn more about WO_3 because of the promise it holds.

WO_3 is an *n*-type semiconductor and was chosen as the semiconductor to be etched into ZnO because of its promising physical and chemical properties. It possesses a narrow bandgap (2.4-2.8 eV) when compared to that of ZnO (3.2-3.37 eV) which enables it to absorb visible light, making it an ideal candidate for photocatalysis. Tungsten oxide (WO_3) posesses excellent photosensitivity, stability and resistance against photocorrosion in aqueous medium, remarkable electron mobility (6.5 cm^2/V s) and good electron storage properties (Zhang *et al*., 2011; Singh *et al*., 2016). In addition, it is cost effective, relatively harmless, exhibits fine interactions with metals, and has high mechanical strength. The ionic radii of WO_3 (0.062 nm) is very close to that of ZnO (0.074 nm), which makes it fit perfectly and inhibit the growth of the crystal sizes.

Despite all the interesting properties of WO_3, studies show that it is difficult to observe spontaneous H_2 formation with WO_3 without modification. This is attributed to the location of its lower CB edge [+0.5 V vs NHE (normal hydrogen electrode) at pH=0] with reference to the standard H^+/H_2 redox level, in addition to the problem of rapid recombination of photogenerated electrons and holes (Dong *et al*., 2017). Furthermore, the relative energy of its conduction band electrons limits its oxygen reduction capacity, and this leads to the build-up of these electrons culminating in a reduced photocatalytic activity (Wicaksana *et al.*, 2014). As a result of these limitations, the optimum utilization of WO_3 as a photocatalyst without any modification is inefficient. To enhance the photocatalytic performance of WO_3, incorporation of other dopants will be necessary (Singh *et al*., 2016).

The incorporation of WO_3 into ZnO at the nanoscale will cause the ZnO conduction band to be placed at the negative side relative to that of WO_3. As the composite is irradiated, the photogenerated electrons of the excited ZnO will move to the conduction band of WO_3 because the conduction band level of WO_3 is positioned lower than that of ZnO. This phenomenon will reduce the photocorrosion problem of ZnO and inhibit recombination.

2.7. Previous studies of WO_3-ZnO heterojunctions

Previous researchers have attempted to synthesize WO_3-ZnO heterojunction to improve the efficiency of ZnO. In 2011, Yu and colleagues synthesized a series of WO_3/ZnO heterojunctions by a precipitation-grinding method and calcining it at different temperatures. To prepare the composites, tungstic acid was first synthesized by mixing sodium tungstate (($Na_2WO_4 \cdot 2H_2O$) with hexadecyl trimethyl ammonium bromide (CTAB) in deionized water under constant stirring. Nitric acid was introduced dropwise into the solution, with subsequent stirring for 120 minutes, and a precipitate was formed. This precipitate was centrifuged, washed thoroughly with deionized H_2O and ethanol, and then dried at 80°C. Zinc hydroxyl carbonate was synthesized by the dissolution of $Zn(NO_3)_2$ and CTAB in deionized water (Solution A). Na_2CO_3 was dissolved in deionized water under constant stirring (Solution B). Solution B was carefully added to solution A under intense stirring, which continued for another hour, leading to the formation of a precipitate. Furthermore, tungstic acid was mixed with the precipitate

(Zinc hydroxyl carbonate) and ground for 30 minutes. The ground mixture was collected, separated, and calcined at different temperatures for 120 minutes.

The XRD patterns of the as prepared heterojunction composites revealed that the ZnO exhibited the hexagonal wurtzite phase with high crystallinity and the crystal planes were indexed (JCPDS 36-1451). No diffraction peaks of WO_3 were observed. This was attributed to very low concentration of WO_3 below the detection limit and high dispersal of WO_3 within the ZnO lattice. The crystal sizes were greatly decreased due to incorporation of WO_3, which restrained the growth of ZnO nanoparticles. This observation is linked to the atomic radii of W^{+6} (~0.068nm) and Zn^{+2} (~0.083nm), which are nearly similar. W^{+6} may have entered the ZnO crystal lattice and inhibited the growth of the ZnO crystal owing to their similar atomic radii. The BET surface areas of the heterojunctions increased with WO_3 content because the ZnO crystallite sizes decreased owing to the incorporation of WO_3. UV-Vis diffuse reflectance spectroscopy showed that pure ZnO had light absorption in the UV range, while the heterojunctions absorption shifted to the visible light range, due to the etching with WO_3. In addition, energy levels may have created oxygen vacancies due to the presence of W^{+6} within the ZnO lattice (He *et al*., 2003).

The heterojunctions were utilized in the photodegradation of Acid Orange (11). The sample with 2 %wt WO_3/ZnO calcined at 600°C exhibited the highest photocatalytic activity with two folds the activity observed for pure ZnO. The increase in temperature caused an increased crystallinity, leading to an enhanced photocatalytic activity due to the inhibition of recombination. Figure 2.7 shows a suggested photocatalytic mechanism. From the different positions of the VB and CB of WO_3 and ZnO, it is suggested that excited ZnO CB electrons will transfer to WO_3 CB, because W^{6+} can capture electrons and be reduced to $W^{5+.}$ In addition, WO_3 holes will transfer to the VB of ZnO. Both scenarios inhibit recombination of photogenerated carriers, leading to increased photocatalytic efficiency. However, if a higher dose of WO_3 is incorporated, it would lead to poor dispersion of WO_3 within the ZnO lattice, and the excess WO_3 will become recombination centers, causing poor photocatalytic activity (Lo, 2006).

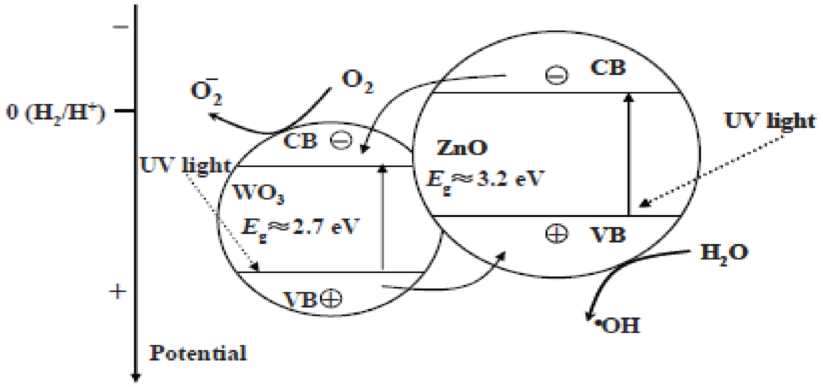

Figure 2. 7. Suggested photocatalytic mechanism for the synthesized WO3/ZnO heterojunction(Yu et al., 2011)

In another study demonstrating the efficacy of constructing heterojunctions, the photo-efficiency of ZnO was enhanced by the incorporation with WO_3. Adhikari *et al.* (2015) synthesized nanocuboid shaped WO_3 and rectangular shaped ZnO by hydrothermal and combustion methods respectively. WO_3 was synthesized via a hydrothermal route using fluoroboric acid (HBF_4). The HBF_4 which is a structure directing agent was added to $Na_2WO_4.2H_2O$ and a precipitate was formed. Hydrothermal treatment was performed at 180°C for 6h to yield WO_3 nanocuboids. A wet chemical combustion method was used to prepare ZnO NPs. Zinc nitrate and oxalic acid were dissolved in water at room temperature and kept in a furnace at 450°C until combustion was complete. A dry porous material was obtained and ground thoroughly for subsequent use in preparing the WO_3-ZnO heterojunction. Measured amounts of WO_3 and ZnO were mixed and ground well for 30 minutes, then the mixture was suspended in water and ultrasonicated for 60 minutes. The solution (colloidal) was oven dried at 80°C and calcined for 120 minutes at 450°C in air, for effective mixing of the metal oxides. Figure 2.8 shows the XRD patterns of WO_3, ZnO and the WO_3-ZnO composite. The characteristic peaks of WO_3 and ZnO are seen in the patterns and correspond to the indexed monoclynic crystal phase and hexagonal wurtzite structure of WO_3 and ZnO, respectively. Figure 2.8c, which has constant and clear distinct peak intensities indicate the patterns of the different loadings of WO_3 in ZnO. UV-DRS (diffuse reflectance spectroscopy) showed that the coupled composite showed a slight red shift when compared to undoped ZnO. Incorporation of WO_3 into ZnO led to the formation of defects in energy levels within the forbidden band.

An increased loading of WO_3 led to further narrowing of the band gaps, as shown in Table 1. The as synthesized heterojunctions were utilized in the photocatalytic degradation of cationic MB and anionic Orange G (OG). Degradation profiles of the photocatalytic experiment are illustrated in Figure 2.9. From the degradation profile, it is observed that the WO_3-ZnO with a 10 % loading was faster than pure ZnO, as it showed the highest photocatalytic decolourization efficiency of 93 % and 89 % for MB and OG, respectively. The higher efficiency of the 10% WO_3-ZnO is ascribed to the difference in energy between the two semiconductors, which caused band gap narrowing. WO_3 acted as visible light absorber, which narrowed the ZnO BG. When the heterojunction is irradiated with visible light, ZnO is inhibited from photogenerating e^- and h^+ due to its wide band gap. This allows WO_3 to absorb the irradiated light to for the generation of e^- and h^+. The electrons (photogenerated) are transferred from WO_3 to the CB of ZnO, thus preventing the recombination in addition to an increase in the number of active species. This means that ZnO trapped the electrons from recombining. The photoelectrons will trap the dissolved O_2 to form $\mathbf{O_2^-}$, while the $\mathbf{h^+}$ (photoinduced) will trap $\mathbf{OH^-}$ to form $^{\bullet}OH$ radicals. Both combine to degrade the dye. A probable equation for this reaction is shown in Equations (2.5-2.11).

Generation of electron-pairs:

$$WO_3 + h\nu \rightarrow WO_3\ (e- - h^+) \qquad 2.5$$

$ZnO + hv \rightarrow ZnO\ (e^- - h^+)$ 2.6

Charge transfer:

$WO_3\ (e^- - h^+)/\ ZnO\ (e^- - h^+) \rightarrow WO_3(e^-)/\ ZnO\ (h^+)$ 2.7

Formation of radicals:

$WO_3(e^-) + O_2 \rightarrow WO_3 + {}^{\bullet}O_2^-$ 2.8

$ZnO\ (h^+) + OH^- \rightarrow ZnO + {}^{\bullet}OH$ 2.9

Degradation of the dye:

$Dye + {}^{\bullet}O_2^-/{}^{\bullet}OH \rightarrow$ Mineral acids $+ CO_2\uparrow + H_2O$ 2.10

$Dye + {}^{\bullet}OH \rightarrow$ Mineral acids $+ CO_2\uparrow + H_2O$ 2.11

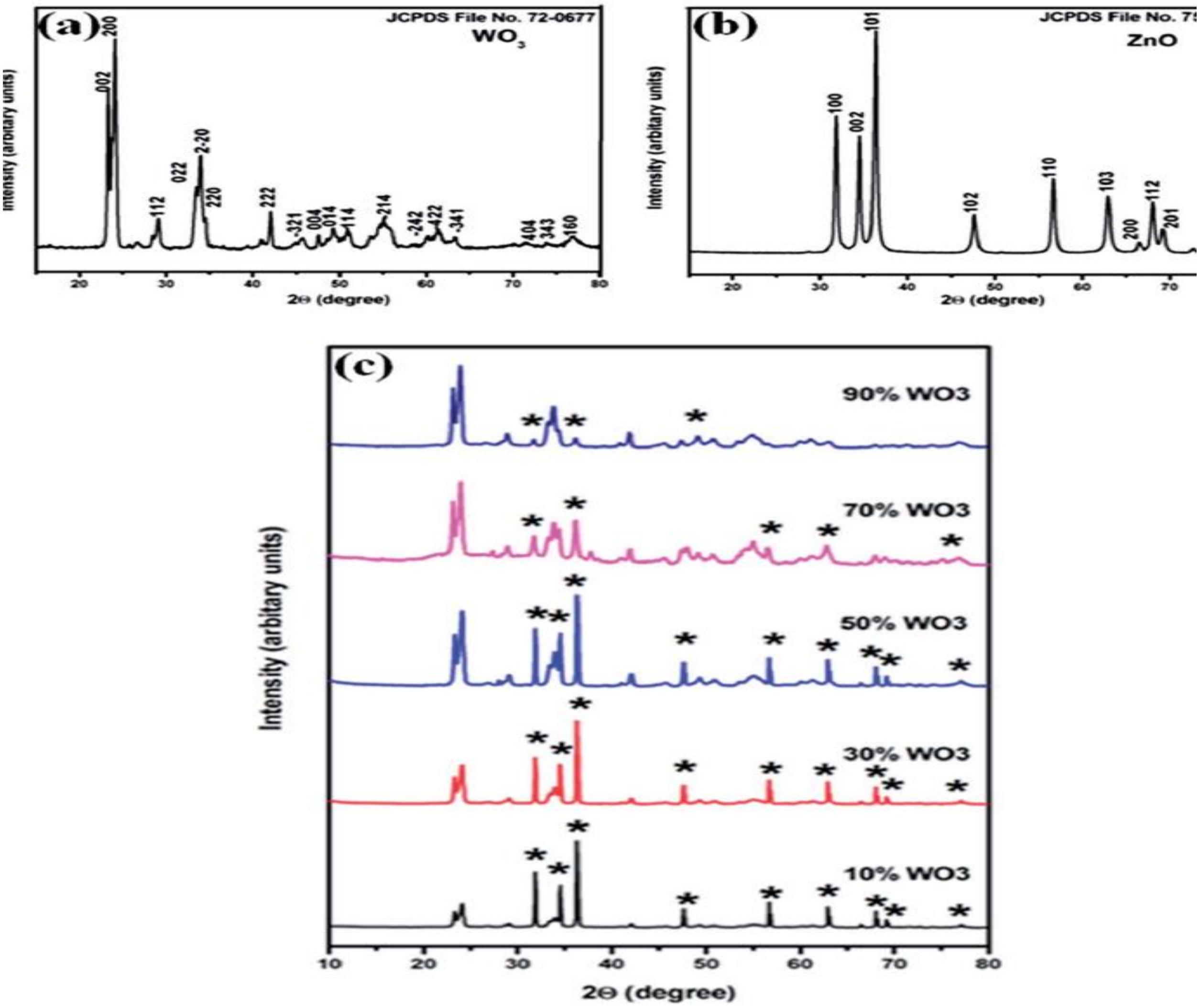

Figure 2. 8. X-ray diffraction patterns of(a) WO_3, (b) ZnO (c) WO_3-ZnO heterojunction (Adhikari et al., 2015).

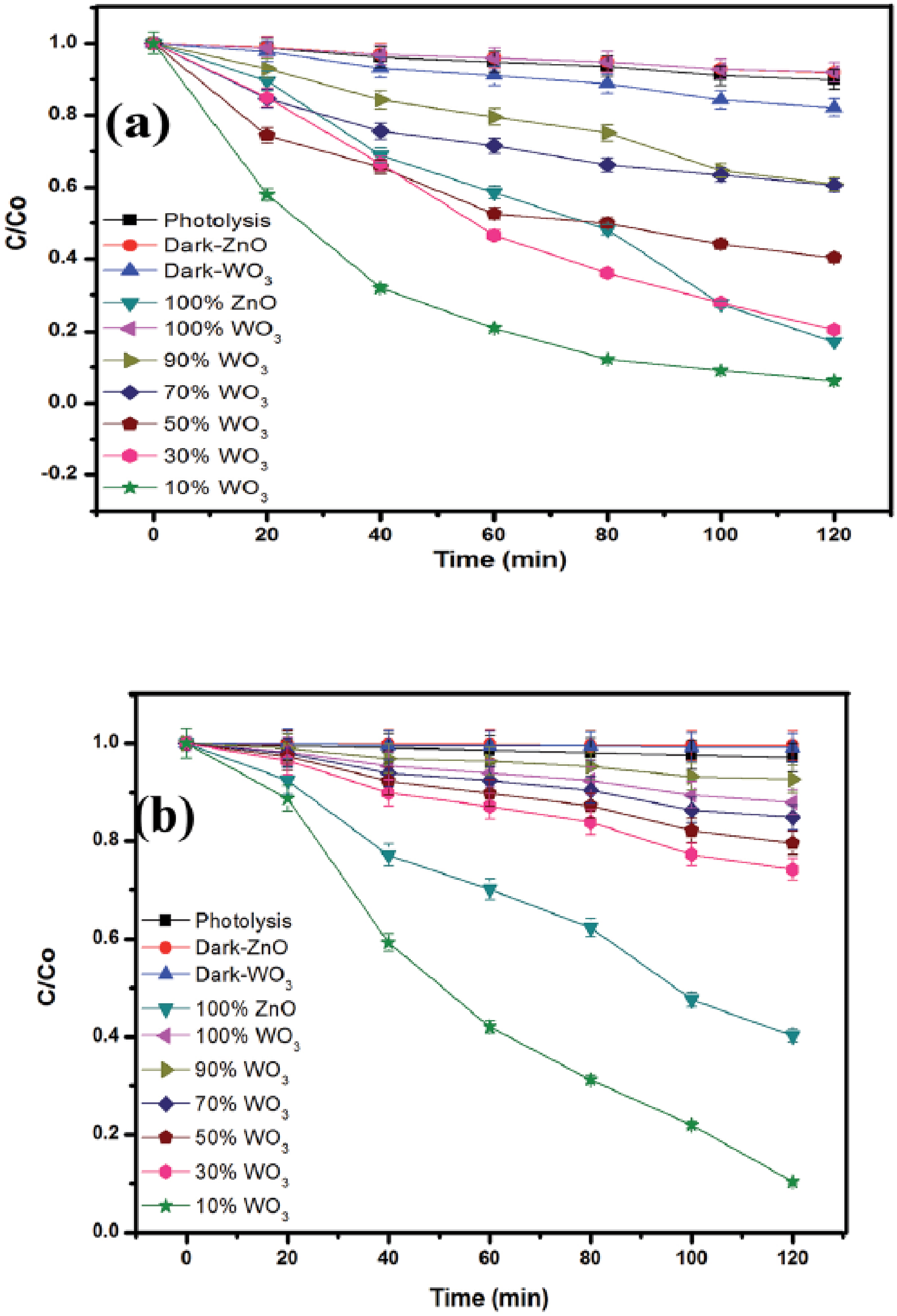

Figure 2. 9. Photocatalytic degradation of(a) MB and (b) OG with different loadings of WO_3-ZnO (Adhikari et al., 2015).

Table 1: Specific surface area and band gap measurements of ZnO, WO_3 and the heterojunctions of different loadings (Adhikari et al.*, 2015).*

Catalyst (%)	SSA (m^2 g^{-1})	Band gap
ZnO 100	17.8	3.20
WO_3 10	15.9	2.98
WO_3 30	14.5	2.52
WO_3 50	11.6	2.55
WO_3 70	9.4	2.25
WO_3 90	6.8	2.25
WO_3 100	5.16	2.78

2.8. Bismuth Based Semiconductors

ZnO, TiO_2 and SnO_2 are photocatalysts widely utilized because of their elevated chemical stability and comparatively low cost. These widely utilized catalysts are well known to only absorb in the UV range because of their wide bandgap. Numerous attempts have been made to explore visible-light - driven photocatalysts to optimize the use of solar energy, and several impressive photocatalysts have been established with strong photocatalytic activity. Bismuth based metal oxides ($Bi_4Ti_3O_{12}$, Bi_2O_3, $BiFeO_3$, $BiFeWO_6$, $BiVO_4$, Bi_2WO_6, Bi_2MoO_6 etc.), oxyhalides (BiOI, BiOBr, BiOCl, and BiOF) and sulfides (Bi_2S_3) are currently attracting significant interests among materials scientists and are classified as emerging materials. Among the aforementioned visible light catalysts, bismuth oxyhalides are considered as very promising due to their excellent photocatalytic activity which is occasioned by their good optical and electrical properties (Arumugam & Choi, 2020).

The crystal structure of BiOX compounds was first reported by Bannister in 1935. BiOX compounds are members of group V-VI-VII ternary oxide semiconductors endowed with a tetragonal matlockite structure expressed as $[M\text{–}_2O_2]$ $[X_m]$, where M = metal and X = halide. As evinced in Figure 2.10, it can be seen that the crystal frame is made up of fluorite-like

[M_2O_2) layers that are sandwiched between two halogen layers and thus, creates a layered shape [X-BiO-Bi-X]. The [X−Bi−O−Bi−X] sheets are stacked in the [001] orientation with non-bonding van der Waal forces in the [001] direction which hold the structure together. In addition, researchers propose that the nature of the structure causes internal static electrical field between the $[M_2O_2]^{2+}$ and the double $[X]^-$ slab along the [001] path leading to efficient separation of photogenerated electron and holes (Ganose *et al*., 2016, Arumugam & Choi, 2020; Zhang *et al*., 2006; Ai *et al*., 2009; Zhang *et al*., 2008; Mi *et al*., 2014).

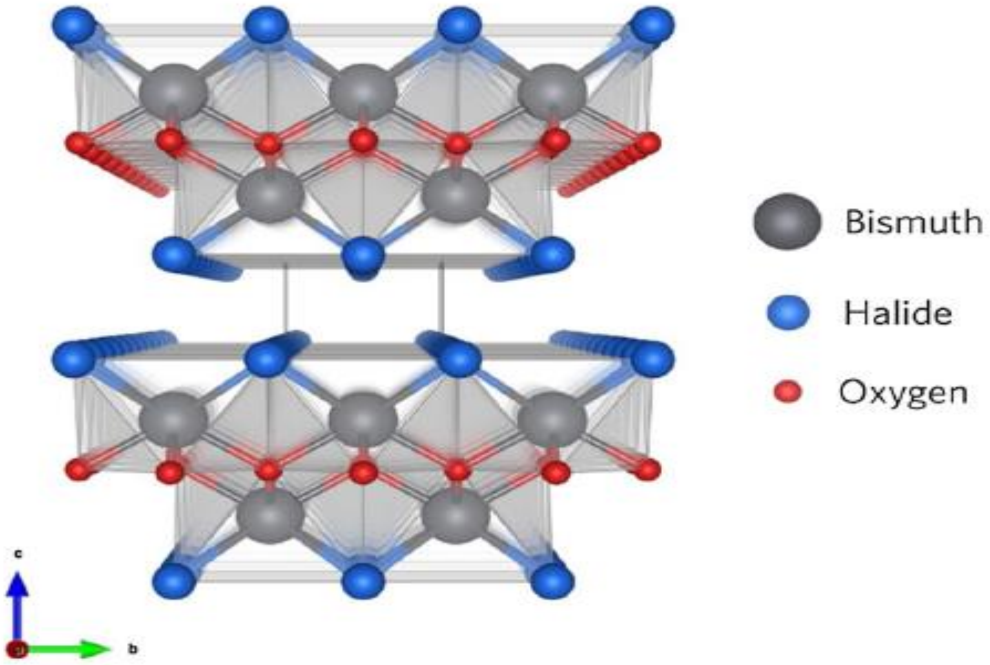

Figure 2. 10. General structure of BiOX (Mi et al., 2014).

The open and layered crystalline structure of BiOX compounds have been reported to exhibit very good photo-activity. For example, Mi and colleagues in 2014 opined that BiOCl shows a greater photocatalytic performance than TiO_2 even under UV irradiation, coupled with the fact that BiOX compounds are also able to extend their light absorption properties (visible light). Among the Bismuth oxyhalide group, BiOI has been identified as a very good photocatalyst for the abatement of wastewater. This accounts for the active research interest in BiOI and is evidenced in the 472 research articles published on BiOI between 2012 to the third quarter of 2020 (as reported on Scopus and shown in Figure 2.11).

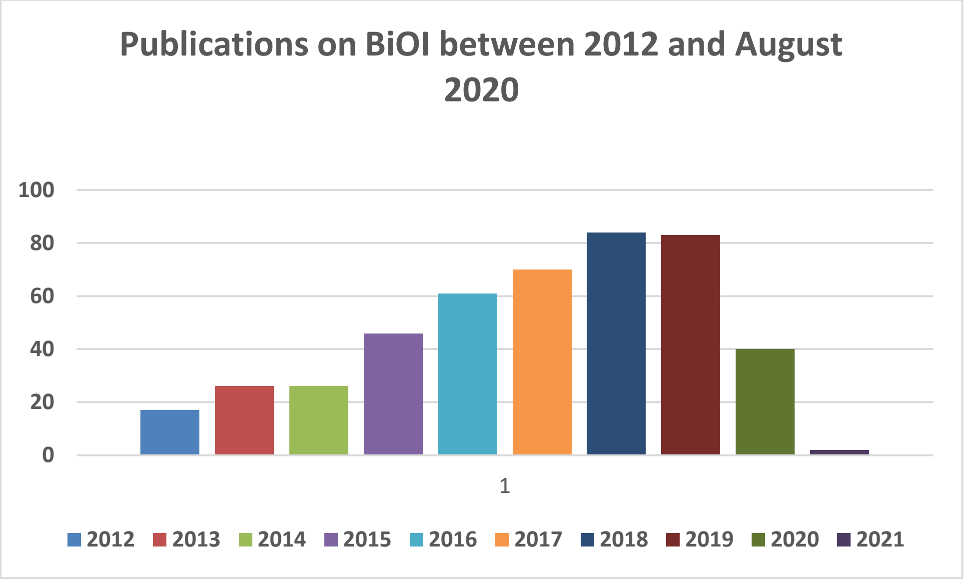

Figure 2. 11. The total number of research articles reported on BiOI material from 2012 to August 2020 (Source: http://www.scopus.com; keywords: "BiOI" and "photocatalysis").

2.8.1. Bismuth Oxyiodide

Among the Bismuth ternary metal oxides, bismuth oxyiodide (BiOI) which has the narrowest band gap, highest photocorrosion stability, is equipped with the strongest absorption under visible light and also exhibits the best photoactivity (Jiang *et al*., 2011; Liu *et al*., 2020). BiOI is a p-type semiconductor equipped with a BG of 1.7-2.1 eV and belongs to the group V-VI-VII ternary semiconductors with layered crystal structures. At the top of the BiOI VB, both O_{2p} and I_{5p} orbits are prevalent while Bi_{6s} and Bi_{6p} orbits dominate the bottom of the CB. The structure of BiOI is such that positive $Bi_xO_y^{n+}$ slabs are interweaved with anionic iodide slabs and each layer is perpendicular to the resulting internal static electric fields as shown in Figure 2.12. These intrinsic electric fields are linked to quick separation of the photogenerated electron and holes (Liu *et al*., 2013).

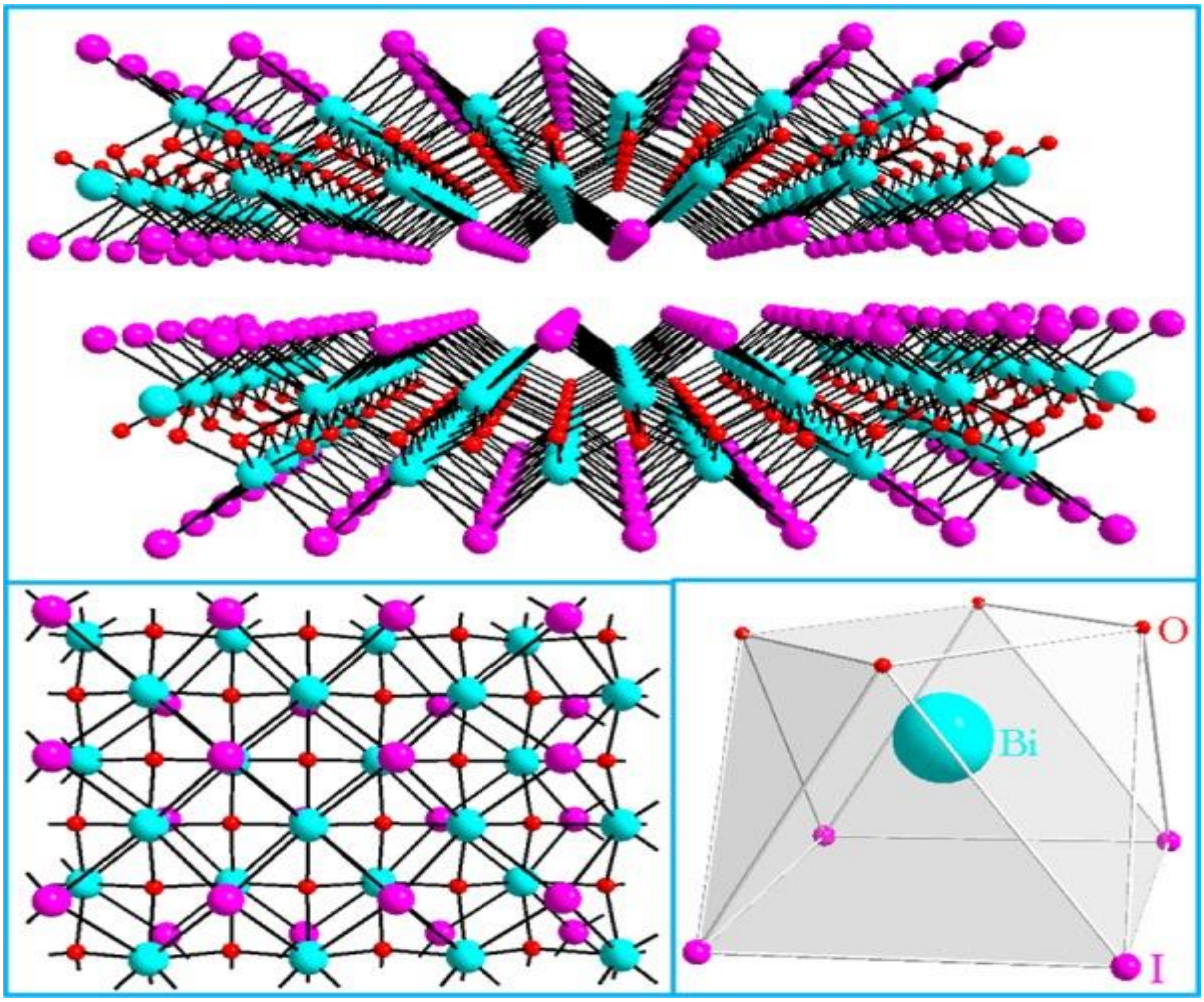

Figure 2. 12. B axis of stacked layers perpendicular to the c axis (top), single layer view (bottom left), and coordination geometry of Bi atom (bottom right)(Kandanapitiye et al., 2014).

Despite the progress made in the synthesis of BiOI, a lot of the synthesis methods have limitations. Some methods take too much time, some require high temperature for the reactions, some require high cost and time (ionic-assisted and microemulsion methods), some methods require and use toxic organic solvents (common in hydrothermal and solvothermal methods), while some procedures require specialized and complicated equipment (electrospinning, sonochemical, low temperature chemical vapour transport approach). This means that it is imperative to develop synthesis methods which are straightforward and facile.

Varying synthesis methods have been proposed by researchers for the purpose of improving its photocatalytic performance. Researchers propose that controlling the physicochemical properties may also improve its photocatalytic activity (Cruz *et al*., 2020). Some of the physical properties that are important for the improvement of the photoactivity of BiOI include morphology, particle size, crystalline structure (Arumugam & Choi, 2020). These can be accomplished by altering parameters such as solvent type, temperature and reaction time, calcination, chemical additives, use of specialized instruments such as hydrothermal autoclave reactor etc.

Various composites of BiOI with assorted morphologies have been synthesized. Some examples include one dimensional nanofibers, two-dimensional flake-like and square-like nanosheets structures, three-dimensional microspheres and hollow microspheres. It is important to add that temperature also plays a role in the phase of BiOI obtained during synthesis as observed in the study by Liu *et al*., (2020). Liu and colleagues synthesized BiOI by utilizing bulk BiI_3 annealed at 300^oC for 3 hours. The sample was washed thoroughly with DI and EtOH and subsequently vacuum dried at 80^oC. The dried samples were separated into 3 and calcined at 350^oC, 400^oC and 450^oC for 3 hours. The XRD patterns show that at 350^oC, the observed peaks are indexed to tetragonal BiOI as no residual phase of BiI_3 could be detected. The sample calcined at 400^oC was attributed to the mixed phase of BiOI and $Bi_4O_5I_2$ while the sample calcined at 450^oC was indexed to monoclinic $Bi_4O_5I_2$. These findings were further buttressed by results obtained from SEM and TEM as seen in Figure 2.13. All 3 samples exhibited characteristic overlapping nanosheets to form 2-dimensional sheet-like structures. This is because the subsequent reactions were only oxidation of BiOI, the release of iodine vapour and the ready loss of the strong reducing iodine ion. This is attributed to the thermal instability of BiOI above 350^oC (Han *et al*., 2015; Liu *et al*., 2020; Putri *et al*., 2019). Currently, 5 bismuth oxyiodide composites with different weights of oxygen are known. They are BiOI, $Bi_4O_5I_2$, $Bi_7O_9I_3$, α-Bi_5O_7I and β-Bi_5O_7I (Han *et al*., 2015; Liu *et al*., 2013; Liao *et* *al*., 2016). Suffice to say that these other derivatives of BiOI mentioned are mainly products of post-treatment (calcination) of BiOI composites after material synthesis.

In a study by Hu *et al*., (2014), BiOI photocatalyst with different morphologies were synthesized via solvothermal method at 160 ^{o}C for 12 hours using various solvents (water, ethanol, ethylene glycol and glycerol). The composites were utilized for the photocatalytic degradation of arsenic solutions. The samples synthesized using water as solvent produced nanosheets with a thickness of 60-70 nm while ethanol assisted synthesis produced hierarchical microspheres with uneven nanosheets of 50 nm as shown in Figure 2.13. Samples synthesized using ethylene glycol exhibited hierarchical structures on the micrometer scale which appeared much bigger than those synthesized via glycerol. The samples had BET surface area measurements of 2 m^2/g, 9 m^2/g, 70 m^2/g and 55 m^2/g representing samples synthesized using water, ethanol, ethylene glycol and glycerol respectively. The glycerol assisted BiOI composites showed the most significant photocatalytic efficiency in the removal of arsenic after 40 minutes of irradiation. This is ascribed to the samples higher surface area (compared to the other sample) which offered more reactive sites for pollutant adsorption and enhanced photo-activity. This is related to the solvent used, as the viscosity may have aided in the control of the morphology of that particular sample. Similarly, Di *et al*., (2014) obtained hollow microspheres of BiOI using a micro-emulsion method while using 1-butyl-3-methylimidazolium iodine ([Bmim]I) as source of iodine. The research group compared the photocatalytic of the as-synthesized samples with BiOI synthesized using KI as precursor. The composites exhibited hollow microspheres and nanosheets with specific surface area measurements of 16 m^2/g and 6 m^2/g respectively. BiOI samples with hollow microspheres showed better photocatalytic activity in the photodegradation of RhB. Just like the study undertaken by Hu *et al*. (2014), the higher comparative surface area facilitated more molecules of the pollutant to adsorb onto the surface of the photocatalyst resulting in a higher photocatalytic efficiency.

A different morphology was obtained in the study by Huang and colleagues in 2014 who synthesized BiOI composite with plate-like morphology using $Bi(NO_3)_3.5H_2O$ and KI as precursors. 1-ethyl-3-methylimidazolium hexafluorophosphate (an ionic liquid) and glacial acetic acid were utilized as solvents. The as-synthesized composite was utilized in the photodegradation of MO. The sample was observed to exhibit 9-fold photo-activity when compared with BiOI synthesized without $[EMIm]PF_6$. This means that the use of $[EMIm]PF_6$ enhanced the surface area of the BiOI and increased the efficiency of the charge separation process to achieve a higher photocatalytic activity. A number of studies on BiOI confirm that surface area is crucial for excellent photocatalytic activity of BiOI.

For this research, BiOI is prepared via a simple and facile hydrothermal process utilizing $Bi(NO_3)_3{\cdot}5H_2O$ and KI as precursors. Ultrapure Millipore water and EtOH were used as solvents, because KI is partially soluble in ethanol but readily soluble in water. A stainless-steel hydrothermal autoclave reactor lined with a Teflon was also used during the hydrothermal treatment to produce pure samples of BiOI.

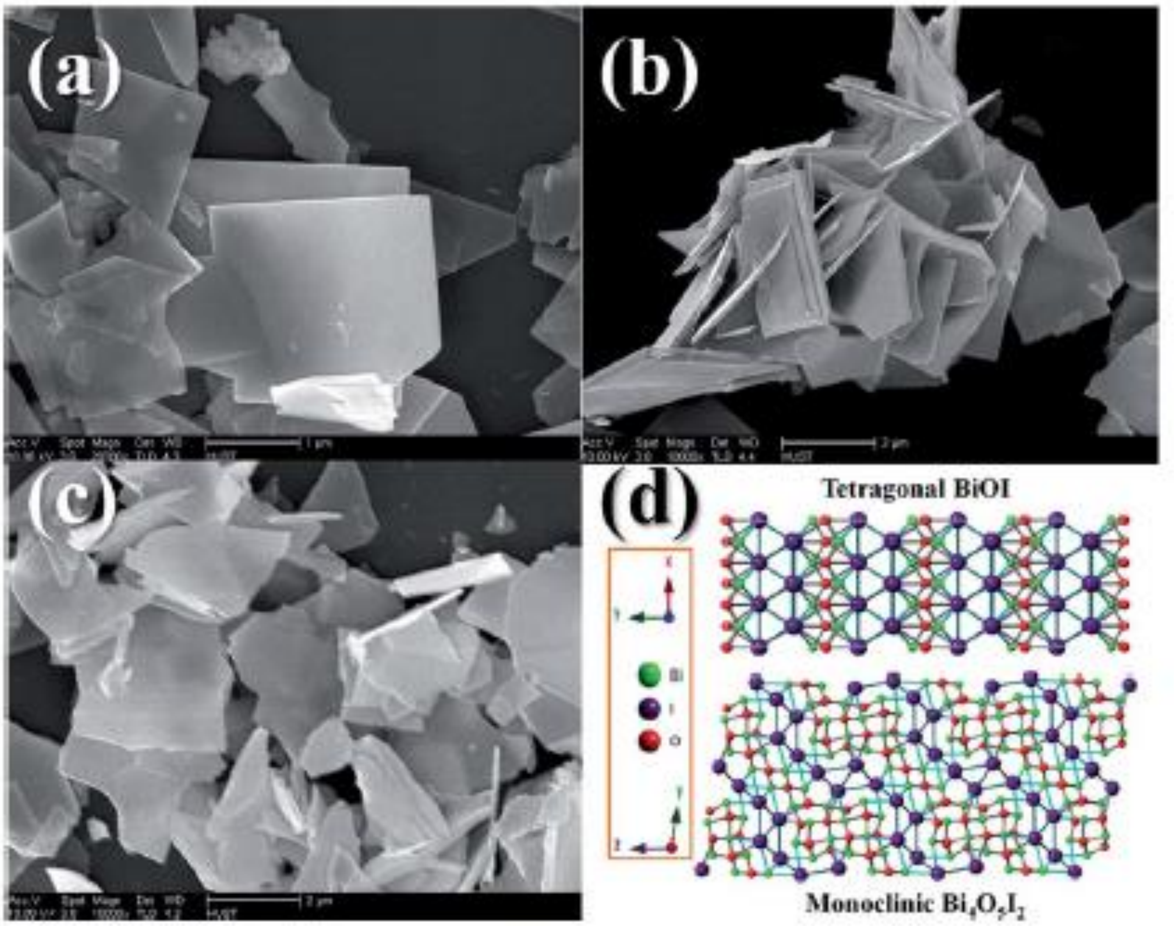

Figure 2. 13. The SEM images and crystal structures of the as synthesized samples. (a) 350 (b) 400 (c) 450 (d) Crystal structures of BiOI and $Bi_4O_5I_2$ *(Liu et al., 2020).*

Despite the possession of a narrow band gap and visible light absorption range, BiOI is plagued with the problem of increased recombination of photogenerated $\mathbf{e^-/h^+}$ which affects its quantum efficiency. In addition, the CB position (which is the reducing potential) is quite low (~ 0.5 eV vs Normal Hydrogen Electrode) which means that BiOI may not be ideal for the generation of hydrogen during photocatalytic water splitting (Dai & Zhao, 2016). In light of this, adequate tailoring is mandatory to enhance the photoactivity of BiOI. To improve the photocatalytic performance of BiOI, researchers have recommended impurity doping, construction of a heterojunction composite, solid solution preparation and making nanostructure design (Chen *et al*., 2013; Wang *et al*., 2008; Zhang *et al*., 2009; Reddy *et al*., 2013; Liu *et al*., 2012; Kuang *et al*., 2015).

2.8.1.1. Modification of BiOI

The modification of BiOI has become an area of much interest to researchers, ever since the discovery of the photocatalytic ability of BiOI. Theoretical studies show that doping the valence band maximum (VBM) of BiOI leads to improvements. Researchers also suggest that coupling n-type photocatalysts to p-type photocatalysts could in fact enhance photocatalytic activity (Zhang *et al*., 2018). This is due to the formation of p-n junction which leads to the improvement of charge separation of the e^- and h^+ because of the inner electric field between inner surfaces of the two semiconductors (Lv *et al*., 2017; Zhang *et al*., 2017). This space-charge region at the interface is capable of directing the electron-hole pairs to travel in the opposite direction as seen in Figure 2.14. Considering these merits, researchers have fabricated p-n semiconductor photocatalyst to enhance the photocatalytic ability of BiOI. This explains the interest in the current investigation in the heterojunction coupling of BiOI based photocatalysts.

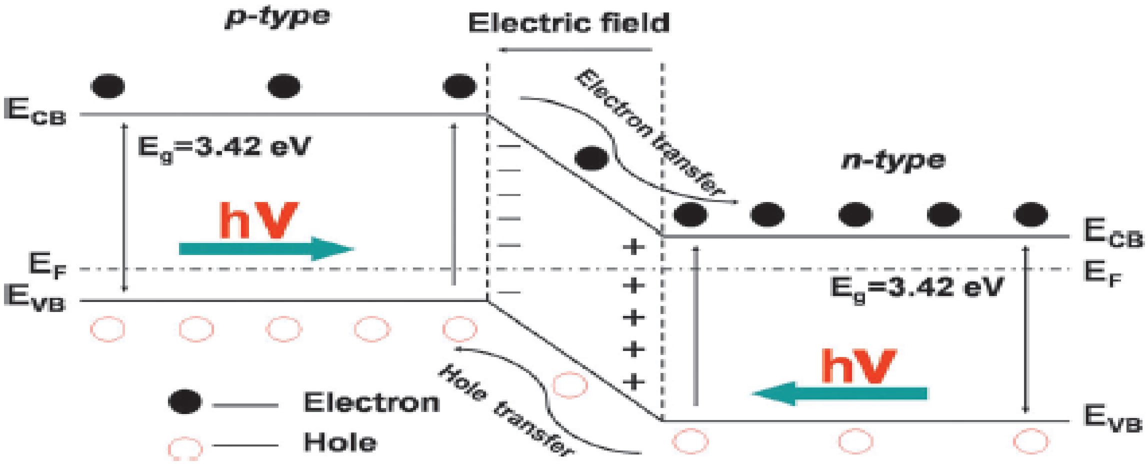

Figure 2. 14. Proposed schematic diagram of separation of electrons and holes in a p-n heterostructure and the energy band structure (Wang et al., 2014).

In 2016, Wang group synthesized heterojunction of p-BiOI nanosheets and n-TiO_2 nanofibers for the photodecolouration of MO under solar irradiation. They observed an efficiency of 92 % for the heterojunction, which was much higher than the TiO_2 nanofiber (less than 10 %

degradation). The study showed that photocatalytic efficiency improved because of the heterojunction. The reasons for this increased photo-activity is ascribed to a much higher SSA, and formation of inner electric field due to diffusion of electron-hole pairs occasioned by space-charge region formed at the p-n heterojunction interfaces. Recombination was inhibited leading to improved charge separation. The nanofiber structure of the TiO_2 played a part in preventing agglomeration of the BiOI nanosheets, which facilitated the transfer of the dye molecules during the photocatalytic process and improved surface reaction rates. Figure 2.15 shows the proposed photocatalytic process of the p-n heterojunction.

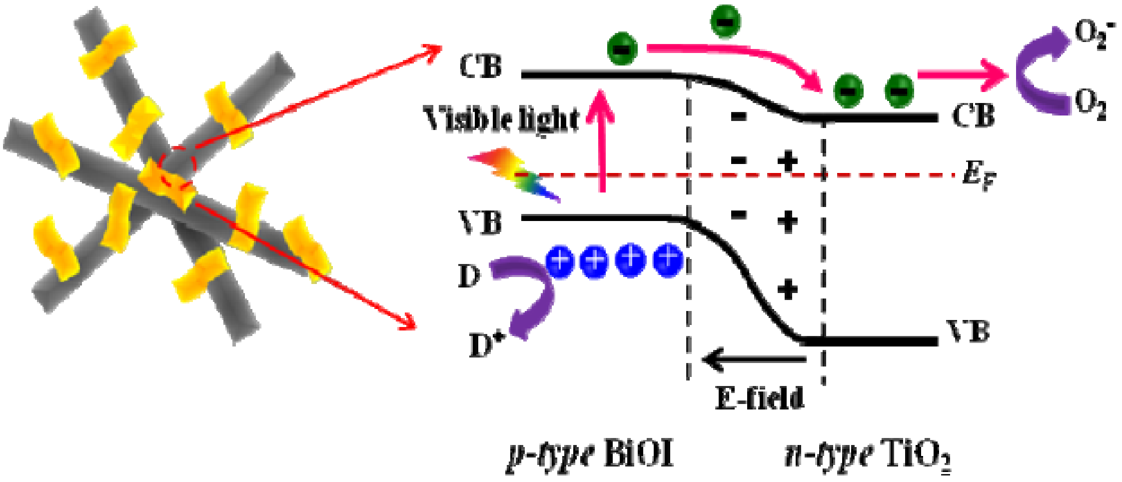

Figure 2. 15. Proposed photocatalytic reaction of the fabricated p-BiOI/n-TiO2 heterojunction (Wang et al., 2016).

Just as the Wang group took the initiative, Li and colleagues in 2018 went a step further by fabricating a heterojunction of p-BiOI and n-TiO_2. The study synthesized this heterojunction with different Bi/Ti molar ratios via biomimetic synthesis and a facile hydrothermal method for photocatalytic selective hydroxylation of phenol (high concentration) under visible light irradiation. The photocatalytic activity of this as synthesized heterojunction was compared with pure BiOI and TiO_2. Due to the poor absorption of TiO_2 in the visible light range, it exhibited the lowest conversion of phenol, while pure BiOI only showed 7.5 % conversion of phenol and poor selectivity for dihydroxybenzene (DHB). The heterostructure with 20 % BiOI-TiO_2 reached a conversion efficiency of 13.5 % and DHB selectivity of 92.1 % after 30 minutes of irradiation. This enhanced photocatalytic activity was ascribed to increased light absorption and efficient charge separation in addition to the narrow bandgap and exposed reactive facets. The BiOI in the heterostructure acted as a photosensitizer. After 4 cycles, the 20 % BiOI showed excellent reusability and maintained high photoactivity by absorbing photons unto its surface, this leads to excitement of electrons and generation of **e^-/h^+.** Migration of the photoexcited electrons generated on the BiOI surface to the CB of TiO_2 occurred because of the p-n junction, leaving holes on the VB of BiOI, as illustrated in Figure 2.16.

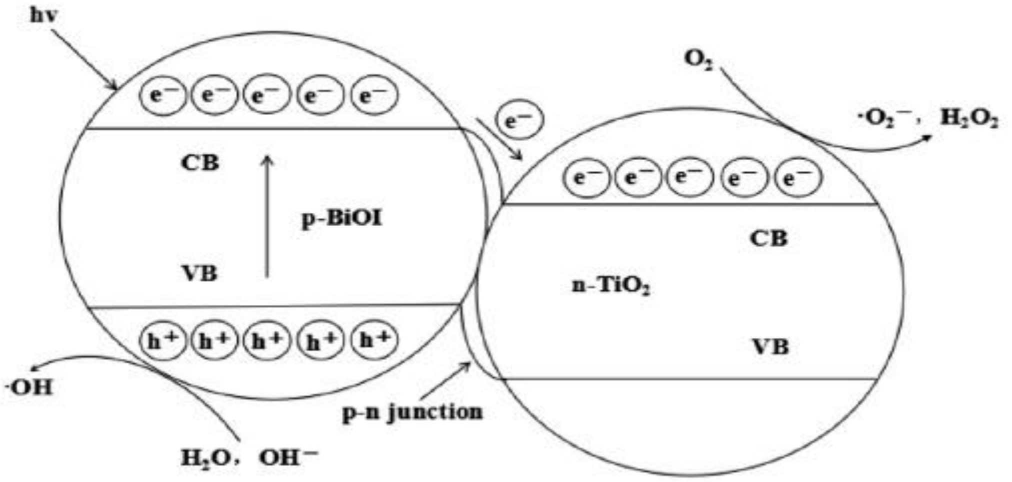

Figure 2. 16. : Proposed schematic diagram of p-BiOI/n-TiO2 charge separation and transfer process (Li et al., 2018).

The p-n heterojunction of BiOI coupled with other materials has become the “way forward” for recent studies. Different composites are currently being used to enhance photocatalytic efficiency. A study by Ao *et al.* (2016) focused on the fabrication of a highly efficient p-n heterostructure of BiOI-$La_2Ti_2O_7$ composite. This composite was fabricated via a hydrothermal route and was utilized for the photocatalytic degradation of X-3B dye, RhB, MO, and CIP (Ciprofloxacin) under irradiation (visible light). On the other hand, pure BiOI, N-TiO_2 and

$La_2Ti_2O_7$ were used to compare the efficiency of the as synthesized heterojunction. As shown in Figure 2.17, the results obtained from this study showed $La_2Ti_2O_7$ only degraded X-3B by 10 %, N-TiO_2 by 14 %, while BiOI achieved 50 % degradation. BiOI- $La_2Ti_2O_7$ performed considerably better than all the other photocatalysts in all the studies. The poor performance of undoped $La_2Ti_2O_7$ was linked to the sensitization effect of the X-3B dye. From the study, it was also discovered that 20 % BiOI loading on $La_2Ti_2O_7$ is the optimum loading as photocatalytic performance was the highest. A decline in photocatalytic activity was observed beyond the 20 % loading because of a reduction in separation efficiency of the photogenerated **e^-/h^+**. Furthermore, loading BiOI beyond 20 % is detrimental to the heterojunction because of the tendency of BiOI to aggregate and agglomerate (Wen *et al.*, 2017). This means that CB electrons of BiOI are unable to migrate to $La_2Ti_2O_7$ CB. The heterojunction was still stable even after 3 cycles of reuse. This study corresponds with the study by Li group who also utilized their heterojunction for over 2 cycles in addition to the 20 % optimum loading of BiOI.

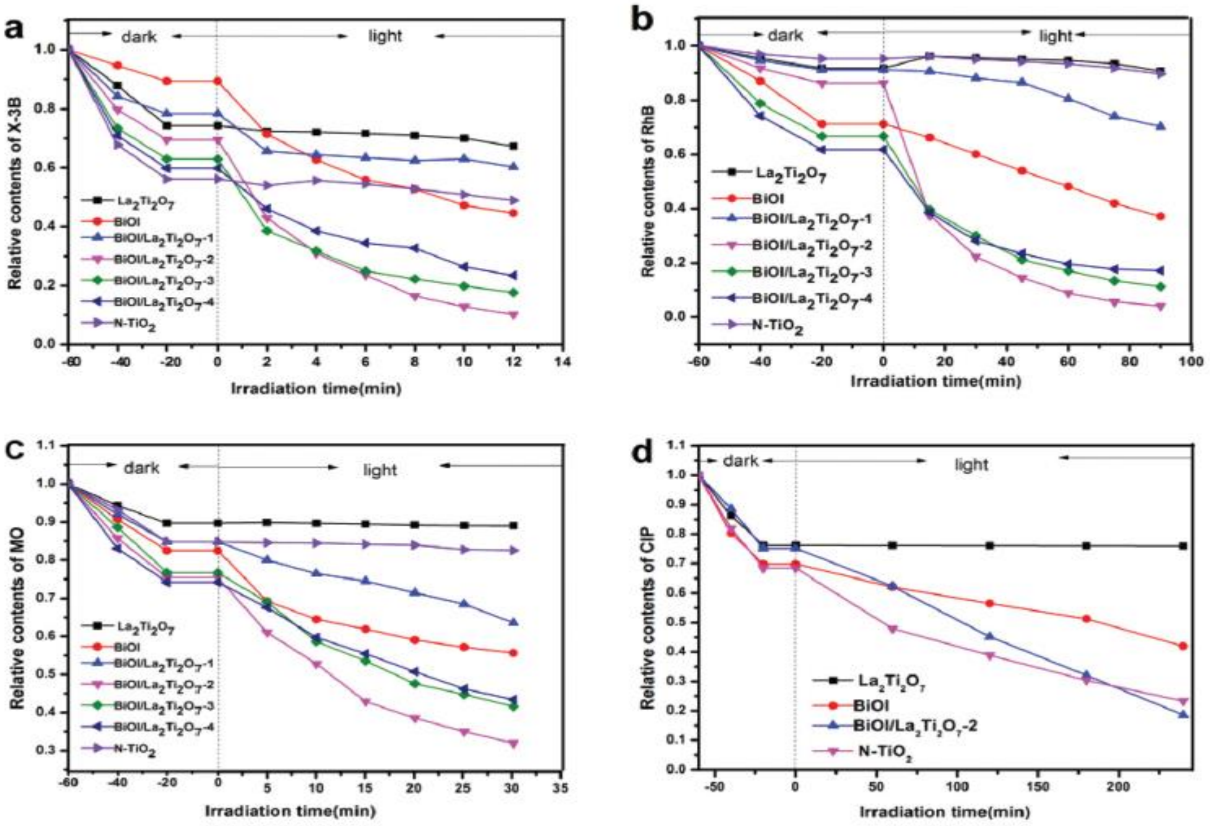

Figure 2. 17. (a) Visible light photodegradation of X-3B at 25mg/l (b) RhB at 5mg/l (c) MO at 15mg/l (d) CIP at 5mg/l (Ao et al., 2016).

The motivation for the current study is evidenced in the fact that ZnO, being an n-type semiconductor, will be ideal to form a heterojunction with BiOI which is a p-type semiconductor. It is proposed that coupling ZnO and BiOI into a heterojunction will improve the photoactivity of the synthesized ZnO because of the high-contact areas enabled by the fast charge transfer channel of BiOI and ZnO. As far as could be established from the available open literature, there are no reported studies that have synthesized BiOI or ZnO-BiOI through a facile hydrothermal process for the photocatalytic degradation of 2-chlorobiphenyl (PCB 1, 2CBP).

2.9. Polychlorinated biphenyls (PCBs)

Polychlorinated biphenyls (PCBs) are synthetic compounds which have been detected in nearly every part of the global environment as pollutants, including water, sediments, air, fish and animals, and human adipose tissue, milk, and serum (Safe, 1992). There are about 209 congeners of PCBs with different structures and an empirical formula of $C_{12}H_{10-n}Cl_n$ (n=1-10) which differs depending on the number and positions of chlorine on the biphenyl skeleton (Khan *et al*., 2007). The commercial production of PCBs is prohibited; however, they still pose major challenges due to the already released PCBs into the environment in addition to the problem of inappropriate disposal of equipment containing PCBs. More than 1 million tons of PCBs are reported to have been produced globally (Furakawa & Fujihara, 2008; Safe, 1992), and over one-third have been dispersed in our environment (Zhang *et al*., 2016). Among the class of pollutants listed as persistent organic pollutants (POPs), polychlorinated biphenyls are among the 12 persistent organic pollutants (POP) compounds, together with the 209 PCB congeners (Li *et al*., 2008). PCBs have been reported to exhibit both thermal and chemical stability, which is beneficial for industrial uses (used as dielectric fluids in capacitors and transformers, hydraulic fluids, rubber plasticizers, adhesives etc.), unfortunately, this also makes them a threat to our environment. They are persistent and show strong resistance to solar photodegradation and microbial biodegradation (Hong *et al*., 1998). PCBs have low water solubility, are lipophilic in nature and can accumulate in high concentrations in aquatic life in addition to the potential adverse effects to human beings (Zhu *et al*., 2012; Hong *et al*., 1998).

Originally PCBs were abated by biodegradation, physical processes such as incineration, solvent extraction, adsorption, and chemical processes such as the use of nanoscale zero-valent iron via de-chlorination (Chu & Kwan, 2003; Jantunen *et al*., 2010; Kubátová *et al*., 2001; Wang *et al*., 2011; Weber *et al*., 2002; Wu *et al*., 2005). Incineration leads to the production of toxic by-products such as polychlorinated dibenzo-p-dioxins and polychlorinated dibenzo-furan, bioremediation is unsuitable because of the highly oxidized and recalcitrant nature of PCBs to biological processes, adsorption requires large quantities of adsorbents and may cause waste disposal problems and regeneration of adsorbent. Some researchers have proposed sorption on activated carbon followed by thermal treatment of the solid residue, or super critical oxidation, however these methods may not be cost effective (Khan *et al.*, 2007; Kaštánek *et al.*, 2004; Nollet *et al.*, 2003). These days, photocatalysis has been proposed for the treatment of PCBs, however there are not a lot of studies in this regard.

2.9.1. 2-Chlorobiphenyl (PCB 1, 2CBP)

The pollutant of interest in this study is 2-chlorobiphenyl (2CBP) was chosen because it is one of the PCB congeners with the highest solubility in aqueous media. This makes it the most probable PCB in an aqueous environment. It has a molecular mass of 188.65 g/mol and a molecular formula of $C_{12}H_9Cl$ and its structure is shown in Figure 2.18. In light of the observed chemical and biological stability of 2CBP, photocatalytic degradation could be an important route for its environmental abatement (Carey *et al.*, 1976). 2CBP has a boiling point of 274^{o}C and a melting point of 34^{o}C.

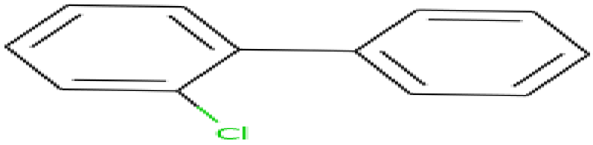

Figure 2. 18. Structure of 2-chlorobiphenyl (National Center for Biotechnology Information, 2021)

Very few studies have been done with respect to the photocatalytic degradation of 2CBP. Wang & Hong, (2000) utilized TiO_2 for the photocatalytic mineralization of 2CBP under different (4) oxygen partial pressures (Po_2) in a closed reactor. The reactions were performed in 100 ml borosilicate glass bottles. A mixture of 2CBP and TiO_2 suspensions were stirred in the dark for 60 minutes to equilibrate adsorption and desorption. To control the Po_2, the reactor headspace was purged with O_2 or N_2. At a low Po_2 of 0.5 kPa, 16 % of the 2CBP was mineralized to CO_2 while 53 %, 84 % and 94 % where mineralized to CO_2 at 4, 21 and 186 kPa respectively after 300 minutes. It was observed that 2CBP reaction rate had a rapid increase at first, and then levelled off progressively with increasing Po_2. This was attributed to the concentration of the OH radical on the surface of the TiO_2.

Huang and colleagues (1996) developed a generator-column technique for the preparation of aqueous solutions of PCBs. A slurry was made when TiO_2 was introduced into the solution under constant stirring. Adsorption-desorption equilibrium was reached in 60 minutes prior to irradiation. Extraction of irradiated suspensions were achieved using hexane followed by a split injection GC/ECD. Hexane extracts were subsequently concentrated for analysis using GC/FTIR/MSD for identification of reaction products. It was observed that over 80 % of the 2-CBP were degraded, and degradation rate increased with decrease in pH in the range of 3 to 10 after a little over 60 minutes of irradiation. The rate of degradation obeyed first-order reaction kinetics.

In another study pertaining to the photodechlorination of 2CBP, Carey and collaborators (1976) degraded 2CBP in the presence of TiO_2 in aqueous suspensions. The 2CBP was prepared using methanol/water solution as solvent in a 50:50 ratio. TiO_2 suspension and the solution were vigorously mixed and irradiated in a closed glass container for 30 minutes. Samples were filtered using a 0.45 µm filter membrane and the methanol was evaporated using a rotary evaporator. Extraction of the aqueous solution was achieved using various solvents such as hexane, benzene and ethyl ether and subsequently concentrated, dried and evaporated. A GC-FID was used to analyze the samples. After irradiation and subsequent GC analysis, 2CBP was recovered 100 % in the solution phase indicating that no reaction took place, thus confirming the stability of 2CBP.

A different observation was made when the Hong group (1998) conducted a study on the photodegradation of 2CBP in water in the presence of TiO_2. Adsorption-desorption equilibrium was attained after 60 minutes of vigorous stirring. Photoexcitation was carried out in Pyrex glass dishes (80mL, cylindrical) and the irradiated solutions were stored in the dark for 120 minutes at room temperature to allow the equilibration of 2CBP and byproducts in the headspace. The rate of degradation fit into a first order relationship as shown in Equation 2.12:

$$\ln(C/C_0) = -k_{obs}t \text{ with a half-life of } t_{1/2} = \ln(2)/k \qquad 2.12$$

where C_0 and C are concentrations of the pollutant at time 0 and t, and k_{obs} is the ascertained pseudo-first order rate constant. TiO_2 degradation efficiency in this study was observed to be at 63 %.

Most studies conducted on photodegradation of 2CBP have been with the application of TiO_2 and they are quite few. It is also important to note that previous studies have worked with very low concentrations due to the stability, difficulty, and difficult degradation mechanism of 2-CBP (Yang *et al.*, 2008; Hong *et al.*, 1998). For example, Hong *et al.* (1998) used 1 ppm in their study, Huang *et al.* (1996) worked with a concentration of 265 ppb, Carey *et al.* (1976) experimented at 25 ppb, Hong and colleagues (1998) conducted their study at 3.8 ppm, while Zhang et al. (1993) conducted their study at 80 ppb. In this study, a concentration of 10 ppm was chosen, which is both interesting and challenging. As far as could be established from the available open literature, no other studies on the photodegradation of 2CBP by the application of WO_3, WO_3-ZnO, BiOI-ZnO or BiOI were recorded in literature. This serves as a strong motivation for the relevance and importance of this study.

3. MATERIALS AND METHODS

3.1. REAGENTS

All chemicals used in this research (as presented in Table 2) were used as received without any further purification.

Table 2: Reagents used for this study.

Chemical	Supplier	Purity
Zinc acetate dihydrate	Associated Chemical Enterprises (ACE)	99.9 %
Ethanol	Associated Chemical Enterprises (ACE)	99.9 %
Bismuth nitrate pentahydrate	Sigma-Aldrich	≥ 98 %
NaOH (pellets)	Wits School of Chemistry	≥ 98 %
Ammonium metatungstate hydrate **$(NH_4)_6H_2W_{12}O_{40}$**	Sigma-Aldrich	≥ 85 %
Potassium iodide	Sigma-Aldrich	≥ 99 %
Oxalic acid dihydrate	Sigma-Aldrich	99 %
Hydrochloric acid	Sigma-Aldrich	≥ 37
2- chlorobiphenyl (PCB No 1)	Sigma-Aldrich	99.6 %
Barium sulfate ($BaSO_4$)	Sigma-Aldrich	99 %
Potassium bromide (KBr)	Sigma-Aldrich	99 %
Methanol	Wits School of Chemistry	99.9 %
NH_4OH	Wits School of Chemistry	28% NH_3 in H_2O, ≥99.99 % trace metals basis

3.2. Instruments

Deionised water purified by a Millipore system was used for all sample preparations. Smartboats disposable paper weighing boats were used for all weighing during the study. Surface morphology and elemental analysis of the as-synthesized composites were determined using a Carl Zeiss Sigma FE-SEM equipped with an Oxford X-act EDS. Optical studies were conducted using a UV 1800 Shimadzu UV-Vis Spectrophotometer. XRD measurements were carried out using a Bruker D2 XRD instrument, while BET surface area measurements and isotherms were obtained using a Micrometrics TriStar 3000 instrument. All hydrothermal synthesis were carried out using a Parr Instruments hydrothermal autoclave reactor equipped with Teflon. The average particle sizes of the as-synthesized composites were calculated from diffraction peaks using the Debye-Scherrer equation, while band gap was calculated via Tauc plots established from UV-Vis spectra. A Hettich ROTOFIX Benchtop Centrifuge was used to separate some particles suspended in liquids during synthesis, while all pH values were determined using an OHAUS Starter 3100 pH meter. A GC-MS QP 2010 equipped with a Rxi-5ms column was used for all our photocatalytic degradation studies. The light source for this study was an AM 1.5G 100 mW/cm^2.

3.3. Synthesis of Nanoparticles

3.3.1. Synthesis of ZnO nanoparticles

ZnO nanoparticles were synthesized via the sol-gel process. ZAD (zinc acetate dihydrate) was used as precursor, ethanol as solvent and oxalic acid as surfactant. Eleven grams of ZAD were dissolved in a beaker containing 300 ml of ethanol, which was subsequently poured into a 3-neck reactor set on a reflux apparatus and water bath. The solution was refluxed at 60^{o}C (±5) under vigorous stirring for 30 minutes. A clear solution was obtained. Oxalic acid was dissolved in a beaker containing 200 ml of EtOH and was subsequently added “drop wise” into the ZAD solution. On addition of oxalic acid, the formation of gels was observed as reflux was continued at 50°C (±5) for 60 minutes. After refluxing, the xerogel was cooled to room temperature and dried overnight in an oven at 80°C. After drying, the sample was collected and calcined at 500°C in a furnace to obtain ZnO nanoparticles. The process is illustrated in Figure 3.1

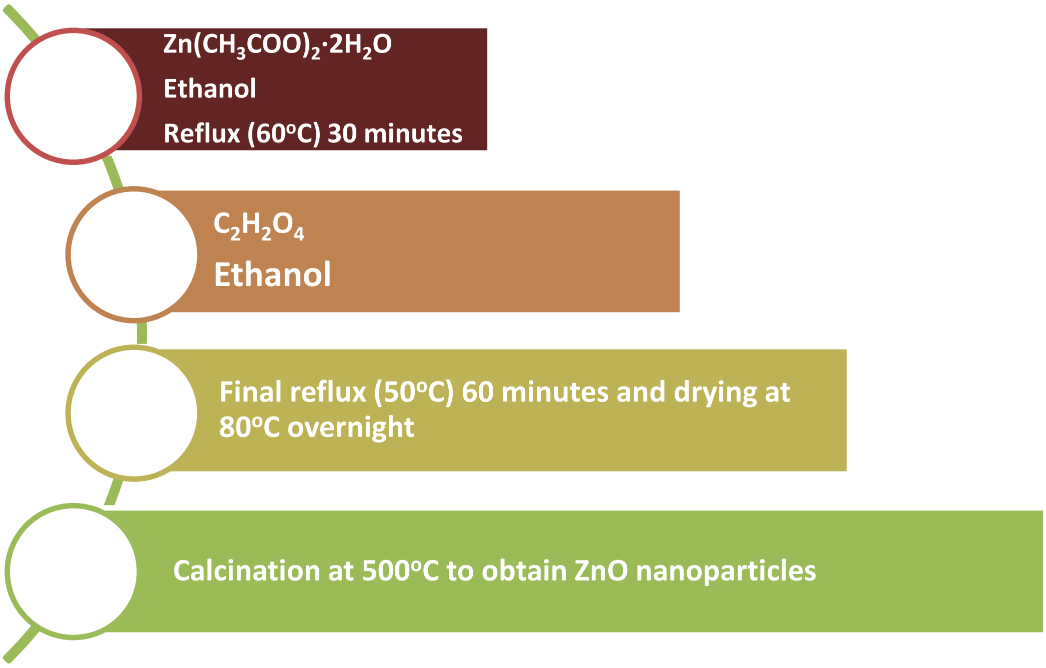

Figure 3. 1. Schematic illustration for the synthesis of ZnO NPs.

3.3.2. Synthesis of WO_3 nanoparticles

The WO_3 nanoparticles were synthesized via a simple hydrothermal process. Ammonium metatungstate hydrate powder (AMT) was dissolved in deionised water and stirred for a few minutes. AMT is readily soluble in water. The solution was transferred to a hydrothermal autoclave reactor and put into an oven at 120°C for 18 hours. The sample was taken out of the autoclave after the reaction and filtered off, washed with water, and then washed with ethanol. The filtered product (white colour) was dried in ambient air and subsequently calcined in a furnace at 500°C for 2 hours to obtain WO_3 NPs as shown in Figure 3.2 (yellow powder).

Figure 3. 2. WO3 powder after calcination in furnace at 500°C for 2 hours.

3.3.3. Synthesis of BiOI nanoplates

The BiOI nanoplates were synthesized via a facile hydrothermal process. Bismuth nitrate pentahydrate (Bi $[NO_3]_3.5H_2O$) and potassium iodide (KI) were utilized as precursors in this synthesis. Bismuth nitrate pentahydrate was dissolved in 60 ml of EtOH and stirred for 30 minutes. Potassium iodide was dissolved in 60 ml of deionised water separately and also stirred for 30 minutes. The KI solution was introduced dropwise into the bismuth nitrate pentahydrate solution as stirring was continued for 60 minutes. As stirring continued, the solution changed from a clear solution to yellow, then to orange, and finally a reddish-brown colour was observed. The reddish-brown solution was subsequently transferred to a hydrothermal autoclave reactor, and placed in an oven at 130°C for 18 hours. The autoclave was taken out of the oven and allowed to cool to avoid the release of iodine gas. The suspension was poured onto a filter paper in a glass funnel, and washed with water and alcohol. Deionised water and alcohol were used to rinse the Teflon of the autoclave. Deionised water was finally used to wash off traces of alcohol on the filter paper. The product on the filter paper was dried and subsequently ground in agate mortar to obtain BiOI nanoplates (Figure 3.3).

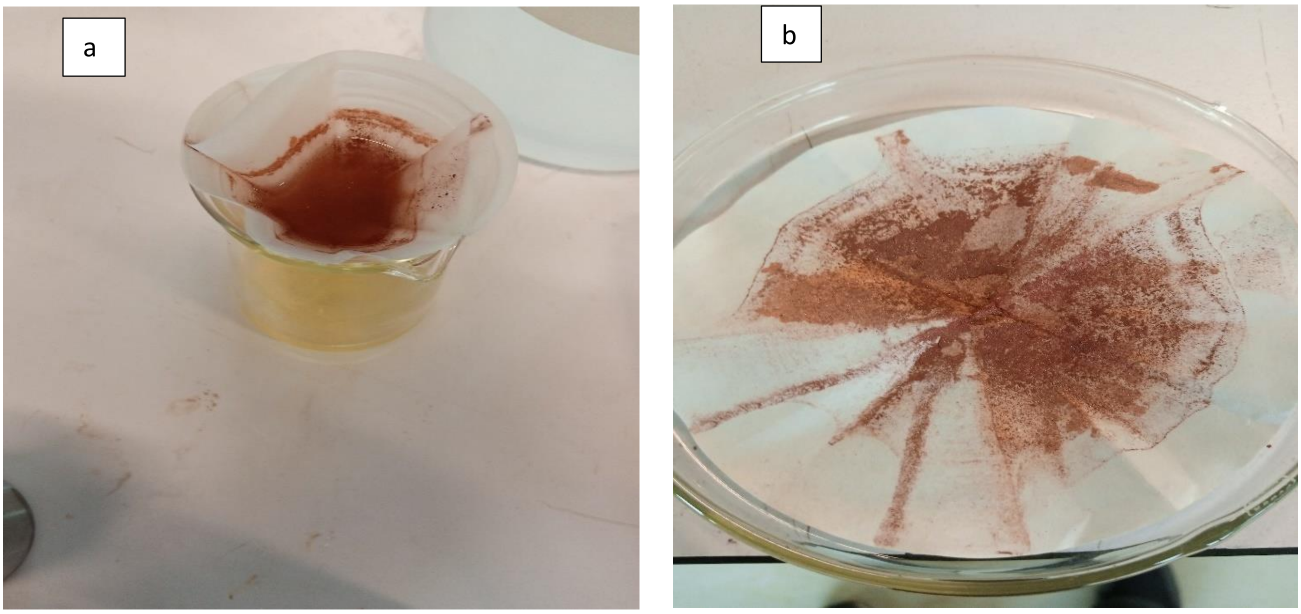

Figure 3. 3. (a) Filtration of suspension obtained after 18-hour reaction in autoclave (b) BiOI nanoplates after filtration.

3.3.4. Synthesis of ZnO-WO_3 heterojunction

To synthesize a ZnO-WO_3 heterojunction of different weight percentages (5, 10, 20 %), ZnO was dispersed in 50 ml deionized water and stirred for 30 minutes. Ammonium hydroxide was used to maintain the pH of the mixture at 6.5. A stoichiometric amount of ammonium metatungstate hydrate $[(NH_4)6H_2W_{12}O_{40}]$ was introduced to the mixture and left to stir for 15 hours. The precipitate formed was filtered, washed several times with deionized water and ethanol, and subsequently air dried. The dried sample was collected, ground in an agate mortar, and subsequently calcined at 500^{o}C for 3 hours to obtain the ZnO-WO_3 heterojunction (Figure 3.4). The final colour of the ZnO-WO_3 is dependent on the loading of WO_3. A higher loading of WO_3 gives a more yellowish colour.

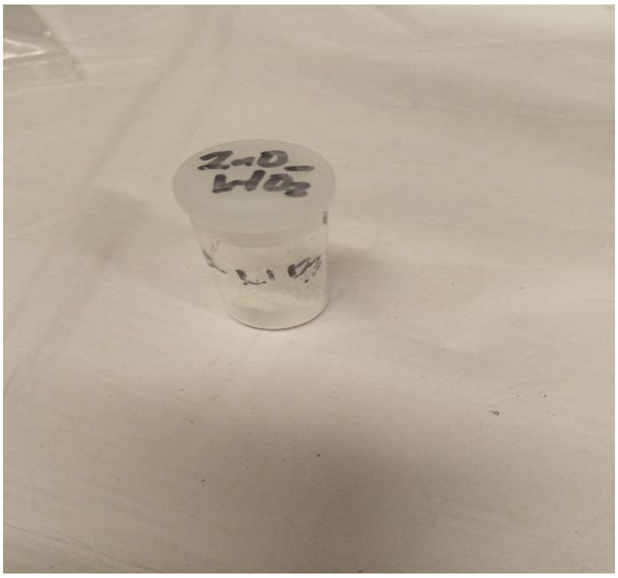

Figure 3. 4. As synthesized ZnO-WO_3 heterojunction.

3.3.5. Synthesis of ZnO-BiOI heterojunction

The ZnO-BiOI was synthesized by a simple and facile process. To synthesize a series of ZnO-BiOI with different weight percentages of BiOI, ZnO was suspended in 30 ml deionised water. Stoichiometric amounts of $Bi(NO_3)_3.5H_2O$ were added to ethanol (30 ml) under vigorous stirring. The latter was poured into the suspension and stirring was continued. A stoichiometric amount of KI was dissolved in deionized water and added dropwise into the mixed liquor under vigorous and continuous stirring. After an hour of stirring, the suspension changed to a yellow colour. The mixed liquor was allowed to stir for 3 hours. The suspension was subsequently centrifuged at 4000 rpm for 15 minutes and dried in ambient air for 18 hours. The dried product was collected and ground in an agate mortar to obtain a series of ZnO-BiOI heterojunctions (Figure 3.5).

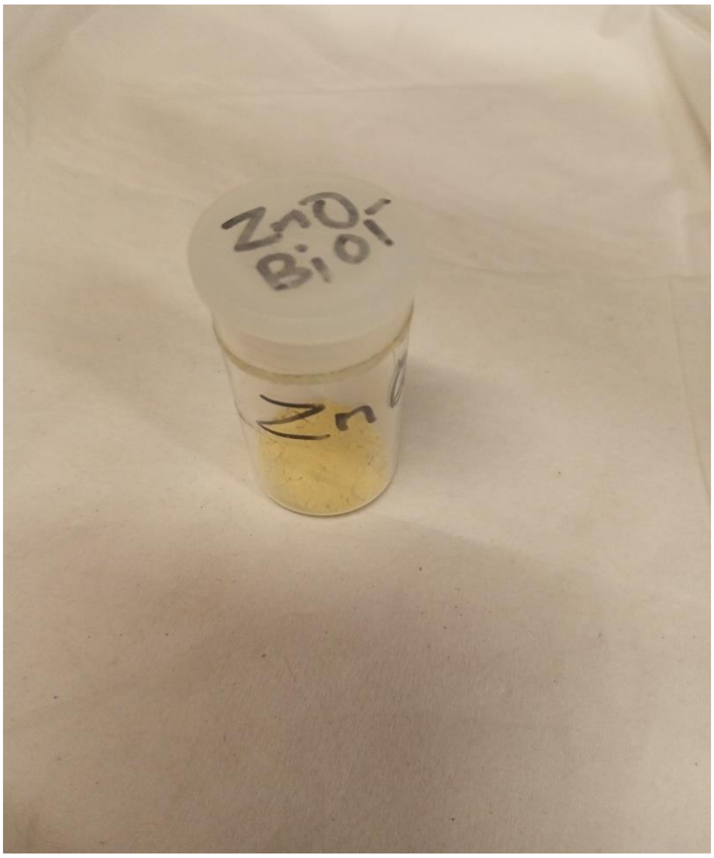

Figure 3. 5. As synthesized ZnO-BiOI heterojunction.

3.4. Preparation and determination of pollutants

A stock solution of 1000 ppm was prepared to save time and conserve materials. In addition, it helps with repeatability during the preparation of actual working concentrations.

3.4.1. Preparation and determination of 2-chlorobiphenyl

An amount of 100 mg of 2-chlorobiphenyl was dissolved in a mixture of methanol and water in a ratio of 85:15, respectively, under constant stirring. Further dilutions of the stock solution were used to obtain the desired concentrations for this study. At intervals, aliquots were taken out to monitor the degradation of 2CBP via a GC-MS instrument.

3.5. Solar Simulator

A AM 1.5G 100 mW/cm^2 instrument was used, which is equivalent to One Sun for all the solar simulations and irradiation in this study (Figure 3.6).

Figure 3. 6. AM 1.5G 100 mW/cm2 Solar simulator

3.6. GC-MS process for 2-CBP measurements

The model pollutant (2-CBP) was analysed using a Shimadzu GC-MS QP 2010 equipped with a Rxi-5ms column of 30m length, an internal diameter of 0.25 mm and a film thickness of 0.25µm. Helium was used as carrier gas and the injector temperature was set at 220^{o}C. 1 µl of sample was auto-injected into the column and the temperature program set at 140^{o}C, held for 4 minutes and then ramped up to 240^{o}C at a rate of 4^{o}C/minute, and subsequently held for 10 minutes. The interphase temperature was set at 200^{o}C, the ion source at 240^{o}C, and the mass per charge set from 35 to 500 m/z. The GC run was initiated after 3 minutes to isolate the solvent peak from the chromatogram because of the solvent cut off point. Our compound of interest was identified at a retention time of between 4 minutes to 10 minutes. The instrument is shown in Figure 3.7.

Figure 3. 7. Shimadzu GC-MS QP 2010 instrument.

3.7. Photodegradation process

All photodegradation experiments were done via a batch process. Working concentrations were prepared from a stock solution of 1000 ppm. Prior to the photodegradation process, the pH was measured, the catalyst dose was weighed, all GC vials were properly cleaned using deionized water with detergent, and then properly rinsed with methanol. The initial concentration of 2-CBP was taken into account. Dark experiments were performed prior to irradiation in order to achieve adsorption-desorption equilibrium between the surface of the catalyst and the organic pollutant. The pollutant was poured into a clean beaker mounted on a stirrer plate and placed at a distance of 4 cm from the light source. At intervals, aliquots were taken out using a syringe, and filtered using a 0.22 µm membrane filter attached to the syringe for measurement on the GC-MS instrument. Prior to GC-MS analysis, samples where equilibrated for 2 hours in a dark box (inside covered with aluminium foil) and stored in the refrigerator at 0^{o}C due to observed rapid fragmentation of the pollutant after irradiation.

The percentage degradation was calculated from Equation 3.1:

$$\textbf{Degradation (\%)} = (C_0 - C_t)/C_0 \times 100 \qquad 3.1$$

where C_0 is the initial 2CBP concentration and C_t is the concentration with respect to time.

4. CHARACTERIZATION OF AS-SYNTHESIZED COMPOSITES

4.1. SEM-EDS

The morphology of the as-synthesized composites were characterized using a Carl Zeiss Sigma FE-SEM equipped with an Oxford X-Act EDS (detector) instrument. Prior to the SEM-EDS analysis, thin layers of the powder samples were mounted on carbon tapped studs. An air duster was used to blow away the excess powders after which a double coating of Au-Pd was applied. During the SEM-EDS analysis, the operating accelerating voltages applied were between 10 – 20 kV. After the SEM analysis, an EDS micro analyzer was used for elemental analysis.

4.1.1 SEM-EDS of ZnO

The morphology of the ZnO nanoparticles synthesized via the sol-gel process was investigated using a FE-SEM. As shown in Figure 4.2, there is an observed high porosity with a sponge-like morphology and agglomeration due to the elevated temperature chemical reactions (500^{o}C). This resulted in a dense morphology due to total decomposition of the organometallic precursor. Crystallite size tends to increase at higher calcination temperature and time because atoms usually obtain more energy at higher temperature to occupy lower energy sites within the crystal lattice (Lin & Kim, 2009).

Elemental composition of the composites was determined using EDS. The EDS spectrum as illustrated in Figure 4.1 shows only Zn and O as elements from the observed peaks. The atomic percentages recorded are 42.58 for Zn and 57.42 for O, which are very close to the stoichiometric value of ZnO as presented in Table 3.

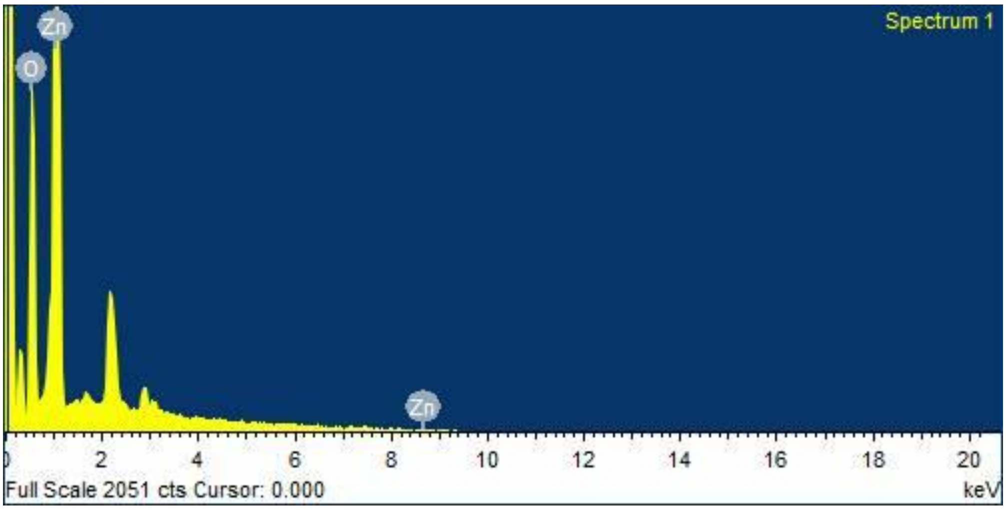

Figure 4. 1. EDS spectrum of the synthesized ZnO.

Table 3: EDS analysis of ZnO.

Element	Weight %	Atomic %
O K	75.18	57.42
Zn L	24.82	42.58
Total	100.00	100.00

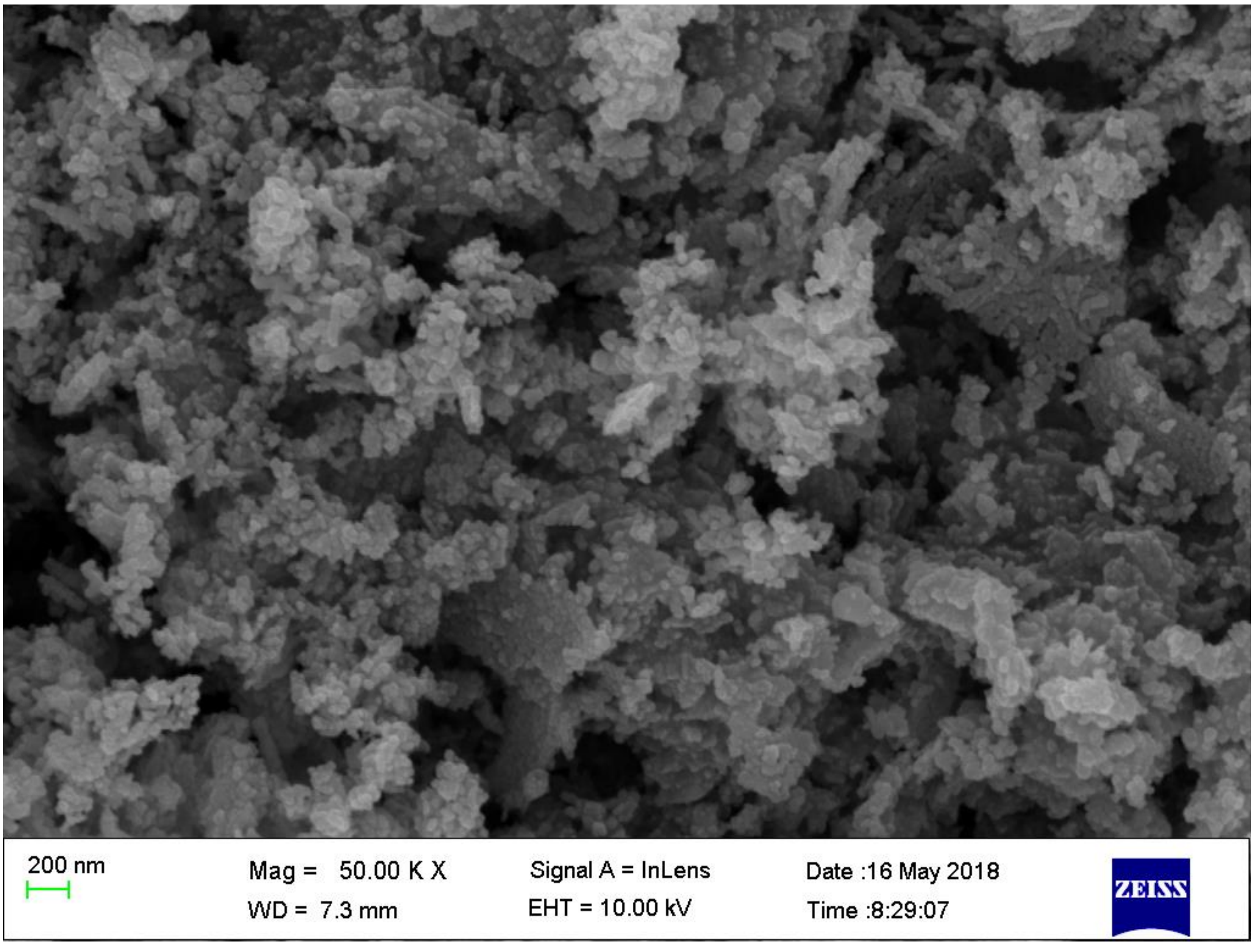

Figure 4. 2. SEM image of the synthesized ZnO NPs.

4.1.2. SEM-EDS of BiOI

Scanning Electron Microscopy of the as-synthesized BiOI catalyst showed irregular shaped plate-like morphology as seen in Figure 4.3. The type of solvents used for the synthesis may have played a role in the observed morphology in addition to the hydrothermal method used. The low viscosity solvents used in the synthesis process contributed to the plate-like morphology due to high diffusion rate of ions. The Yusoff group (2019) also observed a plate-like morphology after direct crushing of $Bi(NO_3)_3.5H_2O$ and KI, after which they added distilled water to form a paste. Their method allowed the mixture to stand for 3 hours at room temperature, and they subsequently washed this mixture several times with distilled water and allowed it to dry overnight in an oven at 80^oC.

The elemental analysis of the BiOI catalyst as shown in Figure 4.4 showed only O, Bi and I as elements present in the sample, thus confirming the purity of the composite. The atomic percentages recorded are presented in Table 4.

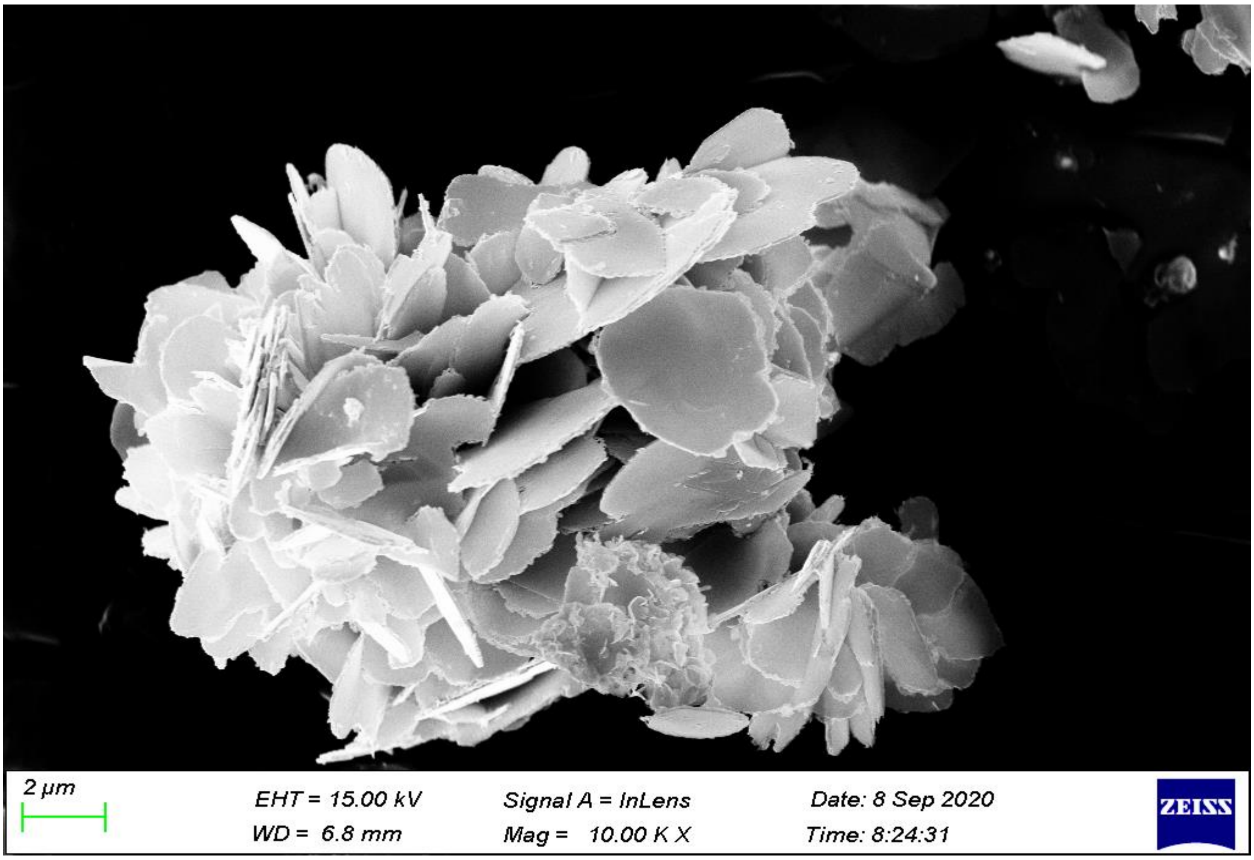

Figure 4. 3. SEM image of the as-synthesized BiOI.

Table 4: EDS analysis of BiOI.

Element	Weight %	Atomic %
O K	7.48	46.41
I L	31.44	24.59
Bi M	61.07	29.00
Total	100.00	100.00

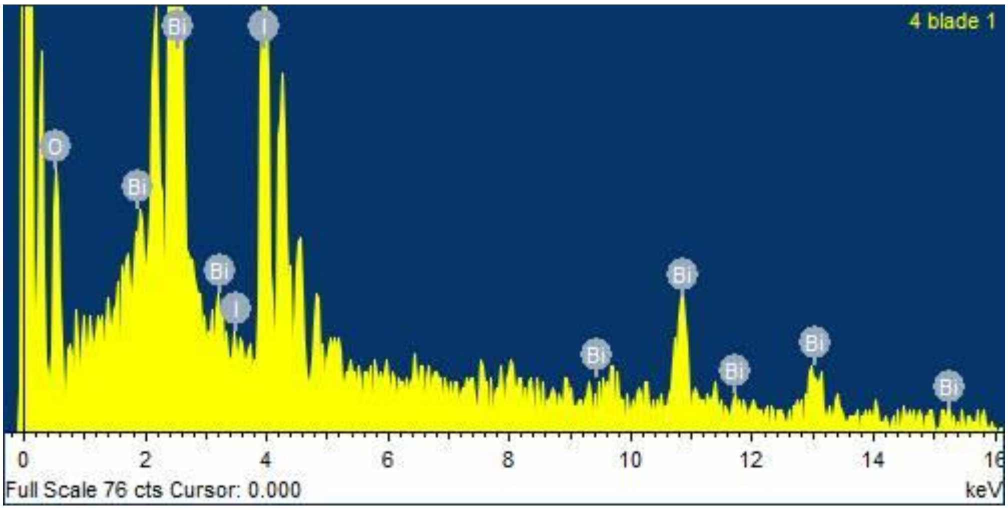

Figure 4. 4. EDS spectrum of the BiOI composite.

4.1.3 SEM-EDS of WO_3

Figure 4.6 shows the SEM image of the WO_3 nanoparticles. There is a combination of highly agglomerated non-homogeneous nanorod assays and pointed end morphology. This can be attributed to the long reaction time in the autoclave and subsequent calcination at elevated temperature. Tehrani and colleagues (2020) also observed the same effect in their study which used $Na_2WO_4.2H_2O$, sodium sulphate and citric acid as starting materials. The reaction time of 18 hours in the Teflon lined autoclave and a calcination temperature of 500^{o}C hours may have caused the agglomeration.

Energy dispersive X-ray spectrum as shown in Figure 4.5 shows only W and O as elements in the composite, indicating that the sample is indeed WO_3. Similarly, the atomic ratio and percentages presented in Table 5 have values in agreement with the established stoichiometry of WO_3. This confirms the purity of the as-synthesized WO_3 nanoparticles.

Table 5: EDS analysis of WO_3.

Element	Weight %	Atomic %
O K	18.42	72.18
W M	81.58	27.82
Total	100.00	100.00

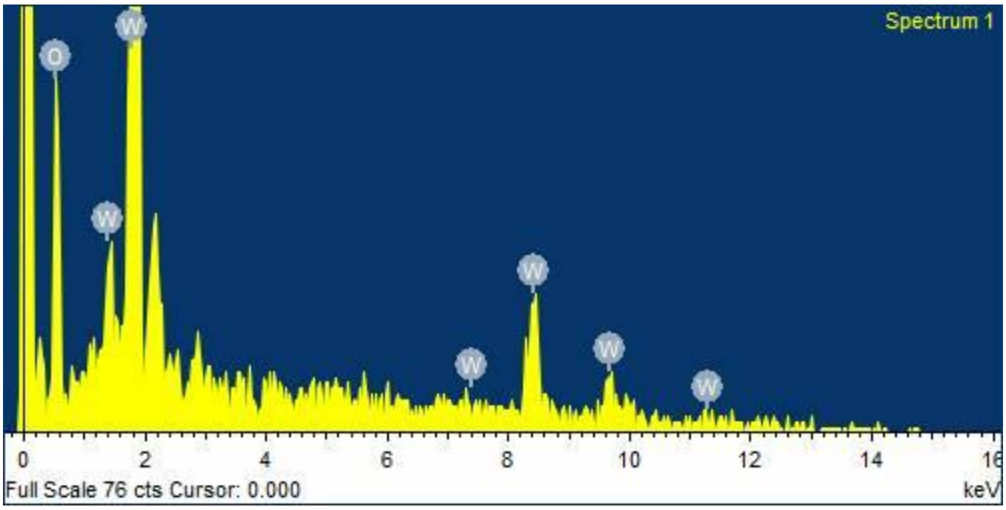

Figure 4. 5. EDS spectrum of the WO_3 catalyst.

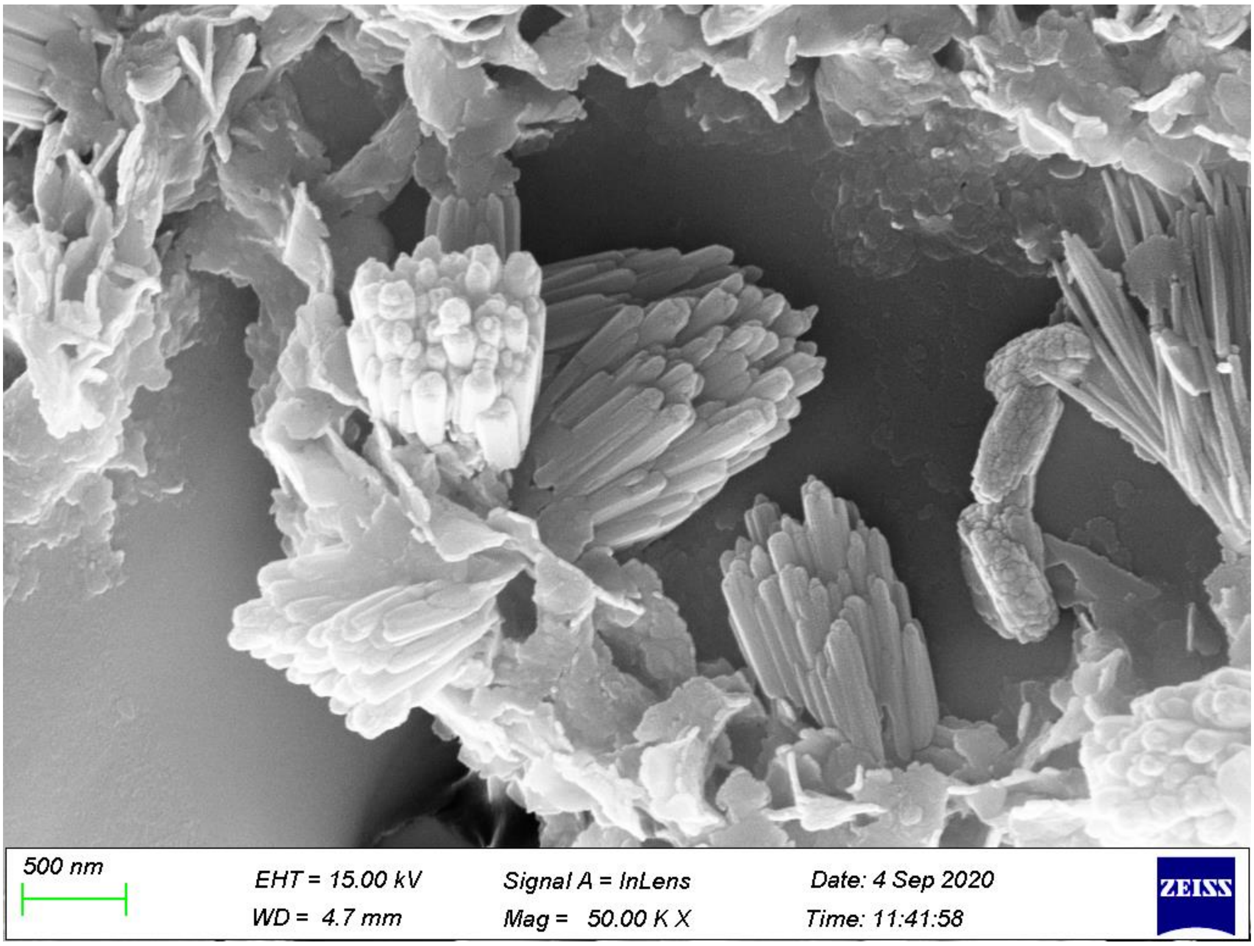

Figure 4. 6. SEM image of WO_3 sample.

4.1.4 SEM-EDS of ZnO-BiOI heterojunction

The SEM images of the ZnO-BiOI heterojunctions (5 %, 10 %, 20 %) show changes in the morphology of the ZnO. The images show non-uniform surfaces. With increased loading of BiOI in the ZnO, one can observe penetration of the rods and rectangular plates with reference to 5 % (Figure 4.7) loading of BiOI. At 10 % (Figure 4.8) loading, there seemed to be more penetration and onset of agglomeration with irregularly shaped aggregates and some plates. The sample with 20 % (Figure 4.9) loading showed more agglomeration, resulting in a sponge-like morphology with pores which could be as a result of further wrapping between ZnO and BiOI aggregates. From these observations, it can be deduced that the morphology very much depends on the loading of BiOI in the heterostructures. The Jiang group (2011) also observed changes in the morphology as BiOI loading decreased in their study, which utilised

$Bi(NO_3)_3.5H_2O$, $Zn(NO_3)_2.6H_2O$, KI, and NaOH as starting materials via a chemical bath method. Incorporation of ZnO and BiOI shows that coexistence between the two photocatalysts significantly affected their crystal growth and morphology. Natkritta *et al*. (2018) also observed a similar outcome in their study, which incorporated 0.25 % BiOI in ZnO to produce photocatalytic films for degradation of methomyl insecticide. They attributed this observation to penetration of ZnO rods into BiOI sheets resulting in high agglomeration. The increased loading of BiOI is mainly responsible for the observed changes in the morphology of the heterojunction.

All the EDS spectra of the heterojunctions (Figures 4.10 - 4.12) confirm the presence of O, Zn, Bi and I as the only elements identified in the heterojunctions. Tables 6, 7, and 8 all show the atomic percentages of the composition of the heterojunctions. As observed, the various atomic percentages changed with increased loading of BiOI within the ZnO lattice.

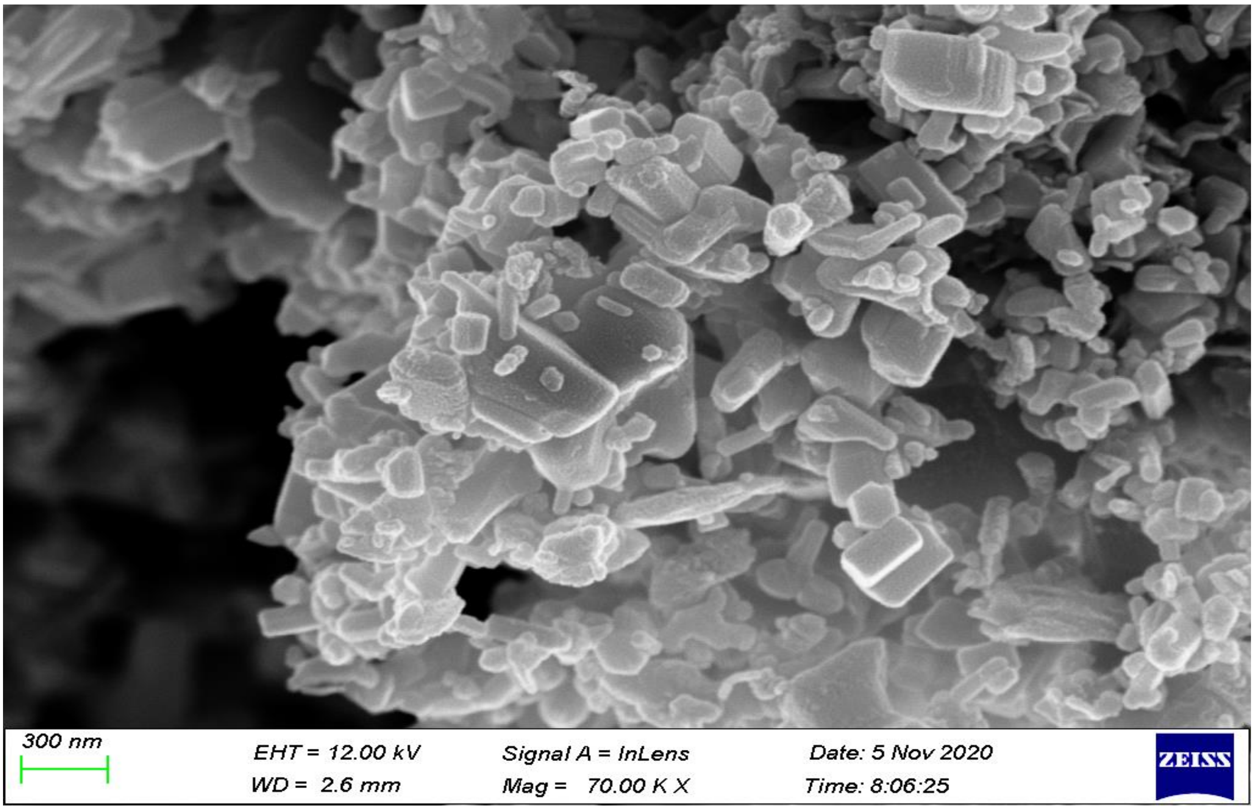

Figure 4. 7. SEM image ZnO-BiOI (5 %).

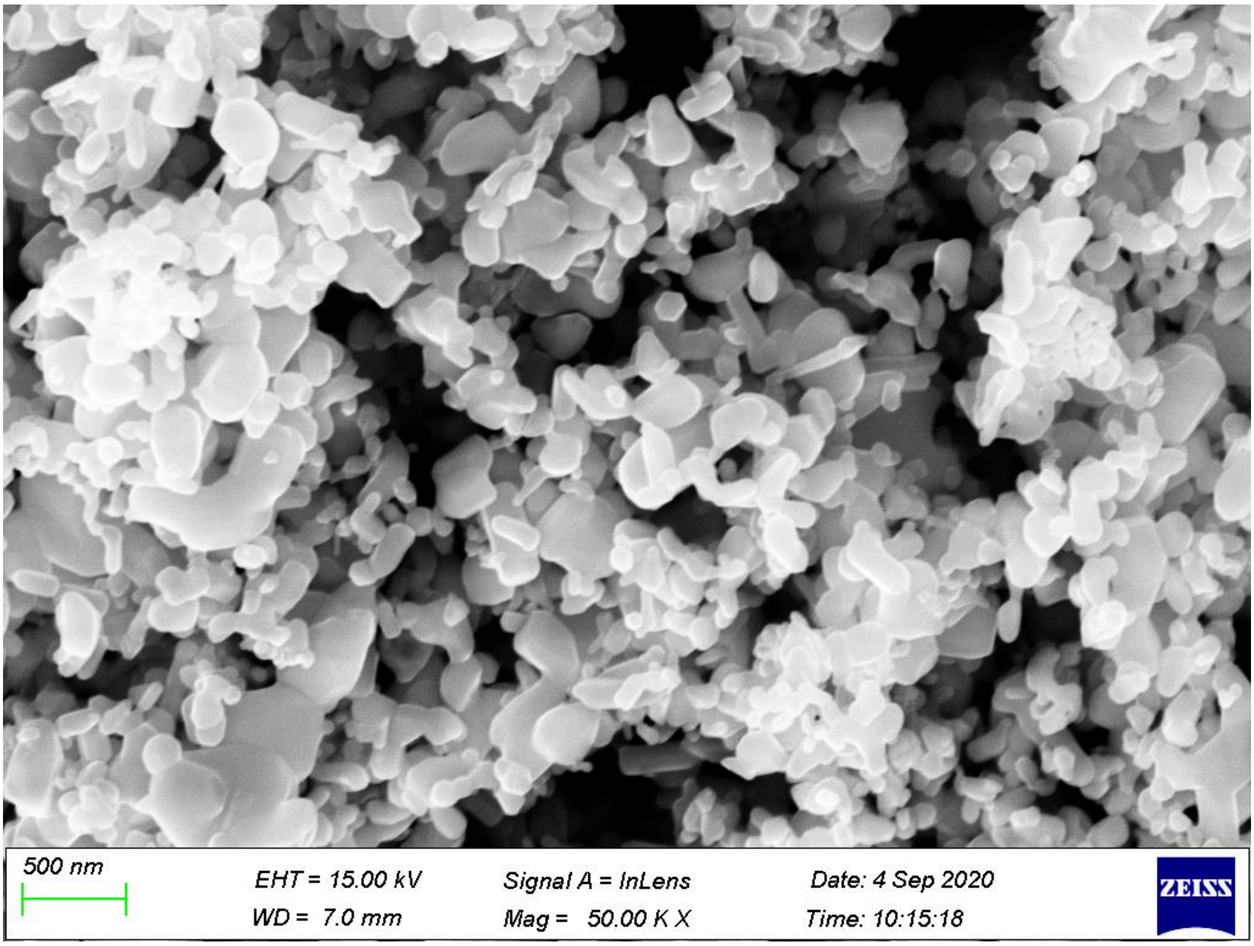

Figure 4. 8. SEM image ZnO-BiOI (10 %).

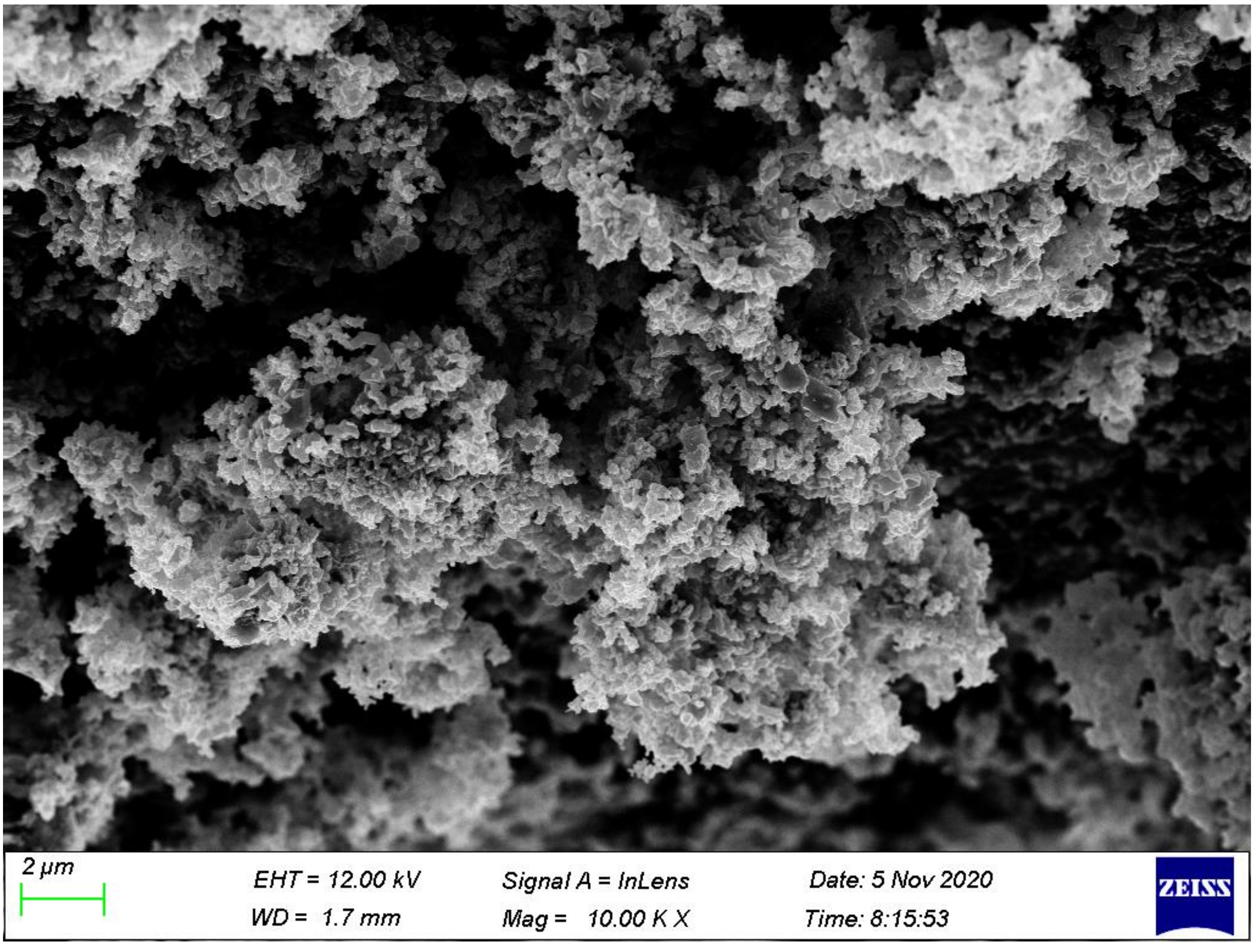

Figure 4. 9. SEM image ZnO-BiOI (20 %).

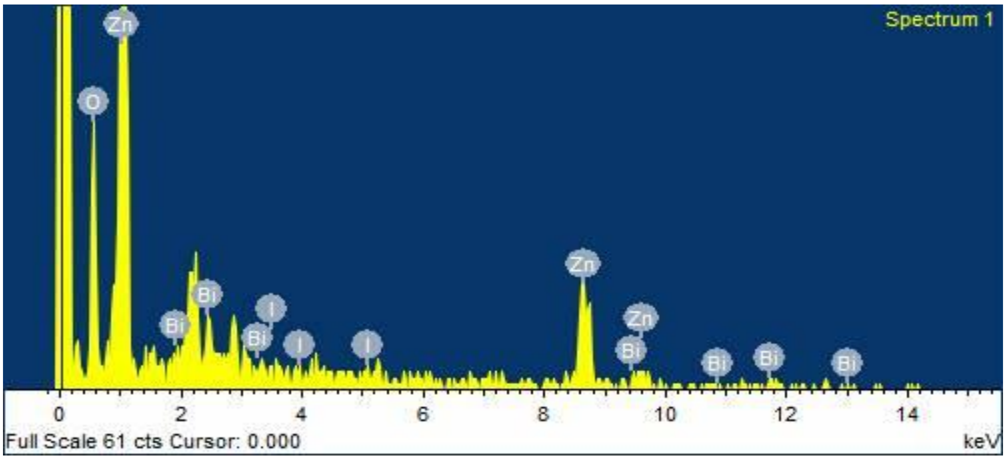

Figure 4. 10. EDS spectrum of ZnO-BiOI (5 %).

Table 6: EDS analysis of ZnO-BiOI 5 %.

Element	Weight %	Atomic %
O K	22.53	55.12
Zn K	73.52	44.02
I L	0.96	0.30
Bi M	2.99	0.56
Total	100.00	100.00

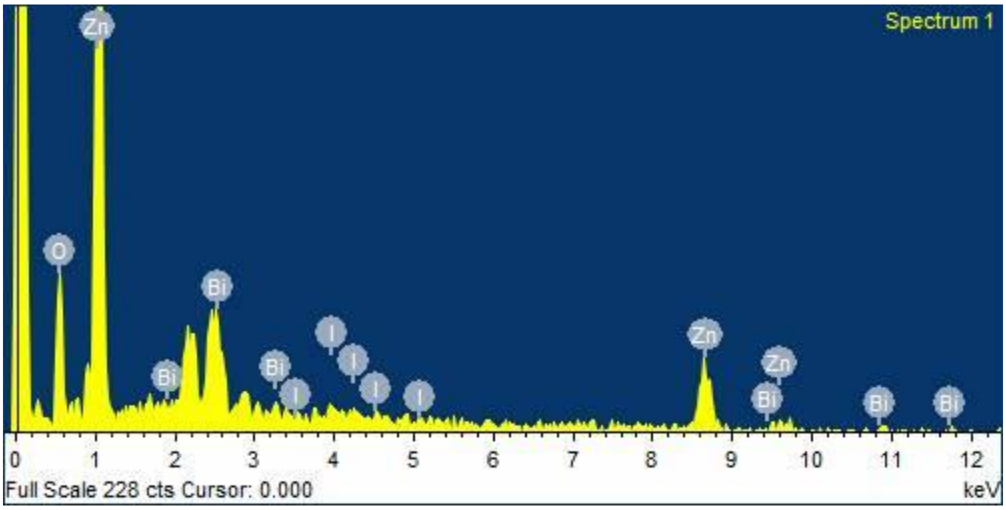

Figure 4. 11. EDS spectrum of ZnO-BiOI (10 %).

Table 7: EDS analysis of ZnO-BiOI 10 %.

Element	Weight %	Atomic %
O K	18.38	51.17
Zn K	65.38	44.55
I L	6.00	2.10
Bi M	10.24	2.18
Total	100.00	100.00

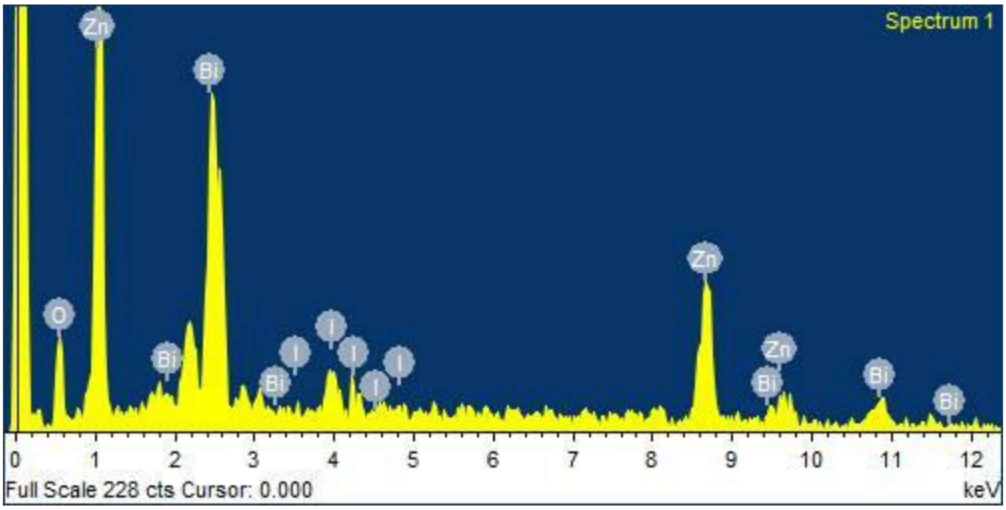

Figure 4. 12. EDS spectrum of ZnO-BiOI (20 %).

Table 8: EDS analysis of ZnO-BiOI 20 %.

Element	Weight %	Atomic %
O K	16.02	50.19
Zn K	53.69	41.17
I L	8.90	3.51
Bi M	21.39	5.13
Total	100.00	100.00

4.1.5 SEM-EDS of ZnO-WO_3 heterojunction

Scanning electron microscopy of the various loadings of WO_3 on the ZnO nanoparticles show agglomeration with no particular uniform morphology as seen in Figures 4.16, 4.17, 4.18. From close observation, one can identify mostly nodular morphology for all the 3 samples. As loading of the WO_3 increased in the ZnO, more agglomeration was observed. This can be attributed to the preparation method and starting materials which may have caused highly dense clusters of small grains which are interconnected. The sample containing 20 % wt WO_3 exhibited the highest level of agglomeration. Generally, the morphologies of all 3 samples do not show remarkable changes as loading increased when it is compared to the SEM images of pure ZnO and WO_3. Lei and colleagues (2019) also observed the same outcome in their synthesis, which combined hydrothermal and impregnation processes, followed by subsequent calcination.

EDS analysis carried out to determine the compositions of the as-synthesized heterojunctions as shown in Figures 4.13, 4.14 and 4.15 show only O, W and Zn as the only elements observed in the samples.

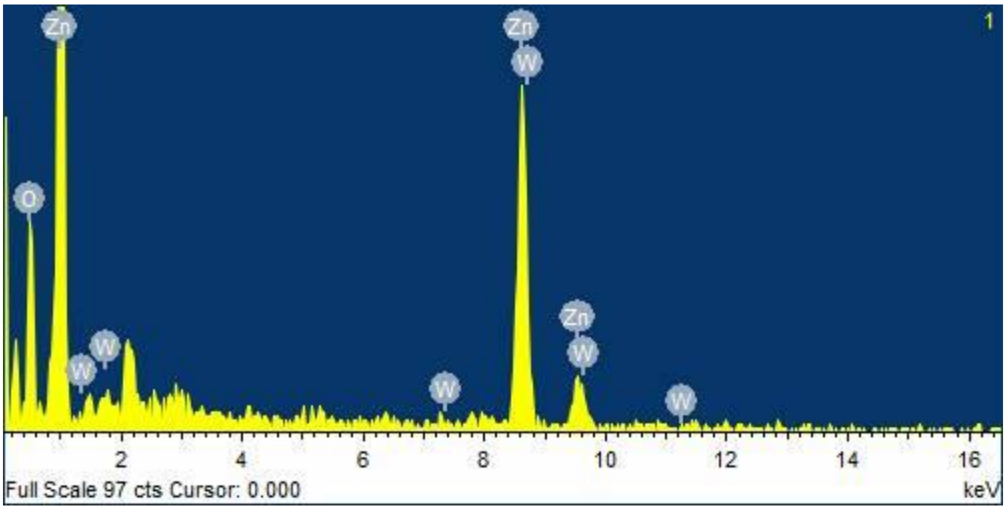

Figure 4. 13. EDS spectrum of ZnO-WO_3 (5 %).

Table 9: EDS analysis of ZnO-WO_3 5 %.

Element	Weight %	Atomic %
O K	20.14	51.75
Zn L	74.97	47.15
W M	4.89	1.10
Total	100.00	100.00

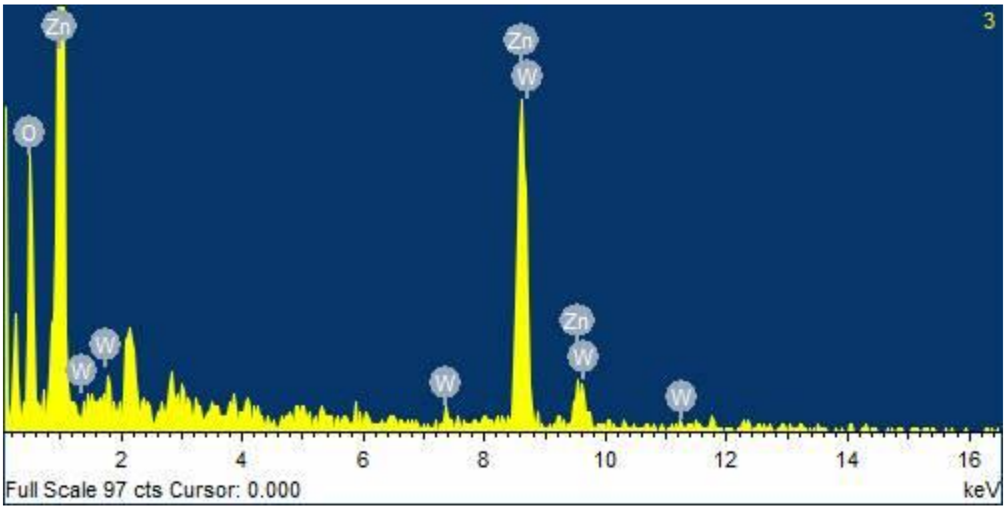

Figure 4. 14. EDS spectrum of ZnO-WO_3 (10 %).

Table 10: EDS analysis of ZnO-WO_3 10 %.

Element	Weight %	Atomic %
O K	25.66	51.75
Zn L	49.11	33.15
W M	25.23	15.10
Total	100.00	100.00

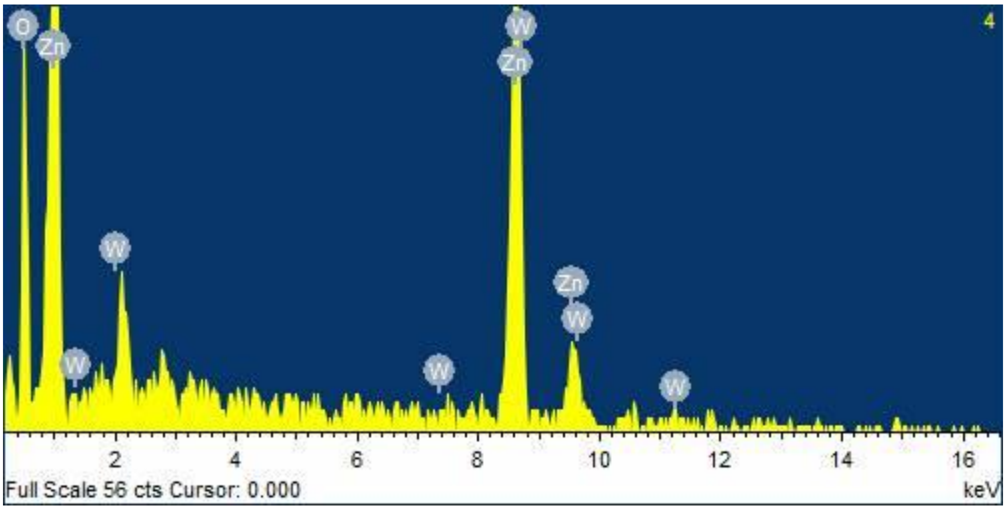

Figure 4. 15. EDS spectrum of ZnO-WO_3 (20 %).

Table 11: EDS analysis of ZnO-WO_3 20 %.

Element	Weight %	Atomic %
O K	20.18	66.99
Zn L	18.98	15.43
W M	60.84	17.58
Total	100.00	100.00

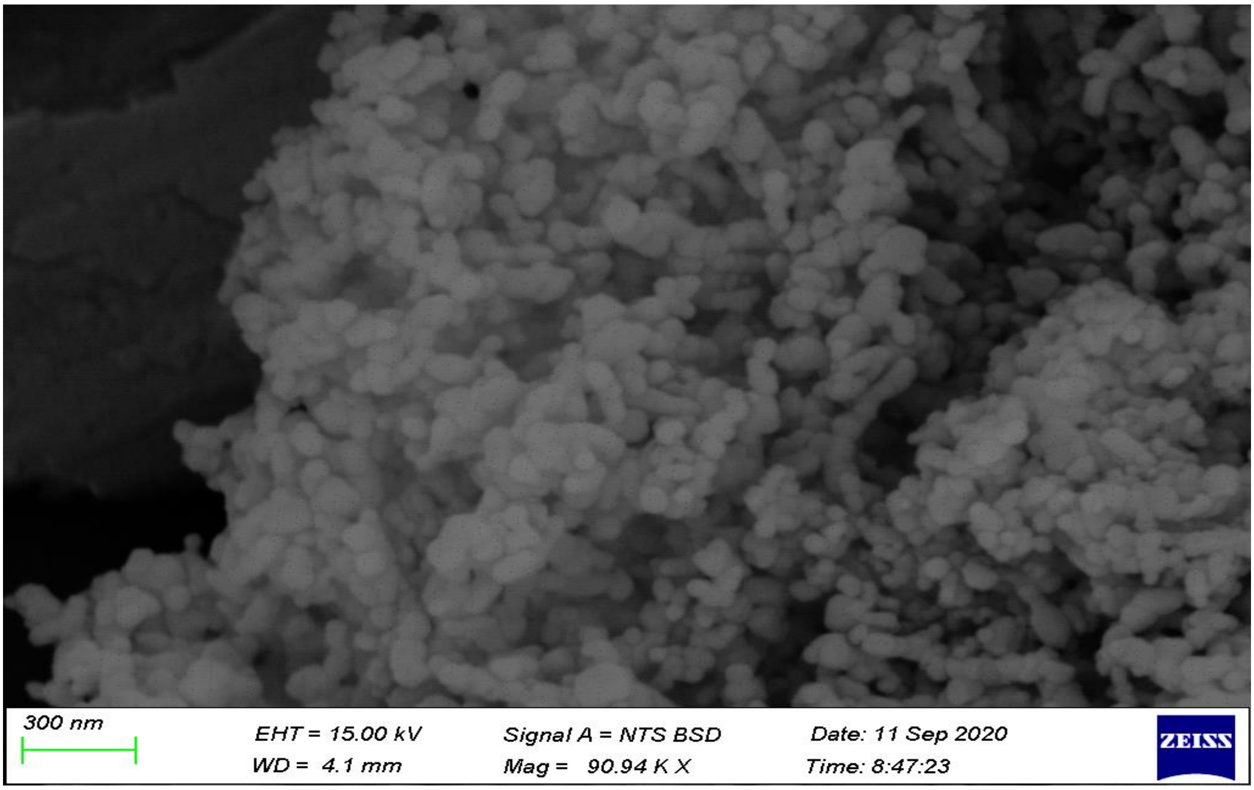

Figure 4. 16. SEM image ZnO-WO$_3$ (5 %).

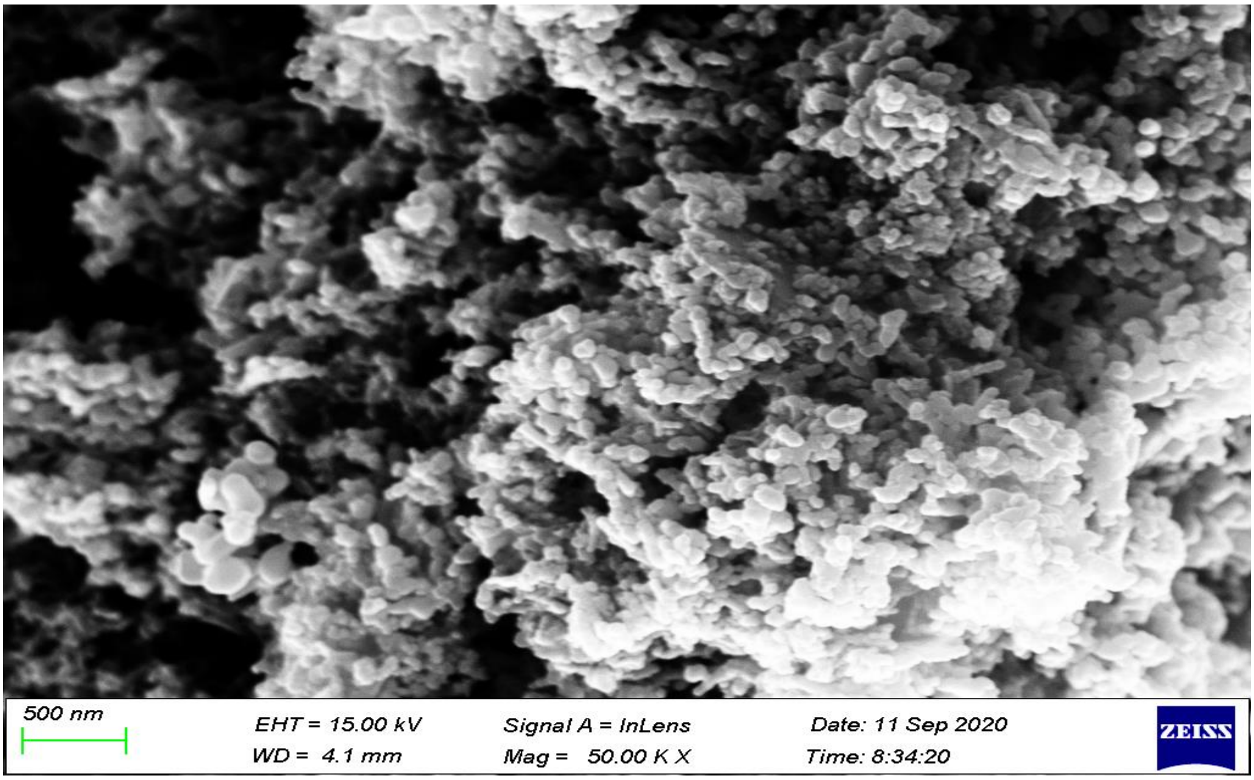

Figure 4. 17. SEM image ZnO-WO$_3$ (10 %).

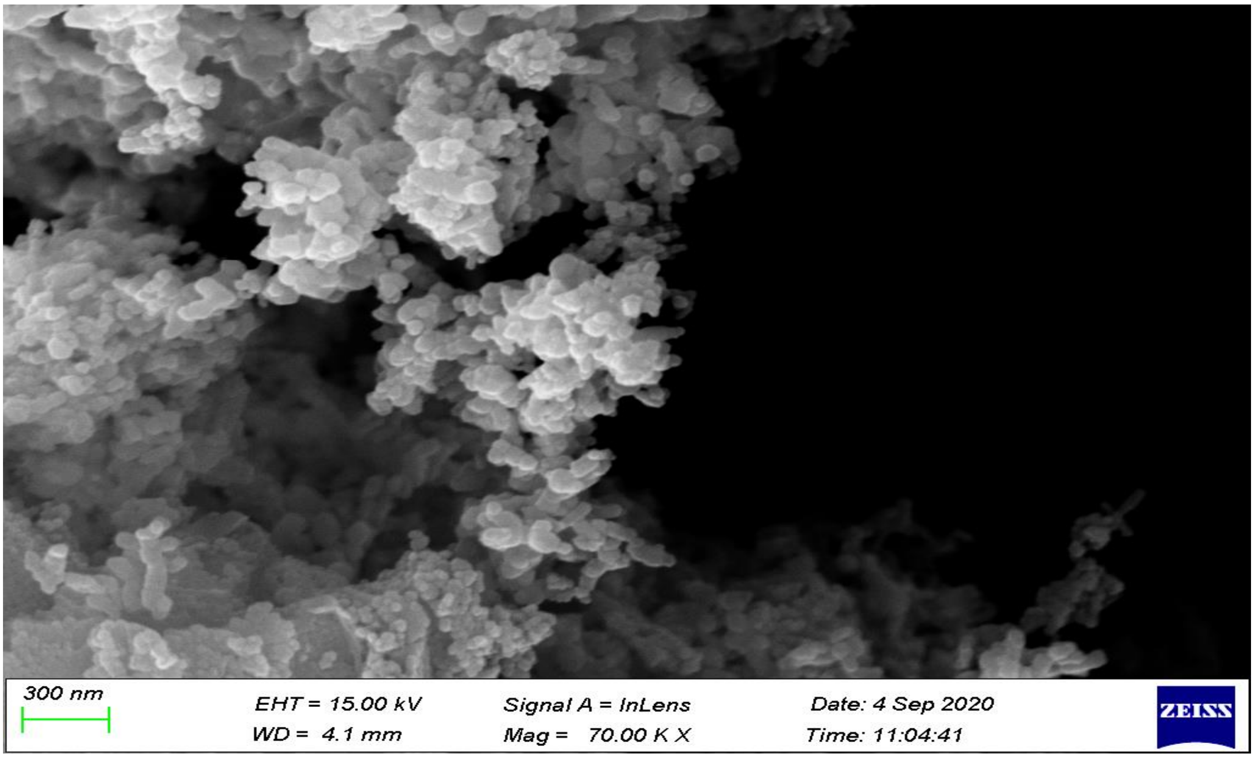

Figure 4. 18. SEM image ZnO-WO_3 (20 %).

4.2. X-ray Diffraction and crystallite sizes

The diffraction patterns and crystallinity of the powder samples were measured using a D2 Phaser Bruker X-ray diffraction instrument. The sample holders were properly cleaned with acetone and an appropriate amount of the individual powder sample was loaded into the sample holder for subsequent analysis using the XRD instrument.

The average crystallite sizes of all the synthesized photocatalysts were calculated from the FWHM obtained from the diffraction peaks using the Debye–Scherrer Equation 4.1.

$$\mathbf{D = k(\lambda /(\beta \cos \theta))} \qquad 4.1$$

where $\lambda = 1.54056$ nm is the wavelength of X-ray diffraction used, θ is the Bragg diffraction angle of the XRD peak, β is the measured broadening diffraction line peak at an angle 2θ at half its maximum intensity (in radian).

4.2.1 XRD pattern and average crystallite size of ZnO

The XRD pattern of the as-prepared ZnO nanoparticles show sharp and intense peaks which were observed at 2θ with values of 31.7°, 34.4°, 36.1°, 47.3°, 56.3°, 62.6°, 66.3°, 67.9° and 69.1° corresponding to (100), (002), (101), (102), (110), (103), (200), (112) and (201) crystal planes of hexagonal ZnO. As displayed in Figure 4.19, the diffraction peaks of pure ZnO are intense and narrow showing high crystalline character. The orientation of the as-synthesized ZnO nanoparticles conformed to the hexagonal wurtzite phase of pure ZnO nanoparticles as indexed on JCPDS 01-075-6445. No impurity peaks were observed, thus confirming the precursors were fully decomposed and no impurities detected. One can attribute the high crystallinity of the sample to the elevated calcination temperature during the synthesis.

The average particle size of the sample was calculated from the most intense peaks of the XRD pattern from the FWHM using the Debye–Scherrer relationship. The particle size was determined to be **37.6 nm** (Table 12), thus confirming that the synthesised ZnO is well within the nanometre size range. The average particle sizes of all the doped ZnO composites are summarised in Table 12.

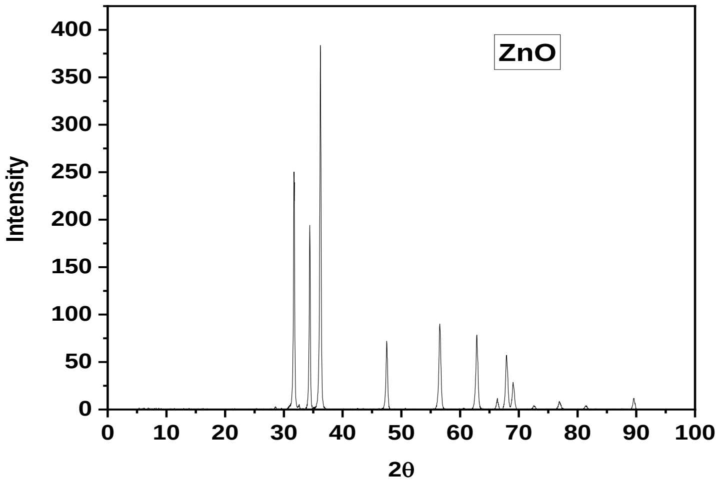

Figure 4. 19. XRD pattern of the as-prepared ZnO nanoparticles.

4.2.2 XRD pattern and average crystallite size of BiOI

The XRD pattern of the as-prepared BiOI photocatalyst is displayed in Figure 4.20 and shows intense peaks. The diffraction peaks of the sample are classified as the tetragonal phase of BiOI and indexed on the JCPDS card number 00-010-0445. From the displayed pattern, it is observed that the sample contains the pure phase of BiOI coexisting with the mixed phases such as Bi_5O_7I, $Bi_7O_9I_3$. This is attributed to the synthesis method and the long hydrothermal reaction time in the autoclave lined with a teflon. The peaks located at 10^o, 30^o, 34^o, 46^o, and 56^o correspond to the (001), (102), (110), (200), and (212) diffraction planes identified, respectively. The intense and sharp diffraction peaks of the sample indicate the high crystallinity of the as-synthesized photocatalyst.

Using the Debye-Sherrer relationship via the FWHM established from the intense XRD peaks, the average crystallite size of the BiOI was calculated as 40 nm. This establishes that the as-synthesized BiOI is well within the nanometre size range.

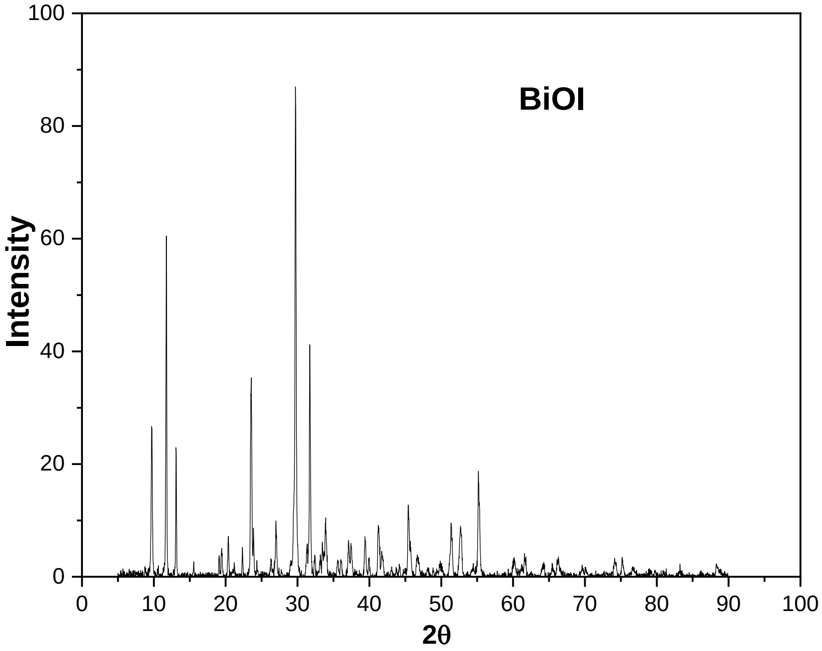

Figure 4. 20. XRD pattern of the as-prepared BiOI nanoparticles.

4.2.3 XRD pattern and average crystallite size of WO_3

The XRD pattern of the WO_3 sample is shown in Figure 4.21, and corresponds to the triclinic phase of tungsten trioxide as indexed on JCPDS card number 00-032-1395. There are no observed impurity peaks, which attest to the purity of the sample and excellent synthesis. Peaks were identified at 23.26°, 24.47°, 26.79°, 28.95°, 34.20°, 49.98°, and 55.89° and correspond to the (001), (110), (101), (200), (201), (220) and (202) crystal planes, respectively.

The Debye-Scherrer equation was used to determine the average crystallite size of the as-prepared WO_3 photocatalyst. The calculated value for the average crystallite size was extrapolated to be 12.98 nm, thus, confirming that the as-synthesized WO_3 is well within the nanometre size scale.

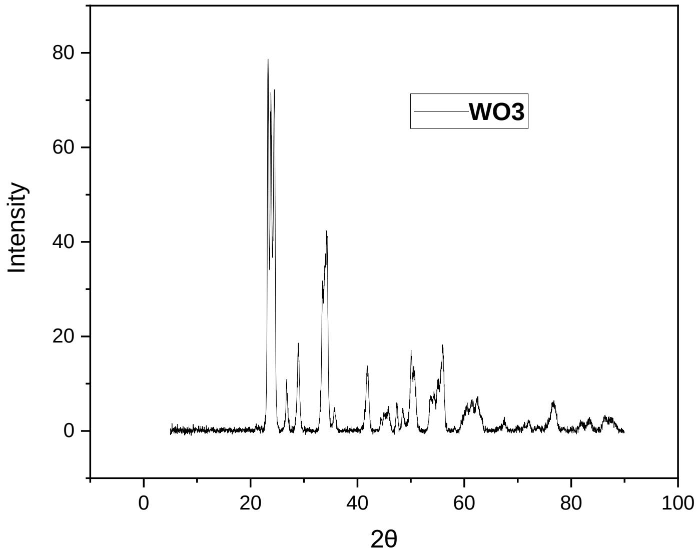

Figure 4. 21. XRD pattern of the as-prepared WO_3 nanoparticles.

4.2.4 XRD pattern and average crystallite sizes of ZnO-BiOI composites

Figure 4.22 shows the XRD pattern of the as-prepared ZnO-BiOI composites corresponding to the different loadings. The pattern for the sample with 5 % BiOI loading does not show peaks of BiOI within the ZnO lattice. This could be due to the detection limit of the instrument, which is also related to the low loading of the BiOI on the ZnO surface. This occurrence is also ascribed to the high dispersion of the BiOI on the surface of the ZnO. The samples with loadings of 10 % and 20 % show some information. At 10 % loading, a peak at 29^o appeared, and corresponds to the 102 diffraction plane of BiOI nanoparticles. At an increased loading of 20 %, the peak at 29^o became more intense, thus confirming the increased loading of the BiOI and its complete integration within the ZnO lattice. A similar trend was observed in the study by Jiang *et al*. (2011). The intensity of the peaks increased with increased loading of BiOI. The XRD patterns of the as-prepared heterojunctions exhibited characteristic peaks of both pure of BiOI and ZnO crystalline phases. There were no other impurity peaks observed in all 3 samples, which confirms the purity of the samples, excellent synthesis, and complete dispersal of the BiOI on the surface of the ZnO nanoparticles.

The crystallite sizes of the composites were calculated using the Debye-Scherrer formula. As shown in Table 12, the sample with the 5 % BiOI had the smallest average crystallite size of 16.4 nm, the sample with 10 % BiOI had an average crystallite size of 31 nm, while the sample with 20 % BiOI loading had an average crystallite size of 45 nm. Average crystallite size increased with increasing loading of BiOI in the ZnO composite. There may have been a penetration of the hexagonal wurtzite crystal structure of ZnO by tetragonal BiOI which would influence crystal growth-induced collapse. This occurrence explains the small crystallite size of the 5 % ZnO-BiOI compared to the other samples. This also explains the increased crystallite size in the other samples.

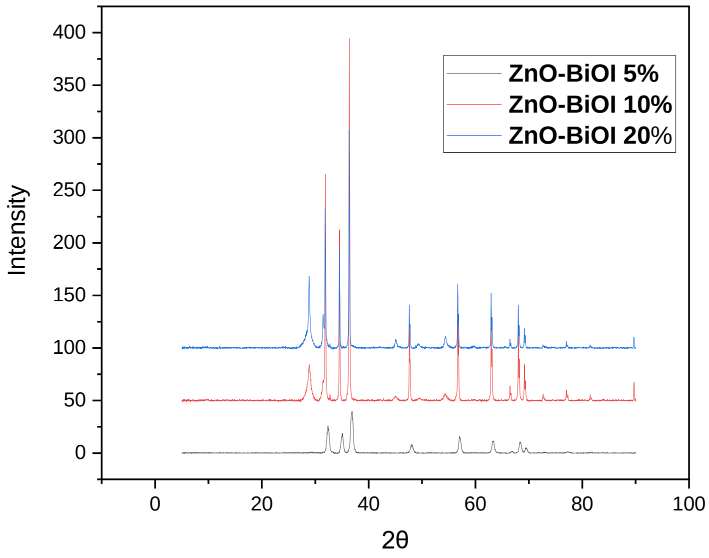

Figure 4. 22. XRD pattern of the as-synthesized ZnO-BiOI (X) nanoparticles with different loadings.

4.2.5 XRD pattern and average crystallite sizes of ZnO-WO_3 composites

Figure 4.23 shows the XRD patterns of the as-prepared ZnO-WO_3 composites with different WO_3 loadings. All the samples can be indexed to the triclinic phase of WO_3 and typical hexagonal wurtzite structure of pure ZnO samples. The intensity of the peaks increased with increased loading of WO_3 in the ZnO lattice. The samples with 5 % and 10 % loading of WO_3 do not show any peaks apart from the peaks of ZnO. This can be attributed to the detection limit of the instrument as well as good dispersal of the WO_3 on the surface of the ZnO. At an increased loading of 20 %, intense peaks were observed at 23.0^o, 24.4^o, 28.0^o and 34.0^o corresponding to the 001, 110, 200 and 201 crystal planes of triclinic WO_3 in addition to the characteristic peaks of hexagonal ZnO. No impurity peaks were observed which shows physical content homogenization in all the composites.

The crystallite sizes of the composites were estimated from the XRD data via the most intense peaks using the Scherrer method. The sample with 5 % loading of WO_3 had an average crystallite size of 35.4 nm, while the sample with 10 % WO_3 content had an average crystallite size of 49 nm. The sample with 20 % loading of WO_3 was estimated to have an average crystallite size of 31 nm. These are presented in Table 12.

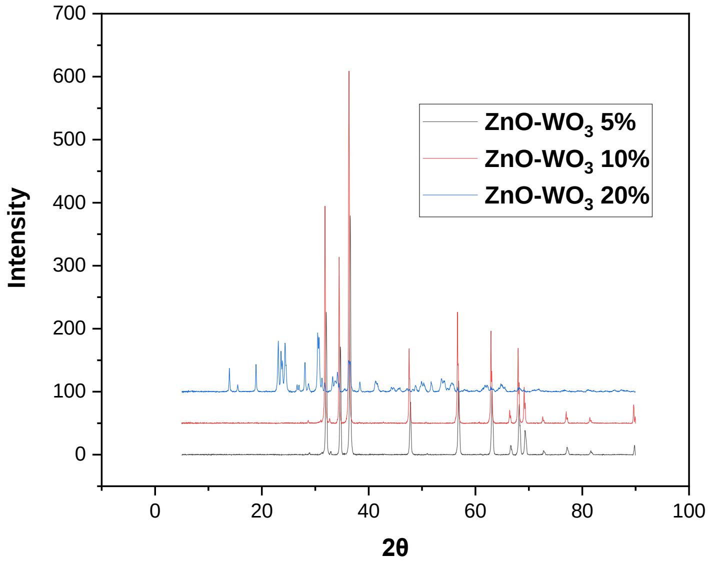

Figure 4. 23. XRD pattern of the as-prepared ZnO-WO_3 (X) nanoparticles with different loadings.

Table 12: FHWM and average crystallite sizes of the as-prepared photocatalysts.

Sample	FHWM	Average Crystallite Size (nm)
ZnO	0.229460	37.6
WO_3	0.653265	12.9
BiOI	0.206788	40.0
ZnO-BiOI 5 %	0.527615	16.4
ZnO-BiOI 10 %	0.279705	31.0
ZnO-BiOI 20 %	0.188655	45.0
ZnO-WO_3 5 %	0.24412	35.4
ZnO-WO_3 10 %	0.17594	49.0

ZnO-WO$_3$ 20 %	0.26869	31.0

4.3. Textual properties of the as-prepared photocatalysts

BET surface area measurement is an important factor that influences photocatalytic activity. This is because semiconductors with comparative larger surface areas tend to exhibit better performance. A large surface area is favourable for the adsorption of more pollutants on the surface of semiconductors, thereby influencing photocatalytic activity. The surface area of the as-synthesized photocatalysts were measured using the standard nitrogen adsorption-desorption isotherm and the Barret-Joyner-Halender (BJH) pore distribution curves. From the nitrogen adsorption-desorption isotherm analysis, the results were compared with the IUPAC classification. The as-prepared catalysts were deduced to follow different isotherm types, thus indicating varied porous structures for the different catalysts.

4.3.1 N$_2$ adsorption-desorption isotherm of BiOI

The BET measurement of the as-prepared BiOI sample showed a specific surface area measurement of 2.61 m^2/g. The study by Hu and colleagues (2014) also observed a surface area measurement within the same range in their study which synthesized BiOI using a variety of solvents and processes. Figure 4.24 shows the nitrogen adsorption-desorption isotherm with almost no hysteresis. This sample bears semblance to a Type IV Isotherm and can be described as mesoporous, but with some distribution of macropores. The corresponding Barret-Joyner-Halenda (BJH) pore diameter distribution plot (Figure 4.25) confirms the variable pore diameter distribution for this sample as 26 nm.

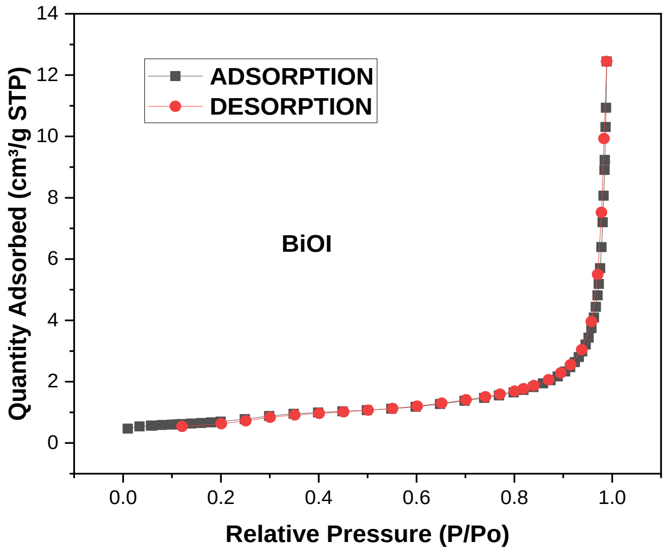

Figure 4. 24. N_2 adsorption-desorption isotherm of BiOI.

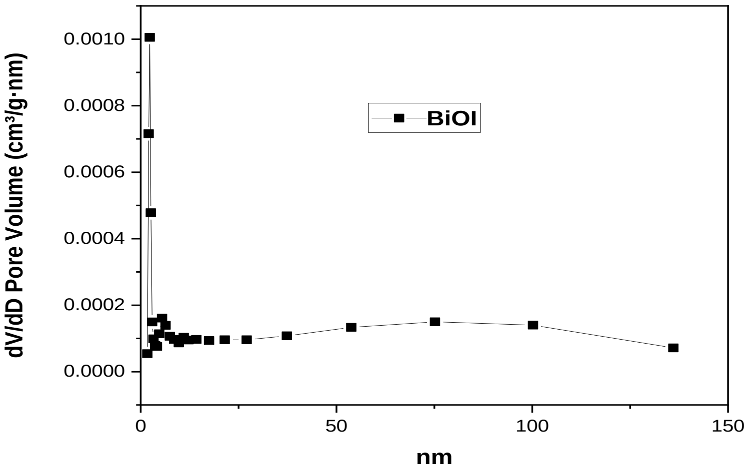

Figure 4. 25. BJH pore size distribution of BiOI.

4.3.2 N_2 adsorption-desorption isotherm of WO_3

A type H_{III} hysteresis loop was observed in WO_3 from the N_2 adsorption-desorption isotherm as shown in Figure 4.26. The surface area was measured as 1.08 m^2/g, which is small compared to the other samples. This decreased surface area is attributed to probable pore blockages. This means that the BET measurement probe gas will not properly adsorb inside the pores. The BJH pore size distribution plot is shown in Figure 4.27 with an average pore size width of 43.2 nm.

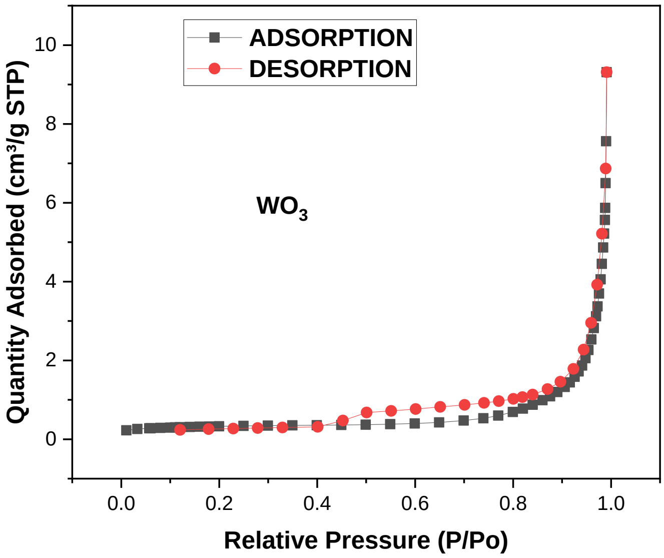

Figure 4. 26. : N_2 adsorption-desorption isotherm of WO_3.

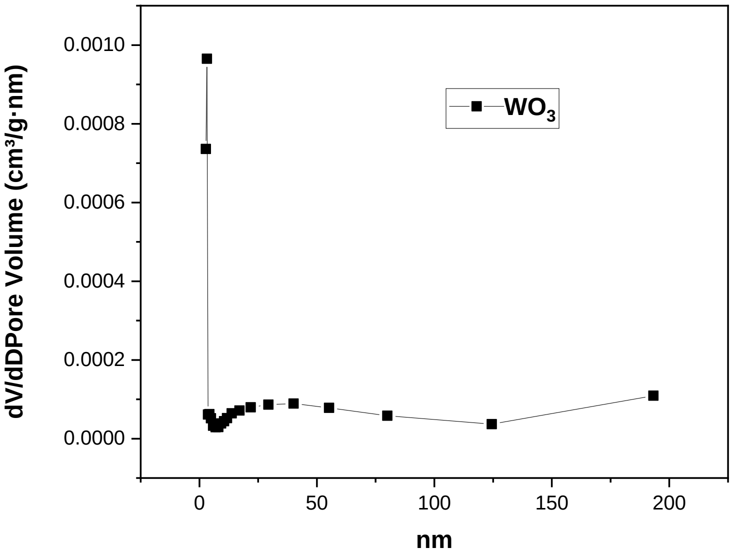

Figure 4. 27. BJH pore size distribution of WO_3.

4.3.3 N_2 adsorption-desorption isotherm of $ZnO-WO_3$ 10 %

The composite resembles a Type III isotherm with no observed hysteresis (Figure 4.28). This is characterized by relatively weak adsorbent-adsorbate interactions with the adsorbed molecules clustering around the most favourable sites. This is attributed to its macroporous nature even though the pore sizes are within the IUPAC mesoporosity classification. The specific surface area was measured to be 5.69 m^2/g, while the pore size distribution (Figure 4.29) confirms a variable distribution with an average pore diameter of 24.5 nm.

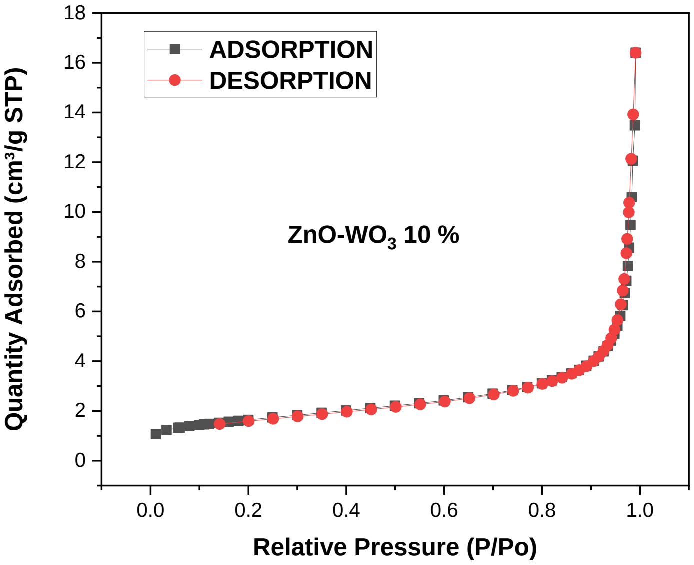

Figure 4. 28. : N_2 adsorption-desorption isotherm of $ZnO-WO_3$ 10 %.

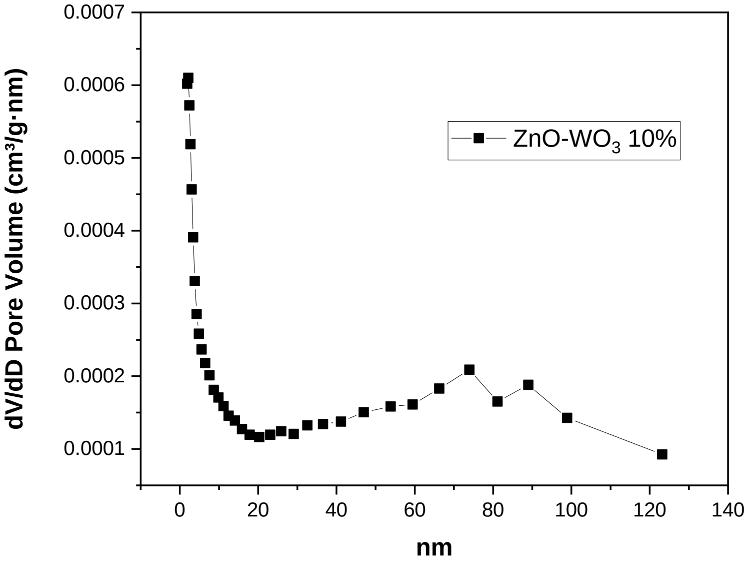

Figure 4. 29. BJH pore size distribution of ZnO-WO₃ 10 %.

4.3.4 N_2 adsorption-desorption isotherm of ZnO-WO_3 5 %

The N_2 adsorption-desorption isotherm of ZnO-WO_3 5 % is nearly similar with that of ZnO-WO_3 10 % with little or no observed hysteresis and is classified as a Type III isotherm (Figure 4.30). The pore sizes are within the IUPAC specified mesoporous pores with some mixture of macropores. The specific surface area measurement is 7.84 m^2/g with the BJH pore size distribution (Figure 4.31) showing variable distribution and average diameter of 20.3 nm.

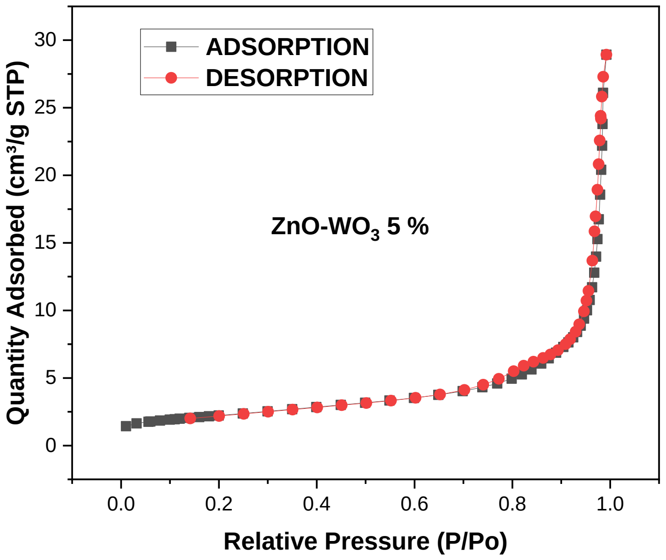

Figure 4. 30. N$_2$ adsorption-desorption isotherm of ZnO-WO$_3$ 5 %.

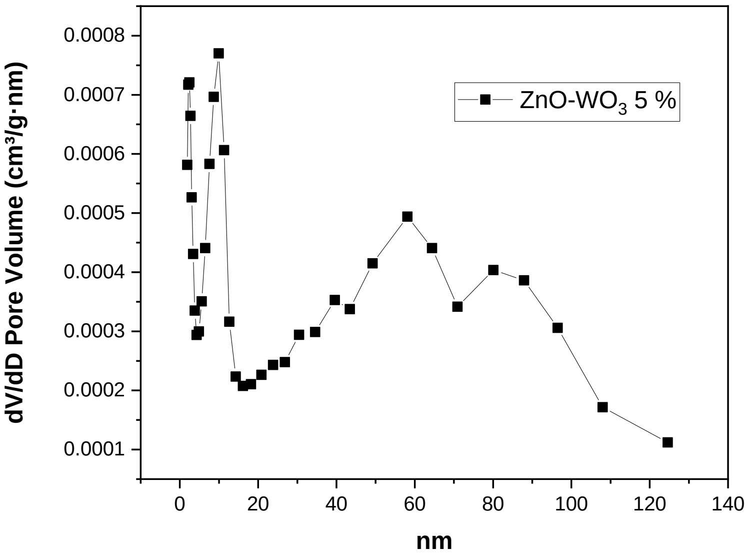

Figure 4. 31. BJH pore size distribution of ZnO-WO$_3$ 5 %.

4.3.5 N$_2$ adsorption-desorption isotherm of ZnO-WO$_3$ 20 %

The ZnO-WO$_3$ 20 % composite exhibits a Type$_{III}$ hysteresis loop and is classified as a Type IV isotherm (Figure 4.32). It is classified as a network of mesopores although the corresponding BJH pore size distribution plot (Figure 4.33) shows some distribution of macropores. This may be attributed to the effect of increased doping of WO_3 within ZnO. The BET measurement shows that the specific surface area of this composite is 5.57 m^2/g, while the BJH average pore is measured to be 32 nm.

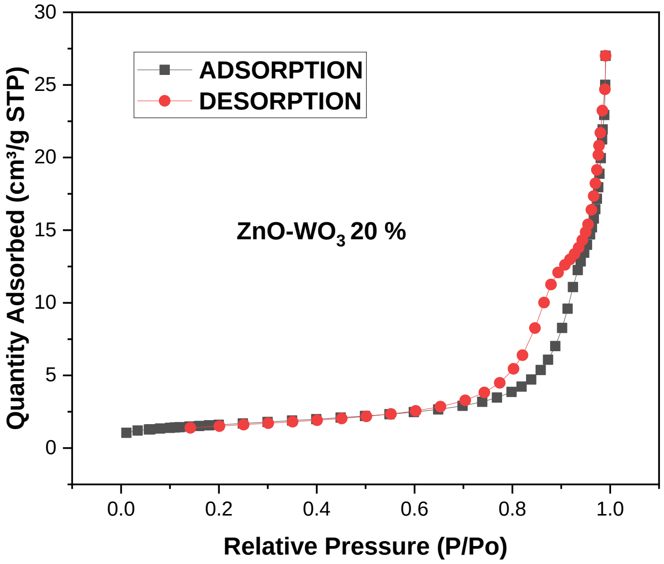

Figure 4. 32. : N_2 adsorption-desorption isotherm of ZnO-WO_3 20 %.

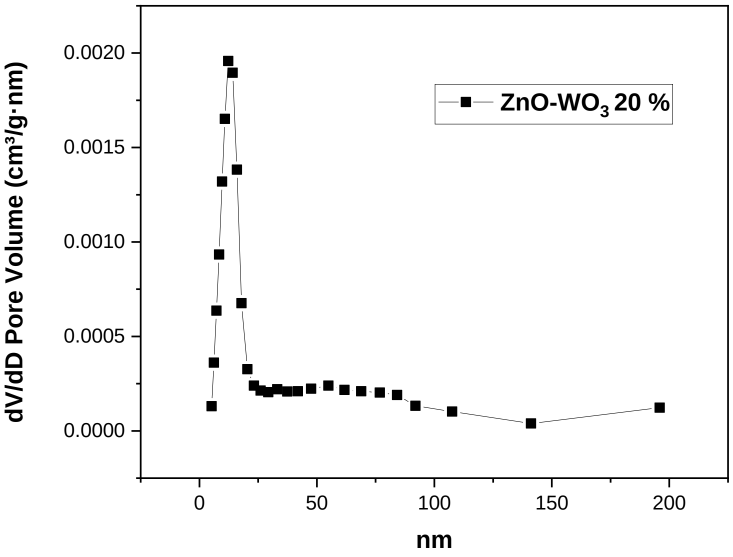

Figure 4. 33. : BJH pore size distribution of ZnO-WO_3 20 %.

4.3.6 N_2 adsorption-desorption isotherm of ZnO-BiOI 5 %

The N_2 adsorption-desorption isotherm of ZnO-BiOI 5 % shows little hysteresis (Type_{III}) and is likened to a Type IV isotherm (Figure 4.34). This is associated with most of the pores being within the IUPAC classification of mesopores. Figure 4.35 shows the BJH pore size distribution and it confirmed that it is mostly mesoporous, although some mixture of macropores are also observed. The average pore size diameter is measured as 31 nm, while the BET measurement shows it has a surface area of 7.31 m^2/g.

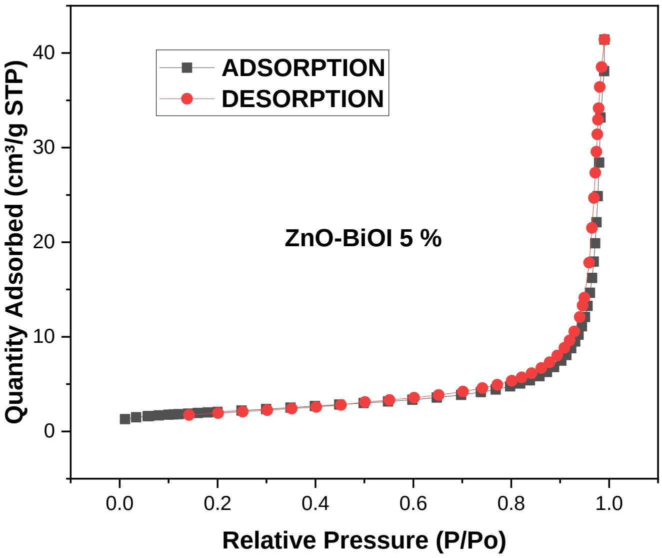

Figure 4. 34. N_2 adsorption-desorption isotherm of ZnO-BiOI 5 %.

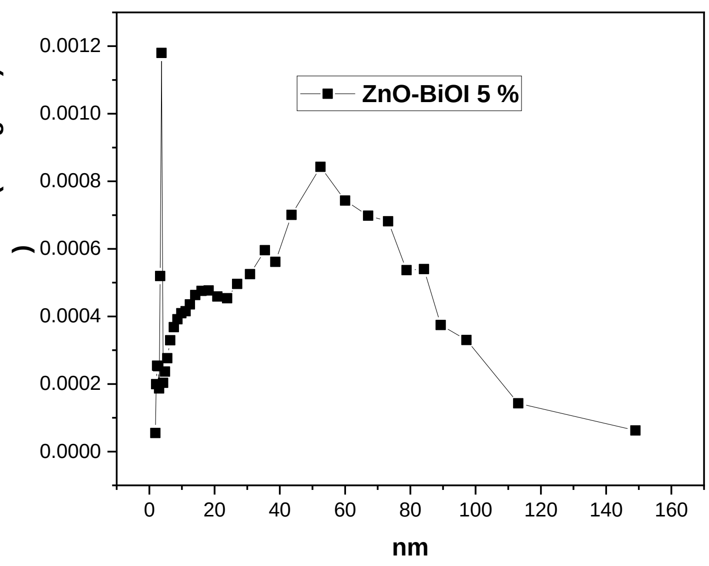

Figure 4. 35. BJH pore size distribution of ZnO-BiOI 5 %.

4.3.7 N_2 adsorption-desorption isotherm of ZnO-BiOI 10 %

The BET surface area measurement showed that this composite had the largest surface area of all. The measured surface area is 19.79 m^2/g with an average pore size diameter of 35 nm. The N_2 adsorption-desorption isotherm (Figure 4.36) had similar characteristics with the ZnO-BiOI 5 % isotherm which had a Type IV isotherm with little H_{III} hysteresis. This shows that both composites have similar starting materials and followed the same synthesis process. The BJH pore size distribution plot (Figure 4.37) is classified as mostly mesoporous with some distribution macropores.

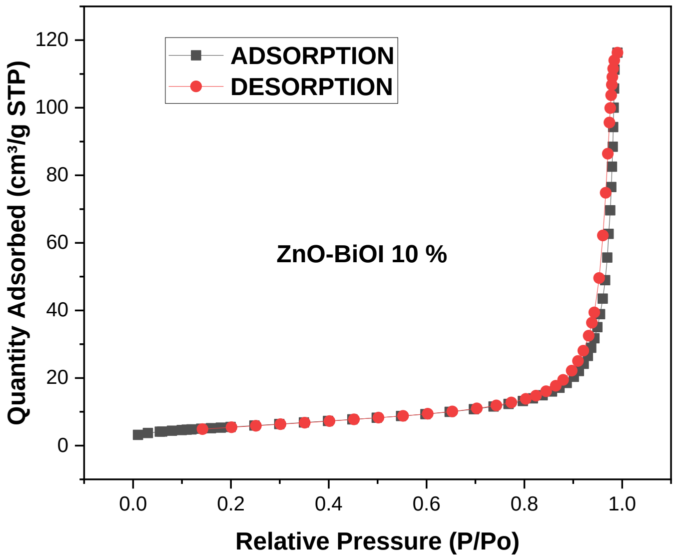

Figure 4. 36. : N_2 adsorption-desorption isotherm of ZnO-BiOI 10 %.

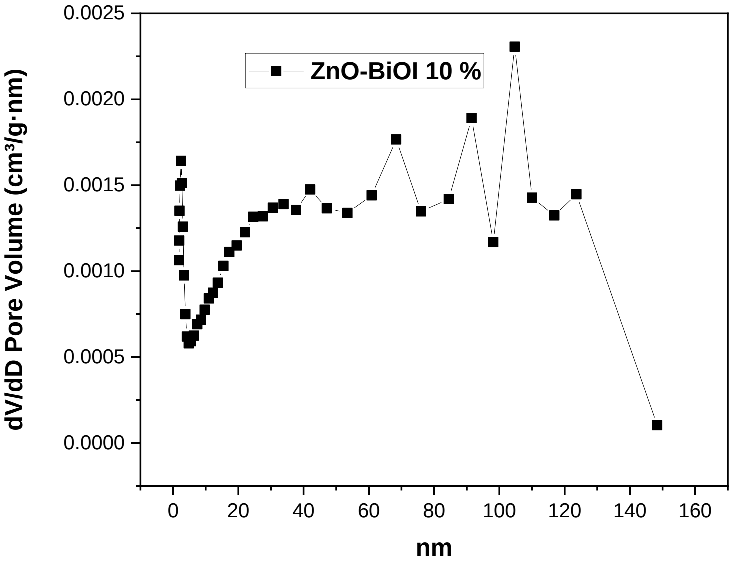

Figure 4. 37. BJH pore size distribution of ZnO-BiOI 10 %.

4.3.8. N_2 adsorption-desorption isotherm of ZnO-BiOI 20 %

The N_2 adsorption-desorption isotherm (Figure 4.38) showed that the ZnO-BiOI 20 % composite exhibited a Type IV isotherm followed by a H_{III} hysteresis loop, thus indicating the mesoporous nature of the composite. The specific surface area of this composite was measured to be 7.30 m^2/g, with an average pore size diameter of 31.5 nm. The corresponding BJH pore size distribution plot (Figure 4.39) showed a mostly mesoporous material with some distribution of macropores, which is in line with the ZnO-BiOI 5 % and ZnO-BiOI 10 % composites.

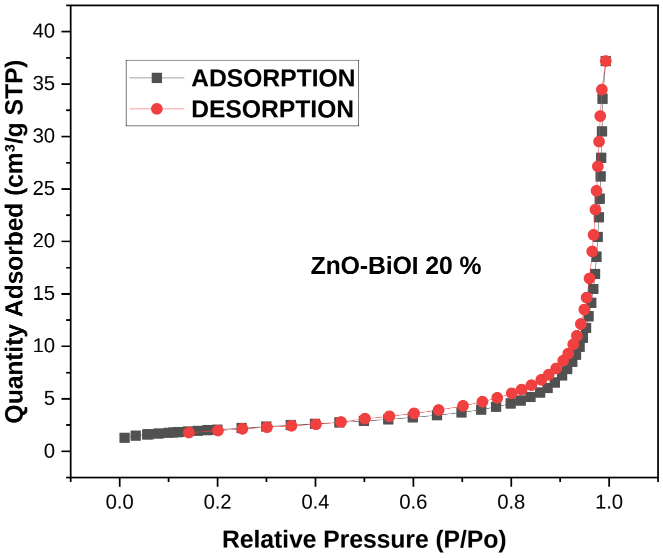

Figure 4. 38. N_2 adsorption-desorption isotherm of ZnO-BiOI 20 %.

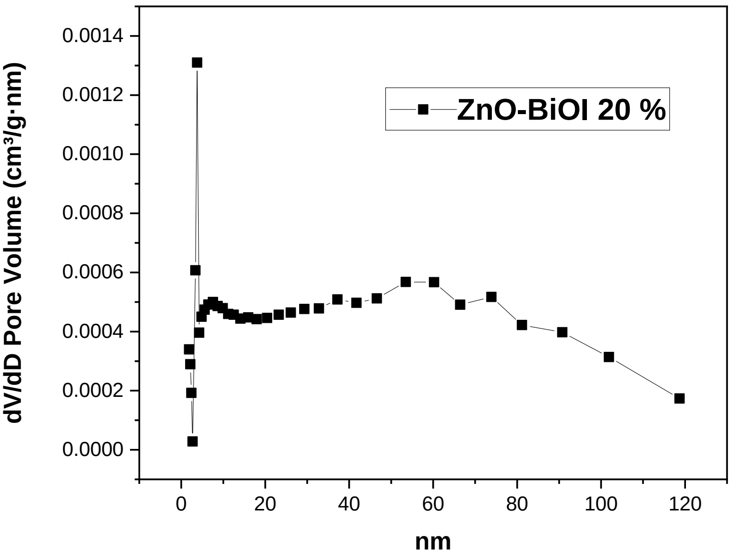

Figure 4. 39. BJH pore size distribution of ZnO-BiOI 20 %.

4.3.9. N_2 adsorption-desorption isotherm of ZnO

The specific surface area of this undoped ZnO sample was measured to be 1.93 m^2/g, with an average pore size diameter of 25.7 nm. The corresponding BJH pore size distribution plot (Figure 4.40) showed a mostly mesoporous material with some distribution of macropores.

From the N_2 adsorption-desorption isotherm shown in Figure 4.41, the ZnO was observed to exhibit a H_{III} hysteresis in a Type V isotherm.

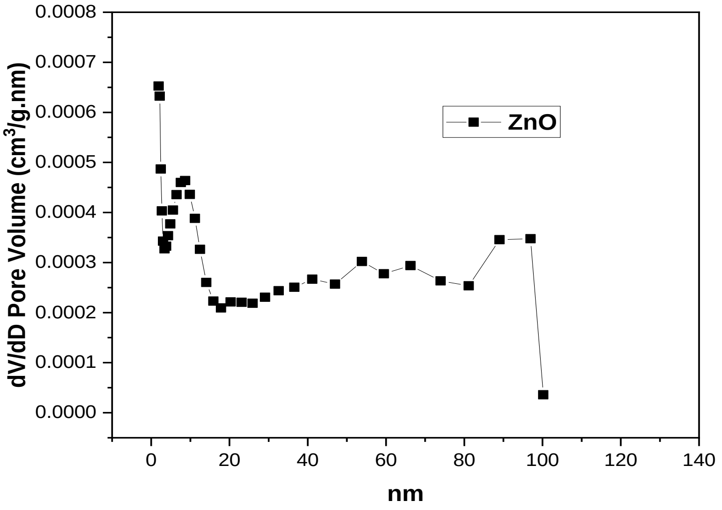

Figure 4. 40. BJH pore size distribution of ZnO.

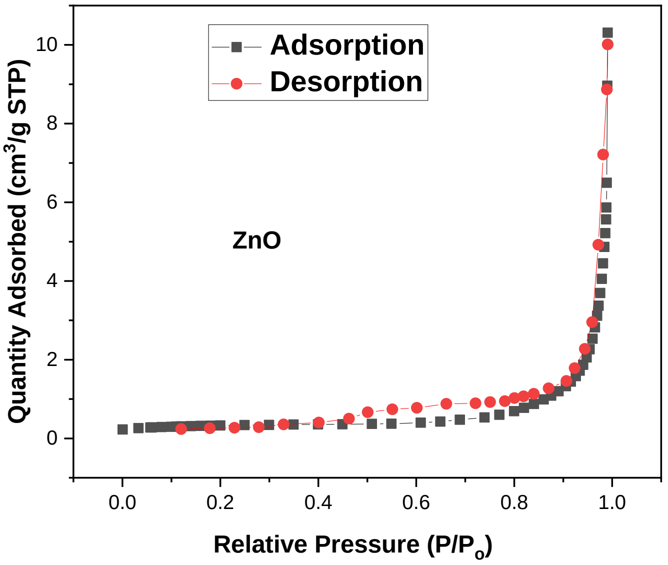

Figure 4. 41. N_2 adsorption-desorption isotherm of ZnO.

Table 13: Textural properties of the as-prepared catalysts.

Catalyst	S_{BET} (m^2/g)	Pore volume (cm^3/g)	Pore size (nm)
BiOI	2.61	0.019	26.0
WO_3	1.08	0.014	43.2

ZnO-WO_3 10 %	5.69	0.021	24.5
ZnO-WO_3 5 %	7.84	0.042	20.3
ZnO-WO_3 20 %	5.57	0.042	32.0
ZnO-BiOI 5 %	7.31	0.064	31.0
ZnO-BiOI 10 %	19.79	0.180	35.0
ZnO-BiOI 20 %	7.30	0.534	31.5
ZnO	1.93	0.012	25.7

4.4. Optical properties

A UV-vis spectrophotometer was used to determine the absorption properties of the composites. All spectra were recorded at room temperature in the range of 200-900 nm. The bandgaps of all the composites were calculated from Tauc's plot via the Kubelka–Munk equation (Equation 4.2) by extrapolating the linear portion of the plot of $\boldsymbol{(\alpha h\nu)^2}$ vs the photon energy.

$$\boldsymbol{\alpha h\nu = A(h\nu - E_g)^n} \qquad 4.2$$

where $\boldsymbol{\alpha}$ is the absorption coefficient, $\boldsymbol{A}$ is a constant, $\boldsymbol{h}$ is Plank's constant, $\boldsymbol{\nu}$ is the photon frequency, $\mathbf{E_g}$ is the band gap, and $\boldsymbol{n}$ is equal to 1/2 or 2 for the transition being direct or indirect, respectively. Extrapolating the linear region in a plot of $(\boldsymbol{\alpha h\nu})^2$ against $\boldsymbol{h\nu}$ gives the band gap values.

4.4.1. ZnO

The absorption spectrum of ZnO showed maximum absorption at 373 nm (Figure 4.42 a), thus showing maximum absorption in the UV region. This observation is in agreement with several other studies (Potti & Srivastava, 2012; He *et al*., 2018; Thein *et al*., 2017)

Figure 4.42 (b) shows the estimated band gap of the ZnO photocatalyst calculated via the Tauc's plot of the absorption spectrum. A band gap of 3.24 eV was estimated, showing the wide band gap nature of ZnO.

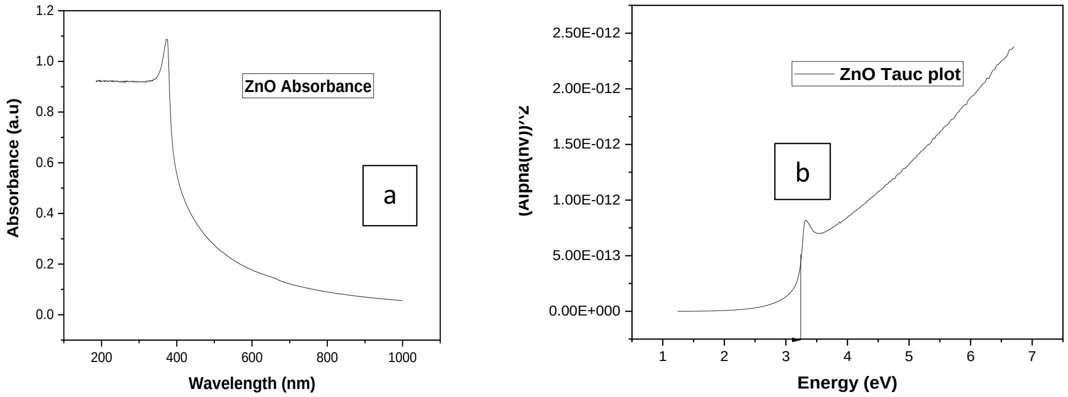

Figure 4. 42. (a) ZnO absorption spectrum (b) ZnO Tauc plot showing band gap.

4.4.2. WO$_3$

Figure 4.43 (a) shows the absorption spectrum of the as-prepared WO$_3$ photocatalyst. The absorbance is observed at around 371 nm. However, an absorption tail was also observed in the visible region. This could be as a result of the presence of pentavalent tungsten (W^{5+}) on the surface of the nanoparticles, which has broad absorption in the visible region as a result of the capture of photo-excited electrons at WO$_3$ trapping sites (Boruah *et al.*, 2020).

The band gap was estimated at 2 eV from the Tauc's plot of the absorption spectrum. Boruah *et al*. (2020) also observed a similar band gap in their work. This very narrow band gap may be due to the formation of oxygen defect levels below the conduction band minimum.

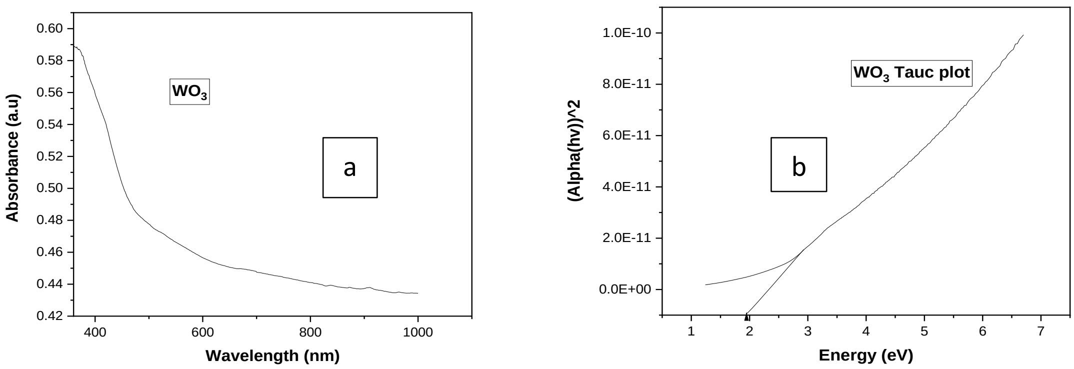

Figure 4. 43. (a) WO_3 absorption spectrum (b) WO_3 Tauc plot showing band gap.

4.4.3. BiOI

The absorption spectrum of the as-synthesized BiOI was observed at 465 nm, thus showing absorption in the visible region (Figure 4.44). In addition, the absorption tail was also observed beyond 600 nm. The study by Qu *et al*. (2020) also observed similar absorbance.

Using the Tauc's plot obtained from the absorption spectrum, the band gap was estimated at 1.23 eV, which shows a very narrow band gap.

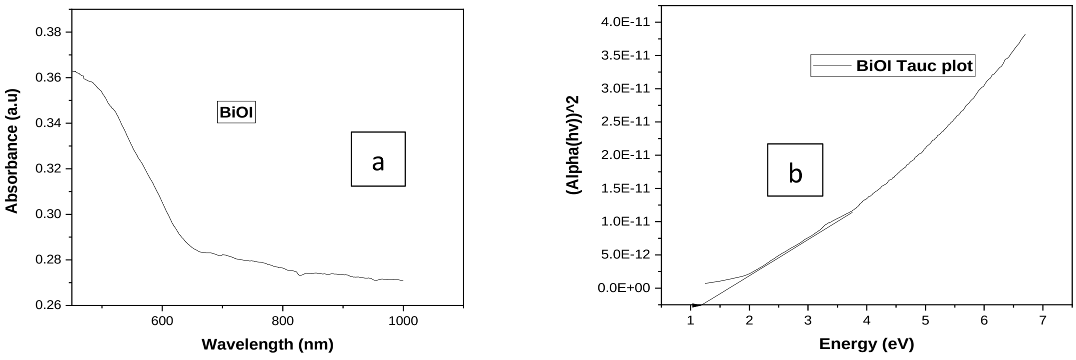

Figure 4. 44. (a) BiOI absorption spectrum (b) BiOI Tauc plot showing band gap.

Figure 4.45 (a) shows the absorption spectra of the as-prepared ZnO-BiOI composites at different BiOI loadings representing ZnO-BiOI 5 %, ZnO-BiOI 10 %, and ZnO-BiOI 20 %. The absorbance of the composites were recorded at 376 nm, 378 nm and 379 nm for ZnO-BiOI

5 %, ZnO-BiOI 10 %, ZnO-BiOI 20 % respectively. There was an observed slight red shift for ZnO-BiOI 10 % and ZnO-BiOI 20 % with an increase in the BiOI loading.

Similarly, a narrowing of the band gaps was observed for the composites as the BiOI loading increased. With reference to the pure ZnO, the band gap was observed at 3.24 eV. However, with the introduction of BiOI at 5 % loading, the band gap narrowed down to 3.08 eV. As the BiOI loading was increased to 10 %, the band gap further narrowed to 3.0 eV. The composite with the highest BiOI loading at 20 % showed the highest band gap narrowing, as the band gap was estimated at 2.20 eV. This observation corresponds to the associated red shift for the absorbance of each of the composites.

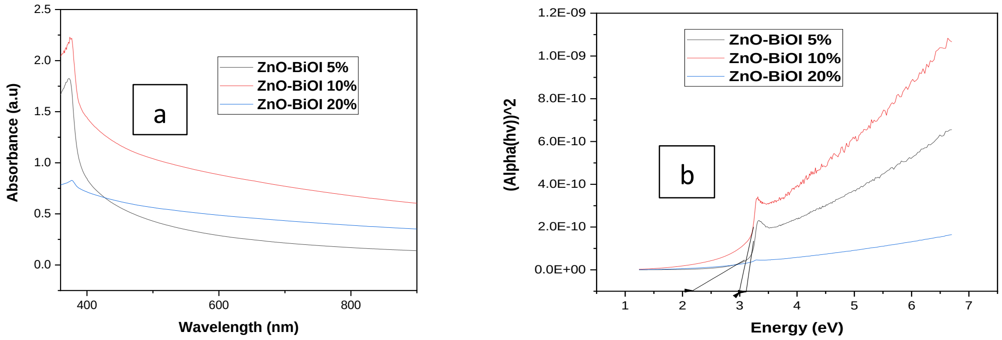

Figure 4. 45. (a) ZnO-BiOI composites absorption spectra (b) ZnO-BiOI composites Tauc plots showing band gap.

4.4.4. ZnO-WO_3 (x %)

The light absorption capacity of the as-prepared ZnO with different WO_3 loadings were investigated using a UV-vis spectrophotometer. The absorption peaks were observed at 376 nm, 377 nm, and 379 nm, representing ZnO-WO_3 5 %, ZnO-WO_3 10 %, and ZnO-WO_3 20 % respectively. A slight red shift in the absorbance for the composites were observed. This means that as loading of WO_3 increased on the surface of the ZnO, a slight red shift occurred. The study by Thein *et al*. (2017) made similar observations.

The optical band gaps of the composites as shown in Figure 4.46 (b) were estimated using the Tauc's relation. The ZnO-WO_3 5 % composite had an estimated band gap of 2.56 eV, showing band gap narrowing from the already established band gap of ZnO (3.24 eV). As the WO_3 loading was increased to 10 %, there may have been a formation of energy level defects in the forbidden band, as the BG was estimated to be 3.16 eV. This is greater than the BG of the ZnO-WO_3 5 % composite, but still lower than the BG of the undoped ZnO. This also explains the further narrowing of the ZnO-WO_3 20 % composite, which was observed to have the narrowest band gap of 2.17 eV. The same observation was made in the study by Adhikari *et al*. (2015).

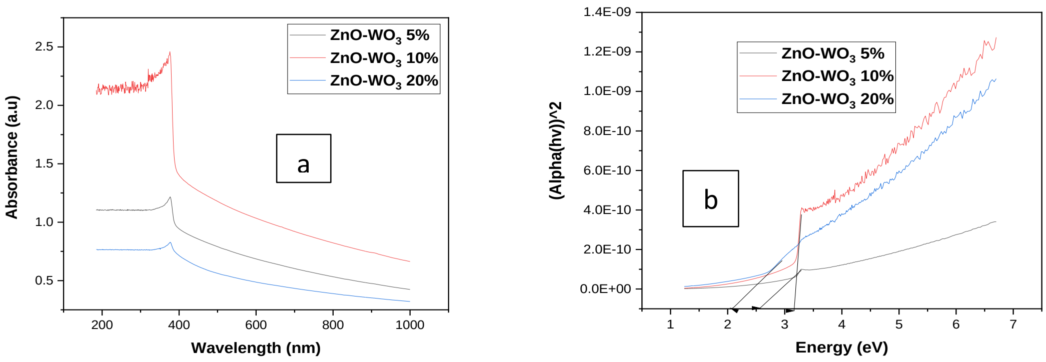

Figure 4. 46. : (a) ZnO-WO_3 composites absorption spectra (b) ZnO-WO_3 composites Tauc plots showing band gap.

5. Photocatalytic Degradation of 2-Chlorobiphenyl

5.1. Photocatalytic protocol

The degradation of 2-chlorobiphenyl under solar simulation was used to assess the photo-activities of the composite photocatalysts. 2CBP was prepared by dissolving the required amount of the pollutant in a 85-15 methanol-water ratio solution. A concentration of 10 ppm of 2CBP in 100ml solvent solution was placed in a beaker, mounted on a stirrer plate and placed directly under the light source. The initial concentration was taken into account. The desired amount of catalyst was introduced thereafter and magnetically stirred in the dark for 30 minutes. This was to enable the establishment of equilibration of adsorption-desorption between the pollutant and the surface of the photocatalyst. During the experiments, the suspensions were magnetically stirred to properly disperse the photocatalysts. The pH of the respective experiments were adjusted using HCl and NH_4OH.

The photocatalytic activities of individual photocatalysts were tested with a AM 1.5G 100 mW/cm^2 solar simulator. The surface of the beaker was covered in order to prevent evaporation during the photocatalytic process. At designated time intervals, aliquots of the mixture were taken out using a syringe and filtered using a 0.22 µm membrane filter attached unto the syringe. This was done to separate the photocatalyst particles.

After irradiation, the filtered samples were equilibrated in a dark box lined with aluminium foil and stored in the refrigerator prior to GC analysis. The concentration of the 2CBP was analysed using a Shimadzu GC-MS QP 2010 equipped with a Rxi-5ms column of 30 m length, an internal diameter of 0.25 mm and a film thickness of 0.25 µm.

5.2. Photocatalytic degradation of 2CBP

5.2.1. Photodegradation of 2CBP by ZnO

A concentration of 10 ppm in 100ml of 2CBP was poured into a 250ml glass beaker and 35 mg of ZnO nanoparticles was added in the solution. The reactions were performed at room temperature and the natural pH of 2CBP is around 7.2. The mixture was magnetically stirred in the dark for 30 minutes to equilibrate adsorption-desorption after which the suspension was exposed to a solar simulator. At intervals (30 minutes), aliquots were taken out for measurement on the GC. Figure 5.1 shows the photodegradation of 2CBP using the ZnO photocatalyst. After a reaction time of 150 minutes, ZnO reached its highest efficiency of 20 %. After 150 minutes there was little or no further degradation. The dark experiments showed that ZnO performed as a photocatalyst rather than absorption as little or no destruction was achieved during the dark experiments. ZnO needed activation by light in order to degrade the 2CBP. The final pH after the reaction was recorded as 6.8.

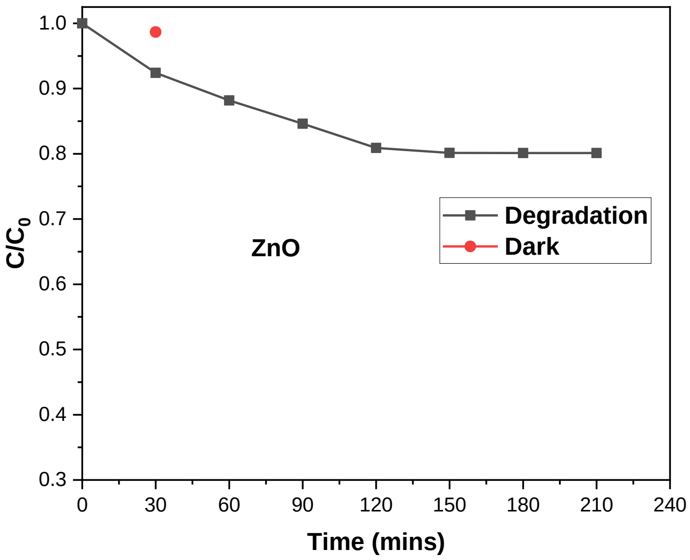

Figure 5. 1. Time dependent photocatalytic degradation of 2CBP by ZnO.

5.2.2. Photodegradation of 2CBP by WO_3

The photocatalytic test of the as-prepared WO_3 was performed by the degradation of 2CBP under solar simulation. WO_3 was added in a beaker containing a concentration of 10 ppm (in 100ml) of 2CBP. Dark experiments were performed in order to establish adsorption-desorption equilibrium between 2CBP and the photocatalyst's surface for 30 minutes, under constant stirring. Irradiation was commenced after dark experiments. Figure 5.2 shows the photocatalytic degradation of 2CBP by WO_3. It is observed that WO_3 performed slightly better than ZnO in the photocatalytic degradation of 2CBP. The highest degradation by WO_3 was observed after 150 minutes of reaction, after which no noticeable further destruction was observed. The highest efficiency observed was 28 % destruction of 2CBP. The pH of the mixture after the reactions was measured as 5.

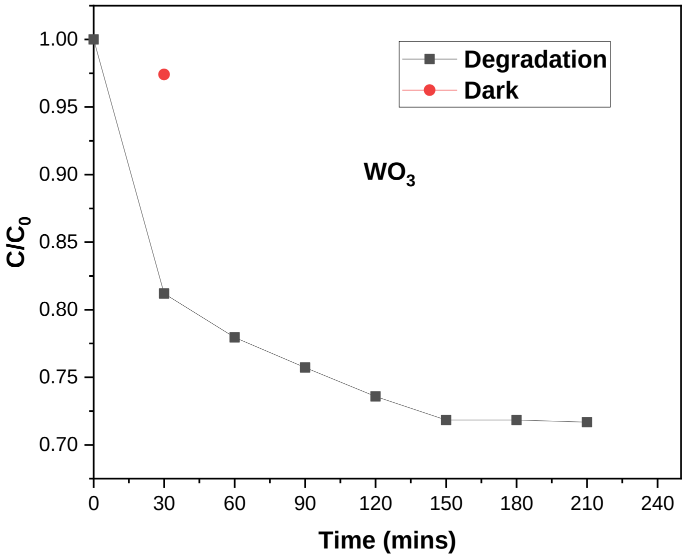

Figure 5. 2. Time dependent photocatalytic degradation of 2CBP by WO_3.

5.2.3. Photodegradation of 2CBP by BiOI

A suspension of 35 mg of BiOI and 100 ml aqueous solution containing a concentration of 10 ppm of 2CBP was placed in a 250 ml beaker. After stirring for 30 minutes to establish adsorption-desorption equilibrium in the dark, an aliquot was taken out, filtered with a 0.22 µm filter attached onto the syringe (in order to remove the photocatalyst particles), and subsequently measured with the GC-MS instrument. The mixture was irradiated with the solar simulator with further aliquots taken out at determined time intervals. Dark experiments showed little or no destruction. The highest destruction was observed after 180 minutes of reaction as 49 % degradation efficiency was observed, thus showing that BiOI was photoexcited to achieve the degradation (Figure 5.3). This performance was considerably higher than those of ZnO and WO_3.

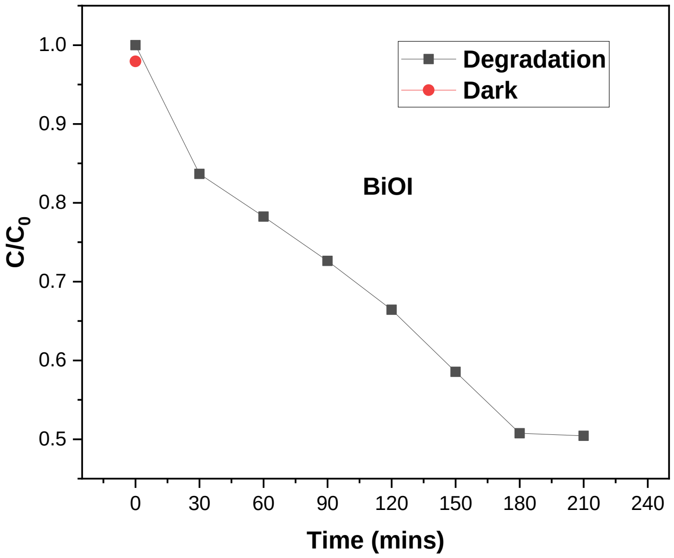

Figure 5. 3. Time dependent photocatalytic degradation of 2CBP by BiOI

5.2.4. Photodegradation of 2CBP by ZnO-BiOI 5 %

ZnO-BiOI 5 % was utilized in the destruction of 2CBP in order to gauge its efficacy. This heterostructure exhibited the lowest photocatalytic activity among all the other photocatalysts in the degradation of the pollutant of interest. The highest efficiency was achieved after 120 minutes before the levelling off of its photocatalytic activity. Only about 7 % efficiency was achieved with this photocatalyst. Dark experiments also showed very little photocatalytic activity as very negligible degradation was observed.

5.2.5. Photodegradation of 2CBP by ZnO-BiOI 10 %

The degradation profile of 2CBP under solar simulation by ZnO-BiOI 10 % is shown in Figure 5.4. At 35 mg catalyst weight, 10 ppm pollutant concentration and the same time intervals as all the other photocatalysts, this heterostructure of ZnO-BiOI 10 % was observed to exhibit the best photocatalytic activity and efficiency. After 150 minutes of reaction time, the photocatalyst heterostructure achieved photodegradation efficiency of 57 %. Beyond this time of 150 minutes, the photocatalytic activity levelled off and no further significant degradation was observed. The performance of this photocatalyst showed more significant activity than the bare photocatalysts of ZnO and WO_3.

5.2.6. Photodegradation of 2CBP by ZnO-BiOI 20 %

The photocatalytic performance of ZnO-BiOI 20 % exhibited much lower activity in comparison with ZnO-BiOI 10% under the same reaction conditions. After 150 minutes of reaction time, this composite achieved its highest activity of 28 % efficiency (Figure 5.4). Longer than 150 minutes showed a levelling off of the photocatalytic activity. This is nearly 2 fold lower than the observed activity of the ZnO-BiOI 10 % composite. Dark experiments showed no significant photocatalytic activity as no significant destruction of the reference pollutant was observed.

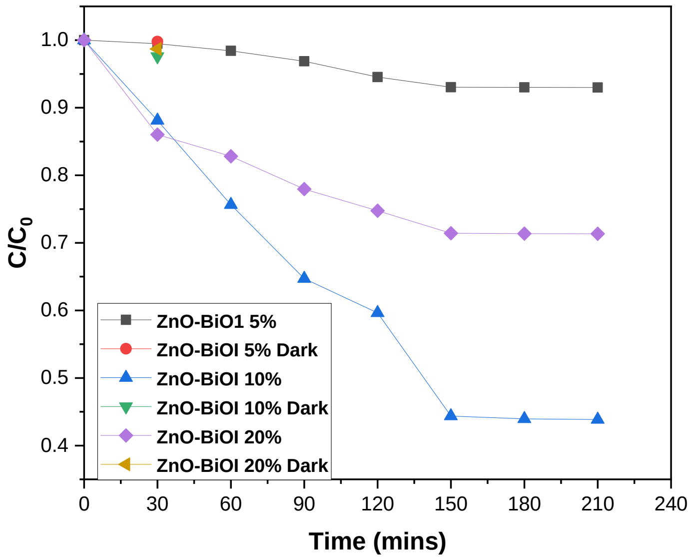

Figure 5. 4. Time dependent photocatalytic degradation of 2CBP by ZnO-BiOI (x%) heterostructures.

5.2.7. Photodegradation of 2CBP by ZnO-WO_3 5 %

Figure 5.5 shows the photodegradation plot of the reference pollutant by the application of ZnO-WO_3 5 %. The effect of the heterojunction is observed as the composite exhibited much higher photo-activity than the bare WO_3 and ZnO. Under similar reaction conditions as all the other catalysts, the composite achieved about 45 % efficiency in the photocatalytic degradation of 2CBP within the allowed reaction time. As observed in the other reactions, the dark experiment did not show any significant destruction of the 2CBP.

5.2.8. Photodegradation of 2CBP by ZnO-WO_3 10 %

As loading of WO_3 within the ZnO lattice increased to 10 %, there was an observed improvement in the photocatalytic activity. The sample with ZnO-WO_3 10 % showed better photocatalytic performance than the bare ZnO, WO_3 and ZnO-WO_3 5 %. At the comparable reaction time, the composite achieved 53 % degradation of 2CBP under similar reaction conditions as the other photocatalysts. However, its performance was observed to be slightly lower than the heterostructure of ZnO-BiOI 10 %. Similarly, dark experiments did not show any significant degradation of 2CBP.

5.2.9. Photodegradation of 2CBP by ZnO-WO_3 20 %

At 20% loading of WO_3 on ZnO, the photocatalytic activity did not perform at the same level as the ZnO-WO_3 10 % composite. However, it still performed better than the bare WO_3 and ZnO. Under similar reaction conditions, the highest photocatalytic efficiency of about 33 % was observed after 150 minutes of reaction time (Figure 5.5). Beyond 150 minutes, the performance of the photocatalyst levelled off as no significant further photocatalytic degradation of 2CBP was observed. Loading beyond 10 % of WO_3 in the ZnO lattice did not increase the photocatalytic performance, activity and efficiency. As observed in all the other reactions, dark experiment did not exhibit significant destruction of the 2CBP via adsorption.

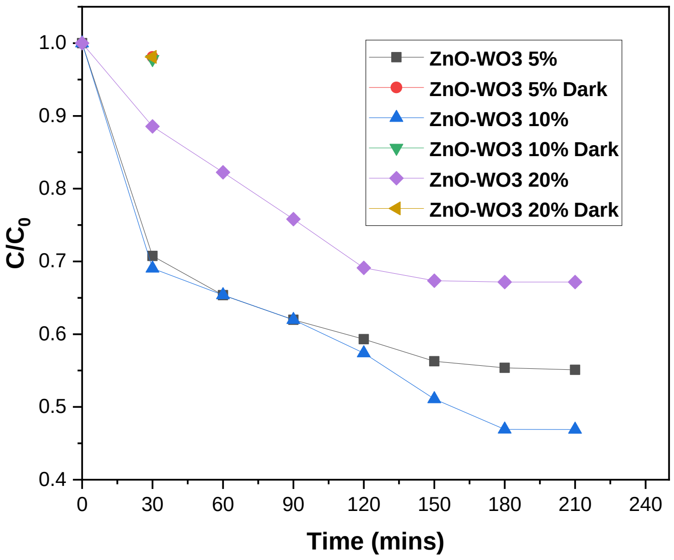

Figure 5. 5. Time dependent photocatalytic degradation of 2CBP by ZnO-WO_3 (x%) heterostructures.

5.2.10. Photodegradation of 2CBP by photolysis

A photolysis experiment was carried out to compare and confirm that the photodegradation of 2CBP in our study was indeed facilitated by the mixing of the photocatalyst in the solution containing 2CBP and subsequent photoexcitation. Under similar reaction conditions as the other experiments, a concentration of 10 ppm of 2CBP was irradiated without adding any photocatalysts. Less than 2 % degradation was observed after 120 minutes of exposure to the light source, after which no further degradation was observed (Figure 5.6). This observed decomposition of 2CBP by direct photolysis is quite negligible when compared with the added catalysts experiments.

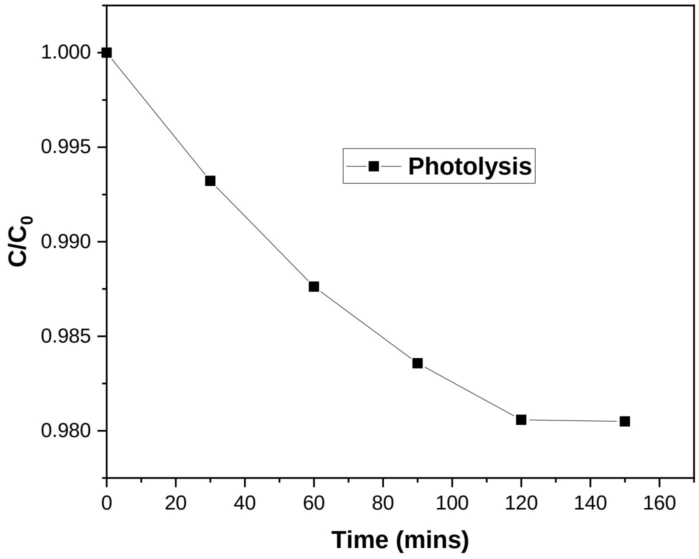

Figure 5. 6. Time dependent photocatalytic degradation of 2CBP by photolysis.

5.3. Discussion

The time dependent photocatalytic degradation plots of 2CBP by the application of different photocatalysts under solar simulation are shown in Figures. 5.1-5.5. For the study, 35 mg of each catalyst was utilized, while the concentration of 2CBP was 10 ppm (100 ml solution). Thirty (30) minutes' intervals were the established time for each aliquot retrieval. The natural pH of 2CBP was around 7.2. All the photocatalysts showed varying degrees of photocatalytic efficiencies. Bare ZnO achieved an efficiency of 20 % at 150 minutes, while bare WO_3 achieved 28 % destruction at same time. BiOI was observed to be the most efficient catalyst (49 %) among all the bare catalysts. The heterostructures comprising ZnO-BiOI 5 %, ZnO-BiOI 10 %, ZnO-BiOI 20 %, ZnO-WO_3 5 %, ZnO-WO_3 10 % and ZnO-WO_3 20 % exhibited varying photocatalytic activities as the observed efficiencies were 7 %, 57 %, 28 %, 45 %, 53 % and 33 % respectively, as shown in Table 14.

The photocatalytic activities of the bare/undoped photocatalysts follow the trend BiOI>WO_3>, ZnO. This is attributed to the quick separation of the electron-hole pairs, before recombination takes place. In addition, BiOI was observed to possess the narrowest band gap among the bare photocatalysts. This may have contributed to its photocatalytic performance.

The fabricated heterojunctions containing 5 % loading of BiOI and WO_3 showed diverse results. The composite containing 5 % WO_3 (45 %) showed a significant activity when compared to its 5 % BiOI (7 %) counterpart, coupled with its slightly larger surface area. The samples loaded with 20% BiOI/WO_3 also showed varying photocatalytic activities, although the difference in efficiencies are not as significant as the composites with 5 % loading. At similar reaction conditions, ZnO-WO3 20 % and ZnO-BiOI 20 % achieved degradation efficiencies of 33 % and 28 % respectively.

The composites of ZnO-BiOI 10% and ZnO-WO_3 10 % were observed to be the photocatalysts with the most significant activities. In this study. ZnO-BiOI 10 % (57 %) achieved approximately two fold the efficiency of ZnO-BiOI 20 % (28 %), while ZnO-WO_3 10 % (53 %) showed much more significant activity than ZnO-WO_3 20 % (33 %). Loading at 20 % (BiOI, WO_3) onto the bare ZnO showed a significant reduction in photocatalytic activity. This may have been caused by the excessive loading which leads to the formation of recombination centres and light penetration depth which exceeded the space charge layer leading to quick recombination of the photogenerated electron-hole pairs (Gnanaprakasam *et al*., 2015)

The composite (ZnO-BiOI 10 %) with the largest surface area (19.79 m^2/g) and a significant pore volume was observed to exhibit the best photocatalytic activity. Heterogeneous photocatalysis is mostly efficient when a photocatalyst is equipped with a large surface area. As already established, photocatalysis mainly occurs on the photocatalyst's surface (Fan *et al*., 2007). Typically, a photocatalyst with a high number of atoms on its surface will have enhanced adsorption properties. Nano sized diameters of nano-structures will make charge separation of the photogenerated electrons and holes easier due to transfer of the charge carriers from the bulk to the surface of the photocatalyst. Thus, a larger surface area leads to the subsequent formation of more hydroxyl radicals for more photocatalytic reaction centres, even though our study did not follow that particular order. Several researchers made similar observations in their respective studies (Flores *et al*., 2014; Moafi *et al*., 2013; Mekasuwandumrong *et al*., 2010; Ameen *et al*., 2012). The as-synthesised composite in our study which had the most significant and largest surface area, in addition to its significantly enhanced pore volume, exhibited the best photocatalytic activity in the destruction of 2CBP.

When a semiconductor with narrow band gap is coated with a wide band gap semiconductor as its outer layer, the narrow band gap semiconductor may be isolated from the liquid electrolyte. This may lead to wider range of light absorption and longer term photostability. Thus, the p-n junction formed by two semiconductors possess strong electric fields generated at the interface. This may result in improved charge separation of electrons and holes and recombination reduction (Jiang *et al*., 2011; Jiang, *et al*., 2017; Natkritta *et al*., 2018).

The construction of ZnO-BiOI 10 % heterostructure enabled the spatial segregation of electrons and holes into different compartments which in turn encountered recombination and also isolated the redox sites on the surface of the photocatalyst. Incorporating semiconductors with different crystal structures and band positions cause more efficient utilization of incident photons and leads to efficient charge separation by the electric field interface.

This enhanced photo-activity of ZnO-BiOI 10 % is also attributed to increased light absorption and efficient charge separation in addition to the narrow bandgap and exposed reactive facets. Thus, the BiOI in the heterostructure acted as a photosensitizer. In addition, coupling ZnO and BiOI into a heterojunction enhanced the photocatalytic activity of the ZnO because of the high-contact areas enabled by the fast charge transfer channel of BiOI and ZnO.

A decline in the photocatalytic activity was observed beyond the 20 % loading of ZnO-WO_3 and ZnO-BiOI heterostructures because of a reduction in separation efficiency of the photoinduced electrons and holes. Furthermore, loading BiOI beyond 20 % is detrimental to the heterojunction because of the tendency of BiOI to aggregate and agglomerate (Wen *et al*., 2017; Jiang *et al*., 2017; Natkritta *et al*., 2018). Thus, ZnO-BiOI 10 % was identified as the optimal photocatalyst for this study.

Table 14: Photocatalytic degradation efficiencies of composites.

Photocatalyst	Degradation efficiency (%)
ZnO	20
WO3	28
BiOI	49
ZnO-BiOI 5 %	7
ZnO-BiOI 10 %	57
ZnO-BiOI 20 %	28
ZnO-WO3 5 %	45
ZnO-WO3 10 %	53
ZnO-WO3 20 %	33

5.4. Photodegradation mechanism of ZnO-BiOI 10 %

The results obtained from the experiment give a strong indication that the superior photodegradation activity of ZnO-BiOI 10 % nanocomposite is due to the p-n heterojunction structure between ZnO and BiOI (Jiang *et al*., 2011; Zhang *et al*., 2020; Jiang *et al*., 2017; Natkritta *et al*., 2018). From the UV-Vis spectra of both ZnO and BiOI, the calculated band gaps were established as 3.24 eV and 1.23 eV respectively. A simplified band energy structure of ZnO and BiOI is shown in Figure 5.7a. ZnO being a typical n-type photocatalyst has its Fermi level close to its CB, while BiOI being a p-type photocatalyst has its Fermi level located close to its VB (Jiang et al., 2011; Zhang et al., 2020; Zhang *et al*., 2018). The introduction of BiOI into the ZnO lattice and subsequent p-n heterojunction construction leads to the realignment of the Fermi levels of the two materials. This causes band bending and creation of electric fields (Yoon *et al*., 2015). Photoexcited electrons transfer to the CB of ZnO, leaving the holes in the BiOI VB (Figure 5.7b). This takes place because the CB of BiOI is more negative than the conduction band of ZnO. In the same way, the VB of ZnO is more positive than that of BiOI. This shows that separation efficiency of the ZnO-BiOI 10 % composite is improved and in turn, the photocatalytic activity is also improved.

The reduction of photocatalytic activity beyond the optimum doping of 10 % is attributed to excessive loading of BiOI onto ZnO. This may have caused BiOI to act as recombination centres leading to a reduced photocatalytic performance. Khatamian *et al*. (2012) attributes this to light penetration depth which exceeded the space charge layer. This makes it easy for the photogenerated electron-hole pairs to recombine, leading to a lower photocatalytic performance. Thus, an optimum concentration of BiOI is mandatory to match the thickness of charge layer and light penetration depth to effectively separate the photogenerated electron-hole pairs. Several studies have observed similar trend (Bechambi *et al*., 2015; Moafi *et al*., 2013; Lam *et al*., 2015; Adhikari *et al*., 2015; Nguyen Thi Thu *et al*., 2016).

From the experimental results, the following photocatalytic mechanism is proposed:

$$BiOI \xrightarrow{h\nu(\lambda \geq 400nm)} BiOI\left(h_{VB}{}^{+} + e_{CB}^{-}\right) \quad 5.1$$

$$BiOI(e_{CB}^{-}) \xrightarrow{transfer} ZnO(e_{CB}^{-}) \quad 5.2$$

$$ZnO(e_{CB}^{-}) + O_{2\,\rightarrow} ZnO + O_2^{\cdot -} \quad 5.3$$

$$O_2^{\cdot -} + H^{+} \rightarrow \dot{O}H \quad 5.4$$

$$O_2^{\cdot -} \; and \; \dot{O}H + 2CBP \rightarrow Degradation(products) \quad 5.5$$

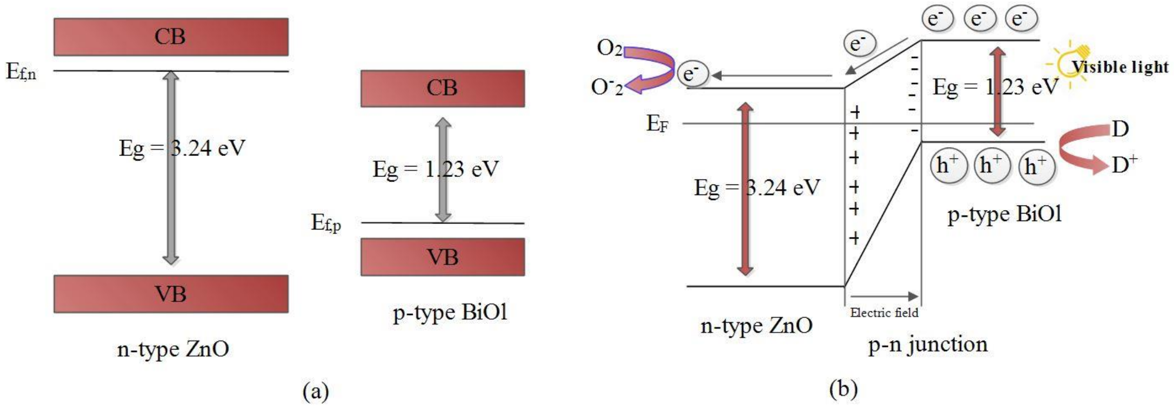

Figure 5. 7. Proposed band energy diagram of ZnO and BiOI before contact (a) and after (b) interfacial contact, formation of p-n junction and charge separation process of ZnO-BiOI heterostructure under solar irradiation.

6. Kinetic Studies

6.1. Reaction kinetics

The pseudo-first order kinetic model has been suggested by researchers as suitable for describing photocatalytic reactions (Goveas et al., 2020; Pandurangan *et al*. 2001; Zhu *et al*. 2012). Hence, this kinetic model was adopted in this study. This kinetic model can be expressed as Equation 6.1.

$$B \xrightarrow[Solar\ simulator]{Catalyst} C \qquad 6.1$$

Where *B* represents the initial 2CBP concentration, and *C* represents the final treated 2CBP concentration. Therefore, taking into consideration the concentration of the initial 2CBP, the differential equation can be derived as Equation 6.2.

$$\frac{dC_B}{dt} = -kC_B \qquad 6.2$$

The integral form of Equation (6.2) yields Equation (6.3)

$$\ln\left[\frac{C_B}{C_{B_0}}\right] = -kt \qquad 6.3$$

Where C_{B_0} is the initial concentration of 2CBP, C_B is the final concentration of the 2CBP at different treatment time, t is the time in minutes, and k is the apparent kinetic rate constant for different photocatalysts. Plotting a graph of $\ln\left[\frac{C_B}{C_{B_0}}\right]$ against t yields a slope equivalent to the apparent kinetic rate constants.

The time at which the measured concentration of the treated wastewater is half the initial concentration (i.e., $C_B = 1/2C_{Bo}$) is regarded as the half-life ($t_{1/2}$) as shown in Equation (6.4):

$$t_{1/2} = \frac{\ln 2}{k} \qquad 6.4$$

Figures 6.1 (a-i) shows the kinetic plots for the different photocatalysts used in this study. This figure also shows the effect of photocatalyst type on the treatment of 2CBP. For this set of experiments, 2CBP was prepared at an initial concentration of 10 ppm in 100ml while the photocatalyst dose used was 35 mg.

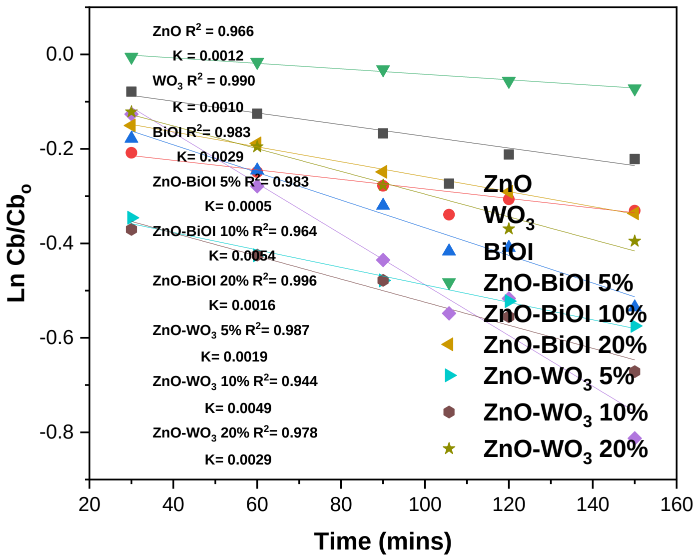

Figure 6. 1. Pseudo-first order kinetic plots of ZnO, WO_3, BiOI, ZnO-WO_3 5 %, ZnO-WO_3 10 %, ZnO-WO_3 20 %, ZnO-BiOI 5 %, ZnO-BiOI 10 %, ZnO-BiOI 20 % respectively on the photocatalytic degradation of the pollutant (Pollutant concentration: 10 ppm, catalyst loading: 35 mg, pH: 7.2).

6.1.1. Reaction Kinetics of undoped photocatalysts

As shown in Figures 6.1, the kinetic rate constant for BiOI catalyst was found to be the highest at 0.0046 min^{-1}, much higher than ZnO [approximately 4 fold; 0.0012 min^{-1}) and WO_3 [approximately 5 fold; 0.0010 min^{-1}] among the bare/undoped photocatalysts under similar reaction conditions. BiOI was found to achieve the highest concentration reduction of 49 % among the bare/undoped photocatalysts.

The half lives of the undoped catalysts are presented in Table 15. As shown, BiOI photocatalyst requires the least time (150.7 minutes)for the measured 2CBP concentration to be halved to the initial concentration. This suggests that BiOI can potentially be used as catalyst for degradation of pollutants in water. The R-squared values affirm the claim that the photocatalytic experiments using the undoped photocatalysts follow the pseudo-first order kinetic model

6.1.2. Reaction Kinetics of ZnO-WO_3 (X) photocatalysts

The degradation kinetics of the experiment by the application of ZnO-WO_3 (X) were investigated. The degradation rates are observed to match well with the pseudo-first order reaction according to the Langmuir–Hinshelwood model, shown in Figures 6.1. The measured rate constants and relative correlation coefficients obtained by fitting the experimental data are shown in Table 15.

Among the ZnO-WO_3 (X) photocatalysts, ZnO-WO_3 10 % was observed to be the highest at 0.0049 min^{-1}. ZnO-WO_3 10 % (53 %) was observed to achieve the highest degradation efficiency when compared to ZnO-WO_3 5 % (45 %) and ZnO-WO_3 20 % (33 %). In addition, the measured rate constant of ZnO-WO_3 10 % is approximately 4 fold that of bare ZnO.

From the kinetics data, it will require 141.5 minutes for the measured 2CBP concentration to be halved to the initial concentration. This suggests that ZnO-WO_3 10 % can potentially be used as catalyst for degradation of pollutants in water. The R-squared values confirm that the photocatalytic experiments using the ZnO-WO_3(X) photocatalysts follow the pseudo-first order kinetic model.

6.1.3. Reaction Kinetics of ZnO-BiOI (X) photocatalysts

The photocatalytic activity of the as synthesized ZnO-BiOI (X) heterostructures were estimated using the degradation kinetics of the 2CBP, the plots of which are shown in Figures 6.1. The rate constant of ZnO-BiOI 5 % was measured to be 0.0005 min^{-1}. As doping was increased to 10 %, the rate constant increased by 11 fold to 0.0054 min^{-1}. At 20 % doping, the rate contant decreased significantly to 0.0016 min^{-1}, which is over 3 fold lower than that of the ZnO-BiOI 10 % composite. When compared to undoped ZnO, the rate constant of the ZnO-BiOI 10 % heterostructure was observed to be nearly 5 fold higher.

The kinetics data show that it requires 128.4 minutes for the measured 2CBP concentration to be halved to the initial concentration when ZnO-BiOI 10 % is applied. The R-squared values affirm that the photocatalytic experiments using the ZnO-BiOI (X) photocatalysts follow the pseudo-first order kinetic model.

From the experimental and kinetics data obtained, it can be deduced that ZnO-BiOI 10 % heterostructure is the most efficient and effective photocatalyst in the photodestruction of 2CBP, for this study. This suggests that ZnO-BiOI 10 % can potentially be used as an efficient and effective catalyst for degradation of pollutants in water.

Table 15: The apparent pseudo-first order reaction kinetic model parameters for the photodegradation of 2CBP using different photocatalyst at similar photoreaction conditions.

S/N	**Photocatalyst**	**K (min^{-1})**	**R^2**	**$t_{1/2}$ (min)**	**Efficiency (%)**
1	**ZnO**	**0.0012**	**0.966**	**577.6**	**20**
2	**WO_3**	**0.0010**	**0.990**	**693.1**	**28**
3	**BiOI**	**0.0046**	**0.983**	**150.7**	**49**
4	**ZnO-BiOI 5 %**	**0.0005**	**0.983**	**1386.3**	**7**
5	**ZnO-BiOI 10 %**	**0.0054**	**0.964**	**128.4**	**57**
6	**ZnO-BiOI 20 %**	**0.0016**	**0.996**	**433.2**	**28**
7	**ZnO-WO_3 5 %**	**0.0036**	**0.987**	**192.5**	**45**
8	**ZnO-WO_3 20 %**	**0.0029**	**0.978**	**239.0**	**33**
9	**ZnO-WO_3 10 %**	**0.0049**	**0.944**	**141.5**	**53**

6.2. Effect of initial 2CBP concentration

The influence of the initial 2CBP concentration on the photodegradation efficiency were studied by varying the concentrations between 10 ppm to 50 ppm using 35 mg of ZnO-BiOI 10 %

photocatalyst. Figure 6.2 shows that the degree of the photodegradation of the pollutant is influenced by the initial pollutant concentration, which diminishes with increasing initial 2CBP concentration. A similar trend was observed by Bechambi *et al*. (2015) for the photodestruction of Bisphenol A using Carbon-doped ZnO. Bechambi and colleagues also suggested some possible reasons for their observation. Firstly, as the initial concentration of 2CBP increases, an increasing number of pollutant molecules are adsorbed onto the photocatalyst's surface while the exposure time to irradiation remains constant. Secondly, the high initial concentration of 2CBP blocks the active sites of the photocatalyst, thereby reducing the photon interaction with those sites.

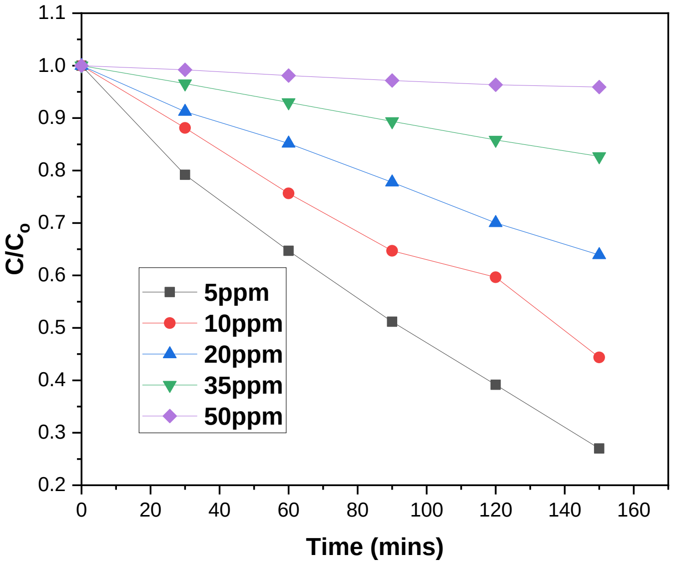

Figure 6. 2. Effect of initial 2CBP concentration on the photodegradation using 10 % ZnO-BiOI.

Figure 6.3 shows the plot of ln(Cb/Cb_o) vs time at varying 2CBP initial concentrations (5-50 ppm). From the linear plots, it can be confirmed that the photodegradation of 2CBP followed pseudo-first order kinetics. The calculated rate constants and their corresponding R^2 values are shown in Table 16.

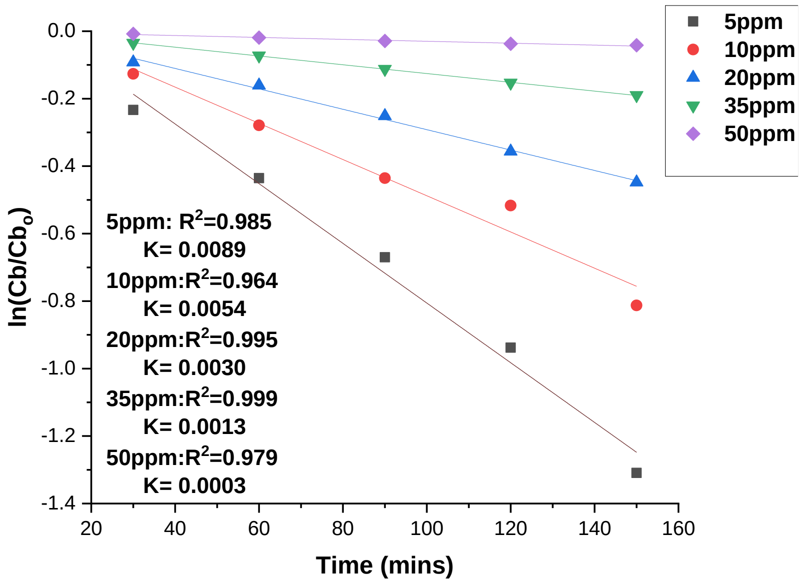

Figure 6. 3. Pseudo-first order plot for the photodegradation of the 2CBP at 5, 10, 20, 35 and 50 ppm initial concentrations.

The plot of the rate constants against the initial concentrations of the pollutant in the wastewater as shown in Figure 6.4, shows that the rate constants reduce with increase in initial concentration. At 5 ppm, 73 % of the 2CBP solutions was degraded when 35 mg/100 ml of ZnO-BiOI 10 % was utilized, as presented in Table 16. Degradation efficiency was lower at higher concentrations. A probable explanation for this is that more molecules of 2CBP are adsorbed on the surface of ZnO-BiOI 10 % photocatalyst as initial concentration of 2CBP is increased. Hydroxyl radicals and superoxide anions formed on the surface of the photocatalyst at constant irradiation are overwhelmed by the increasing 2CBP molecules, leading to decreased photocatalytic activity. In addition, photons are obstructed before they reach the surface of the photocatalyst as concentration of 2CBP increases. This leads to reduced photon absorption and decreased photocatalytic efficiency. This observation agrees with the hypothesis that higher initial concentration of the pollutant blocks some of the active sites of the photocatalyst which reduces the photon interaction with those active sites, thereby slowing down the rate at which the treatment takes place.

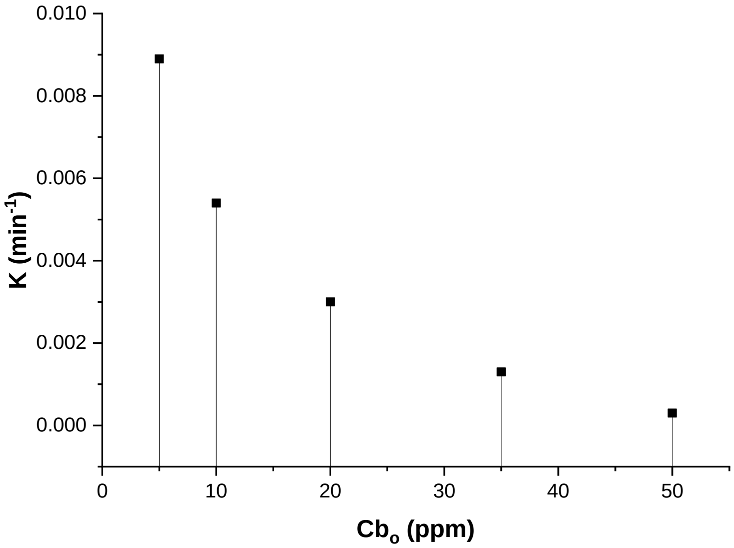

Figure 6. 4. Effect of pollutant initial concentration (10 % ZnO-BiOI: 35 mg, pH: 7.2) on the kinetic rate constant.

Table 16: Effect of initial pollutant concentration on the photodegradation of 2CBP.

Initial 2CBP Concentration (ppm)	Degradation (%)	K_{app} (min^{-1})	R^2
5	**73**	**0.0089**	**0.985**
10	**57**	**0.0054**	**0.964**
20	**36**	**0.0030**	**0.995**
35	**17**	**0.0013**	**0.999**
50	**4**	**0.0003**	**0.979**

6.3. Effect of catalyst dose

The catalyst dose used during the photocatalytic process is a significant influencing factor that affects pollutant degradation. Five different catalyst doses (35 mg, 70 mg, 85 mg, 100 mg and 150 mg) were applied, to study its effect on 2CBP degradation. Figure 6.5 shows the pseudo-first order kinetic model plots for the degradation of the pollutant at 35 mg - 150 mg catalyst dose loadings.

As catalyst dose was doubled to 70 mg, the rate constant also increased by over 64 % (from 0.0054-0.0085 min^{-1}). At 85 mg photocatalyst weight, a slight (approximately 10 %) reduction of the rate constant was observed (from 0.0085-0.0077 min^{-1}). Loading beyond 85 mg led to a significant (approximately 75 %) reduction in the rate constant, as shown in Table 17. This is in agreement with the photocatalytic plot of the degradation of 2CBP by using varying doses of ZnO-BiOI 10 % heterostructure, as shown in Figure 6.6.

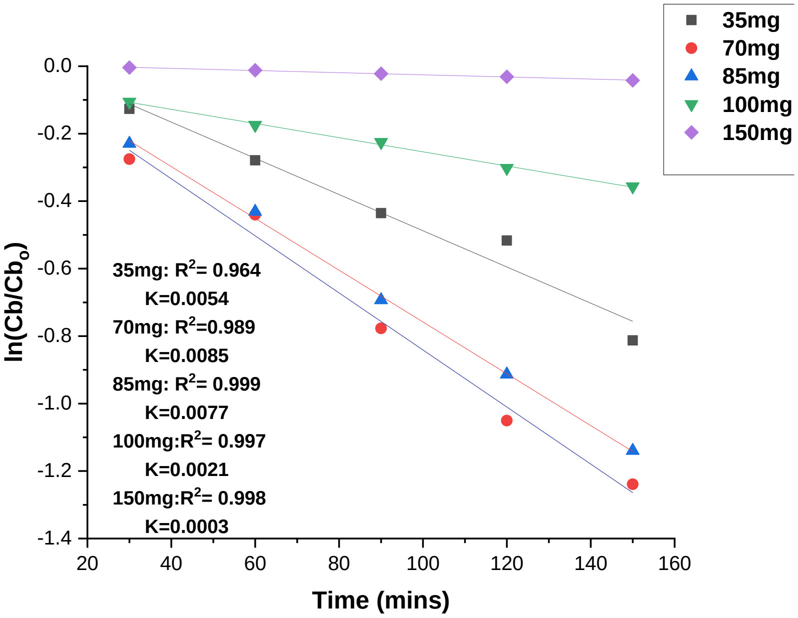

Figure 6. 5. Pseudo-first order plot for the photodegradation of 2CBP at 35 mg - 150 mg catalyst (10 % ZnO-BiOI) doses.

Table 17: Effect of catalyst dose on the photodegradation of 2CBP.

Catalyst dose(mg)	Degradation (%)	K_{app} (min^{-1})	R^2
35	**57**	**0.0054**	**0.964**
70	**57**	**0.0085**	**0.989**
85	**71**	**0.0077**	**0.999**
100	**30**	**0.0013**	**0.997**
150	**4**	**0.0003**	**0.998**

Generally, degradation rate of organic pollutants will increase with an increase in photocatalyst concentration. This is attributed to increased hydroxyl radicals generation because of the presence of more active sites at higher doses. As the catalyst load increases, there is a tendency for it to agglomerate due to particle-particle interaction, culminating in a reduced surface area for light absorption, and decreased photocatalytic activity (Ahmed *et al*., 2011). As the catalyst load increases, active sites will increase. However, at a certain point, light penetration will decrease significantly due to excess particle concentration (Adesina, 2004). According to Ahmed *et al*. (2011), excess catalyst loading will lead to an increase in turbidity, light scattering, and a lower photocatalytic activity. Excess ZnO-BiOI 10 % caused excess opacity, and a screening effect, which acted as a shield hindering light penetration. This means that surface area available for light harvesting was reduced, leading to poor photocatalytic activity (Kashif & Ouyang, 2009; Chen *et al*., 2007; Lea & Adesina, 1998).

Bahrami & Nezamzadeh-ejhieh (2015) identified that an increase in the catalyst dose is advantageous to the formation of photogenerated electrons-holes, as well as ROS (reactive oxygen species), which are responsible for the pollutant degradation. Nevertheless, as the catalyst dose is increased, it gets to a certain point where the particles agglomerate which reduces the active adsorption sites on the catalyst, thereby leading to a reduction in the photocatalytic activity.

Furthermore, a surplus catalyst dose has been found to create a light screening effect that leads to the reduction of the photocatalyst’s surface area during irradiation, thereby decreasing its photocatalytic efficiency (Hu *et al*., 2012). Similar observations were made by Bechambi *et al*. (2015).

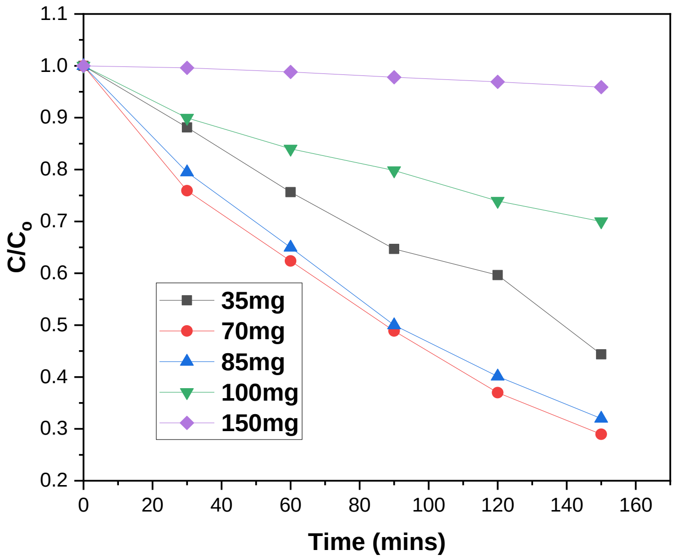

Figure 6. 6. Effect of catalyst dose on the photodegradation of 2CBP using 10 % ZnO-BiOI.

6.4. Effect of pH

Five initial pH values for 10 ppm (2, 5, 7.2, 9.1 and 11.3 respectively) of 2CBP solution were used to study its effect on the degradation of 2CBP. After performing a linear regression between ln(C/C_o) and the photocatalytic reaction time, it was observed that the photodegradation reactions exhibited pseudo-first-order reaction kinetics at all pH values. Figure 6.7 shows the kinetics graphs of the effect of pH on the photodestruction of 2CBP by the application of a ZnO-BiOI 10 % heterostructure catalyst. The best rate constant was observed at pH 7.2 (which is the natural pH of 2CBP, for this study). When the pH was raised, the rate constants at pH 9 (over 7 fold reduction from 0.0054 to 0.0007 K min^{-1}) and 11.3 (over 18 fold reduction) reduced significantly. At a pH of 5, the rate constant reduced by half. Much lower pH (2) resulted in a further reduction in the rate constant. The data is presented in Table 17.

Similarly, the degradation plots (Figure 6.8) show a lower degradation in slightly acidic media (pH 5; 34 % degradation efficiency), a much lower degradation at very acidic media (pH 2; 20 %), and significantly lower degradation in alkaline media (pH 9 = 10 %; pH 11 = 5 % approx).

The study by Yang *et al*. (2008) corroborates the observations and findings in this experiment. Yang and co-workers observed their best degradation at the natural pH of 2CBP, a lower degradation in slightly acidic media, a much lower degradation at very acidic media and significantly lower degradation in alkaline media. Huang *et al*. (1996) also observed an increase in the destruction rate of 2CBP with the decrease of pH in the range of 3 to 10. Adsorption of contaminant molecules onto the surface of a photocatalyst is influenced by pH values (Li *et al*., 2010). The photodegradation process is also dependent on the pH values of the reaction media. Solution pH has an effect on a photocatalysts surface charge, hydroxyl radicals formation and the contaminant molecules' deionization. Hanafi & Sapawe (2020) stated that a solution's optimum pH is very much dependent on the contaminant's properties. The $pH_{(pzc)}$ is an important property of photocatalysts in aqueous environment. When pH of the solution is lower than the $pH_{(pzc)}$, catalyst surface charge will be positive, while it will be negative if it is higher than the $pH_{(pzc)}$. Thus, pH is crucial because the surface charge of the photocatalyst affects the interfacial electron transfer and the photoredox process.

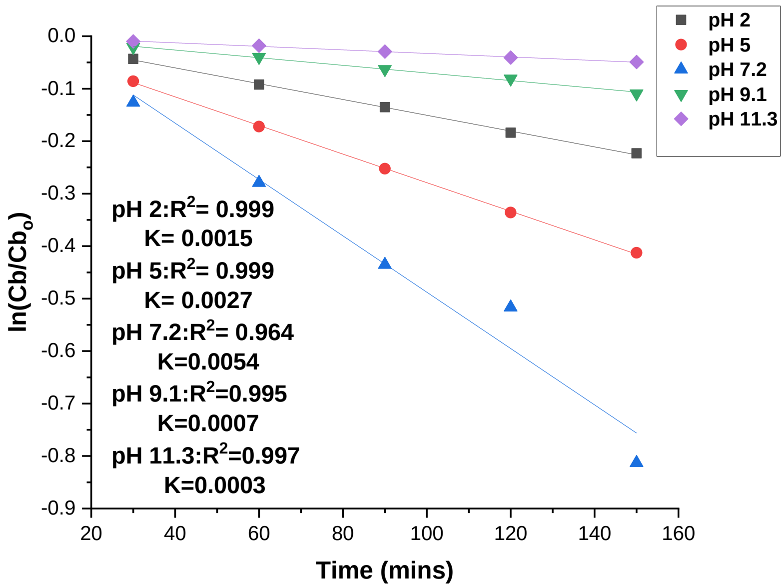

Figure 6. 7. Pseudo-first order plot for the photocatalytic degradation of 2CBP at pH of 2, 5, 7.2, 9 and 11 (catalyst dose: 35 mg; pollutant concentration: 10 ppm; 10 % ZnO-BiOI).

Table 18: Effect of pH on the photodegradation of 2CBP.

pH	**Degradation (%)**	**K_{app} (min^{-1})**	**R^2**
2	**20**	**0.0015**	**0.999**
5	**34**	**0.0027**	**0.999**
7.2	**57**	**0.0054**	**0.964**
9.1	**10**	**0.0007**	**0.995**
11.3	**5**	**0.0003**	**0.997**

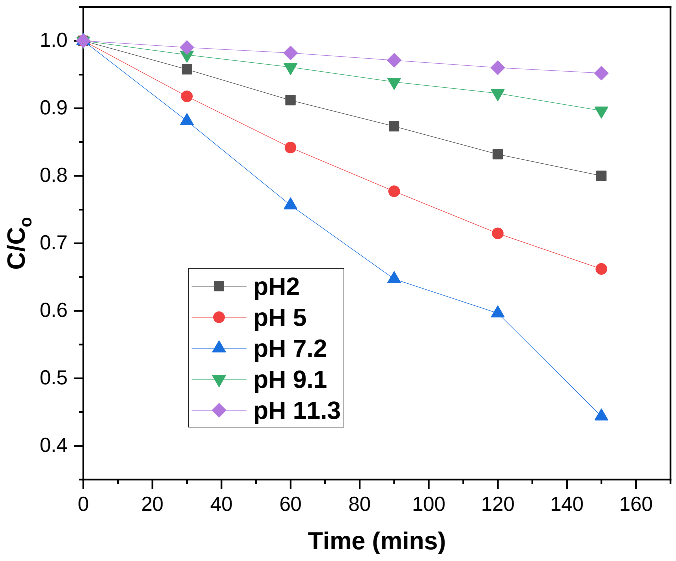

Figure 6. 8. Effect of pH on the photocatalytic degradation of 2CBP using 10 % ZnO-BiOI.

7. Conclusions and recommendations

7.1. Conclusions

In this study, the synthesis of various photocatalysts/heterojunctions for abatement of 2-chlorobiphneyl in aqueous media was carried out.

Objectives 1, 2 and 3: Nanocomposites of ZnO, WO_3 and BiOI were synthesized using several methods such as a sol gel process, a hydrothermal process, as well as direct and facile synthesis methods.

Objectives 4 and 5: Heterostructures were successfully fabricated through the grafting of BiOI and WO_3 unto ZnO at different weight loadings. BiOI and WO_3 were doped into ZnO at 5 %, 10 % and 20 % weight loadings.

Objectives 6 and 7: The as synthesized bare catalysts and heterostructures were characterized by SEM, EDX, BET, UV-Vis, XRD. The results obtained from characterization showed that:

- All elemental analysis confirmed the purity of the as-synthesized photocatalysts as all the composites analysed showed only the presence of the target elements.
- The average crystallite sizes were not significantly affected with respect to the effect of loading of WO_3 and BiOI into ZnO.
- The N_2 adsorption-desorption isotherms showed that nearly all the as-synthesized composites were mesoporous and displayed Type IV isotherms, with the exception of ZnO; which exhibited a Type V isotherm. Some of the isotherms indicated a mixture of mesopores and macropores in the tested materials. The surface area measurements increased with the construction of heterojunctions. However, these increments did not follow any particular trend.

- There were slight red shifts observed in the absorbance of ZnO as WO_3 and BiOI were incorporated into the ZnO. The absorption tails of the heterostructures were well inside the visible light region. All the calculated band gaps decreased/narrowed with increased loading of WO_3 and BiOI into ZnO, with the exception of ZnO-WO_3 10 %. This was attributed to the formation of energy level defects within the forbidden band.

Objectives 8 and 9: The as-synthesized photocatalysts and heterostructures were applied in the photodestruction of 2-chlorobiphenyl. The photocatalytic experiments showed that the ZnO-BiOI 10 % heterostructure with a band gap of 3.0 eV, surface area of 19.79 m^2/g, pore volume of 0.180 cm^3/g and a pore size of 35 nm showed the best photo-activity in the degradation of 2CBP. BiOI showed the best photocatalytic activity among the bare photocatalysts.

Objective 10: The kinetics of the photocatalytic reactions were fitted to a pseudo-first order kinetics model. From the kinetic data, it can be deduced that:

- ZnO-BiOI 10 % exhibited the highest kinetic rate constant of 0.0054 min^{-1} and also showed the best photocatalytic efficiency of 57 %. Observations from the kinetic model shows that ZnO-BiOI 10 % degraded 2CBP rapidly up to a treatment peak at 150 minutes. These observations suggest that ZnO-BiOI 10 % can be used as an efficient photocatalyst.
- The degree of the photocatalytic degradation of 2CBP decreased with increasing initial 2CBP concentration. The rate constants increased at 70 and 85 mg, but decreased as more catalyst was used. When the pH was varied, the highest rate constant was achieved at pH 7.2.

Objective 11: The influence of pH on the photocatalytic degradation of 2CBP by application of ZnO-BiOI 10 % was investigated. The reaction kinetics of this experiment were also modelled. The kinetics data from this experiment showed that:

- The influence of pH on the photodestruction of 2CBP followed a pseudo-first order kinetic model.
- The best rate constant of 0.0054 min^{-1} was at observed at pH 7.2.
- When the pH was raised, the rate constants at pH 9.1 (over 7fold reduction from 0.0054 to 0.0007 min^{-1}) and 11.3 reduced significantly.
- At pH 5, the rate constant reduced by half. A much lower pH (2) caused a further reduction in the rate constant. The photocatalyst fared better in acidic media, in comparison to alkaline media.
- The degradation plots show a lower degradation in slightly acidic media (pH 5; 34 % degradation efficiency), a much lower degradation in very acidic media (pH 2; 20 %), and more significantly lower degradation in alkaline media (pH 9.1 = 10 %; pH 11.3 = 5 % approx)

Objective 12: The influence of the initial 2CBP concentration on the photodestruction efficiency were studied, and the kinetics of the reaction were modelled. Some of the observations made are:

- The linear plots confirmed that the photodestruction of 2CBP followed pseudo-first order kinetics.
- The degree of the photodegradation of the pollutant is influenced by the initial pollutant concentration, which diminished with increasing initial 2CBP concentration.
- The plot of the rate constants against the initial concentrations of the pollutant in the wastewater showed that the rate constants reduce with an increase in its initial concentration

- At 5 ppm, 73 % of the 2CBP solutions was degraded when 35 mg/100 ml of ZnO-BiOI 10 % was utilized.
- Degradation efficiency was lower at higher concentrations.

Objective 13: The influence of initial photocatalyst dose on the photodegradation of 2CBP was investigated. The reaction kinetics model affirmed that pseudo-first-order kinetics applied. Some of the other findings include:

- Doubling of the catalyst dose from 35 to 70 mg led to an increase in the rate constant from 0.0054 to 0.0085 min^{-1}.
- At 85 mg, the rate constant reduced slightly to 0.0077 min^{-1}.
- Loading beyond 85 mg led to significant reduction in the rate constant

7.2. Recommendations

Due to time constraints and some challenges encountered (many of it due to Covid 19 restrictions) the following recommendations are put forward:

- 2CBP was selected as the reference pollutant in this study to evaluate the photo-activities of the various as-synthesized photocatalysts. Photocatalysis can further be evaluated to degrade a larger variety of organic pollutants such as pharmaceutical wastes, BTEX, other different phenolic compounds, emerging pollutants such as perfluorinated compounds and water disinfection byproducts.
- The techniques of HPLC, GC-MS can further be deployed to study the intermediate products and monitor the temporal course of the reaction in greater detail during the photodegradation process.

- Catalyst stability is another important factor which needs studying. The reusability of the catalyst after each photodegradation run is important in order to ascertain how many runs the catalyst is able to undertake and its efficiency for each run.
- It is recommended that a photocatalyst reactor is constructed in which a photocatalyst can be irradiated by solar light while a pollutant containing solution flows through it. Successful proof of this concept will facilitate an engineering design to apply the concept of photocatalytic degradation of contaminated waste streams in practical applications.
- A preliminary techno-economic study to determine the financial feasibility of applying this concept in practice would be useful and contribute to its eventual application in practice.

REFERENCES

Adesina, A. A. (2004). Industrial exploitation of photocatalysis: Progress, perspectives and prospects. *Catalysis Surveys from Asia*, *8*(4), 265–273. https://doi.org/10.1007/s10563-004-9117-0

Adhikari, S., Sarkar, D., & Madras, G. (2015). Highly efficient WO3-ZnO mixed oxides for photocatalysis. *RSC Advances*, *5*(16), 11895–11904. https://doi.org/10.1039/c4ra13210f

Ahmad, M., Ahmed, E., Zafar, F., Khalid, N. R., Niaz, N. A., Hafeez, A., Ikram, M., & Khan, M. A. (2015). Enhanced photocatalytic activity of Ce-doped ZnO nanopowders synthesized by combustion method. *Journal of Rare Earths*, *33*(3), 255–262. https://doi.org/10.1016/S1002-0721(14)60412-9

Ahmad, R., Ahmad, Z., Khan, A. U., Mastoi, N. R., Aslam, M., & Kim, J. (2016). Photocatalytic systems as an advanced environmental remediation: Recent developments, limitations and new avenues for applications. *Journal of Environmental Chemical Engineering*, *4*(4), 4143–4164. https://doi.org/10.1016/j.jece.2016.09.009

Ahmed, S., Rasul, M. G., Brown, R., & Hashib, M. A. (2011). Influence of parameters on the heterogeneous photocatalytic degradation of pesticides and phenolic contaminants in wastewater: A short review. *Journal of Environmental Management*, *92*(3), 311–330. https://doi.org/10.1016/j.jenvman.2010.08.028

Ai, Z., Ho, W., Lee, S., & Zhang, L. (2009). Efficient Photocatalytic Removal of NO in Indoor Air with Hierarchical Bismuth Oxybromide Nanoplate Microspheres under Visible Light. *Environmental Science and Technology*, *43*(11), 4143–4150. https://doi.org/10.1021/es9004366

Akyol, A., Yatmaz, H. C., & Bayramoglu, M. (2004). Photocatalytic decolorization of Remazol Red RR in aqueous ZnO suspensions. *Applied Catalysis B: Environmental*, *54*(1), 19–24. https://doi.org/10.1016/j.apcatb.2004.05.021

Alhakimi, G., Studnicki, L. H., & Al-Ghazali, M. (2003). Photocatalytic destruction of potassium hydrogen phthalate using TiO 2 and sunlight: application for the treatment of industrial wastewater. *Journal of Photochemistry and Photobiology A: Chemistry*, *154*, 219–228. https://doi.org/10.1016/S1010-6030(02)00329-5

Ali, A. M., Ismail, A. A., Najmy, R., & Al-Hajry, A. (2014). Preparation and characterization of ZnO-SiO2thin films as highly efficient photocatalyst. *Journal of Photochemistry and Photobiology A: Chemistry*, *275*, 37–46. https://doi.org/10.1016/j.jphotochem.2013.11.002

Ameen, S., Seo, H., Akhtar, M. S., & Shik, H. (2012). Novel graphene / polyaniline nanocomposites and its photocatalytic activity toward the degradation of rose Bengal dye. *Chemical Engineering Journal*, *210*, 220–228. https://doi.org/10.1016/j.cej.2012.08.035

Amornpitoksuk, P., Suwanboon, S., Sangkanu, S., Sukhoom, A., Muensit, N., & Baltrusaitis, J. (2012). Synthesis , characterization , photocatalytic and antibacterial activities of Ag-doped ZnO powders modified with a diblock copolymer. *Powder Technology*, *219*, 158–164. https://doi.org/10.1016/j.powtec.2011.12.032

Anandan, S., & Miyauchi, M. (2011). Ce-doped ZnO (CexZn1-xO) becomes an efficient visible-light-sensitive photocatalyst by co-catalyst (Cu2+) grafting. *Physical Chemistry Chemical Physics*, *13*(33), 14937–14945. https://doi.org/10.1039/c1cp21514k

Anta, J. A., Guillén, E., & Tena-Zaera, R. (2012). ZnO-Based Dye-Sensitized Solar Cells. *The*

Journal of Physical Chemistry C, *116*(21), 11413–11425. https://doi.org/10.1021/jp3010025

Ao, Y., Wang, K., Wang, P., Wang, C., & Hou, J. (2016). Fabrication of novel p-n heterojunction BiOI/La2Ti2O7 composite photocatalysts for enhanced photocatalytic performance under visible light irradiation. *Dalton Transactions*, *45*(19), 7986–7997. https://doi.org/10.1039/c6dt00862c

Armelao, L., Barreca, D., Bottaro, G., Gasparotto, A., Maccato, C., Maragno, C., Tondello, E., Štangar, U. L., Bergant, M., & Mahne, D. (2007). Photocatalytic and antibacterial activity of TiO2 and Au/TiO2 nanosystems. *Nanotechnology*, *18*(37). https://doi.org/10.1088/0957-4484/18/37/375709

Arumugam, M., & Choi, M. Y. (2020). Recent progress on bismuth oxyiodide (BiOI) photocatalyst for environmental remediation. *Journal of Industrial and Engineering Chemistry*, *81*, 237–268. https://doi.org/10.1016/j.jiec.2019.09.013

Bahrami, M., & Nezamzadeh-ejhieh, A. (2015). Effect of the supported ZnO on clinoptilolite nano-particles in the photodecolorization of semi-real sample bromothymol blue aqueous solution. *Materials Science in Semiconductor Processing*, *30*, 275–284. https://doi.org/10.1016/j.mssp.2014.10.006

Banerjee, D., Lao, J. Y., Wang, D. Z., Huang, J. Y., Ren, Z. F., Steeves, D., Kimball, B., & Sennett, M. (2003). Large-quantity free-standing ZnO nanowires. *Applied Physics Letters*, *83*(10), 2061–2063. https://doi.org/10.1063/1.1609036

Banerjee, P., Chakrabarti, S., Maitra, S., & Dutta, B. K. (2012). Zinc oxide nano-particles - Sonochemical synthesis, characterization and application for photo-remediation of heavy metal. *Ultrasonics Sonochemistry*, *19*(1), 85–93. https://doi.org/10.1016/j.ultsonch.2011.05.007

Bannister, F. (1935). The crystal-structure of the bismuth oxyhalides. *Journal of the Mineralogical Society*, *23*(149). https://doi.org/10.1180/minmag.1935.024.149.01

Bechambi, O., Sayadi, S., & Najjar, W. (2015). Photocatalytic degradation of bisphenol A in the presence of C-doped ZnO: Effect of operational parameters and photodegradation mechanism. *Journal of Industrial and Engineering Chemistry*, *32*, 201–210. https://doi.org/10.1016/j.jiec.2015.08.017

Behera, O. (2008). *Synthesis and Characterization of ZnO nanoparticles of various sizes and Applications in Biological systems* [National Institute of Technology Rourkela Rourkela-769 008, Orissa, India]. http://ethesis.nitrkl.ac.in/2645/1/Omkar_Behera_thesis.pdf

Behnajady, M. A., Modirshahla, N., & Hamzavi, R. (2006). Kinetic study on photocatalytic degradation of C . I . Acid Yellow 23 by ZnO photocatalyst. *Journal of Hazardous Materials*, *133*, 226–232. https://doi.org/10.1016/j.jhazmat.2005.10.022

Benhebal, H., Chaib, M., Salmon, T., Geens, J., Leonard, A., Lambert, S. D., Crine, M., & Heinrichs, B. (2013). Photocatalytic degradation of phenol and benzoic acid using zinc oxide powders prepared by the sol-gel process. *Alexandria Engineering Journal*, *52*(3), 517–523. https://doi.org/10.1016/j.aej.2013.04.005

Bessegato, G. G., Guaraldo, T. T., de Brito, J. F., Brugnera, M. F., & Zanoni, M. V. B. (2015). Achievements and Trends in Photoelectrocatalysis: from Environmental to Energy Applications. *Electrocatalysis*, *6*(5), 415–441. https://doi.org/10.1007/s12678-015-0259-9

Bitenc, M., & Crnjak Orel, Z. (2009). Synthesis and characterization of crystalline hexagonal bipods of zinc oxide. *Materials Research Bulletin*, *44*(2), 381–387. https://doi.org/10.1016/j.materresbull.2008.05.005

Bora, L. V., & Mewada, R. K. (2017). Visible/solar light active photocatalysts for organic effluent treatment: Fundamentals, mechanisms and parametric review. *Renewable and Sustainable Energy Reviews*, *76*(April), 1393–1421. https://doi.org/10.1016/j.rser.2017.01.130

Boruah, P. J., Khanikar, R. R., & Bailung, H. (2020). Synthesis and Characterization of Oxygen Vacancy Induced Narrow Bandgap Tungsten Oxide (WO3−x) Nanoparticles by Plasma Discharge in Liquid and Its Photocatalytic Activity. *Plasma Chemistry and Plasma Processing*, *40*(4), 1019–1036. https://doi.org/10.1007/s11090-020-10073-3

Carey, J. H., Lawrence, J., & Tosine, H. M. (1976). Photodechlorination of PCB's in the presence of titanium dioxide in aqueous suspensions. In *Bulletin of Environmental Contamination and Toxicology* (Vol. 16, Issue 6, pp. 697–701). https://doi.org/10.1007/BF01685575

Chakma, S., & Moholkar, V. S. (2015). Ultrasonics Sonochemistry Investigation in mechanistic issues of sonocatalysis and sonophotocatalysis using pure and doped photocatalysts. *Ultrasonics - Sonochemistry*, *22*, 287–299. https://doi.org/10.1016/j.ultsonch.2014.06.008

Chan, S. H., Wu, T. Y., Juan, J. C., & Teh, C. Y. (2011). Recent developments of metal oxide semiconductors as photocatalysts in advanced oxidation processes (AOPs) for treatment of dye waste-water. *Journal of Chemical Technology & Biotechnology*, *86*(April 2011), 1130–1158. https://doi.org/10.1002/jctb.2636

Chandiran, A. K., Abdi-Jalebi, M., Nazeeruddin, M. K., & Grätzel, M. (2014). Analysis of electron transfer properties of ZnO and TiO2 photoanodes for dye-sensitized solar cells. *ACS Nano*, *8*(3), 2261–2268. https://doi.org/10.1021/nn405535j

Chandrasekaran, P., Viruthagiri, G., & Srinivasan, N. (2012). The effect of various capping agents on the surface modifications of sol-gel synthesised ZnO nanoparticles. *Journal of Alloys and Compounds*, *540*, 89–93. https://doi.org/10.1016/j.jallcom.2012.06.032

Chen, C. C., Lu, C. S., Chung, Y. C., & Jan, J. L. (2007). UV light induced photodegradation of malachite green on TiO2nanoparticles. *Journal of Hazardous Materials*, *141*(3), 520–528. https://doi.org/10.1016/j.jhazmat.2006.07.011

Chen, L., Huang, R., Xiong, M., Yuan, Q., He, J., Jia, J., Yao, M., Luo, S., Au, C., & Yin, S. (2013). Room-Temperature Synthesis of Flower-Like BiOX (X □ Cl, Br, I) Hierarchical Structures and Their Visible-Light Photocatalytic Activity. *Inorganic Chemistry*, *52*, 11118−11125. https://doi.org/10.1021/ic401349j

Chen, W. J., Liu, W. L., Hsieh, S. H., & Tsai, T. K. (2007). Preparation of nanosized ZnO using α brass. *Applied Surface Science*, *253*(16), 6749–6753. https://doi.org/10.1016/j.apsusc.2007.01.091

Cheng, H., Huang, B., Dai, Y., Qin, X., & Zhang, X. (2010). One-Step Synthesis of the Nanostructured AgI / BiOI Composites with Highly Enhanced Visible-Light Photocatalytic Performances. *Langmuir Article*, *26*(19), 6618–6624. https://doi.org/10.1021/la903943s

Chiu, W. S., Khiew, P. S., Cloke, M., Isa, D., Tan, T. K., Radiman, S., Abd-Shukor, R., Hamid, M. A. A., Huang, N. M., Lim, H. N., & Chia, C. H. (2010). Photocatalytic study of two-dimensional ZnO nanopellets in the decomposition of methylene blue. *Chemical Engineering Journal*, *158*(2), 345–352. https://doi.org/10.1016/j.cej.2010.01.052

Choi, K., Kang, T., & Oh, S. G. (2012). Preparation of disk shaped ZnO particles using surfactant and their PL properties. *Materials Letters*, *75*, 240–243. https://doi.org/10.1016/j.matlet.2012.02.031

Choi, W., Termin, A., & Hoffmann, M. R. (1994). The role of metal ion dopants in quantum-sized TiO2: Correlation between photoreactivity and charge carrier recombination dynamics. *Journal of Physical Chemistry*, *98*(51), 13669–13679. https://doi.org/10.1021/j100102a038

Chu, W., & Kwan, C. Y. (2003). Remediation of contaminated soil by a solvent/surfactant system. *Chemosphere*, *53*(1), 9–15. https://doi.org/10.1016/S0045-6535(03)00389-8

Chun, H., Yizhong, W., & Hongxiao, T. (2000). Destruction of phenol aqueous solution by photocatalysis or direct photolysis. *Chemosphere*, *41*, 1205–1209.

Ciciliati, M. A., Silva, M. F., Fernandes, D. M., De Melo, M. A. C., Hechenleitner, A. A. W., & Pineda, E. A. G. (2015). Fe-doped ZnO nanoparticles: Synthesis by a modified sol-gel method and characterization. *Materials Letters*, *159*, 84–86. https://doi.org/10.1016/j.matlet.2015.06.023

Coleman, V. A., & Jagadish, C. (2006). Basic Properties and Applications of ZnO. *Zinc Oxide Bulk, Thin Films and Nanostructures, December,* 1–20. https://doi.org/10.1016/B978-008044722-3/50001-4

Colmenares, J. C., Kuna, E., Jakubiak, S., Michalski, J., & Kurzydłowski, K. (2015).

Polypropylene nonwoven filter with nanosized ZnO rods: Promising hybrid photocatalyst for water purification. *Applied Catalysis B: Environmental*, *170–171*, 273–282. https://doi.org/10.1016/j.apcatb.2015.01.031

Colón, G., Hidalgo, M. C., Navío, J. A., Pulido Melián, E., González Díaz, O., & Doña Rodríguez, J. M. (2008). Highly photoactive ZnO by amine capping-assisted hydrothermal treatment. *Applied Catalysis B: Environmental*, *83*(1–2), 30–38. https://doi.org/10.1016/j.apcatb.2008.01.033

Cruz, A. M., Rodríguez, F. E. L., Reyna-Cavasos, K. A., & Lopez-Cuella, E. (2020). Synthesis of bismuth oxyiodide (BiOI) by means of microwaves in glycerol with high photocatalytic activity for the elimination of - NO x and - SO 2. *Research on Chemical Intermediates*, *46*(1), 923–941. https://doi.org/10.1007/s11164-019-03998-8

Dai, W., & Zhao, Z. (2016). Electronic Structure and Optical Properties of BiOI as a Photocatalyst Driven by Visible Light. *Catalysts*, *6*, 1–15. https://doi.org/10.3390/catal6090133

Daneshvar, N., Salari, D., & Khataee, A. R. (2004). Photocatalytic degradation of azo dye acid red 14 in water on ZnO as an alternative catalyst to TiO 2. *Journal of Photochemistry and Photobiology A: Chemistry*, *162*, 317–322. https://doi.org/10.1016/S1010-6030(03)00378-2

Di, J., Xia, J., Ge, Y., Xu, L., Xu, H., & He, M. (2014). Reactable ionic liquid-assisted rapid synthesis of BiOI hollow microspheres at room temperature with enhanced photocatalytic activity †. *Journal of Materials Chemistry A*, *2*, 15864–15874. https://doi.org/10.1039/c4ta02400a

Dindar, B., & Içli, S. (2001). Unusual photoreactivity of zinc oxide irradiated by concentrated sunlight. *Journal of Photochemistry and Photobiology A: Chemistry*, *140*(January), 263–268. https://doi.org/10.1016/S1010-6030(01)00414-2

Dong, P., Hou, G., Xi, X., Shao, R., & Dong, F. (2017). WO3-based photocatalysts: morphology control, activity enhancement and multifunctional applications. In *Environmental Science: Nano* (Vol. 4, Issue 3, pp. 539–557). https://doi.org/10.1039/c6en00478d

Draper, R. B., & Fox, M. A. (1990). Titanium Dioxide Photosensitized Reactions Studied by Diffuse Reflectance Flash Photolysis in Aqueous Suspensions of TiO2 Powder. *Langmuir*, *6*(8), 1396–1402. https://doi.org/10.1021/la00098a013

Faisal, M., Ismail, A. A., Ibrahim, A. A., Bouzid, H., & Al-sayari, S. A. (2013). Highly efficient photocatalyst based on Ce doped ZnO nanorods : Controllable synthesis and enhanced photocatalytic activity. *Chemical Engineering Journal*, *229*, 225–233. https://doi.org/10.1016/j.cej.2013.06.004

Fan, X. X., Yu, T., Zhang, L. Z., Chen, X. Y., & Zou, Z. G. (2007). Photocatalytic degradation of acetaldehyde on mesoporous TiO2: Effects of surface area and crystallinity on the photocatalytic activity. *Chinese Journal of Chemical Physics*, *20*(6), 733–738. https://doi.org/10.1088/1674-0068/20/06/733-738

Fang, Y., Li, Z., Xu, S., Han, D., & Lu, D. (2013). Optical properties and photocatalytic activities of spherical zno and flower-like zno structures synthesized by facile hydrothermal method. *Journal of Alloys and Compounds*, *575*, 359–363. https://doi.org/10.1016/j.jallcom.2013.05.183

Flores, N.M., Pal, U., Galeazzia, R., & Sandoval, A. (2014). Effects of morphology, surface area, and defect content on the photocatalytic dye degradation performance of ZnO nanostructures. *Royal Society of Chemistry Advances*, *4*(77), 41099–41110. https://doi.org/10.1039/C4RA04522J

Frade, T., Melo Jorge, M. E., & Gomes, A. (2012). One-dimensional ZnO nanostructured films: Effect of oxide nanoparticles. *Materials Letters*, *82*, 13–15. https://doi.org/10.1016/j.matlet.2012.05.028

Furakawa, K., & Fujihara, H. (2008). Microbial degradation of polychlorinated biphenyls: Biochemical and molecular features. *Journal of Bioscience and Engineering*, *105*(5), 433–449.

Ganose, A. M., Cu, M., Butler, K. T., Walsh, A., & Scanlon, D. O. (2016). Interplay of Orbital and Relativistic E ff ects in Bismuth Oxyhalides: BiOF, BiOCl, BiOBr, and BiOI. *Chemistry of Materials*, *28*, 1980–1984. https://doi.org/10.1021/acs.chemmater.6b00349

García-Montaño, J., Enech, X., García-Hortal, J. A., Torrades, F., & Peral, J. (2008). The testing of several biological and chemical coupled treatments for Cibacron Red FN-R azo dye removal. *Journal of Hazardous Materials*, *154*, 484–490. https://doi.org/10.1016/j.jhazmat.2007.10.050

Garcia, S. P., & Semancik, S. (2007). Controlling the morphology of zinc oxide nanorods crystallized from aqueous solutions: The effect of crystal growth modifiers on aspect ratio. *Chemistry of Materials*, *19*(16), 4016–4022. https://doi.org/10.1021/cm061977r

Giannakopoulou, T., Todorova, N., Giannouri, M., Yu, J., & Trapalis, C. (2014). Optical and photocatalytic properties of composite TiO 2 / ZnO thin films. *Catalysis Today*, *230*, 174–180. https://doi.org/10.1016/j.cattod.2013.10.003

Gnanaprakasam, A., Sivakumar, V. M., & Thirumarimurugan, M. (2015). Influencing Parameters in the Photocatalytic Degradation of Organic Effluent via Nanometal Oxide Catalyst : A Review. *Indian Journal of Materials Science*, *2015*, 1–16. https://doi.org/10.1155/2015/601827

Gouma, P. I., & Lee, J. (2012). Sol-Gel Processed Oxide Photocatalysts. In *Advances in Sol-Gel Derived Materials and Technologies* (pp. 217–238). Springer 2012. https://doi.org/DOI 10.1007/978-1-4614-1957-0

Gouvêa, C. a, Wypych, F., Moraes, S. G., Durán, N., Nagata, N., & Peralta-Zamora, P. (2000). Semiconductor-assisted photocatalytic degradation of reactive dyes in aqueous solution. *Chemosphere*, *40*(4), 433–440. https://doi.org/http://dx.doi.org/10.1016/S0045-6535(99)00313-6

Goveas, J. J., Shetty, S., Mascarenhas, N. P., D'Souza, R. M., & Gonsalves, R. A. (2020). Electrochemical synthesis of ZnO-WO3 nanocomposites and their photocatalytic activity. *Journal of Applied Electrochemistry*, *50*(4), 501–511. https://doi.org/10.1007/s10800-020-01407-2

Gupta, A., Saurav, J. R., & Bhattacharya, S. (2015). Solar light based degradation of organic pollutants using ZnO nanobrushes for water filtration. *RSC Advances*, *5*(87), 71472–71481. https://doi.org/10.1039/C5RA10456D

Hagfeldt, A., & Grätzel, M. (1995). Light-Induced Redox Reactions in Nanocrystalline Systems.

Chemical Reviews, *95*(1), 49–68. https://doi.org/10.1021/cr00033a003

Hahn, Y.B. (2011). Zinc oxide nanostructures and their applications. *Korean Journal of Chemical Engineering*, *28*(9), 1797–1813. https://doi.org/10.1007/s11814-011-0213-3

Han, A., Fung, S., Xiu, C., & Toy, Y. (2015). Bismuth oxyiodide heterojunctions in photocatalytic degradation of phenolic molecules. *Research on Chemical Intermediates, 41*, 9509–9520. https://doi.org/10.1007/s11164-015-1976-7

Hanafi, M. F., & Sapawe, N. (2020). Influence of pH on the photocatalytic degradation of methyl orange using nickel catalyst. *Materials Today: Proceedings, 31*, 339–341. https://doi.org/10.1016/j.matpr.2020.06.094

Hasnidawani, J. N., Azlina, H. N., Norita, H., & Bonnia, N. N. (2016). Synthesis of ZnO Nanostructures Using Sol-Gel Method. *Procedia Chemistry*, *19*, 211–216. https://doi.org/10.1016/j.proche.2016.03.095

He, H. Y., Huang, J. F., Cao, L. Y., & Wu, J. P. (2010). Photodegradation of methyl orange aqueous on MnWO4 powder under different light resources and initial pH. *Desalination*, *252*(1–3), 66–70. https://doi.org/10.1016/j.desal.2009.10.024

He, L., Tong, Z., Wang, Z., Chen, M., Huang, N., & Zhang, W. (2018). Effects of calcination temperature and heating rate on the photocatalytic properties of ZnO prepared by pyrolysis. *Journal of Colloid and Interface Science*, *509*, 448–456. https://doi.org/10.1016/j.jcis.2017.09.021

He, Y., Wu, Z., Fu, L., Li, C., Miao, Y., Cao, L., Fan, H., & Zou, B. (2003). Photochromism and Size Effect of WO 3 and WO 3 - TiO 2 Aqueous Sol. *Chemical Materials*, 4039–4045.

https://doi.org/10.1021/cm034116g

Herrmann, J. (2005). Heterogeneous photocatalysis : state of the art and present applications. *Topics in Catalysis*, *34*. https://doi.org/10.1007/s11244-005-3788-2

Hoffmann, M. R., Martin, S. T., Choi, W., & Bahnemann, D. W. (1995). Environmental Applications of Semiconductor Photocatalysis. *Chemical Reviews*, *95*(1), 69–96. https://doi.org/10.1021/cr00033a004

Hong, C.S., Wang, Y., & Bush, B. (1998). Kinetics and products of the TiO2 photocatalytic degradation of 2-chlorobiphenyl in water. *Chemosphere*, *36*(7), 1653–1667.

Hosseini, S. M., Sarsari, I. A., Kameli, P., & Salamati, H. (2015). Effect of Ag doping on structural, optical, and photocatalytic properties of ZnO nanoparticles. *Journal of Alloys and Compounds*, *640*, 408–415. https://doi.org/10.1016/j.jallcom.2015.03.136

Hu, J., Weng, S., Zheng, Z., Pei, Z., Huang, M., & Liu, P. (2014). Solvents mediated-synthesis of BiOI photocatalysts with tunable morphologies and their visible-light driven photocatalytic performances in removing of arsenic from water. *Journal of Hazardous Materials*, *264*, 293–302. https://doi.org/10.1016/j.jhazmat.2013.11.027

Hu, M. Z. C., Payzant, E. A., & Byers, C. H. (2000). Sol-gel and ultrafine particle formation via dielectric tuning of inorganic salt-alcohol-water solutions. *Journal of Colloid and Interface Science*, *222*(1), 20–36. https://doi.org/10.1006/jcis.1999.6610

Hu, X., Fan, J., Zhang, K., & Wang, J. (2012). Chemosphere Photocatalytic removal of organic pollutants in aqueous solution by Bi 4 Nb x Ta (1 À x) O 8 I. *Chemosphere*, *87*(10), 1155–1160. https://doi.org/10.1016/j.chemosphere.2012.02.023

Huang, C. P., Dong, C., & Tang, Z. (1993). Advanced chemical oxidation: Its present role and potential future in hazardous waste treatment. *Waste Management*, *13*(5–7), 361–377. https://doi.org/10.1016/0956-053X(93)90070-D

Huang, I. W., Hong, C. S., & Bush, B. (1996). Photocatalytic degradation of PCBs in TiO2 aqueous suspensions. *Chemosphere*, *32*(9), 1869–1881. https://doi.org/10.1016/0045-6535(96)00080-X

Huang, W. I., Hong, C. S., & Bush, B. (1996). Photocatalytic degradation of PCBs in TiO2 aqueous suspensions. *Chemosphere*, *32*(9), 1869–1881.

Huang, Y., Li, H., Balogun, M. S., Liu, W., Tong, Y., Lu, X., & Ji, H. (2014). Oxygen vacancy induced bismuth oxyiodide with remarkably increased visible-light absorption and superior photocatalytic performance. *ACS Applied Materials and Interfaces*, *6*(24), 22920–22927. https://doi.org/10.1021/am507641k

Hussein, F. H., & Abass, T. A. (2010). Photocatalytic treatment of textile industrial wastewater. *International Journal of Chemical Sciences*, *8*(3), 1353–1364.

Ibhadon, A., & Fitzpatrick, P. (2013). Heterogeneous Photocatalysis: Recent Advances and Applications. *Catalysts*, *3*(1), 189–218. https://doi.org/10.3390/catal3010189

Inoue, Y. (2009). Photocatalytic water splitting by RuO 2 -loaded metal oxides and nitrides with d 0 - and d 10 -related electronic configurations. *Energy & Environmental Science*, 364–386. https://doi.org/10.1039/b816677n

Iqbal, J., Liu, X., Zhu, H., Wu, Z. B., & Zhang, Y. (2009). Raman and highly ultraviolet red-shifted near band-edge properties of LaCe-co-doped ZnO nanoparticles. *Acta Materialia*, *57*(16), 4790–4796. https://doi.org/10.1016/j.actamat.2009.06.056

Jagadish, C & Pearton, S. (2006). Zinc oxide bulk, thin films and nanostructures. In *Processing, properties and applications* (1 edition, p. 589). Elsevier Science. www.sciencedirect.com/science/book/9780080447223

Jantunen, A. P. K., Koelmans, A. A., & Jonker, M. T. O. (2010). Modeling polychlorinated biphenyl sorption isotherms for soot and coal. *Environmental Pollution*, *158*(8), 2672–2678. https://doi.org/10.1016/j.envpol.2010.04.022

Jayah, N. A., Yahaya, H., Mahmood, M. R., Terasako, T., Yasui, K., & Hashim, A. M. (2015). High electron mobility and low carrier concentration of hydrothermally grown ZnO thin films on seeded a-plane sapphire at low temperature. *Nanoscale Research Letters*, *10*(1), 1–10. https://doi.org/10.1186/s11671-014-0715-0

Jiang, J; Wang, H; Chen, X; Li, S; Xie, T; Wang, D; Lin, Y. (2017). Enhanced photocatalytic degradation of phenol and photogenerated charges transfer property over BiOI-loaded ZnO composites. *Journal of Colloid And Interface Science*, *494*, 130–138. https://doi.org/10.1016/j.jcis.2017.01.064

Jiang, J., Zhang, X., Sun, P., & Zhang, L. (2011). ZnO / BiOI Heterostructures : Photoinduced Charge-Transfer Property and Enhanced Visible-Light Photocatalytic Activity. *The Journal of Physical Chemistry C*, *115*, 20555–20564. https://doi.org/10.1021/jp205925z

Jiao, S., Zhang, K., Bai, S., Li, H., Gao, S., Li, H., Wang, J., Yu, Q., Guo, F., & Zhao, L. (2013). Controlled morphology evolution of ZnO nanostructures in the electrochemical deposition: From the point of view of chloride ions. *Electrochimica Acta*, *111*(3), 64–70.

https://doi.org/10.1016/j.electacta.2013.08.050

Johar, M. A., Afzal, R. A., Alazba, A. A., & Manzoor, U. (2015). Photocatalysis and Bandgap Engineering Using ZnO Nanocomposites. *Advances in Materials Science and Engineering*, *2015*. https://doi.org/10.1155/2015/934587

José-Yacamán, M., Gutierrez-Wing, C., Miki, M., Yang, D. Q., Piyakis, K. N., & Sacher, E. (2005). Surface diffusion and coalescence of mobile metal nanoparticles. *Journal of Physical Chemistry B*, *109*(19), 9703–9711. https://doi.org/10.1021/jp0509459

Kandanapitiye, M. S., Gao, M., Molter, J., Flask, C. A., & Huang, S. . (2014). Synthesis, Characterization, and X-ray Attenuation Properties of Ultrasmall BiOI Nanoparticles: Toward Renal Clearable Particulate CT Contrast Agents. *Inorganic Chemistry*, *53*, 10189–10194. https://doi.org/10.1021/ic5011709

Kandavelu, V., Kastien, H., & Thampi, K. R. (2004). Photocatalytic degradation of isothiazolin-3-ones in water and emulsion paints containing nanocrystalline TiO 2 and ZnO catalysts. *Applied Catalysis B: Environmental*, *48*, 101–111. https://doi.org/10.1016/j.apcatb.2003.09.022

Kanel, S. R., & Al-Abed, S. R. (2011). Influence of pH on the transport of nanoscale zinc oxide in saturated porous media. *Journal of Nanoparticle Research*, *13*(9), 4035–4047. https://doi.org/10.1007/s11051-011-0345-8

Kannadasan, N., Shanmugam, N., Cholan, S., Sathishkumar, K., Viruthagiri, G., & Poonguzhali, R. (2014). The effect of Ce 4 + incorporation on structural , morphological and photocatalytic characters of ZnO nanoparticles. *Materials Characterization*, *97*, 37–46.

https://doi.org/10.1016/j.matchar.2014.08.021

Kansal, S. K., Singh, M., & Sud, D. (2008). Studies on TiO2 / ZnO photocatalysed degradation of lignin. *Journal of Hazardous Materials*, *153*, 412–417. https://doi.org/10.1016/j.jhazmat.2007.08.091

Karimi, L., Zohoori, S., & Yazdanshenas, E. . (2014). Photocatalytic degradation of azo dyes in aqueous solutions under UV irradiation using nano-strontium titanate as the nanophotocatalyst. *Journal of Saudi Chemical Society*, *18*(5), 581–588. https://doi.org/10.1016/j.jscs.2011.11.010

Kashif, N., & Ouyang, F. (2009). Parameters effect on heterogeneous photocatalysed degradation of phenol in aqueous dispersion of TiO2. *Journal of Environmental Sciences*, *21*(4), 527–533. https://doi.org/10.1016/S1001-0742(08)62303-7

Kaštánek, P., Demnerová, K., & Ma, Y. (2004). Decontamination of wastewater contaminated by polychlorinated biphenyls (PCBs). *Water Science and Technology*, *50*(2), 131–138. https://doi.org/10.2166/wst.2004.0107

Kayaci, F., Vempati, S., Donmez, I., Biyikli, N., & Uyar, T. (2014a). Role of zinc interstitials and oxygen vacancies of ZnO in photocatalysis: a bottom-up approach to control defect density. *Nanoscale*, *6*(17), 10224–10234. https://doi.org/10.1039/C4NR01887G

Kayaci, F., Vempati, S., Donmez, I., Biyikli, N., & Uyar, T. (2014b). Selective isolation of the electron or hole in photocatalysis: ZnO–TiO2 and TiO2–ZnO core– shell structured heterojunction nanofibers via electrospinning and atomic layer deposition. *Nanoscale*, *6*(11), 5735–5745. https://doi.org/10.1039/c3nr06665g

Khaki, M. R. D., Shafeeyan, M. S., Raman, A. A. A., & Daud, W. M. A. W. (2017). Application of doped photocatalysts for organic pollutant degradation - A review. *Journal of Environmental Management*, *198*, 78–94. https://doi.org/10.1016/j.jenvman.2017.04.099

Khan, G. M., Kim, G. Y., Akinrelere, T. S., & Moon, S. H. (2007). Electroenzymatic mineralization of 2-chlorobiphenyl in synthetic wastewater. *Desalination*, *211*(1–3), 212–221. https://doi.org/10.1016/j.desal.2006.03.595

Khatamian, M., Khandar, A. A., Divband, B., Haghighi, M., & Ebrahimiasl, S. (2012). Heterogeneous photocatalytic degradation of 4-nitrophenol in aqueous suspension by Ln (La 3+, Nd 3+ or Sm 3+) doped ZnO nanoparticles. *Journal of Molecular Catalysis A: Chemical*, *365*(3), 120–127. https://doi.org/10.1016/j.molcata.2012.08.018

Kisch, H. (2013). Semiconductor photocatalysis - Mechanistic and synthetic aspects. *Angewandte Chemie - International Edition*, *52*(3), 812–847. https://doi.org/10.1002/anie.201201200

Kochuveedu, S. T., Jang, Y. H., Jang, Y. J., & Kim, D. H. (2013). Visible light active photocatalysis on block copolymer induced strings of ZnO nanoparticles doped with carbon. *Journal of Materials Chemistry A*, *1*(3), 898–905. https://doi.org/10.1039/c2ta00263a

Kolodziejczak-Radzimska, A., & Jesionowski, T. (2014). Zinc oxide-from synthesis to application: A review. *Materials*, *7*(4), 2833–2881. https://doi.org/10.3390/ma7042833

Kormann, C., Bahnemann, D. W., & Hoffmann, M. R. (1988). Photocatalytic production of H2O2 and organic peroxides in aqueous suspensions of TiO2, ZnO, and desert sand. *Environmental Science and Technology*, *22*(7), 798–806.

https://doi.org/10.1021/es00172a009

Kuang, P., Ran, J., Liu, Z., Wang, H., & Li, N. (2015). Enhanced Photoelectrocatalytic Activity of BiOI Nanoplate – Zinc Oxide Nanorod p – n Heterojunction. *Chemistry-A European Journal*, *21*, 15360–15368. https://doi.org/10.1002/chem.201501183

Kubátová, A., Erbanová, P., Eichlerová, I., Homolka, L., Nerud, F., & Šašek, V. (2001). PCB congener selective biodegradation by the white rot fungus Pleurotus ostreatus in contaminated soil. *Chemosphere*, *43*(2), 207–215. https://doi.org/10.1016/S0045-6535(00)00154-5

Kumar, S. G., & Rao, K. S. R. K. (2015). Zinc oxide based photocatalysis: Tailoring surface-bulk structure and related interfacial charge carrier dynamics for better environmental applications. *RSC Advances*, *5*(5), 3306–3351. https://doi.org/10.1039/c4ra13299h

Kumar, S. G., & Rao, K. S. R. K. (2017). Comparison of modification strategies towards enhanced charge carrier separation and photocatalytic degradation activity of metal oxide semiconductors (TiO2, WO3and ZnO). *Applied Surface Science*, *391*, 124–148. https://doi.org/10.1016/j.apsusc.2016.07.081

Kumaresan, N., Ramamurthi, K., Ramesh Babu, R., Sethuraman, K., & Moorthy Babu, S. (2017). Hydrothermally grown ZnO nanoparticles for effective photocatalytic activity. *Applied Surface Science*, *418*, 138–146. https://doi.org/10.1016/j.apsusc.2016.12.231

Kuriakose, S., Choudhary, V., Satpati, B., & Mohapatra, S. (2014). Enhanced photocatalytic activity of ag-zno hybrid plasmonic nanostructures prepared by a facile wet chemical method. *Beilstein Journal of Nanotechnology*, *5*(1), 639–650.

https://doi.org/10.3762/bjnano.5.75

Kuriakose, S., Satpati, B., & Mohapatra, S. (2014). Enhanced photocatalytic activity of Co doped ZnO nanodisks and nanorods prepared by a facile wet chemical method. *Physical Chemistry Chemical Physics*, *16*(25), 12741–12749. https://doi.org/10.1039/c4cp01315h

Kusumam, T. V. A., Panakkal, T., Divya, T., & Nikhila, M. P. (2016). Morphology controlled synthesis and photocatalytic activity of zinc oxide nanostructures. *Ceramics International*, *42*(3), 3769–3775. https://doi.org/10.1016/j.ceramint.2015.11.025

Lam, S. M., Sin, J. C., Abdullah, A. Z., & Mohamed, A. R. (2015). Sunlight responsive WO3/ZnO nanorods for photocatalytic degradation and mineralization of chlorinated phenoxyacetic acid herbicides in water. *Journal of Colloid and Interface Science*, *450*, 34–44. https://doi.org/10.1016/j.jcis.2015.02.075

Law, M., Greene, L. E., Johnson, J. C., Saykally, R., & Yang, P. (2005). Nanowire dye-sensitized solar cells. *Nature Materials*, *4*(6), 455–459. https://doi.org/10.1038/nmat1387

Lea, J., & Adesina, A. A. (1998). The photo-oxidative degradation of sodium dodecyl sulphate in aerated aqueous TiO2suspension. *Journal of Photochemistry and Photobiology A: Chemistry*, *118*(2), 111–122. https://doi.org/10.1016/S1010-6030(98)00375-X

Lee, K. M., Lai, C. W., Ngai, K. S., & Juan, J. C. (2016). Recent developments of zinc oxide based photocatalyst in water treatment technology: A review. *Water Research*, *88*(November), 428–448. https://doi.org/10.1016/j.watres.2015.09.045

Lei, R., Zhang, H., Ni, H., Chen, R., Gu, H., & Zhang, B. (2019). Novel ZnO nanoparticles modified WO 3 nanosheet arrays for enhanced photocatalytic properties under solar light illumination. *Applied Surface Science*, *463*, 363–373. https://doi.org/10.1016/j.apsusc.2018.08.218

Lettieri, S., Santamaria Amato, L., Maddalena, P., Comini, E., Baratto, C., & Todros, S. (2009). Recombination dynamics of deep defect states in zinc oxide nanowires. *Nanotechnology*, *20*(17). https://doi.org/10.1088/0957-4484/20/17/175706

Li, B., Chen, X., Zhang, T., Jiang, S., Zhang, G., Wu, W., & Ma, X. (2018). Photocatalytic selective hydroxylation of phenol to dihydroxybenzene by BiOI/TiO 2 p-n heterojunction photocatalysts for enhanced photocatalytic activity. *Applied Surface Science*, *439*, 1047–1056. https://doi.org/10.1016/j.apsusc.2017.12.220

Li, D., & Haneda, H. (2003). Morphologies of zinc oxide particles and their effects on photocatalysis. *Chemosphere*, *51*, 129–137.

Li, F., Sun, S., Jiang, Y., Xia, M., Sun, M., & Xue, B. (2008). Photodegradation of an azo dye using immobilized nanoparticles of TiO2supported by natural porous mineral. *Journal of Hazardous Materials*, *152*(3), 1037–1044. https://doi.org/10.1016/j.jhazmat.2007.07.114

Li, G. R., Hu, T., Pan, G. L., Yan, T. Y., Gao, X. P., & Zhu, H. Y. (2008). Morphology - Function Relationship of ZnO : Polar Planes , Oxygen Vacancies , and Activity. *Journal of Physical Chemistry C*, *112*, 11859–11864.

Li, Guanhua, Zhang, L., & Zhang, Z. (2008). Determination of polychlorinated biphenyls in water using dynamic hollow fiber liquid-phase microextraction and gas chromatography-mass spectrometry. *Journal of Chromatography A*, *1204*(1), 119–122. https://doi.org/10.1016/j.chroma.2008.07.081

Li, Guoting, Li, F., Zhang, P., Li, Y., & Yuan, C. (2010). Multiple effect of pH on photocatalytic degradation of Orange II using TiO2. *Advanced Materials Research*, *113–116*, 1878–1883. https://doi.org/10.4028/www.scientific.net/AMR.113-116.1878

Li, M., & Li, J. C. (2006). Size effects on the band-gap of semiconductor compounds. *Materials Letters*, *60*(20), 2526–2529. https://doi.org/10.1016/j.matlet.2006.01.032

Li, X., Yu, J., Low, J., Fang, Y., Xiao, J., & Chen, X. (2015). Engineering heterogeneous semiconductors for solar water splitting. *Journal of Materials Chemistry A: Materials for Energy and Sustainability*, *3*(November 2014), 2485–2534. https://doi.org/10.1039/C4TA04461D

Li, Y., Xie, W., Hu, X., Shen, G., Zhou, X., Xiang, Y., Zhao, X., & Fang, P. (2010). Comparison of dye photodegradation and its coupling with light-to-electricity conversion over TiO2and ZnO. *Langmuir*, *26*(1), 591–597. https://doi.org/10.1021/la902117c

Liao, C., Ma, Z., Chen, X., He, X., & Qiu, J. (2016). Controlled synthesis of bismuth oxyiodide toward optimization of photocatalytic performance. *Applied Surface Science*, *387*, 1247–1256. https://doi.org/10.1016/j.apsusc.2016.06.140

Lim, S. K., Hwang, S. H., Kim, S., & Park, H. (2011). Preparation of ZnO nanorods by microemulsion synthesis and their application as a CO gas sensor. *Sensors and Actuators, B: Chemical*, *160*(1), 94–98. https://doi.org/10.1016/j.snb.2011.07.018

Lin, L. Y., & Kim, D. E. (2009). Effect of annealing temperature on the tribological behavior of ZnO films prepared by sol-gel method. In *Thin Solid Films* (Vol. 517, Issue 5, pp. 1690–1700). https://doi.org/10.1016/j.tsf.2008.10.018

Linsebigler, A. L., Lu, G., & Yates, J. T. (1995). Photocatalysis on TiO2Surfaces: Principles, Mechanisms, and Selected Results. *Chemical Reviews*, *95*(3), 735–758. https://doi.org/10.1021/cr00035a013

Liu, Hang, Cai, J., Luo, M., Chen, C., & Hu, P. (2020). Novel mesoporous bismuth oxyiodide single-crystal nanosheets with enhanced catalytic activity. *RSC Advances*, *10*(10), 5913–5918. https://doi.org/10.1039/c9ra10451h

Liu, Hong, Cao, W., Su, Y., Wang, Y., & Wang, X. (2012). Synthesis , characterization and photocatalytic performance of novel visible light induced Ag/BiOI. *Applied Catalysis B, Environmental*, *111–112*, 271–279. https://doi.org/10.1016/j.apcatb.2011.10.008

Liu, Jing, Hu, Z., Peng, Y., Huang, H., Li, Y., Wu, M., Ke, X., Tendeloo, G. Van, & Su, B. (2016). 2D ZnO mesoporous single-crystal nanosheets with exposed {0001}polar facets for the depollution of cationic dye molecules by highlyselective adsorption and photocatalytic decomposition. *Applied Catalysis B: Environmental*, *181*, 138–145. https://doi.org/10.1016/j.apcatb.2015.07.054

Liu, Jinping, Huang, X., Duan, J., Ai, H., & Tu, P. (2005). A low-temperature synthesis of multiwhisker-based zinc oxide micron crystals. *Materials Letters*, *59*(28), 3710–3714. https://doi.org/10.1016/j.matlet.2005.06.043

Liu, Jinping, Huang, X., Li, Y., Sulieman, K. M., Sun, F., & He, X. (2006). Selective growth and properties of zinc oxide nanostructures. *Scripta Materialia*, *55*(9), 795–798. https://doi.org/10.1016/j.scriptamat.2006.07.010

Liu, Q., Ma, D., Hu, Y., Zeng, Y., & Huang, S. (2013). Various Bismuth Oxyiodide Hierarchical

Architectures : Alcohothermal-Controlled Synthesis , Photocatalytic Activities , and Adsorption Capabilities for Phosphate in Water. *Applied Materials and Interfaces*, *3*, 3–10. https://doi.org/10.1021/am4036702

Liu, W., Wang, M., Xu, C., & Chen, S. (2012). Facile synthesis of g-C3N4/ZnO composite with enhanced visible light photooxidation and photoreduction properties. *Chemical Engineering Journal*, *209*, 386–393. https://doi.org/10.1016/j.cej.2012.08.033

Lizama, C., Freer, J., Baeza, J., & Mansilla, H. D. (2002). Optimized photodegradation of Reactive Blue 19 on TiO 2 and ZnO suspensions. *Catalysis Today, 76,* 235–246.

Lo, T. (2006). Cationic and Anionic Poly (N -isopropylacrylamide) Based Submicron Gel Particles : Electrokinetic Properties and Colloidal Stability. *Journal of Physical Chemistry B*, 4629–4636. https://doi.org/10.1021/jp0540508

Look, D. C. (2001). Recent advances in ZnO materials and devices. *Materials Science and Engineering B, 80,* 383–387.

Lu, Y., Lin, Y., Wang, D., Wang, L., Xie, T., & Jiang, T. (2011). A High Performance Cobalt-Doped ZnO Visible Light Photocatalyst and Its Photogenerated Charge Transfer Properties. *Nano Research*, *4*(11), 1144–1152. https://doi.org/10.1007/s12274-011-0163-4

Lu, Y., Wang, L., Wang, D., Xie, T., Chen, L., & Lin, Y. (2011). A comparative study on plate-like and flower-like ZnO nanocrystals surface photovoltage property and photocatalytic activity. *Materials Chemistry and Physics*, *129*(1–2), 281–287. https://doi.org/10.1016/j.matchemphys.2011.04.004

Lv, C., Chen, G., Zhou, X., Zhang, C., Wang, Z., Zhao, B., & Li, D. (2017). Oxygen-Induced

Bi5+-Self-Doped Bi4V2O11 with a p-n Homojunction Toward Promoting the Photocatalytic Performance. *ACS Applied Materials and Interfaces*, *9*(28), 23748–23755. https://doi.org/10.1021/acsami.7b05302

Mahdavi, R., & Ashraf Talesh, S. S. (2017). The effect of ultrasonic irradiation on the structure, morphology and photocatalytic performance of ZnO nanoparticles by sol-gel method. *Ultrasonics Sonochemistry*, *39*(May), 504–510. https://doi.org/10.1016/j.ultsonch.2017.05.012

Mai, F. D., Chen, C. C., Chen, J. L., & Liu, S. C. (2008). Photodegradation of methyl green using visible irradiation in ZnO suspensions. Determination of the reaction pathway and identification of intermediates by a high-performance liquid chromatography-photodiode array-electrospray ionization-mass spectrometry. *Journal of Chromatography A*, *1189*(1–2), 355–365. https://doi.org/10.1016/j.chroma.2008.01.027

Mai, F. D., Lu, C. S., Wu, C. W., Huang, C. H., Chen, J. Y., & Chen, C. C. (2008). Mechanisms of photocatalytic degradation of Victoria Blue R using nano-TiO 2. *Separation and Purification Technology*, *62*, 423–436. https://doi.org/10.1016/j.seppur.2008.02.006

Mauro, A. Di, Fragalà, M. E., Privitera, V., & Impellizzeri, G. (2017). ZnO for application in photocatalysis: From thin films to nanostructures. *Materials Science in Semiconductor Processing*, *69*(July 2016), 44–51. https://doi.org/10.1016/j.mssp.2017.03.029

Mclaren, A., Valdes-Solis, T., Li, G., & Tsang, S. C. (2009). Shape and Size Effects of ZnO Nanocrystals on Photocatalytic Activity. *Journal of the American Chemical Society*, *001*, 12540–12541. https://doi.org/doi:10.1021/ja9052703

Mehrjouei, M., Müller, S., & Möller, D. (2015). A review on photocatalytic ozonation used for the treatment of water and wastewater. *Chemical Engineering Journal*, *263*, 209–219. https://doi.org/10.1016/j.cej.2014.10.112

Mekasuwandumrong, O., Pawinrat, P., Praserthdam, P., & Panpranot, J. (2010). Effects of synthesis conditions and annealing post-treatment on the photocatalytic activities of ZnO nanoparticles in the degradation of methylene blue dye. *Chemical Engineering Journal*, *164*(1), 77–84. https://doi.org/10.1016/j.cej.2010.08.027

Mi, Y., Wen, L., & Zhao, H. (2014). A highly efficient visible-light driven photocatalyst Two dimensional square-like bismuth oxyiodine nanosheets. *Dalton Transactions*, *43*(25). https://doi.org/10.1039/c4dt00798k

Mijin, D., Savić, M., Snežana, P., Smiljanić, A., Glavaški, O., Jovanović, M., & Petrović, S. (2009). A study of the photocatalytic degradation of metamitron in ZnO water suspensions. *Desalination*, *249*(1), 286–292. https://doi.org/10.1016/j.desal.2008.10.030

Moafi, H. F., Zanjanchi, M. A., & Shojaie, A. F. (2013). Tungsten-doped ZnO nanocomposite: Synthesis, characterization, and highly active photocatalyst toward dye photodegradation. *Materials Chemistry and Physics*, *139*(2–3), 856–864. https://doi.org/10.1016/j.matchemphys.2013.02.044

Mondal, K., & Sharma, A. (2016). Photocatalytic Oxidation of Pollutant Dyes in Wastewater by TiO 2 and ZnO nano-materials – A Mini-review. *Indian Institute of Tecnology*, *January 2015*, 36–72.

Natkritta, N., Channei, D., Inceesungvorn, B., & Zhao, C. (2018). Visible Light-Driven

BiOI/ZnO Photocatalyst Films and Its Photodegradation of Methomyl Insecticide. *KMUTNB International Journal of Applied Science and Technology*, *11*(4), 297–304. https://doi.org/10.14416/j.ijast.2018.08.003

Naveed Ul Haq, A., Nadhman, A., Ullah, I., Mustafa, G., Yasinzai, M., & Khan, I. (2017). Synthesis Approaches of Zinc Oxide Nanoparticles: The Dilemma of Ecotoxicity. *Journal of Nanomaterials*, *2017*(Table 1). https://doi.org/10.1155/2017/8510342

Neppolian, B., Choi, H. C., Sakthivel, S., Arabindoo, B., & Murugesan, V. (2002). Solar/UV-induced photocatalytic degradation of three commercial textile dyes. *Journal of Hazardous Materials*, *89*(2–3), 303–317. https://doi.org/10.1016/S0304-3894(01)00329-6

Nguyen Thi Thu, T., Nguyen Thi, N., Tran Quang, V., Nguyen Hong, K., Nguyen Minh, T., & Le Thi Hoai, N. (2016). Synthesis, characterisation, and effect of pH on degradation of dyes of copper-doped TiO2. *Journal of Experimental Nanoscience*, *11*(3), 226–238. https://doi.org/10.1080/17458080.2015.1053541

Nikoobakht, B., Wang, X., Herzing, A., & Shi, J. (2013). Scalable synthesis and device integration of self-registered one-dimensional zinc oxide nanostructures and related materials. *Chemical Society Reviews*, *42*(1), 342–365. https://doi.org/10.1039/C2CS35164A

Nollet, H., Roels, M., Lutgen, P., Meeren, P. Van Der, & Verstraete, W. (2003). Removal of PCBs from wastewater using fly ash. *Chemosphere*, *53*, 655–665. https://doi.org/10.1016/S0045-6535(03)00517-4

Ohtani, B. (2013). Titania Photocatalysis beyond Recombination: A Critical Review. *Catalysts*, *3*(4), 942–953. https://doi.org/10.3390/catal3040942

Okte, A. N., Resat, M. S., & Inel, Y. (2001). Photocatalytic Degradation of 1, 3-Dihydroxy-5-methoxybenzene in Aqueous Suspensions of TiO2: An Initial Kinetic Study. *Journal of Catalysis*, *198*(2), 172–178. https://doi.org/10.1006/jcat.2000.3091

Ong, C. B., Ng, L. Y., & Mohammad, A. W. (2018). A review of ZnO nanoparticles as solar photocatalysts: Synthesis, mechanisms and applications. *Renewable and Sustainable Energy Reviews*, *81*(August 2017), 536–551. https://doi.org/10.1016/j.rser.2017.08.020

Pandurangan, A., Kamala, P., Uma, S., Palanichamy, M., & Murugesan, V. (2001). Degradation of basic yellow auramine O-A textile dye by semiconductor photocatalysis. *Indian Journal of Chemical Technology*, *8*(6), 496–499.

Pardeshi, S. K., & Patil, A. B. (2009). Effect of morphology and crystallite size on solar photocatalytic activity of zinc oxide synthesized by solution free mechanochemical method. *Journal of Molecular Catalysis A: Chemical*, *308*(1–2), 32–40. https://doi.org/10.1016/j.molcata.2009.03.023

Peirò, P. R. G. M. J. M. (1999). Nanostructred Metal Oxides Supported on Stainless Steel Wire Meshes: Versatile Monolithic Catalysts for Environmental and Energy Applications. *Psicothema*, *11*(003), 679–689.

Pelizzetti, E., & Minero, C. (1994). Metal Oxides as Photocatalysts for Environmental Detoxification. *Comments on Inorganic Chemistry*, *15*(5–6), 297–337. https://doi.org/10.1080/02603599408035846

Pierre, A. C. (1998). Phase Transformations. In *Introduction to Sol-Gel Processing* (pp. 279–308). Springer US. https://doi.org/10.1007/978-1-4615-5659-6_7

Pirhashemi, M., Habibi-Yangjeh, A., & Rahim Pouran, S. (2018). Review on the criteria anticipated for the fabrication of highly efficient ZnO-based visible-light-driven photocatalysts. *Journal of Industrial and Engineering Chemistry*, *62*, 1–25. https://doi.org/10.1016/j.jiec.2018.01.012

Polshettiwar, V., Baruwati, B., & Varma, R. S. (2009). Self-Assembly of Metal Oxides into Synthesis and Application in Catalysis. *ACS Nano*, *3*(3), 728–736. https://doi.org/10.1021/nn800903p

Potti, P. R., & Srivastava, V. C. (2012). Comparative studies on structural, optical, and textural properties of combustion derived ZnO prepared using various fuels and their photocatalytic activity. *Industrial and Engineering Chemistry Research*, *51*(23), 7948–7956. https://doi.org/10.1021/ie300478y

Poulios, I., & Aetopoulou, I. (2017). Photocatalytic Degradation of the Textile Dye Reactive Orange 16 in the Presence of TiO2 Suspensions. *Environmental Technology*, *3330*(November). https://doi.org/10.1080/09593332008616843

Pouretedal, H. R., Norozi, A., Keshavarz, M. H., & Semnani, A. (2009). Nanoparticles of zinc sulfide doped with manganese, nickel and copper as nanophotocatalyst in the degradation of organic dyes. *Journal of Hazardous Materials*, *162*(2–3), 674–681. https://doi.org/10.1016/j.jhazmat.2008.05.128

Prasada Rao, T., & C. Santhosh Kumar, M. (2012). Resistivity Stability of Ga Doped ZnO Thin Films with Heat Treatment in Air and Oxygen Atmospheres. *Journal of Crystallization Process and Technology*, *02*(02), 72–79. https://doi.org/10.4236/jcpt.2012.22010

Putri, A. A., Kato, S., Kishi, N., & Soga, T. (2019). Study of annealing temperature effect on the photovoltaic performance of BiOI-based materials. *Applied Sciences (Switzerland)*, *9*(16). https://doi.org/10.3390/app9163342

Qi, K., Cheng, B., Yu, J., & Ho, W. (2017). Review on the improvement of the photocatalytic and antibacterial activities of ZnO. *Journal of Alloys and Compounds*, *727*, 792–820. https://doi.org/10.1016/j.jallcom.2017.08.142

Qu, Z., Su, Y., Sun, L., Liang, F., & Zhang, G. (2020). Study of the structure, electronic and optical properties of BiOI/Rutile-TiO2 heterojunction by the first-principle calculation. *Materials*, *13*(2). https://doi.org/10.3390/ma13020323

Rajabi, Z., Moghadassi, A. R., Hosseini, S. M., & Mohammadi, M. (2013). Preparation and characterization of polyvinylchloride based mixed matrix membrane filled with multi walled carbon nano tubes for carbon dioxide separation. *Journal of Industrial and Engineering Chemistry*, *19*(1), 347–352. https://doi.org/10.1016/j.jiec.2012.08.023

Rajamanickam, D., & Shanthi, M. (2016). Photocatalytic degradation of an organic pollutant by zinc oxide – solar process. *Arabian Journal of Chemistry*, *9*, S1858–S1868. https://doi.org/10.1016/j.arabjc.2012.05.006

Raji, R., Sibi, K. S., & Gopchandran, K. G. (2018). Applied Surface Science ZnO : Ag nanorods as efficient photocatalysts : Sunlight driven photocatalytic degradation of sulforhodamine B. *Applied Surface Science*, *427*, 863–875. https://doi.org/10.1016/j.apsusc.2017.09.050

Raveendran, P., Fu, J., Wallen, S. L., Hill, C., & Carolina, N. (2003). Completely " Green " Synthesis and Stabilization of Metal Nanoparticles. *Journal of the American Chemical*

Society, 13940–13941. https://doi.org/10.1021/ja029267j

Reddy, K. H., Martha, S., & Parida, K. M. (2013). Fabrication of Novel p - BiOI / n-ZnTiO 3 Heterojunction for Degradation of Rhodamine 6G under Visible Light Irradiation. *Inorganic Chemistry*, *52*, 6390−6401. https://doi.org/10.1021/ic400159m

Rehman, S., Ullah, R., Butt, A. M., & Gohar, N. D. (2009). Strategies of making TiO2 and ZnO visible light active. *Journal of Hazardous Materials*, *170*(2–3), 560–569. https://doi.org/10.1016/j.jhazmat.2009.05.064

Rezaei, M & Habibi-Yangjeh, A. (2013). Simple and large scale refluxing method for preparation of Ce-doped ZnO nanostructures as highly efficient photocatalyst. *Applied Surface Science*, *265*, 591–596. https://doi.org/10.1016/j.apsusc.2012.11.053

Rudd, A. L., & Breslin, C. B. (2000). Photo-induced dissolution of zinc in alkaline solutions. *Electrochimica Acta*, *45*(10), 1571–1579. https://doi.org/10.1016/S0013-4686(99)00322-9

Safe, S. (1992). Toxicology , Structure-Function Relation- ship , and Human and Environmental Health Impacts of Polychlorinated Biphenyls : Progress and Problems by Stephen Safe. *Environmental Health Perspectives*, *100*, 259–268.

Sakthivel, S., Neppolian, B., Shankar, M. V., Arabindoo, B., Palanichamy, M., & Murugesan, V. (2003). Solar photocatalytic degradation of azo dye: Comparison of photocatalytic efficiency of ZnO and TiO2. *Solar Energy Materials and Solar Cells*, *77*(1), 65–82. https://doi.org/10.1016/S0927-0248(02)00255-6

Salem, M. A., Shaban, S. Y., & Ismail, S. M. (2015). Photocatalytic Degradation of Acid Green 25 using ZnO and Natural Sunlight Photocatalytic Degradation of Acid Green 25 using ZnO and Natural Sunlight. *International Journal of Emerging Technology and Advanced Engineering*, *March*, 1–5.

Samadi, M., Shivaee, H. A., Pourjavadi, A., & Moshfegh, A. Z. (2013). Synergism of oxygen vacancy and carbonaceous species on enhanced photocatalytic activity of electrospun ZnO-carbon nanofibers: Charge carrier scavengers mechanism. *Applied Catalysis A: General*, *466*, 153–160. https://doi.org/10.1016/j.apcata.2013.06.024

Samadi, M., Zirak, M., Naseri, A., Khorashadizade, E., & Moshfegh, A. Z. (2015). Recent progress on doped ZnO nanostructures for visible-light photocatalysis. *Thin Solid Films*, *605*, 2–19. https://doi.org/10.1016/j.tsf.2015.12.064

Sapkal, R. T., Shinde, S. S., Waghmode, T. R., Govindwar, S. P., Rajpure, K. Y., & Bhosale, C. H. (2012). Photo-corrosion inhibition and photoactivity enhancement with tailored zinc oxide thin films. *Journal of Photochemistry & Photobiology, B: Biology*, *110*, 15–21. https://doi.org/10.1016/j.jphotobiol.2012.02.004

Sathishkumar, P., Sweena, R., Wu, J. J., & Anandan, S. (2011). Synthesis of CuO-ZnO nanophotocatalyst for visible light assisted degradation of a textile dye in aqueous solution. *Chemical Engineering Journal*, *171*(1), 136–140. https://doi.org/10.1016/j.cej.2011.03.074

Schneider, J., Matsuoka, M., Takeuchi, M., Zhang, J., Horiuchi, Y., Anpo, M., & Bahnemann, D. W. (2014). Understanding TiO 2 Photocatalysis : Mechanisms and Materials. *Chemical Reviews*, *114*, 9919–9986. https://doi.org/10.1021/cr5001892

Scuderi, V., Impellizzeri, G., Romano, L., Scuderi, M., Brundo, M. V., Bergum, K., Zimbone, M., Sanz, R., Buccheri, M. A., Simone, F., Nicotra, G., Svensson, B. G., Grimaldi, M. G., &

Privitera, V. (2014). An enhanced photocatalytic response of nanometric TiO2wrapping of Au nanoparticles for eco-friendly water applications. *Nanoscale*, *6*(19), 11189–11195. https://doi.org/10.1039/c4nr02820a

Shafaei, A., Nikazar, M., & Arami, M. (2010). Photocatalytic degradation of terephthalic acid using titania and zinc oxide photocatalysts: Comparative study. *Desalination*, *252*(1–3), 8–16. https://doi.org/10.1016/j.desal.2009.11.008

Sharma, A., Rao, P., Mathur, R. P., & Ameta, S. C. (1995). Photocatalytic reactions of xylidine ponceau on semiconducting zinc oxide powder. *Journal of Photochemistry and Photobiology, A: Chemistry*, *86*(1–3), 197–200. https://doi.org/10.1016/1010-6030(94)03933-L

Singh, S., Srivastava, V. C., & Lo, S. L. (2016). Surface modification or doping of WO3 for enhancing the photocatalytic degradation of organic pollutant containing wastewaters: A review. In *Materials Science Forum* (Vol. 855, pp. 105–126). https://doi.org/10.4028/www.scientific.net/MSF.855.105

Sirelkhatim, A., Mahmud, S., & Seeni, A. (2015). Review on Zinc Oxide Nanoparticles : Antibacterial Activity and Toxicity Mechanism. *Nano-Micro Letters*, *7*, 219–242. https://doi.org/10.1007/s40820-015-0040-x

Sobana, N., & Swaminathan, M. (2007). The effect of operational parameters on the photocatalytic degradation of acid red 18 by ZnO. *Separation and Purification Technology*, *56*(1), 101–107. https://doi.org/10.1016/j.seppur.2007.01.032

Štengl, V., Henych, J., Slušná, M., Tolasz, J., & Zetková, K. (2015). ZnO/Bi2O3nanowire composites as a new family of photocatalysts. *Powder Technology*, *270*(Part A), 83–91. https://doi.org/10.1016/j.powtec.2014.09.047

Štrbac, D., Aggelopoulos, C. A., Štrbac, G., Dimitropoulos, M., Novaković, M., Ivetić, T., & Yannopoulos, S. N. (2018). Photocatalytic degradation of Naproxen and methylene blue: Comparison between ZnO, TiO2and their mixture. *Process Safety and Environmental Protection*, *113*, 174–183. https://doi.org/10.1016/j.psep.2017.10.007

Swaminathan, M., Manickavachagam, M., & Sillanpaa, M. (2014). Advanced oxidation processes for wastewater treatment 2013. *International Journal of Photoenergy*, *2014*(February). https://doi.org/10.1155/2015/363167

Taylor, P., Lam, S., Sin, J., Abdullah, A. Z., & Mohamed, A. R. (2012). Degradation of wastewaters containing organic dyes photocatalysed by zinc oxide : a review. *Desalination and Water Treatment*, *May 2013*, 37–41. https://doi.org/10.1080/19443994.2012.664698

Tehrani, F. S., Ahmadian, H., & Aliannezhadi, M. (2020). Hydrothermal synthesis and characterization of WO3 nanostructures: Effect of reaction time. *Materials Research Express*, *7*(1). https://doi.org/10.1088/2053-1591/ab66fc

Thein, M. T., Chim, J. E., Pung, S. Y., & Pung, Y. F. (2017). Highly UV light driven WOx@ZnO nanocomposites synthesized by liquid impregnation method. *Journal of Industrial and Engineering Chemistry*, *46*, 119–129. https://doi.org/10.1016/j.jiec.2016.10.022

Thejaswini, T. V. L., Prabhakaran, D., & Maheswari, M. A. (2017). Ultrasound assisted synthesis of nano-rod embedded petal designed α-Bi2O3-ZnO nanoparticles and their ultra-responsive visible light induced photocatalytic properties. *Journal of Photochemistry and Photobiology A: Chemistry*, *335*, 217–229. https://doi.org/10.1016/j.jphotochem.2016.12.001

Thennarasu, G., & Sivasamy, A. (2013). Metal ion doped semiconductor metal oxide nanosphere particles prepared by soft chemical method and its visible light photocatalytic activity in degradation of phenol. *Powder Technology*, *250*, 1–12. https://doi.org/10.1016/j.powtec.2013.08.004

Tian, C., Zhang, Q., Wu, A., Jiang, M., Liang, Z., Jiang, B., & Fu, H. (2012). Cost-effective large-scale synthesis of ZnO photocatalyst with excellent performance for dye photodegradation. *Chemical Communications*, *48*(23), 2858–2860. https://doi.org/10.1039/c2cc16434e

Tijani, J. O., Fatoba, O. O., Madzivire, G., & Petrik, L. F. (2014). A review of combined advanced oxidation technologies for the removal of organic pollutants from water. *Water, Air, and Soil Pollution*, *225*(9). https://doi.org/10.1007/s11270-014-2102-y

Tolosa, N. C., Lu, M.-C., Mendoza, H. D., & Rollon, A. P. (2011). Factors affecting the photocatalytic oxidation of 2,4 dichlorophenol using modified titanium dioxide catalyst under visible light. *Sustainable Environmental Research*, *21*(6), 381–387.

Ushio, M., & Sumiyoshi, Y. (1993). Synthesis of ZnO single crystals by the flux method. *Journal Of Materials Science*, *28*, 218–224. https://doi.org/10.1007%2FBF00349054

Vahtrus, M., Andris, Š., Polyakov, B., Oras, S., Antsov, M., Doebelin, N., Lõhmus, R., Nõmmiste, E., & Vlassov, S. (2016). Effect of cobalt doping on the mechanical properties of ZnO nanowires. *Materials Characterization*, *121*, 40–47. https://doi.org/10.1016/j.matchar.2016.09.027

Vempati, S., Chirakkara, S., Mitra, J., Dawson, P., Nanda, K. K., & Krupanidhi, S. B. (2012). Unusual photoresponse of indium doped ZnO / organic thin film heterojunction Unusual photoresponse of indium doped ZnO / organic thin film heterojunction. *Applied Physics Letters*, *162104*(100). https://doi.org/10.1063/1.4704655

Vinita, M., Praveena Juliya Dorathi, R., & Palanivelu, K. (2010). Degradation of 2,4,6-trichlorophenol by photo Fenton's like method using nano heterogeneous catalytic ferric ion. *Solar Energy*, *84*(9), 1613–1618. https://doi.org/10.1016/j.solener.2010.06.008

Vinu, R., & Madras, G. (2011). Photocatalytic Degradation of water pollutants using nano-TiO2. In *Energy Efficiency and Renewable Energy Through Nanotechnology, Green Energy and Technology* (pp. 627–677). Springer-Verlag London Limited 2011. https://doi.org/10.1007/978-0-85729-638-2-19

Vu, T. T., del Río, L., Valdés-Solís, T., & Marbán, G. (2013). Fabrication of wire mesh-supported ZnO photocatalysts protected against photocorrosion. *Applied Catalysis B: Environmental*, *140–141*, 189–198. https://doi.org/10.1016/j.apcatb.2013.04.023

Wahab, R., Ansari, S. G., Kim, Y. S., Seo, H. K., & Shin, H. S. (2007). Room temperature synthesis of needle-shaped ZnO nanorods via sonochemical method. *Applied Surface Science*, *253*(18), 7622–7626. https://doi.org/10.1016/j.apsusc.2007.03.060

Wan, L., Yan, S., Feng, J., Yang, Z., Fan, X., Li, Z., & Zou, Z. (2012). Solvothermal synthesis of core-shell ZnO hollow microhemispheres. *Colloids and Surfaces A: Physicochemical and*

Engineering Aspects, *396*, 46–50. https://doi.org/10.1016/j.colsurfa.2011.12.039

Wang, Fangxiao, Liang, L., Shi, L., & Sun, J. (2014). CO2-assisted synthesis of mesoporous carbon/C-doped ZnO composites for enhanced photocatalytic performance under visible light. *Dalton Transactions*, *43*, 16441–16449. https://doi.org/10.1039/c4dt02098g

Wang, Feng, Qin, X., Guo, Z., Meng, Y., Yang, L., & Ming, Y. (2013). Hydrothermal synthesis of dumbbell-shaped ZnO microstructures. *Ceramics International*, *39*(8), 8969–8973. https://doi.org/10.1016/j.ceramint.2013.04.096

Wang, Huanli, Zhang, L., Chen, Z., Hu, J., Li, S., Wang, Z., Liu, J., & Wang, X. (2014). Semiconductor heterojunction photocatalysts: design, construction, and photocatalytic performances. *Chemical Society Reviews*, *43*(15), 5234–5244. https://doi.org/10.1039/c4cs00126e

Wang, Huihu, Xie, C., Zhang, W., Cai, S., Yang, Z., & Gui, Y. (2007). Comparison of dye degradation efficiency using ZnO powders with various size scales. *Journal of Hazardous Materials*, *141*, 645–652. https://doi.org/10.1016/j.jhazmat.2006.07.021

Wang, J., Xia, Y., Zhao, H., Wang, G., Xiang, L., Xu, J., & Komarneni, S. (2017). Oxygen defects-mediated Z-scheme charge separation in g-C3N4/ZnO photocatalysts for enhanced visible-light degradation of 4-chlorophenol and hydrogen evolution. *Applied Catalysis B: Environmental*, *206*, 406–416. https://doi.org/10.1016/j.apcatb.2017.01.067

Wang, K., Shao, C., Li, X., Miao, F., Lu, N., & Liu, Y. (2016). Heterojunctions of p-BiOI Nanosheets/n-TiO2 Nanofibers: Preparation and Enhanced Visible-Light Photocatalytic Activity. *Materials*, *9*(2), 1–12. https://doi.org/10.3390/ma9020090

Wang, R., Xin, J. H., Yang, Y., Liu, H., Xu, L., & Hu, J. (2004). The characteristics and photocatalytic activities of silver doped ZnO nanocrystallites. In *Applied Surface Science* (Vol. 227, Issues 1–4, pp. 312–317). https://doi.org/10.1016/j.apsusc.2003.12.012

Wang, W., Huang, F., Lin, X., & Yang, J. (2008). Visible-light-responsive photocatalysts x BiOBr –(1 À x) BiOI. *Catalysis Communications, 9*, 8–12. https://doi.org/10.1016/j.catcom.2007.05.014

Wang, X., Summers, C. J., & Wang, Z. L. (2004). Large-scale hexagonal-patterned growth of aligned ZnO nanorods for nano-optoelectronics and nanosensor arrays. *Nano Letters*, *4*(3), 423–426. https://doi.org/10.1021/nl035102c

Wang, Yongbing, & Hong, C. S. (2000). TiO2-mediated photomineralization of 2-chlorobiphenyl: The role of O2. *Water Research*, *34*(10), 2791–2797. https://doi.org/10.1016/S0043-1354(00)00009-9

Wang, Yu, Zhou, D., Wang, Y., Zhu, X., & Jin, S. (2011). Humic acid and metal ions accelerating the dechlorination of 4-chlorobiphenyl by nanoscale zero-valent iron. *Journal of Environmental Sciences*, *23*(8), 1286–1292. https://doi.org/10.1016/S1001-0742(10)60543-8

Wang, Z. L. (2004). Nanostructures of zinc oxide. *Materials Today*, *7*(6), 26–33. https://doi.org/10.1016/S1369-7021(04)00286-X

Wang, Z. L. (2008). Splendid one-dimensional nanostructures of zinc oxide: A new nanomaterial family for nanotechnology. *ACS Nano*, *2*(10), 1987–1992. https://doi.org/10.1021/nn800631r

Weber, R., Takasuga, T., Nagai, K., Shiraishi, H., Sakurai, T., Matuda, T., & Hiraoka, M. (2002). Dechlorination and destruction of PCDD, PCDF and PCB on selected fly ash from municipal waste incineration. *Chemosphere*, *46*(9–10), 1255–1262. https://doi.org/10.1016/S0045-6535(01)00268-5

Wen, J., Li, X., Liu, W., Fang, Y., Xie, J., & Xu, Y. (2015). Photocatalysis fundamentals and surface modification of TiO 2 nanomaterials. *Chinese Journal of Catalysis*, *36*(12), 2049–2070. https://doi.org/10.1016/S1872-2067(15)60999-8

Wen, X. J., Niu, C. G., Zhang, L., & Zeng, G. M. (2017). Novel p-n heterojunction BiOI/CeO2 photocatalyst for wider spectrum visible-light photocatalytic degradation of refractory pollutants. *Dalton Transactions*, *46*(15), 4982–4993. https://doi.org/10.1039/c7dt00106a

Wicaksana, Y., Liu, S., Scott, J., & Amal, R. (2014). Tungsten trioxide as a visible light photocatalyst for volatile organic carbon removal. In *Molecules* (Vol. 19, Issue 11, pp. 17747–17762). https://doi.org/10.3390/molecules191117747

Wu, C., Shen, L., Zhang, Y., & Huang, Q. (2011). Solvothermal synthesis of Cr-doped ZnO nanowires with visible light-driven photocatalytic activity. *Materials Letters*, *65*(12), 1794–1796. https://doi.org/10.1016/j.matlet.2011.03.070

Wu, H. C., Li, S. H., & Lin, S. W. (2012). Effect of Fe concentration on Fe-doped anatase TiO 2 from GGA + U calculations. *International Journal of Photoenergy*, *2012*. https://doi.org/10.1155/2012/823498

Wu, J. J., Liu, S. C., Wu, C. T., Chen, K. H., & Chen, L. C. (2002). Heterostructures of ZnO-Zn coaxial nanocables and ZnO nanotubes. *Applied Physics Letters*, *81*(7), 1312–1314.

https://doi.org/10.1063/1.1499512

Wu, W., Xu, J., Zhao, H., Zhang, Q., & Liao, S. (2005). A practical approach to the degradation of polychlorinated biphenyls in transformer oil. *Chemosphere*, *60*(7), 944–950. https://doi.org/10.1016/j.chemosphere.2004.11.079

Xiao, J., Xie, Y., & Cao, H. (2015). Organic pollutants removal in wastewater by heterogeneous photocatalytic ozonation. *Chemosphere*, *121*(November 2017), 1–17. https://doi.org/10.1016/j.chemosphere.2014.10.072

Xie, Q., Dai, Z., Liang, J., Xu, L., Yu, W., & Qian, Y. (2005). Synthesis of ZnO three-dimensional architectures and their optical properties. *Solid State Communications*, *136*(5), 304–307. https://doi.org/10.1016/j.ssc.2005.07.023

Xiong, G., Solar, F., & Pal, U. (2007). Correlations among size , defects , and photoluminescence in ZnO nanoparticles. *Journal of Applied Physics*. https://doi.org/10.1063/1.2424538

Xu H, Xu T, Zhu S, Z. Y. (2008). Photocorrosion Inhibition and Enhancement of Photocatalytic Activity for ZnO via Hybridization with C 60. *Environmental Science & Technology*, *42*(21), 8064–8069. https://doi.org/10.1021/es801484x

Yan, H., Wang, X., Yao, M., & Yao, X. (2013). Band structure design of semiconductors for enhanced photocatalytic activity: The case of TiO2. *Progress in Natural Science: Materials International*, *23*(4), 402–407. https://doi.org/10.1016/j.pnsc.2013.06.002

Yang, B., Wang, S., Yu, G., & Zhou, Y. (2008). Electrocatalytic reduction of 2-chlorobiphenyl in contaminated water using palladium-modified electrode. *Separation and Purification*

Technology, *63*, 353–359. https://doi.org/10.1016/j.seppur.2008.05.025

Yang, L. L. (2010). Synthesis and characterization of ZnO nanostructures. In *Physica Scripta* (Vol. T126, Issue 1327). https://doi.org/10.1088/0031-8949/2006/T126/029

Yang Y, Li Y, Zhu Li, He H, Hu L, Huang J, Hu F, He B, Y. Z. (2013). Shape control of colloidal Mn doped ZnO nanocrystals and their visible light photocatalytic properties †. *Nanoscale*, 10461–10471. https://doi.org/10.1039/c3nr03160h

Yoon, H. J., Choi, Y. I., Jang, E. S., & Sohn, Y. (2015). Graphene, charcoal, ZnO, and ZnS/BiOX (X = Cl, Br, and I) hybrid microspheres for photocatalytic simulated real mixed dye treatments. *Journal of Industrial and Engineering Chemistry*, *32*, 137–152. https://doi.org/10.1016/j.jiec.2015.08.010

Yu, C., Yang, K., Shu, Q., Yu, J. C., Cao, F., & Li, X. (2011). Preparation of WO3/ZnO Composite Photocatalyst and Its Photocatalytic Performance. *Chinese Journal of Catalysis*, *32*(3–4), 555–565. https://doi.org/10.1016/s1872-2067(10)60212-4

Yu, L., Chen, W., Li, D., Wang, J., Shao, Y., He, M., Wang, P., & Zheng, X. (2015). Inhibition of photocorrosion and photoactivity enhancement for ZnO via specific hollow ZnO core / ZnS shell structure. *Applied Catalysis B, Environmental*, *164*, 453–461. https://doi.org/10.1016/j.apcatb.2014.09.055

Yue, S., Lu, J., & Zhang, J. (2009). Controlled growth of well-aligned hierarchical ZnO arrays by a wet chemical method. *Materials Letters*, *63*(24–25), 2149–2152. https://doi.org/10.1016/j.matlet.2009.06.055

Yuhas, B. D., Zitoun, D. O., Pauzauskie, P. J., He, R., & Yang, P. (2006). Transition-Metal

Doped Zinc Oxide Nanowires. *Angewandte Chemie International Edition*, *45*, 420–423. https://doi.org/10.1002/anie.200503172

Yusoff, M. A., Imam, S. S., Shah, I., & Adnan, R. (2019). Photocatalytic activity of bismuth oxyiodide nanospheres and nanoplates. *Materials Research Express*, *6*(8). https://doi.org/10.1088/2053-1591/ab2918

Zangeneh, H., Zinatizadeh, A. A. L., Habibi, M., Akia, M., & Hasnain Isa, M. (2015). Photocatalytic oxidation of organic dyes and pollutants in wastewater using different modified titanium dioxides: A comparative review. *Journal of Industrial and Engineering Chemistry*, *26*, 1–36. https://doi.org/10.1016/j.jiec.2014.10.043

Zelmanov, G., & Semiat, R. (2008). Phenol oxidation kinetics in water solution using iron(3)-oxide-based nano-catalysts. *Water Research*, *42*(14), 3848–3856. https://doi.org/10.1016/j.watres.2008.05.009

Zhang, C., Fei, W., Wang, H., Li, N., Chen, D., Xu, Q., Li, H., He, J., & Lu, J. (2020). p-n Heterojunction of BiOI/ZnO nanorod arrays for piezo-photocatalytic degradation of bisphenol A in water. *Journal of Hazardous Materials*, *399*(May), 123109. https://doi.org/10.1016/j.jhazmat.2020.123109

Zhang, J., Shi, F., Lin, J., Chen, D., Gao, J., Huang, Z., Ding, X., & Tang, C. (2008). Self-Assembled 3-D Architectures of BiOBr as a Visible Light-Driven Photocatalyst. *Chemical Materials*, *20*(9), 2937–2941. https://doi.org/10.1021/cm7031898

Zhang, K. H. L., Wu, R., Tang, F., Li, W., Oropeza, F. E., Qiao, L., Lazarov, V. K., Du, Y., Payne, D. J., Macmanus-Driscoll, J. L., & Blamire, M. G. (2017). Electronic Structure and

Band Alignment at the NiO and SrTiO3 p-n Heterojunctions. *ACS Applied Materials and Interfaces*, *9*(31), 26549–26555. https://doi.org/10.1021/acsami.7b06025

Zhang, K., Liu, C., Huang, F., Zheng, C., & Wang, W. (2006). Study of the electronic structure and photocatalytic activity of the BiOCl photocatalyst. *Applied Catalysis B: Environmental*, *68*(3–4), 125–129. https://doi.org/10.1016/j.apcatb.2006.08.002

Zhang, L., Du, L., Yu, X., Tan, S., Cai, X., Yang, P., Gu, Y., & Mai, W. (2014). Significantly enhanced photocatalytic activities and charge separation mechanism of Pd-decorated ZnO-graphene oxide nanocomposites. *ACS Applied Materials and Interfaces*, *6*(5), 3623–3629. https://doi.org/10.1021/am405872r

Zhang, M., Qin, J., Yu, P., Zhang, B., & Ma, M. (2018). Facile synthesis of a ZnO – BiOI p – n nano-heterojunction with excellent visible-light photocatalytic activity. *Beilstein Journal of Nanotechnology*, *9*, 789–800. https://doi.org/10.3762/bjnano.9.72

Zhang, P., Scrudato, R. J., Pagano, J. J., & Roberts, R. N. (1993). Photodecomposition of PCBs in aqueous systems using TiO2 as catalyst. *Chemosphere*, *26*(6), 1213–1223. https://doi.org/doi.org/10.1016/0045-6535(93)90207-L

Zhang, W., Yu, T., Han, X., & Ying, W. (2016). Removal of 2-ClBP from soil–water system using activatedcarbon supported nanoscale zerovalent iron. *Journal of Environmental Sciences*, *47*, 143–152. https://doi.org/10.1016/j.jes.2015.12.032

Zhang, Xi, Zhang, L., Xie, T., & Wang, D. (2009). Low-Temperature Synthesis and High Visible-Light-Induced Photocatalytic Activity of BiOI / TiO 2 Heterostructures. *Journal of Physical Chemistry*, 7371–7378. https://doi.org/10.1021/jp900812d

Zhang, Xianghui, Lu, X., Shen, Y., Han, J., Yuan, L., Gong, L., Xu, Z., Bai, X., Wei, M., Tong, Y., Gao, Y., Chen, J., Zhou, J., & Wang, Z. L. (2011). Three-dimensional WO3 nanostructures on carbon paper: Photoelectrochemical property and visible light driven photocatalysis. *Chemical Communications*, *47*(20), 5804–5806. https://doi.org/10.1039/c1cc10389j

Zheng, Z., Huang, B., Meng, X., Wang, J., Wang, S., Lou, Z., Wang, Z., Qin, X., Zhang, X., & Dai, Y. (2013). Metallic zinc- assisted synthesis of Ti3+self-doped TiO2with tunable phase composition and visible-light photocatalytic activity. *Chemical Communications*, *49*(9), 868–870. https://doi.org/10.2217/EBO.12.465

Zhu, X., Zhou, D., Cang, L., & Wang, Y. (2012). TiO2 photocatalytic degradation of 4-chlorobiphenyl as affected by solvents and surfactants. *Journal of Soils and Sediments*, *12*(3), 376–385. https://doi.org/10.1007/s11368-011-0464-y

Zielińska, B., Grzechulska, J., Kaleńczuk, R. J., & Morawski, A. W. (2003). The pH influence on photocatalytic decomposition of organic dyes over A11 and P25 titanium dioxide. *Applied Catalysis B: Environmental*, *45*(4), 293–300. https://doi.org/10.1016/S0926-3373(03)00178-4

Znaidi, L. (2010). Sol-gel-deposited ZnO thin films: A review. *Materials Science and Engineering B: Solid-State Materials for Advanced Technology*, *174*(1–3), 18–30. https://doi.org/10.1016/j.mseb.2010.07.001

Zyoud, A., Zu'bi, A., Helal, M.H.S., Park, D., Campet, G., Hilal, H. S. (2015). Optimizing photo-mineralization of aqueous methyl orange by nano-ZnO catalyst under simulated natural conditions. *Journal of Environmental Health Science and Engineering*, 13:46.

https://doi.org/10.1186/s40201-015-0204-0